وزارة التعليم العالي و البحث العلمي

**BADJI MOKHTAR-ANNABA UNIVERSITY**
**UNIVERSITÉ BADJI MOKHTAR-ANNABA**

**جامعة باجي مختار - عنابة**

**Faculté des Sciences de l'ingénieur Année 2008**
**Département de Génie Civil**

# THESE

Présentée en vue de l'obtention du diplôme de

## DOCTORAT

# EFFECTS OF NONLINEAR DYNAMIC SOIL – STRUCTURE INTERACTION ON THE RESPONSE OF BUILDINGS

Option

Géotechniques et Structures

Par

**GOUASMIA Abdelhacine**

DEVANT LE JURY SUIVANT

| | | |
|---|---|---|
| Président : | **Pr REDJEL Bachir** | Université Badji Mokhtar – Annaba |
| Rapporteur : | **Dr DJEGHABA Kamel** | Université Badji Mokhtar – Annaba |
| Examinateur : | **Dr HADIDENE Yazid** | Université Badji Mokhtar – Annaba |
| Examinateur : | **Pr HAMMAMI Mounir** | Université de Skikda |
| Examinateur : | **Dr BENMARCE Abdelaziz** | Université de Guelma |
| Examinateur : | **Dr MOKRANI Larbi** | Université de Setif |

# Abstract

A Matlab computer program for numerical modeling is proposed for the prediction of soil-structure interaction effects on structures due to wave propagation.

A hybrid finite element formulation based on pseudo-spectral methods, that is spectral finite element method (SFEM) is used to describe the wave through soil propagation in buildings. The modeling of the soil represents the key feature of the prediction model. Both direct and substructure methods are applied to model the soil structure system, where the soil is supposed as horizontally layered visco-elastic or Mohr-coulomb half-space for which the rigorous Green's functions are derived. Nonlinearities of the superstructure and at the interface between the foundation and the soil are taken into account. Based on an indirect boundary integral method, the dynamic stiffness matrix of different foundation types at the surface of the layered half-space is calculated. This frequency dependent relation, between the structure-soil interaction forces and the displacements of the foundations, is transformed to a recursive evaluation of the forces in the time domain. This time domain analysis enables the prediction model to account for non-linear behavior in a further stage of the research. Based on the Green's functions of the layered half-space, the spectral density of the ground-borne vibrations is predicted.

The applications of the thesis demonstrate the importance of the accurate and consistent soil model both for the evaluation of the structure-soil interaction forces as well as for the prediction of the ground-borne vibrations. The prediction model is applied to identify parameters that have a large impact on the generation and the propagation of vibrations due to seismic waves.

# Résumé

On propose un programme de calcul sous Matlab, pour la modélisation numérique des effets de l'interaction sol-structure sur la réponse dynamique de ces dernières dues à la propagation des ondes. Une formulation hybride des éléments finies basée sur des méthodes pseudo-spectrales, la méthode des éléments finis spectraux est utilisée pour décrire la propagation des ondes dans le sol jusqu'au bâtiments. La modélisation du sol représente l'étape principale du modèle numérique. Les deux méthodes directes et de sous-structure sont appliquées pour la modélisation du système sol-structure, où le sol est supposé un demi-espace à multi-couches horizontales. Deux modèles de comportement du sol sont pris en compte, l'un viscoélastique et l'autre basé sur le critère Mohr-Coulomb pour lequel les fonctions de Green sont déduites. Les non-linéarités de la superstructure et à l'interface entre la fondation et le sol sont prises en considération. Se basant sur une formulation indirecte des éléments de frontières, la matrice dynamique de rigidité pour différents types de fondations superficielle ou partiellement enterrées est calculée. La relation entre les forces et les déplacements des fondations fonction de la fréquence est transformée en une évaluation récursive des forces dans le domaine de temps. Cette analyse dans le domaine des temps permet donc l'étude du comportement non linéaire du système sol-structure. Les fonctions de Green du demi-espace, sont utilisées pour déduire la densité spectrale des ondes de propagation dans le sol. Les applications numériques données démontrent la nécessité d'un bon modèle qui tient compte le plus correctement possible des effets de l'ISS. Ceci est une étape essentielle dans l'évaluation des forces d'interaction ainsi que pour la prévision des vibrations dues à la propagation des ondes dans le sol. Le modèle ainsi obtenu est utilisé pour identifier les paramètres ayant un grand impact sur la génération et la propagation des vibrations dues aux ondes séismiques.

# Acknowledgements

First of all, I must thank my supervisor Dr. Kamel Djeghaba for letting me finish my work and recommending it as sufficient for a doctoral thesis. I would also express my thanks to Dr. Erdal Şafak, of the U.S. Geological Survey and member of the American Society of Concrete Engineering (ASCE) who have provided me with good quality research papers, which have been proven to be valuable for improving my thesis.

Finally, I am very much in debt for the moral support I received from my family. Especially my wife had to suffer from much frustration, yet she was always there when I was short of thoughts, " I wanted here to be there and not here just in my mind ". I just can hope that one day I will be able to pay back for everything.

And as this is very important to me, as I am going to repeat this another time for another research work, but hopefully in a better way than the current anarchy.

# Contents

# List of Figures

# List of Tables

# Chapter 1

# 1. Introduction

## 1.1 Problem outline and motivation of research

### 1.1.1 Vibrations in structures

Vibrations in structures, especially in buildings may cause the following problems. Depending on the amplitudes of structural vibrations, the resulting may range from nuisance to occupants to life threat and full damage to buildings.

Following the new concept in structural design based on the so-called Performance Based Design (PBD), damage caused to buildings is described as a change in the properties and/or position of structural members. Among the possible consequences, we may distinguish, failure of beams and/or columns, reduction of the structural capacity of a member or the whole structure and loss of serviceability due to cracks.

The vibrations in structures can arise from many different sources among which industrial activities, construction works such as tunnel boring and earthquakes etc. These structural vibrations are well known and have been thoroughly investigated, especially in the field of structural dynamics and earthquake engineering for the case of large scale projects such as nuclear power plants and other important structures such as dams and long bridges.

The higher urbanization of the cities in the northern of Algeria, makes these cities vulnerable to such near field seismic waves, as what had happened in Boumerdes, where an earthquake of magnitude 7 have caused a lot of damages even to recent buildings. Regarding the increasing interest in building performance under severe shaking, this type of problems, i.e. soil structure interaction and near source effects is becoming more and more important.

The extension of the current Algerian code (RPA 99) [89] to include soil structure interaction and site effects has been planned. A further extension of the code to improve the performance of structures would be to include near source effects, as what had happened in Boumerdes on May 21st 2003, as mentioned earlier.

The increasing interest for the problem of soil structure interaction effects (SSI) for ordinary structures, which are the most vulnerable among the built in environment has triggered off the need for a better insight in the physical phenomena involved in SSI problems. Therefore, the development and validation of a numerical prediction model that takes into account SSI effects is treated in this thesis. Even though the validation is mainly focused on SSI, the numerical prediction model is generally applicable to other types of structural vibrations.

### 1.1.2 The utility of a numerical model

Empirical models derived from experimental tests and in situ measurements are commonly used for the study of SSI effects on structures. The application of those models is limited to situations similar to those covered by the experimental measurements. An extrapolation to different soil conditions having different characteristics has to be avoided. Furthermore, empirical models do not clarify the physical mechanisms involved in SSI problems and parametric studies can not be based on empirical models. However, empirical models continue to be used in design practice, which may result in inadequate or too conservative unsafe structures and, consequently, important economical loss.

In almost all seismic building codes, the structure response and foundation loads are computed neglecting the soil-structure interaction that is a fixed base analysis of the structure is performed. The belief is thought that SSI always plays a favorable role in decreasing the inertia forces; this is clearly related to the standard shape of code spectra which almost invariably possess a gently descending branch beyond a constant spectral acceleration plateau. Lengthening of the period, due to SSI, moves the response to a region of smaller spectral accelerations. However there is evidence that some structures founded on soft soils are vulnerable to SSI. Examples are given by Gazetas and Mylonakis [37].

This has been recognized in some codes as Eurocode 8, where it is stated clearly that "The effects of dynamic soil-structure interaction shall be taken into account in the case of:

- structures where P-δ effects play a significant role;
- structures with massive or deep seated foundations;
- slender tall structures;
- structures supported on very soft soils, with average shear wave velocity less than 100 m/s.

The effects of soil-structure interaction on piles shall be assessed..."

In addition, an annex to the code describes the general effect of SSI and a specific chapter analyzes its effects on foundations and the way to deal with it. To the best of our knowledge Eurocode 8 is the only code which recognizes the importance of kinematic interaction for foundations, to quote:

"Bending moments developing due to kinematic interaction shall be computed only when two or more of the following conditions occur simultaneously:

- the subsoil profile is of class C (soft soil), or worse, and contains consecutive layers with sharply differing stiffness,
- the zone is of moderate or high seismicity, $\alpha > 0.10$,
- the supported structure is of importance category I or II."

Note that implicitly for "normal" soil profiles and ordinary buildings kinematic interaction need not be computed.

The simplest way to consider SSI effects is to assume that the building is supported by a rigid foundation. This results in a minimum number of additional degrees-of-freedom (three translations and three rotations), but may lead to restrictive and too simple representation of the real building. Studies which model the flexibility of foundations are rare [29] [50] and difficult to evaluate in the absence of strong motion records from in situ experiments. As far as we know, there exists no strong motion records program to document distortions and warping of foundations of structures during passage of seismic waves [108].

The extent to which SSI alters the apparent frequencies of the system response and changes of the time functions of absolute and relative displacements, rotations, shear forces and bending moments in the structure ranges from negligible to profound, and depends mainly on the relative stiffness of the soil and the structure. Recordings of strong structural motion show that destructive shaking is usually accompanied by nonlinear response of the foundation soils [78] [80], and that the time dependent changes of the apparent frequencies of response are usually accompanied by significant contribution of SSI [81]. Since the success of base-isolation systems, control of structural response, and of health monitoring depends on accurate representation of the anticipated and of recorded motions, it is clear that the nonlinear SSI phenomena must be included in the analysis.

Experimental studies of SSI are best conducted in full-scale, in actual buildings during micro tremors [69] [70], forced vibrations [20], and earthquake excitation [46]. It is difficult to conduct SSI tests in laboratories, not only because of the constraints imposed by the need to satisfy to similarity laws, but mainly because it is almost impossible to model the half space boundary conditions for the soils.

Mathematical modeling of structures, for the purpose of response analyses, aims to find those representations which will satisfy all the modeling requirements and the constraints of the available analytical tools.

For analytical representation of the incident waves, and for linear response analyses, the foundation soil has to be of simple geometry. With the analytical approach, it is practical to consider only simple topographic irregularities [40] [109] and simple soil and alluvium layers [51] [52]. More complicated surface topography and layering must be represented by finite element or finite boundary models.

Simple symmetric structures can be modeled by analytical methods and can be analyzed by wave propagation approach. Geometrically irregular structures and those which are expected to experience nonlinear response must be modeled by lumped masses, finite elements or by other discrete representations [85]. Simple surface or embedded foundations can be approximated by rigid slabs, when the soil is relatively soft and when the foundation and the structure are expected to experience only small relative deformations. However, it is difficult to predict intuitively how realistic is such an assumption and the decision should be guided by data and experience from full-scale tests on similar structures. Soft (flexible) foundations can be represented by discrete lumped mass interconnected foundations [87], and this can be combined with finite element representation of the structure.

## 1.2 Objectives

The main objective of the present research is to validate a model for the prediction of seismic free field wave propagations to a structure model accounting for dynamic SSI effects. The second objective is the process of implementing a coupling between the finite element method (FEM) and the spectral element methods (SEM) for nonlinear soil structure interaction (SSI) problems in MATLAB. This results in a new hybrid method called spectral finite element method (SFEM) which will be used for SSI problems, and a new Matlab Toolbox is obtained. The validation of the numerical model for the prediction of seismic free field wave propagations to a structure model accounting for dynamic SSI effects is also verified. It is assumed that the forces transmitted from the structure to the soil and the incident wave field are not influenced by the presence of adjacent structures. This uncoupling of the SSI problem allows to apply a substructure approach, that is a solution in two stages, the first one dealing with the computation of the incident wave field, the second one coupling the calculated incident free field wave motion to the structure, this approach is best suited for nonlinear time analysis. The response of the structure due to the incident wave field is calculated using a subdomain formulation for dynamic SSI [2]. The structure having a finite dimension and the semi-infinite soil medium are treated by means of the spectral finite element method (SFEM), where special absorbing boundary conditions, the so-called perfectly matched layers (PML) are introduced and used with SFEM. An attempt has also been made to use BEM for the semi-infinite soil medium, using the Green's functions for the homogeneous or the layered half-space, which automatically takes into account the radiation condition.

This kind of problem (SSI) belongs to the field of earthquake engineering, where the response of the structure is calculated due to an incident wave field where the frequency content of typical earthquakes is in between the range 0-10Hz.

The third objective of this research is the validation of the resulting model for wave induced vibrations in buildings by means of an extensive parametric study based on a large number of case studies and with one building with known dynamic characteristics and varying soil conditions. A detailed investigation of input parameters in particular the dynamic characteristics of the building, the foundation shape and flexibility and the dynamic soil characteristics has been performed.

The use of a full Finite Element (FE) model for a single building is advocated to assess vibration problems. In practice, it used to be that FE modeling and dynamic SSI analysis is only performed for buildings of considerable societal importance (nuclear power plants, hospitals) and for critical work spaces as micro-electronics laboratories and rarely for ordinary buildings, that is residential buildings.

This particular problem is considered, and this case was well documented within the frame of experimental studies through PEER and NEES reports. Furthermore, building a complete structural model allows to obtain a better insight in the decay of vibrations from the far field (free field) to the near field and the soil foundation (this is part of the soil adjacent to the foundation where most of the nonlinearities will happen), as well as the amplification per story over the height of the building. This would not have been possible with a simple 1D model of the structure on a half-space.

The original contributions of this research work are the following:
A clear overview of the numerical modeling for wave induced vibrations in buildings is given. For this purpose, a hybrid SFEM is used and a Matlab Toolbox grouping all the necessary programs and tools is obtained and validated. Plane incident waves are assumed in the modeling of SSI due to earthquakes as the distance between the epicenter and the region of interest is usually very large. An alternative implementation method for the incident wave field may be easily deduced and introduced in the numerical model to account for ambient vibrations, where the frequency content is in the range (1-80Hz) compared to the frequency content of typical earthquakes which is in the range (0 - 10Hz) as mentioned earlier.

A parametric study to determine factors influencing wave propagation induced vibrations in buildings is undertaken. The influence of the type of foundation on the overall structural response is thoroughly investigated. The availability of test results of a seven-storey reinforced concrete hotel building located in the city of Van Nuys in Los Angeles [80] enabled us to perform a large number of case studies, such as the effect of SSI in vibration isolation.
Matlab numerical computer programs are also developed for the following methods: FEM, BEM, FEM-BEM as they serve for comparisons with the new method SFEM, which is introduced recently to SSI problems. Theses Matlab scripts are intended to be inserted at a latter stage into Matlab main program as an independent toolbox solving SSI problems.

## 1.3 Organization of the text

A numerical model for wave induced vibrations in buildings is presented.

In Chapter 2, the subject is introduced and it is explained where this work fits in the state-of-the-art. The original contributions are emphasized, classical methods such FEM, BEM are presented as well as indirect and hybrid methods based on wave propagation. The new spectral method is presented where it will be coupled to FEM to form a new method applied for the first time to soil structure interaction analysis.

In Chapter 3, basics of wave propagation in the soil is introduced. Conservation law, conservation of mass and momentum as well constitutive law in the presence of various wave types are introduced to form the variational formulation of the problem of the numerical model.

In Chapter 4, we introduce and validate a pseudo-spectral method based on the tensorial differential formulation of the equations of elastodynamics, adapted to the treatment of half-spaces and layered soil domains. We show this for some application cases, based on Matlab codes developped for this purpose. We highlight the interesting effects related to topography, and underline also its intrinsic limitations. We deduce the need for using a more flexible method than the traditional differential formulation (finite differences, spectral or pseudo-spectral methods) for the treatment of realistic cases based on a variational method.

In Chapter 5, for the solution of wave equations in the presence of unbounded domains, it is necessary to use absorbing boundaries to somewhat limit the domain under consideration and by the same time simulate the nature for unbounded domains. For this reason, highly accurate absorbing conditions called perfectly matched layers have been developed in the context of time harmonic elastodynamics by utilising insights obtained from the electromagnetic fields. This new concept has been developed and implemented into a Matlab computer code and later on will be implemented in the spectral finite element Matlab code.

Chapters 6 and 7, constitutes the heart of this thesis, we introduce and develop a variational formulation of a high nature of the equations of elastodynamics, known as "the spectral finite element method", and we highlight its properties on various traditional problems of increasing complexity (Lamb's problem, problem of Garvin, Rayleigh waves…). Then we present the application of this

method at more complex models taking into account the presence of the structure, for which strong effects in particular related to topography are highlighted. We obtain in particular strong local amplifications of the acceleration and displacement fields in such models.
We will analyze the results provided by the of the spectral finite element method (SFEM) on a certain number of complicated models. We finish this study with by calculating soil structure interaction effects in 2-D structures, for which reference solutions exist .

In Chapter 8, a vast parametric study is performed; some conclusions on the effect of dynamic soil structure interaction (SSI) and of the influence of the type of foundation, building height and soil properties are drawn. SFEM, is then used for a real 5 storey reinforced concrete building.

In Chapter 9, important conclusions of this work are recapitulated and some suggestions for future research are given.

All the work done using SFEM has been implemented in a Matlab computer program developed in the course of this thesis work.

## Chapter 2

# 2. State of the art of soil-structure-interaction methods

This chapter gives an overview of the state-of-the-art of the used deterministic methods for solving soil-structure-interaction (SSI) problems. This chapter considers the classical tools, such as the FEM and the BEM, and indirect methods, such as the spectral finite element method (SFEM).

The FEM will be described in more detail than the other methods, because, most state-of-the-art methods are based on the FEM, and the FEM is coupled to the spectral element method in later stage and finally the FEM is used in numerous validation examples throughout this dissertation. The SFEM, will be used in this thesis, is the main topic and is considered only briefly here in order to show its relationship with the other methods. In chapter 6, the SFEM will be studied in more detail including the theoretical background, the convergence and the accuracy.
This overview makes a distinction between uncoupled systems, either structure or soil, and coupled structure-soil systems. The coupled structure-soil problems are considered for both the FEM and the SFEM. The BEM is discussed with two extensions. Various generalizations and extensions of the FEM have been proposed in literature, which are presented in a structured manner in section 2.3. The last section considers the indirect spectral methods.

## 2.1 Finite element method

### 2.1.1 Introduction

The FEM has proven to be one of the most suitable tools for solving many real-life engineering problems, which consist of finding the spatial distribution and possibly the temporal distribution of field variables in a continuous medium. Examples of such engineering problems can be found in the field of continuum solid mechanics, fluid mechanics and acoustics. Furthermore, the FEM is capable of handling multi-physical problems, such as the one at hand where wave propagates from the soil medium to the structure, referred generally as soil-structure wave based methods. The considered problems are described mathematically by a set of partial differential equations (PDE) together with a set of appropriate boundary conditions and initial conditions.

### 2.1.2 FEM strategy

If one assumes that either a steady-state or static linear mathematical model is available, which describes the spatial distribution of the field variables accurately. Then, the exact solution of this model is approximated by employing the following FEM strategy.

1. Subdivide the continuous domain in a finite number of sub-domains, i.e. the finite elements.

2. Within each element, approximate the solution by a linear combination of simple polynomial basis functions or interpolation functions. The contribution of each basis function forms a degree of freedom (DOF) of the FE model. In general, the DOF are nodal values of the considered field variables.
3. The approximation solution violates the governing set of PDE and possibly some boundary conditions. Enforce the residuals on these relations to zero in some integral way. This can be achieved by application of either a variational principle, a weighted residual approach or a global physical statement (e.g. the principle of virtual work).
4. Apply the Galerkin approach to the integral description obtained in the previous step in order to transform the continuous element model in a set of linear algebraic equations, which is the element FE model.
5. Assemble all element FE models to obtain the global FE model.
6. Solve the FE model for the unknown DOF. The approximation solution is then already available in discrete locations, because the DOF are nodal values of the considered field variables. Approximate the field variables in arbitrary locations by application of the element basis functions.

### 2.1.3 Characteristics of FEM

The discussion on the FEM is concluded with an overview of the advantageous and disadvantageous characteristic features of the method.

Geometrical flexibility:
The FEM is unrestricted with respect to geometrical features of the boundary of the considered problem domain due to the application of the isoparametric mapping procedure.

Sparsely populated model:
The FE models are sparsely populated, which allows one to use very efficient skyline solvers. For uncoupled problems the FE models are symmetric, which even further improves the efficiency of skyline solvers.

Frequency independent sub-matrices:
The mass matrices, the stiffness matrices and the structure-soil coupling matrix are real and frequency independent, which allows one to use the modal superposition technique based on a standard eigen-value decomposition. This improves the efficiency significantly for a broadband analysis of uncoupled problems. The efficiency improvement is less pronounced for coupled structure-soil problems. This may be compensated by the application of the component mode synthesis [18].

Model size:
The FE models are large. This is certainly the case for coupled structure-soil problems, which require the simultaneous consideration of a large structural FE sub-model and a large soil FE sub-model. For real-life engineering problems these FE models may contain millions of DOF.

Accuracy:
The FE approximation error is controlled for low frequencies by the "rule of thumb" $kh = 1$. This rule is not sufficient for increasing frequencies. Due to the large but limited available computational resources, the application of this type of rules restricts the FEM to low frequency applications. Furthermore, the approximation accuracy decreases for secondary field variables.

Complex and frequency dependent submatrices:

The soil damping matrix is generally complex and frequency dependent through the presence of a complex and frequency dependent impedance value. The efficiency of the modal superposition technique decreases due to this property.

# 2.2 Boundary element method

## 2.2.1 Introduction

The BEM is a well established alternative method for the FEM for various engineering problems. The application of boundary integral formulations forms the basis of the BEM. These boundary integral formulations relate the field variables in the problem domain  to boundary variables. In this way, the BEM follows a two step procedure.

- First, the boundary variables are approximated by application of a FE type of strategy to a set of boundary integral formulations.
- Then, the field variables are recovered by application of the boundary integral formulations with the approximated boundary variables.

Two main classes of BEM are recognized, namely the direct BEM and the indirect BEM.

- The direct BEM is based on the direct boundary integral formulations, which relate the field variables to physically meaningful boundary variables. For example in wave based SSI systems, the domain pressure is related to both the boundary pressure and the normal velocity. The direct BEM is applicable to either bounded problems or unbounded problems with a closed boundary surface (3D) or curve (2D).
- In case of either combined bounded/unbounded problems or unbounded problems including an open boundary, the indirect BEM is required. This class of BEM uses indirect boundary integral formulations, which relate the field variables to boundary potentials, which do not have a direct physical meaning. For example in SSI systems, the domain pressure is related to a distribution of single layer and double layer potentials at an open boundary.

Since this research considers bounded problems only, namely interior SSI problems or bounded structural dynamic problems, only the class of direct BEM is discussed here. More specific, this section discusses the application of the direct collocation BEM to interior SSI problems.

## 2.2.2 Direct boundary integral formulation

The direct boundary integral formulation relates the pressure at a position in a given domain , which is governed by the homogeneous Helmholtz equation, to the pressure and the normal velocity at position at the boundary.

The Green’s kernel function associated with free field response of an acoustic source at a given position is needed, this makes use of Hankel function of the second kind.

If a wave source at a position located inside the domain, the free field response in terms of green's functions takes its effect into account. This response is subtracted from the overall domain pressure field such that the resulting pressure field satisfies the homogeneous Helmholtz equation and the corresponding boundary conditions.

## 2.2.3 Boundary variable approximation

A similar strategy, as used in the FEM, is used for the boundary variable approximation. The boundary is subdivided in a large number of small boundary elements. Within each boundary element, a linear combination of simple polynomial basis functions approximates the boundary variables.

The same set of local basis functions stored in a row vector are used both for the pressure approximation and for the normal velocity approximation. This is a reasonable choice since the continuity requirements for both boundary fields are the same.

The application of the direct boundary integral formulation states that the pressure at each point in the domain depends on the boundary pressure and normal velocity of all boundary points. Therefore, the local boundary variable approximations are assembled resulting in the global boundary variable approximations.

### 2.2.4 Solution procedure

The BE model consists of *n* algebraic equations in 2 *n* DOF. In order to obtain a unique solution, the BE model requires n constraint relations, which follow from the incorporation of the boundary conditions. The pressure approximation in the problem domain follows from the two step procedure mentioned before. First, the BE model is solved. Then, the pressure approximation results from application of the direct boundary integral formulation using the boundary variable approximations.

### 2.2.5 Characteristic features of BEM

The direct collocation BEM applied to interior SSI problems exhibits the following features.

- The BE models are small compared with FE models since their construction involves only the approximation of a small set of boundary variables.
- The BE model matrices are fully populated since all boundary variable DOF influence the pressure in each domain position through the application of the direct boundary integral formulation.
- The BE model matrices are non-symmetric by definition.
- The BE model matrices depend implicitly on the wave-number *k*. Therefore, the application of a modal superposition technique based on a standard eigenvalue decomposition is not possible.
- The BE model matrices are complex due to the application of the Green’s kernel function.
- The BE model generation requires special care for the integral evaluation due to the singularity of the Green’s kernel function.
- The velocity field approximation in the problem domain does not involve a loss in accuracy as in case of the FEM since the derivation of the direct boundary integral formulation can be performed analytically.
- The direct collocation BEM can hardly compete with the FEM for interior SSI problems.

The strength of the direct collocation BEM, or of the BEM in general, because of the fully populated matrices, and are very difficult to implement in computer programs. Since these topics are beyond the scope of this dissertation, the BEM is not considered further in the sense that the newly developed approaches are verified using analytical solutions or FE results only.

Although the direct collocation BEM cannot compete with the FEM for bounded problems and although the BEM is not considered in the various numerical validation examples, the remainder of this section discusses briefly two extensions of the BEM reported in literature.

### 2.2.6 Extension of BEM

The BE model generation is computationally demanding. The associated model matrices are fully populated, complex and wave-number *k* dependent. Furthermore, the evaluation of the involved boundary integrals needs special attention due to the singularity of the integrands. This section considers two extensions of the BEM which are computational less expensive.

#### 2.2.6.1 Regular grid method

Bespalov [7] proposes the regular grid method (RGM) for electro-magnetic scattering problems and extends its application to exterior acoustic problems. The basic idea is to split the Green's kernel function, namely in a singular part and in a regular part. Subsequently, the BE model matrices split in two parts too. The singular part of the Green's kernel function has only a compact support. The corresponding BE model matrices are computed in the conventional way. However, due to the compact support of the Green's kernel function, these BE model matrices are sparsely populated.
The regular part of the Green's kernel function is continuous and it is therefore well suited for approximation. For that purpose, an auxiliary regular grid, consisting of a 4 × 4 × 4 node cell, is selected for each boundary point. The interpolation of the nodal values forms the regular part of the Green's kernel approximation. The corresponding BE model matrices are approximated. These approximate BE model contributions are sparsely populated due to the local approximation defined on the auxiliary regular grids. Due to the sparsity of the global approximate BE model, efficient skyline solvers can be used.

#### 2.2.6.2 Fast multipole BEM

Instead of using a local approximation of the Green's kernel functions, the fast multipole BEM (FM-BEM) uses two different expansion systems, one for the near field response pattern of a source point and one for the far field response pattern [95]. The basic concepts of the fast multipole algorithm are explained below.

- The contributions of the boundary variables in a patch of boundary elements are accumulated as multipole coefficients in one representative point of the patch.
- The wave response at each representative point is computed for the multipole excitation of all representative points.
- The wave response at each representative point is translated to the boundary DOF of all elements in the corresponding patch. These three steps represent the far field effect.
- For each boundary DOF in a patch of boundary elements, the contributions of the boundary variables in the considered patch, and in its neighboring patches, are accounted for in the conventional way. This step represents the near field effect.

The efficiency of the FM-BEM is improved further by implementing this fast multipole algorithm hierarchically, where the near field and far field effect of patches are combined using additional representative points. This results in the multilevel FM-BEM. Schneider compares the BEM and the multilevel FM-BEM with respect to (i) memory requirements, to (ii) computational costs and to (iii) accuracy. The numerical experiments illustrate

- that both the required memory and the computational costs reduce substantially in case of the extended BEM while the accuracy is still of an acceptable level,
- that the accuracy depends more on the complexity of the boundary than the multilevel FM-BEM,
- and that, in case of short wave predictions, this reduces to the direct BEM whereas the multilevel FM-BEM is still more efficient than the conventional BEM.

## 2.3 Generalization and extension of finite element method

### 2.3.1 Classes of FEM

The FEM is restricted to low-frequency applications due to vastly increasing model sizes, which are required to control the approximation error. For low frequencies, the approximation error is governed mainly by the interpolation error. However, the interpolation error gets polluted for increasing frequencies. The erroneous prediction of the numerical dispersion causes this pollution effect. Therefore, by reducing or even eliminating the dispersion error, the FE accuracy is improved significantly at higher frequencies, which allows one to enlarge the frequency application range of the FEM.

Many classes of improved FEM have emerged, and this section discusses several of those classes applied to either uncoupled interior SSI problems or uncoupled continuum mechanical problems, namely

- stabilized FEM,
- generalized FEM including meshless methods,
- multi-scale FEM,
- and the classical FEM with a modified integration rule.

Besides these classes of improved FEM, this section discusses some domain decomposition or sub-structuring approaches, since these approaches allow (i) an enlargement of the overall FE model sizes and (ii) high efficient parallel implementations.

The first results are very promising. Therefore the implementation of this new approach may improve commercial FE codes for SSI substantially with only a minimal amount of efforts.

### 2.3.2 Domain decomposition

The section on the generalization and on the extension of the FEM is finished by briefly considering some domain decomposition strategies. Domain decomposition allows one to investigate larger problems. For that purpose, the large problems are decomposed in several smaller sub-problems.

Domain decomposition methods combine ideas from various disciplines, such as from the theory on PDE, structural dynamics, linear algebra, calculus and graph theory. Obviously, the subject of domain decomposition is too extensive to discuss it thoroughly in this dissertation. Therefore, this section refers only to some interesting techniques.

## 2.4 Indirect Trefftz method

### 2.4.1 Introduction

Already in 1926, Trefftz proposes the use of this a priori knowledge in the definition of approximate solutions. The approximate solutions, used in the so-called Trefftz approach, satisfy the governing domain equations but violate the boundary conditions. Originally, the Trefftz approach is introduced as a counterpart for the Rayleigh-Ritz approach in order to obtain an error bound on the Rayleigh-Ritz prediction in case of a potential problem.

Only half a century later, researchers have picked up the idea of Trefftz again as they recognize its potential advantages in numerical prediction methods. This has led to a class of numerical methods which are generally called Trefftz methods. The reader is referred to the introduction in [55] for a historical overview of the development of the Trefftz methods. Kita and Kamiya [57] provide a detailed overview of most accepted Trefftz methods of which this section only considers a small portion.

This section discusses only indirect Trefftz methods. The term ‘indirect’ denotes that the DOF of the associated model have no direct physical meaning. The computation of the indirect Trefftz approximation solution always requires an additional post-processing step. The SFEM, which forms the topic of this research project, belongs to the class of indirect Trefftz methods. In addition to the indirect Trefftz methods, a whole class of direct Trefftz methods exists. The term ‘direct’ denotes that the associated model uses physically meaningful DOF. Direct Trefftz methods are based on a weighted residual formulation of the governing equations using weighting functions, which satisfy the domain equations a priori (Trefftz functions). After integration by parts, the weighted residual formulation consists of boundary integrals only. The involved boundary fields are approximated in a similar way as in the direct

BEM. However, instead of using singular Green's kernel functions as weighting functions, the direct Trefftz methods use a linear combination of regular Trefftz functions. Since the SFEM does not belong to the class of direct Trefftz methods, these methods are not considered further.

This section considers three classes of indirect Trefftz methods, which have been applied in the research field of either structural dynamics, acoustics, wave propagation or structure-wave based methods.

- The first class consists of the hybrid-Trefftz FEM (HT-FEM). This method is based on an indirect approach to couple nonconforming Trefftz fields using the Lagrange multiplier technique. The principles behind the HT-FEM are well suited for the coupling of the SFEM to the FEM.
- The second class consists of methods, which apply a direct approach to couple nonconforming Trefftz fields based on either a least-squares approach, a weighted residual approach or a variational principle. The SFE is a member of this class.
- The third class consists of the spectral FEM. This method combines the indirect Trefftz approach with the dynamic stiffness method. Some computational efficient mid frequency methods have been derived from the spectral FEM for structural dynamic applications.

## 2.4.2 Hybrid-Trefftz FEM

Jirousek report on the first attempts to incorporate the indirect Trefftz method in a FE framework which resulted in the hybrid-Trefftz FEM (HT-FEM) [45]. Since the late 1970s, the HT-FEM has been applied to various types of engineering problems, which has been reported in many publications. However, the efforts made to apply the HTFEM to steady-state dynamic problems are limited. Two examples from literature are given here. Farhat, Harari, and Hetmaniuk [31] and Farhat, Wiedemann-Goiran, and Tezaur [33] derive a HT-FEM for the Helmholtz problem, which they call the discontinuous Galerkin method and Cisma¸ siu [103] propose the application of the HT-FEM for elasto-dynamic applications.

The principles behind the HT-FEM are well suited for the coupling of the FEM and the spectral methods. This paragraph merely summarizes these principles based on the following HT-FEM modelling procedure.

- The problem domain is subdivided into finite elements.
- In each element a linear combination of Trefftz functions, extended by appropriate particular solution functions, approximates the exact solution.
- The field approximation satisfies the governing domain equations exactly but violates the boundary conditions and the inter-element continuity conditions. The application of the Lagrange multiplier technique enforces the involved residuals to zero in an integral sense. This requires the introduction of an independent boundary field for each element, the so called Lagrange multiplier. It consists of a linear combination of independent basis functions.
- All condensed element models are assembled using the standard procedure of the direct stiffness method, as implemented in standard FE codes.
- The global hybrid-Trefftz FE model is solved for the unknown Lagrange multiplier contribution factors. The field variable approximations inside each element are obtained in a post-processing step.

The HT-FEM controls the pollution effect inherently better than the FEM. However, the application of a priori knowledge of the exact solution leads to ill-conditioned numerical models. This is a common feature of all indirect Trefftz methods [121]. However, by taking special care for the definition of both the Trefftz functions and the Lagrange multiplier basis functions, the HT-FEM is capable of providing accurate predictions for a wider frequency range than the FEM. Furthermore, a hybrid-Trefftz element is compatible with classical finite elements. This suggests that the indirect coupling procedure based on the Lagrange multiplier technique can be used to couple the FEM and the spectral element methods SEM too.

## 2.4.3 Methods based on direct coupling of nonconforming Trefftz fields

This section discusses three indirect Trefftz methods, which are based on the indirect coupling of nonconforming Trefftz fields, namely

- the SEM,
- the Trefftz least-squares FEM (TLS-FEM).

These methods follow the same modelling procedure but they differ with respect to (i) the application, to (ii) the applied Trefftz fields, to (iii) the applied integral formulations and to (iv) some implementation specific features.

### 2.4.3.1 Modelling procedure

The modelling procedure of the indirect Trefftz methods, considered in this section, is as follows.

- The problem domain is subdivided in non-overlapping convex Trefftz subdomains.
- In each Trefftz subdomain, a similar Trefftz approximation is used as in case of the HT-FEM with the unknown Trefftz DOF stored in column vectors.
- As mentioned before, the Trefftz approximation satisfies the governing domain equation exactly but violates the boundary conditions and the continuity conditions between two adjacent subdomains (non-conforming Trefftz fields). The application of some integral formulation, which is method dependent, enforces the violation on the boundary and continuity conditions to zero in an averaged way. The Trefftz DOF in a given subdomain are coupled directly to the Trefftz DOF in an adjacent subdomain via the coupling matrix and the associated coupling vector. The Trefftz component model is formulated in a given subdomain is connected with one subdomain only. The extension to multiple connected subdomains is straightforward.
- The assembly of all Trefftz component models is simple bookkeeping procedure, which does not involve the add operation as in case of the direct stiffness method employed by the FEM and the HT-FEM.
- The global Trefftz model is solved for the unknown Trefftz DOF. The field variable approximations inside each Trefftz subdomain are obtained in a post-processing step.

### 2.4.3.2 Wave based method

The WBM [26] has been applied to many steady-state dynamic problems, such as plate bending problems, acoustic problems and structural-wave problems. Several technical papers are available in literature discussing these WBM applications, [112] [86]. These papers illustrate that the WBM is capable of providing more accurate results in wider frequency range than the FEM. The method is named after the set of Trefftz functions, which consists of propagating and evanescent wave functions. These wave functions are defined for large convex subdomains. Model refinement consists of enlarging the basis of Trefftz functions per subdomain rather than increasing the number of subdomains.

The application of either a least-squares approach or a weighted residual approach enforces the violation of the boundary and continuity conditions to zero. This results in two slightly different WB models. For example in an acoustic application, the pressure continuity is enforced in the WB model generation for a given subdomain and the velocity continuity in the WB model generation for another subdomain.

### 2.4.3.3 Trefftz least-squares FEM

Stojek propose the TLS-FEM for the analysis of a static mechanical problem, and later he extends the application of the TLS-FEM to the Poisson problem and to the Helmholtz problem [100]. In case of the Helmholtz problem, the TLS-FEM uses generalized harmonic functions as Trefftz functions. Additional special purpose functions are introduced for non-convex subdomains which increase the accuracy substantially. Stojek investigates the convergence of the TLS-FEM by increasing both the number of subdomains and the number of Trefftz functions inside each subdomain. In both cases the TLS-FEM outperforms the FEM.

Originally, the TLS-FEM is based on a least-squares approach where all continuity conditions are enforced for each subdomain in the TLS-FEM model generation. In case of the WBM only half of the continuity conditions are enforced per subdomain. Later on, Stojek introduces the TLS-FEM based on a similar weighted residual approach as used in the WBM. The TLS-FEM may be implemented easily in a standard FE program. This requires the introduction of an additional FE mesh, which allows a standard assembly procedure of the direct stiffness method.

#### 2.4.3.4 Variational theory of complex rays

The variational theory of complex rays (VTCR) has been applied for elastodynamic problems and for steady-state plate bending problems only [61]. These references illustrate that the VTCR provides the same level of accuracy in the mid frequency range as the FEM, however with substantially less computational efforts.

The VTCR is based on a two-scale Trefftz approximation similar to the generalized FEM. A fine scale approximation, which consists of highly oscillatory interior modes, edge modes and corner modes, is multiplied with a coarse scale solution consisting of polynomial functions. Opposed to the generalized FEM, this product satisfies the domain equations exactly (Trefftz functions). The application of a variational principle enforces the violation of the boundary and continuity conditions to zero. At the interface between two subdomains, the variational principle divides the virtual transmission energy equally over the two subdomains. This implies that all continuity conditions are enforced for each subdomain similar to the TLS-FEM. The spatial distribution of the field approximation loses physical meaning in the mid frequency range. The effective quantities in this frequency range are spatial averaged values of the displacements, the elastic energy, the kinetic energy and the dissipation power. The VTCR approximates these effective quantities. These approximate effective quantities are computed in the postprocessing step.

### 2.4.4 Spectral element method

The third class of indirect Trefftz methods, considered here, is formed by the spectral element method (SEM). This method combines the indirect Trefftz approach with the dynamic stiffness method [61] for steady-state structural dynamic analyses. The objective of these analyses is to predict the mechanical wave propagation through a built-up structure. Since the dynamic field variables are represented in terms of frequency and wavenumber spectra, the dynamic stiffness method is referred to as the SFEM.

The SFEM is a very efficient numerical method, but its application is limited to built-up structures of regularly shaped components only. A derived spectral FEM has emerged to overcome this drawback, namely the waveguide FEM, which is considered briefly in this section.

#### 2.4.4.1 Spectral FEM

The SFEM combines the Trefftz approach with the direct stiffness method in the sense that the submodels or elements are assembled as in the standard FEMwhile the basis functions satisfy the domain equations exactly. Similar to the classical FEM, the spectral FEM is based on a variational principle. Two types of problems are considered, namely (i) problems, which are governed by an ordinary differential equation in one independent spatial variable, and (ii) problems, which are governed by a partial differential equation in two or three independent spatial variables.

First consider problems, which are governed by an ordinary differential equation in one spatial variable, for example, the wave propagation through beam structures. The SFEM modelling procedure is as follows.

- The 1D problem domain is subdivided in many finite elements, such that all geometrical, material and mechanical discontinuities occur at the element interfaces.
- In each element, a homogeneous ordinary differential equation governs the steady-state dynamic response. The exact solution consists of a finite number of homogeneous solution functions. These

functions are linearly combined to obtain basis functions for which the corresponding contribution factors are nodal values of the field variables stored in a column vector.

- The application of a variational principle results in a spectral element model.
- All spectral element models are assembled by application of the direct stiffness method.
- The solution of the global spectral FE model gives the exact nodal solutions of the field variables.

The exact solutions inside the elements are obtained in a post-processing step. Lee and Lee [62] illustrate that the SFEM outperforms the classical FEM also in case of a distributed load over the 1D elements although it does not provide exact solutions.

Next consider problems, which are governed by a partial differential equation in two or three independent spatial variables, for example, the wave propagation through plate structures. The SFEM modelling procedure is similar to its application for beam structures. However, in case of unloaded homogeneous plate elements, the exact solution consists of an infinite number of homogeneous solution functions. In order to cope with this infinite set, the second and third step in the modelling procedure are modified as is indicated below.

- The SFEM requires the subdivision in rectangular plate elements, which are aligned in the x-direction. Furthermore, the boundary conditions do not vary in the x-direction. In that case, the exact solution can be expanded by an infinite set of y-dependent wave functions, each multiplied with a finite number of *x*-dependent wave functions. The unknown contribution factors of each wave function is expressed in terms of the boundary values at the edges oriented in the y-direction.
- The application of a variational principle results in the spectral element model, which is assembled using the direct stiffness method.

In practice, the infinite set of wave functions is truncated in order to allow the implementation in a computer code. Therefore, the SFEM provides only approximate solutions in general. Using perfectly matched layers (PML) [6] [98] will overcome these shortcomings and improves the results. Due to the incorporation of a priori knowledge of the exact solution by application of the wave function, the SFEM is more efficient than the FEM.

## 2.5 Conclusions

This chapter gives an extensive overview of the state-of-the art of deterministic computer aided engineering tools for the steady-state dynamic response analysis of (i) interior acoustic problems, of (ii) plate bending problems and of (iii) interior structural-acoustic problems. The most accepted tool for these type of analyses is probably the FEM. Section 4.1 reviews the FEM where its application to interior wave propagation problems gets most attention. Not only is the FE modelling procedure expanded in detail, but also the convergence and the accuracy of the method are discussed thoroughly.

The investigation of the accuracy reveals that the FEM suffers from the pollution effect caused by the dispersion error. In order to control this pollution effect, which gains importance at increasing frequencies, a vastly growing number of elements is required. This feature restricts the application of the FEM to the low frequency range. Several generalizations and extensions of the FEM try to control the pollution effect more efficiently by reducing the dispersion error in order to enlarge the low frequency application range. This is achieved by

- stabilizing the weak form of the weighted residual formulation,
- incorporating a priori knowledge of the exact solution in the approximation space, either in a multiplicative way or an additive way,
- or by simply shifting the Gauss points for the integral evaluation to unconventional locations.

The occurrence of the dispersion error cannot be removed by these measures, but the resulting improved FEMs suffer less from the pollution effect than the classical FEM. An alternative way to extend the frequency range of the FEM is the application of domain decomposition or substructuring. This approach is based on the idea of divide and conquer: solving many small problems can be computational less expensive than solving a few large problems. An additional advantage of the domain decomposition is that it is well suited for parallelization.

Another well established, deterministic tool for steady-state dynamic problems is the BEM. This method is based on boundary integral formulations, which relate the field variables to a set of boundary variables. Since only a set of boundary variables needs to be considered, the involved model sizes in the BEM are small compared with the FEM. However, the computational efficiency of the BEM is most pronounced for unbounded problems, which are not consider in this research project. Already in 1926, Trefftz proposed the use of a priori knowledge of the solution in numerical methods. In the late 1970s, researchers started to develop methods based on his idea, which are referred to as Trefftz methods. The key feature is to apply an approximate solution, which a priori satisfies the governing domain equations but which violates the boundary conditions (indirect Trefftz methods). Several indirect Trefftz methods are reviewed, which are categorized as follows

- the hybrid Trefftz FEM,
- the methods based on the direct coupling of nonconforming Trefftz fields, such as the WBM,
- and the spectral FEM.

All indirect Trefftz methods suffer inherently less from the dispersion error than the FEM with all its extensions and generalizations. Therefore, these methods have the potential to widen the frequency application range of the low-frequency deterministic methods. This research focuses on the further development of the SFEM, because the SFEM is applicable to a wide range of interior structural-wave based problems.

Chapter 3

# 3. Wave propagation in an elastic medium

## 3.1 Introduction

As soon as one is interested in the propagation of waves in real structures, it is necessary to resort to numerical methods to solve the equations of elastodynamics in the medium considered. Indeed, we know analytical or semi-analytical solutions with these problems of propagation only in extremely simple cases (homogeneous models or formed by plane layers for example). Since the beginning of the 1970s, with the advent of the data-processing techniques and the spectacular increase in the capacities of computers, as well from the point of view of their computing speed, as well from the point of view of their memory size, sophisticated numerical techniques were born.

Approximate methods, such as the ray theory for example, based on a high frequency approximation, or methods calculating the whole wave field (finite differences, spectral and pseudo-spectral methods, finite elements, integral methods…) have made it possible to make relatively easy the calculation of synthetic seismograms in 2D complex structures and to approach calculation in 3D structures.

In the last few years, it appeared clearly, that the majority of the above mentioned methods, although very effective in many cases, suffered from intrinsic limitations which restricted the application to realistic models. Indeed, we may ask the following question: if we wish to calculate the whole wave field propagating in a 2D model or a complex 3D structure, presenting for example non-plane layers with strong contrasts in speed and Poisson's ratio, also presenting a broken surface topography, then, which method among those available will be able to answer our questions? In particular, how one can take into account topography? Is it possible to model a discontinuity of the free face? Is it possible to solve the difficult problem of Rayleigh waves propagating at an interface (Stoneley problem) of a given structure? In the case of elastic properties of a heterogeneous medium, is it possible to define a clear and precise space-time diagram?

In the case of realistic 3D models (grid having several million points), are we going to be strongly limited by the cost of the proposed methods? Are we able to predict site effects of real three-dimensional structures? May these methods be adapted to the modern architectures of supercomputers (massive parallelism)? As surprising as it can appear, an inventory of the existing techniques in the literature did not make it possible to answer positively the whole of the above questions. Excluding approximate methods, such as the ray's theory, because we want to model the whole of the wave field, including surface waves and interfaces, moreover without making particular assumption on the frequency content of the propagated waves. The most common approach then consists in solving the equations of the elastodynamic problem written in differential form, using for example finite difference techniques or a pseudo-spectral type. Finite difference methods were largely used for 2D cases, and more recently in 3D, for modeling of wave propagation.

Unfortunately, finite differences produce artifacts, called grid dispersion or numerical dispersion, in zones where the wave field presents a strong gradient, or when too coarse grids are used. For traditional diagrams of centered finite differences, of second or fourth order, a minimum of 15 points of the smaller wavelength of the propagated signal (approximately 8 points in the case of a fourth order diagram) is necessary [2] [28]. Dispersion and anisotropy related to the grid can be reduced while using, instead of the centered finite difference formulation, the formulation of the grid based on the equations of linear elastodynamics in the form of a first order symmetrical hyperbolic system [69] [97]. These diagrams are however expensive, indeed they require the storage of a significant number of variables from a data-processing point of view. Centered finite difference schemes of the fourth order in space and time, based on the modified wave equation [28] [10] [85] [25] [23], allow obtaining a significant improvement in term of precision and a considerable reduction in the calculation cost. Optimized operators were also proposed for the diagrams in quincunx, by increasing the frequency range for which the error of the diagram remains limited by a maximum value that one gives [65], unfortunately such diagrams are based on a separate treatment of the error in space discretization and error in temporal discretization [78].

If one can decrease as much as possible the error of the scheme by sufficiently refining the grid calculation, in space and in time, the price to be paid is obviously a proportional increase in computing time and memory size, which can prove to be very penalizing, especially in 3D case. Then, for soil structure and geophysics applications which require a large effort of calculation, such as wave propagation in 3D realistic geological structures [48], it is often difficult to find a balance between a weak numerical dispersion and a reasonable computing time. If the model presents a surface topography or a soil structure interaction, the problem becomes more complex. Even if various techniques were proposed to incorporate such cases of soil structure and curved topographies or interfaces in the finite difference schemes, for example a discretization in stairs of interfaces [14] , or the introduction of a curvilinear frame of reference with a geometrical transformation ad hoc [74], or "the interpolation" of the model on both sides of the interface [109], such treatments remain limited to simple geometries, and lead to noisy diffraction. Moreover, many of these schemes become unstable as soon as the curve of the surface becomes large. Another disadvantage of the finite differences is their incapacity to implement the condition of free surface with the same numerical precision as in the interior of the model, particularly when schemes of high order are used. Thus, finite differences techniques seem less adapted for the modeling of the surface waves (Rayleigh) and other interface waves (Stoneley) in real models.

In addition, finite element methods based on a variational formulation of the wave equation, which allow to take into account the boundary conditions (in particular the free surface condition), although they are adapted to the treatment of complex geometries and really heterogeneous models, were much used in the field of seismology [95]. Indeed, traditional finite element methods are limited in practice to weak polynomial approximation orders, and remain not very precise and dispersive in the case of wave equation [34] [9] [104]. The traditional finite elements of a higher nature also pose some problems difficult to solve, such as the appearance of noisy and parasitic waves, and the fact that they do not lead naturally to completely explicit numerical methods, which means that it is necessary to invert a matrix whose bandwidth grows with the order of the polynomial used. Let us note that recently, space-time finite element methods were introduced in elastodynamics and opened interesting perspectives [68] [70].

In addition to the above presented methods, it is also possible to seek a solution of the wave equation by using an integral representation of the problem, having discretized quantities on the physical boundaries of the domain considered. That led, these last years, with the development of various boundaries methods based either on the domain decomposition of a family of functions, or on the introduction of Green's functions.

The approach was largely extended by many authors in order to study the behavior of structures presenting irregular topographies [66]. In the same spirit, boundary methods based on the superposition of solutions obtained from sources having singularities placed outward (near the border) of the studied area were proposed for two-dimensional and three-dimensional problems, boundary conditions being automatically satisfied within the least squares meaning [33]. Direct or indirect boundary element methods, using the fundamental solutions like weighted functions and making use of Green's theorem, allowed to calculate precise solutions to various elastodynamic problems.

Whereas the direct methods formulate the problem in terms of unknown displacements and tractions, the indirect methods formulate the problem in terms of the unknown force density and moment density factors on the boundary. Combination of the Green's functions in a discrete wave number with an indirect integral representation, by using distributions of sources, or with a direct method [77], have led to the development of many interesting methods for the propagation of elastic waves, with the advantage that the

solution is sought in a space dimension decreased by one from the studied physical field (the interfaces alone are being considered).
However, the methods of this kind are very often limited to the resolution of homogeneous layer problems in the case of a linear material behavior (and because of the absence of simple expression for Green's functions for non homogeneous non layered domains). Moreover, the linear systems that one have to solve are very large (for realistic soil structure problems that may include site effects), dense and generally nonsymmetrical. The profit in term of memory size and computing time, that one would intuitively expect to find from such methods, is thus not always obvious since models of realistic size including structures are studied. To remedy this disadvantage, it is possible to truncate certain coefficients of the linear system, which will result in a significant reduction of the size of the system, but at the price of a more or less significant degradation of the precision of the numerical results.

The spectral methods, introduced in fluid mechanics at the beginning of the eighties in order to obtain a better precision of the numerical solution of differential equations, were also used, more recently, into elastodynamics [84].
The initial idea consists in using a decomposition method of the domain into truncated Fourier series does not make it possible to take into account non-periodic boundary conditions, such as the condition of free surface for example. Some numerical tricks, like the "zero padding" were proposed but appeared not very precise [84]. The bases of circular functions were thus quickly replaced by bases of orthogonal polynomials (polynomials of Chebyshev or Legendre for the space decomposition for example), which led to the introduction of the so-called pseudo-spectral methods [59]. This technique was used much during the last twenty years, in particular, because of its precision, its low number of points per wavelength necessary to obtain almost a propagation not presenting numerical dispersion, and finally because of the good adaptation of this method to the vectorial calculator architectures. These approaches enter the class of collocation methods, for which the numerical solution must satisfy the differential form (strong form) of the wave equation on a suitably selected points. The choice of the collocation points is of crucial importance for the precision of the method, and it is important to note that the number of collocation points must be equal to the dimension of the space of approximation (i.e. the maximum degree of the polynomials used for the approximation of the solution).
Another important remark is that these collocation points, that are for the Legendre polynomials or for the Chebyshev polynomials, do not have a uniform spacing, but densify on the edges of the domain. This constitutes a significant limitation of the pseudo-spectral methods because, the points near the edges are very close to each other near the edges of the grid, we can show that the maximum time step value $\Delta t$, in the case of a conditionally stable time diagram , behaves like $N^{-2}$ , where N is the number of collocation points in a direction of the grid, and thus the stability criterion becomes quickly very unfavorable when N increases for better precision of the space discretization.
Moreover, these global methods remain limited to very simple geometries and interfaces, such the case of slightly deformed squares or cubes, because of the difficulty of finding a global transformation grid sufficiently regular towards the reference square or cubic areas. In addition, the global pseudo-spectral methods written in their strong formulation, suffer of the same type of difficulties as the finite difference methods for taking into account of the conditions of free surface. The natural idea consisting of coupling the domain decomposition technique with spectral methods was quickly proposed. However, the need for explicitly imposing connection conditions between sub-domains heavily burdens the algorithm.
In the first part of this thesis, we will show that an approach based on pseudo-spectral methods makes it possible to obtain interesting results for sufficiently regular models, but we will also clearly show the limitations of this approach since a realistic model will have to be taken into account. The pseudo-spectral approach introduced into this first part will be original in the sense that, we will use a tensorial notation of the space derivatives, from which we will show that it makes it possible to reduce significantly the calculation cost of the method compared to the formulations used traditionally in the literature.
In this context, by becoming aware of the great similarity existing between the collocation methods and the variational formulation using consistent quadratures, it appears clearly that the spectral methods are

very close to the finite element methods in their high order versions called p and h – p. This has led to the development, initially in the field of fluid mechanics, of the of the spectral element method [84], and with the recent approaches suggested by Seriani and Priolo for the elastodynamic problem [96]. In the second part of this thesis, which constitutes the main part of this work, we will introduce a spectral element method allowing to solve the hyperbolic second order system describing the elastic wave propagation in a complicated medium, for 2D as well for 3D. The potentialities of the introduced method will be shown for various traditional 2D problems, of which some are considered to be difficult to handle by other numerical modeling techniques.

The principal differences between our approach and that proposed by Faccioli et al.[30] lie in the way of formulating the variational problem, and especially in the way of imposing coupling conditions between elements (we impose only one $C^0$ continuity by an assembly of the system, in the same way as in the finite element method when using p or h – p types). Even if the particular choice of the polynomials and the points of collocation do not affect appreciably the error made for the space discretization, it affects strongly the conditioning and the structure of the matrices of the algebraic equations system to solve, which is critical for the effectiveness of the algorithm, in particular in its degree of parallelization [34]. This approach leads to a really explicit diagram (diagonal mass matrix), and makes it possible to preserve the benefits of the summation-factorization algorithms [30]. The spectral element method proposed in this thesis, derived from a weak formulation of the equations of elastodynamics, allows combining in a natural way the geometrical flexibility of the variational methods of a weak order with the fast convergence rate characterizing the spectral approximations. This good property of convergence comes from the high accuracy of the space resulting from the use of the rule of Gauss-Lobatto-Legendre. Moreover, this space precision is preserved in the majority of the situations for which non-constant coefficients must be used within each element, i.e. in the case of a heterogeneous medium (elastic properties of the medium not constants), or in the case of a deformed geometry (non-constant jacobien of transformation) [30] [17] [105].

In this work, we were motivated, by the study of two types of problems: the first is the complete modeling (wave form, volume waves, surface and interface waves) of the elastic wave propagation in complicated mediums, in order to understand and to extract the physical information contained in the seismic data coming from recordings carried out in these difficult structures. The study of soil structure interaction problems presenting such phenomena (diffraction, coupling of modes, generation of Rayleigh waves and surface waves, effects of localization and amplification of the displacement and acceleration fields) must call upon numerical techniques providing very precise solutions, that take into account in a clear way the boundary conditions as well for surface interfaces in a heterogeneous medium. The second problem is that of the site effects.

The movements of the soil can be amplified in a very significant way (at various frequencies) because of topography or local geology. This was observed for many earthquakes; in particular, 3D effects related to surface topography, or the sedimentary layers present in the model, can lead to complex phenomena such as amplification and scattering. Such effects can modify the movements of the soil in a very broad proportion, and are thus of a paramount interest in the prevention of the seismic risks and for the analysis and design of structures built in such zones. It is thus particularly interesting to be able to develop numerical techniques making it possible to model with precision such effects.

The modeling of wave propagation in complex elastic media can call upon different forms of numerical techniques, of which, the most current are recalled in the second part of this chapter, showing their principal characteristics. All these techniques having in common, the description of bodies by using the theory of elasticity, whose basics were established by Cauchy and Poisson at the beginning of the XIXème century, we recall in the first part of this chapter the principal results of this theory. The description will be inevitably brief, for more details on this theory, the reader will refer to many traditional works on theory of elasticity.

## 3.2 Tensor of deformation

The goal of the theory of elasticity is the study of the mechanics of solid bodies considered as continuous mediums (macroscopic approach). Under the effect of the forces applied to them, the bodies considered undergo deformation, resulting in a change of their form as well by a change of their volume. Let us note *r* the vector position of a point of the body, $x_i$ its components in a frame of reference which one defines. After deformation of the body, its points have moved, noting $r'$ (with $x_i'$ components) the new vector position of this point material. The displacement vector of this point is then:

$$u = r' - r \tag{3.1}$$

Generally, knowing the vector displacement in each point of the body is enough to determine the deformation of that body. Let us consider two infinitely close points. Let us note *dr* having a component $dx_i$, the vector connecting these two points before deformation, and $dr'$ , of component $dx_i'$, the vector connecting the same two points after deformation. The distance between the two points before deformation is then

$$dl = \sqrt{\sum_i dx_i^2} \tag{3.2}$$

$$dl' = \sqrt{\sum_i dx_i'^2} \tag{3.3}$$

Taking the square of equation (3.2), and making use of the following relation $dx_i' = dx_i + du_i$ , and by implying the summation on the index *i*, we obtain

$$dl^2 = dx_i^2 \tag{3.4}$$

And then

$$dl'^2 = dx_i'^2 = (dx_i + du_i)^2 \tag{3.5}$$

So now if we introduce the relation $du_i = \frac{\partial u_i}{\partial u_k} dx_k$ , we can rewrite the element length in the form

$$dl'^2 = dl^2 + 2\frac{\partial u_i}{\partial u_k} dx_i dx_k + \frac{\partial u_i}{\partial u_k}\frac{\partial u_i}{\partial u_l} dx_k dx_l \tag{3.6}$$

Note that we used here, as it will be always the case, unless otherwise specified, the convention of summation on indices, known as Einstein convention, which has the merit to reduce the notations considerably.

The above expression can be simplified by noticing that, the indices being dumb, it is possible in the third term to invert the indices *i* and *l*, and to rewrite the second term in symmetrical form $\left(\frac{\partial u_i}{\partial u_k} + \frac{\partial u_k}{\partial u_i}\right) dx_i dx_k$ , which leads to the following expression

$$dl'^2 = dl^2 \varepsilon_{ik} dx_i dx_k \tag{3.7}$$

where the tensor $\varepsilon_{ik}$, is symmetrical by definition $(\varepsilon_{ik} = \varepsilon_{ki})$, and is called deformation tensor, and is given by

$$\varepsilon_{ik} = \frac{1}{2}\left( \frac{\partial u_i}{\partial x_k} + \frac{\partial u_k}{\partial x_i} + \frac{\partial u_l}{\partial x_i}\frac{\partial u_l}{\partial x_k} \right) \tag{3.8}$$

In many practical cases and in particular when for the study of the elastic wave propagation, it is possible to suppose small disturbances and this assumption holds in the field of linear elasticity. Then, the last term of equation (3.8), which is of the second order, can be neglected; this makes it possible to find the traditional expression for infinitesimal deformations

$$\varepsilon_{ik} \cong \frac{1}{2}\left( \frac{\partial u_i}{\partial x_k} + \frac{\partial u_k}{\partial x_i} \right) \tag{3.9}$$

This is the expression that will be used throughout this thesis.

# 3.3 Conservation Law

Starting from the fundamental conservation laws (conservation of mass, momentum and angular momentum), expressed in total form, we can find their local expression on the assumption of a continuous medium. We work in an Euclidean space having a Cartesian frame of reference. In seismology, the distinction between Lagrangian approach and Eulerian (both developed by Leonhard Euler) is seldom necessary, because the space fluctuations of displacements, strains and stresses have wavelengths much larger than the displacement amplitudes of the particles. In this particular case, and from a practical point of view, there does not exist difference between the evaluation of a gradient in a fixed point (Eulerian approach) or a given particle in movement (Lagrangian approach).

## 3.3.1 Conservation of mass

Suppose that $M(t)$ is the mass of an object of volume $V(t)$ in the time domain. For an isolated system, there is no creation of mass, the law of total conservation of mass is thus written

$$\frac{dM}{dt}(t) = 0 \tag{3.10}$$

If we introduce the density of mass $\rho(x, t)$, then the total mass of volume $V(t)$ is written

$$M(t) = \iiint_{V(t)} \rho(\mathrm{x}, t) dV \tag{3.11}$$

The volume $V(t)$ follows the matter in its movement, the condition (3.11) results in

$$\iiint_{V(t)} \frac{\partial \rho(\mathrm{x},t)}{\partial t} dV + \iint_{S(t)} \rho(\mathrm{x},t)\upsilon_j(\mathrm{x},t) n_j dS = 0 \tag{3.12}$$

Noting $S(t)$ as the contour of $V(t)$, $n_j$ the $j^{th}$ external normal component of $S(t)$, and $V_j(t)$ the $j^{th}$ speed component of the particle at $x$ and instant *t*. Using the theorem of divergence, we obtain

$$\iiint_{V(t)} \left( \frac{\partial \rho(\mathrm{x},t)}{\partial t} + \partial_j(\rho(\mathrm{x},t)\upsilon_j(\mathrm{x},t)) \right) dV = 0 \tag{3.13}$$

This expression being true for any volume *V*, the integrand is continuous, and then we deduce the law of conservation of mass as

$$\frac{\partial \rho(\mathrm{x},t)}{\partial t} + \mathrm{div}(\rho(\mathrm{x},t)\upsilon(\mathrm{x},t)) = 0 \tag{3.14}$$

### 3.3.2 Conservation of momentum

By definition, the momentum contained in the volume $V(t)$ is given by

$$P(\mathrm{x},t) = \iiint_{V(t)} \rho(\mathrm{x},t)\upsilon(\mathrm{x},t) dV \tag{3.15}$$

The force acting on this volume is the sum of the forces of external origin applied to this volume

$$F_{ext}(t) = \iiint_{V(t)} f(\mathrm{x},t) dV \tag{3.16}$$

and of the interior forces resulting from the traction exerted on the surface $S(t)$ of volume $V(t)$

$$F_{\mathrm{int}}(t) = \iint_{S(t)} \tau(\mathrm{x},t) dS \tag{3.17}$$

where the vector traction is given by

$$\tau_i = \sigma_{ij} n_j \tag{3.18}$$

the tensor $\sigma_{ij}$ is called constraint tensor , and $n_j$ being the $j^{th}$ component of the normal external to $S(t)$. By using this definition of the traction as well as the divergence theorem, we have

$$F_{\mathrm{int}}(t) = \iint_{S(t)} \sigma_{ij}(\mathrm{x},t) n_j(\mathrm{x},t) dS = \iiint_{V(t)} \partial_j \sigma_{ij}(\mathrm{x},t) dV \tag{3.19}$$

Now we write the total conservation of momentum, or second Newton's law, we obtain

$$\frac{dP}{dt}(t) = F_{\text{ext}}(t) + F_{\text{int}}(t) \tag{3.20}$$

With the expression of momentum (3.15) and external forces (3.16) and interior (3.17), we deduce

$$\frac{\partial \rho \upsilon_i}{\partial t} + \partial_j(\rho \upsilon_i \upsilon_j) = f_i + \partial_j \sigma_{ij} \tag{3.21}$$

which gives the well known form of conservation of momentum written in local form

$$\frac{\partial \rho \upsilon_i}{\partial t} + \partial_j(\rho \upsilon_i \upsilon_j - \sigma_{ij}) = f_i \tag{3.22}$$

### 3.3.3 Conservation of the angular momentum

In the case of infinitesimal deformations, the law of conservation of angular momentum results in the symmetry of the constraints tensor $(\sigma_{ij} = \sigma_{ji})$.

## 3.4 Equations of elastodynamics

### 3.4.1 Constitutive Law

To be able to solve the system of conservation equations described above, it is necessary to give a law connecting the constraints in the medium to the history of its deformations, i.e. to define the rheology of the medium. Such a law is called constitutive law of the material. There are many traditional rheology models, for example of the elastic type, visco-elastic, plastic, visco-plastic, fluid…Within the framework of this thesis, we were interested more particularly in the elastic and elastic-plastic material models.
That is to say $\sigma(\mathrm{x},t) = \{\sigma_{ij}(\mathrm{x},t)\}$ the constraints tensor and $\varepsilon(\mathrm{x},t) = \{\varepsilon_{ij}(\mathrm{x},t)\}$ the tensor of the deformations in a point *x* of the medium at the moment *t*. The medium is known as elastic if the constraints at the moment *t* (at point *x*) depend only on the deformations at the moment *t* (in the same point *x* ). For small deformations, a Taylor development gives

$$\sigma_{ij} = \sigma_{ij}^0 + c_{ijkl}\varepsilon_{kl} + \frac{1}{2} d_{ijklmn}\varepsilon_{klmn} + \ldots \tag{3.23}$$

For sufficiently small deformations, one can keep only the first term of the development, which gives Hooke's law (sometimes called generalized Hooke's law)

$$\sigma_{ij}(\mathrm{x},t) = \sigma_{ij}(\mathrm{x},t_0) + c_{ijkl}(x)\varepsilon_{kl}(\mathrm{x},t) \tag{3.24}$$

The term $\sigma_{ij}(\mathrm{x},t_0)$ is called prestress, and corresponds to the stress state of the system when it is in equilibrium. Thanks to the constitutive law, the tensors $c_{ijkl}, d_{ijklmn}, \ldots$ being given, we can at any instant calculate the stress field *σ* from the strain field *ε*. If we add this law to the stated conservation laws given in equations (3.14) and (3.22) above, and with the definition of the strain tensor (equation 3.9), we then have a complete set of equations allowing to describe the studied system.

### 3.4.2 Small strain equations

Developing and rearranging the terms of the conservation momentum equation (equation 3.22), we get

$$\rho \frac{\partial \upsilon_i}{\partial t} - \partial_j \sigma_{ij} + \rho \upsilon_j \partial_j \upsilon_i + \upsilon_i \left( \frac{\partial \rho}{\partial t} + \partial_j (\rho \upsilon_j) \right) = f_i \tag{3.25}$$

According to the conservation mass equation (equation 3.14), the last term on the left of equation (3.25) is null, therefore

$$\rho \frac{\partial \upsilon_i}{\partial t} - \partial_j \sigma_{ij} + \rho \upsilon_j \partial_j \upsilon_i = f_i \tag{3.26}$$

Within the framework of the of the elastic wave propagation, we can reasonably make the assumption of a medium subjected only to small disturbances, that is small strains. This approximation makes it possible to neglect certain terms, and led to the classical equation, which we will use thereafter

$$\rho \frac{\partial^2 u_i}{\partial t^2} = \partial_j \sigma_{ij} + f_i \tag{3.27}$$

### 3.4.3 Isotropic elastic medium

In the case of a linear elastic material, having the tensor of the elastic parameters $c_{ijkl}$ will be enough to link the constraints to the deformations in any point of the material. This tensor has the following symmetries:

$$\begin{aligned} &c_{ijkl} = c_{klij} \text{ (major symmetries)} \\ &c_{ijkl} = c_{klij} = c_{ijlk} \text{ (minor symmetries)} \end{aligned} \tag{3.28}$$

Moreover, $c$ is positive definite :

$$c_{ijkl} \psi_{ij} \psi_{kl} > \alpha |\psi| \text{ with } \alpha > 0 \qquad \forall \psi,\ \psi_{ij} = \psi_{ji} \neq 0 \tag{3.29}$$

The simplest case for an elastic medium is the case where the properties of the medium are the same in all directions of the space dimension. Such a medium is known as isotropic material. In such a case, only two elastic parameters are needed to characterize the relationship between the constraints and the strains. We can for example use the two Lamé's constants λ and μ and write Hooke's law in the form

$$\sigma_{ij} = \lambda \delta_{ij} \varepsilon_{kk} + 2\mu \varepsilon_{ij} \tag{3.30}$$

that comes to say that

$$c_{ijkl} = \lambda\delta_{ij}\delta_{kl} + \mu\delta_{ik}\delta_{jl} + \mu\delta_{il}\delta_{jk} \tag{3.31}$$

where $\delta_{ij}$ represents the Kronecker's symbol, defined by $\delta_{ij} = 1$ if $i = j$ otherwise $\delta_{ij} = 0$.
If the two Lamé's constants $\lambda$ and $\mu$ are one possible parameterization in the isotropic elastic case, obviously it is not the only one. One of the major defects of the Lamé's parameters is that they are not linked in a direct way to an easily measurable physical quantity. Among the other measurable parameters frequently used, let us quote for example:

- Bulk modulus $K = \lambda + \frac{2}{3}\mu$
- Young's modulus $E = \dfrac{\mu(3\lambda + 2\mu)}{\lambda + \mu}$
- Poisson's ratio $\nu = \dfrac{\lambda}{2(\lambda + \mu)}$
- Compression wave velocity (P waves) $c_p = \sqrt{\dfrac{\lambda + 2\mu}{\rho}}$
- Shear wave velocity (S waves) $c_s = \sqrt{\dfrac{\mu}{\rho}}$

Some useful properties of these parameters can be cited. The Poisson's ratio is such that

$$-1 < \nu \leq \frac{1}{2} \tag{3.32}$$

Values of Poisson's ratio in the vicinity of the limit $\nu = \frac{1}{2}$ correspond to a slightly consolidated medium. It is interesting to note that need for being able to define an energy density which is of a definite positive form imposes only the condition $\nu > -1$ and not $\nu > 0$. Noting that for the majority of rocks, Poisson's ratio is in between 0.20 and 0.35.

The relationship between S and P wave velocities are such that

$$c_s < \frac{c_p}{\sqrt{2}} \tag{3.33}$$

from which the name of these waves stands for (P = as Primary, S = as Secondary), the P waves always arrive first, before the S waves. It is also attributed to the following definition (P = as Pressure) and (S = as Shear), the P waves being compression waves of and the S waves as shearing waves.

## 3.4.4 Hyperbolic system of first or second order

We have just seen that the wave equations of the isotropic linear elastic case can be written in the following form

$$\rho \frac{\partial^2 u_i}{\partial t^2} = \partial_j \sigma_{ij} + f_i$$
$$\varepsilon_{ij} = \frac{1}{2}(\partial_j u_i + \partial_i u_j)$$
$$\sigma_{ij} = \lambda \delta_{ij} \varepsilon_{kk} + 2\mu \varepsilon_{ij}$$

We are thus in the presence of a second – order hyperbolic system for the unknown displacement field *u*. We thus expect to find solutions of diffusive type, in particular the existence of plane waves as a particular solution of the system in the homogeneous case.

Let us note that it is possible to rewrite the above equations in the form of a first order hyperbolic system in time by choosing the unknown factors displacement, speed and the constraints [47] [48]. If we are interested only at the speed and the constraints, the system can be reformulated in a simple manner, for example for a 2D case we write :

$$\frac{\partial U}{\partial t} = A \frac{\partial U}{\partial x} + B \frac{\partial U}{\partial y} + S \tag{3.34}$$

with

$$U = \left[\upsilon_x, \upsilon_y, \sigma_{xx}, \sigma_{yy}, \sigma_{xy}\right]^T \tag{3.35}$$

and

$$S = \left[f_x, f_y, 0, 0, 0\right]^T \tag{3.36}$$

while having posed

$$A = \begin{pmatrix} 0 & 0 & \rho^{-1} & 0 & 0 \\ 0 & 0 & 0 & 0 & \rho^{-1} \\ \lambda + 2\mu & 0 & 0 & 0 & 0 \\ \lambda & 0 & 0 & 0 & 0 \\ 0 & \mu & 0 & 0 & 0 \end{pmatrix} \tag{3.37}$$

and

$$B = \begin{pmatrix} 0 & 0 & 0 & 0 & \rho^{-1} \\ 0 & 0 & 0 & \rho^{-1} & 0 \\ 0 & \lambda & 0 & 0 & 0 \\ 0 & \lambda + 2\mu & 0 & 0 & 0 \\ \mu & 0 & 0 & 0 & 0 \end{pmatrix} \tag{3.38}$$

## 3.4.5 Boundary conditions

In practice, in the case of a numerical problem, the studied domain is never infinite, but is limited even by the fact that the memory size of the used machine used for calculation is limited. We do have physical boundaries of the domain (primarily free surfaces, corresponding to a Neumann condition, and rigid edges, corresponding to a Dirichlet condition), and the so-called numerical boundaries of the domain, limiting the medium in an artificial manner, on which there must be posed absorbing boundary conditions.

Thus let us now define the limits problem in which we ought to solve. That is an open no-homogeneous elastic limited domain $\Omega$ having a boundary $\partial\Omega$, and $\overline{\Omega}$ the corresponding closed domain field, $\Gamma^{\text{int}}$ the physical boundary, $\Gamma_{abs}^{ext}$ the numerical boundary on which absorbing boundary conditions must be introduced, and $\mathrm{I} = [0 , \mathrm{T} ] \subset \mathrm{R}_+$ the time interval of study. According to the physical problems that one wishes to model, three types of boundary conditions can exist:

1. Boundary conditions in constraint terms $\Gamma_r^{\text{int}}$

$$\tau_i =\& \sigma_{ij} n_j \qquad \text{on} \qquad \Gamma_r^{\text{int}} \times \mathrm{I} \tag{3.39}$$

where $\tau = \tau(\mathrm{x}, t)$ is the traction condition imposed on the boundary, and *n* the outward normal on $\Gamma$. A condition of null traction on the boundary, i.e. $\tau = \tau(\mathrm{x}, t) = 0;\ \forall t \in \mathrm{I}$, corresponds to the very important particular case, of a free surface condition.

2. Dirichlet boundary conditions (imposed displacement) on $\Gamma_g^{\text{int}}$

$$u_i = g_i \qquad \text{on} \qquad \Gamma_g^{\text{int}} \times \mathrm{I} \tag{3.40}$$

where $g = g(\mathbf{x}, t)$ is the displacement imposed on the boundary.  These conditions correspond to the case of a rigid edge boundary.

3. Radiation conditions (absorbant conditions) on $\Gamma_{abs}^{ext}$

When it is supposed that the physical domain under consideration extends toward infinity in one or more directions (which is only a view of mind, since actually any physical domain is inevitably limited), it is not possible to directly use the spectral element method without running up against the problem of the numerical modeling of the wave propagation in an infinite or semi-infinite medium. The traditional approaches to solve this difficulty is to replace the initial given problem by a limited domain by introducing a fictitious boundary (absorbing boundary) on which are imposed suitable boundary conditions. A condition of radiation must be introduced on this fictitious border $\Gamma_{abs}^{ext}$ in order to replace the external field. The correct writing of a condition of this type is a complex problem which will not be studied here; see for example Givoli [38] for a very complete study on this subject.

Recently, exact non-local boundary conditions, using an asymptotic development of the solution in the external field were proposed, but they present the disadvantage of being particularly complicated to implement. Following Aubry et al. [2], a development in a wave number of the equations of elastodynamics written in Fourier domain is carried out, in order to obtain an expression for the impedance of the fictitious boundary. Such an approximation is exact only for relatively high frequencies, and especially for normal incidental waves on the absorbing boundaries. With order zero (used in this research work), such an approximation is very similar to the traditional dampers proposed by Lysmer and Kuhlemeyer [72]:

$$\tau = c_p(\rho \mathrm{v})_N + c_s(\rho \mathrm{v})_T \qquad \text{on} \qquad \Gamma_{abs}^{ext} \times \mathrm{I} \tag{3.41}$$

where $\tau$ is the traction on the boundary, and $(\rho \mathrm{v})_N$ as well $(\rho \mathrm{v})_T$ are respectively the normal and tangential components of the momentum on the absorbing surface.

By considering plane absorbent edges, the condition which we used is written here for a 2D example for a plane edge located according to its *z* minimal:

$$\begin{aligned} \frac{\partial u_x}{\partial t} &= c_s \frac{\partial u_x}{\partial z} + (c_p - c_s)\frac{\partial u_z}{\partial x} \\ \frac{\partial u_z}{\partial t} &= c_p \frac{\partial u_z}{\partial z} + (c_p - c_s)\frac{\partial u_x}{\partial x} \end{aligned} \tag{3.42}$$

The improvement of equation 3.42 gives :

$$\begin{aligned} \frac{\partial u_x}{\partial t} &= c_s \frac{\partial u_x}{\partial z} \\ \frac{\partial u_z}{\partial t} &= c_p \frac{\partial u_z}{\partial z} \end{aligned} \tag{3.43}$$

In a number of numerical simulations that we will show in the following sections of this work, the problem involved in the introduction of absorbing conditions will often constitute the principal source of numerical error, because of the wave reflections coming from the absorbent boundaries. An unquestionable improvement would consist in using a paraxial approximation of a higher nature, a combination of paraxial approximations [44], or even a radically different approach, in non-local matter, such as that proposed by Givoli [38], but at the price of a significant algorithmic complication.

### 3.4.6 Excitation of the medium

An excitation source can be introduced into the medium either as a force located in a point of the grid, or as an explosion (a specific pure compression point load).The time dependent source can in theory be any signal having a limited frequency band. Most of the time, as it is often used; a Ricker type function (second time Gaussian derivative) will be used. We can also, as is the case for plane waves for example, not to introduce a source explicitly, but to impose at the initial time a field of displacement, velocity and acceleration.

Often, it is possible to introduce as a source, an arbitrary seismic moment tensor **m** ( **x** , *t* ), that is, a symmetrical tensor of row two having all the properties of a stress tensor, for which the equivalent force is given by

$$f(\mathrm{x},t) = -\operatorname{div} \mathrm{m}(\mathrm{x},t) \tag{3.44}$$

### 3.4.7 Variational formulation of the problem

We saw previously that the elastodynamic linear equations could be written in the form:

$$\left.\begin{aligned}\rho\dot{v} &= \mathrm{div}[\sigma]+\mathrm{f}\\ \rho\dot{u} &= \rho \mathrm{v}\end{aligned}\right\} \text{ in } \Omega\times \mathrm{I} \tag{3.45}$$

with the initial conditions as

$$\left.\begin{aligned}\mathrm{u}(\mathrm{x},t)\big|_{t=0} &= \mathrm{u}_0(\mathrm{x})\\ \mathrm{v}(\mathrm{x},t)\big|_{t=0} &= \mathrm{v}_0(\mathrm{x})\end{aligned}\right\} \text{ in } \Omega \tag{3.45}$$

where we noted $\Omega$ the studied unbounded elastic domain, $\overline{\Omega}$ the bounded domain, $\Gamma^{\mathrm{int}}$ its physical boundary, $\Gamma_{abs}^{ext}$ the numerical boundary on which absorbing boundary conditions are imposed, and $\mathrm{I}=[0,T]\subset R_+$ the time interval of study. $u:\overline{\Omega}\times\mathrm{I}\rightarrow R^{n_d}$ represents the displacement field; $\mathrm{v}:\overline{\Omega}\times\mathrm{I}\rightarrow R^{n_d}$ the velocity field; $\mathrm{u}_0:\overline{\Omega}\rightarrow R^{n_d}$ the initial displacement field; and $\mathrm{v}_0:\overline{\Omega}\rightarrow R^{n_d}$ the initial velocity field. That is to say also $\rho:\Omega\rightarrow R_+^{n_d}$ the density field, and $\mathrm{f}:\Omega\rightarrow R^{n_d}$ the voluminal force field. We suppose also that the medium is having free initial conditions, i.e. $\sigma(\mathrm{x},0)=0$.
Let us suppose also that the stress tensor is given in the linear case by the generalized Hooke's law, because of symmetries of the *c* tensor, and then we can write:

$$\sigma(\nabla \mathrm{u}) = \mathrm{c}:\nabla \mathrm{u} \tag{3.47}$$

that is to say

$$\sigma_{ij} = c_{ijkl}\varepsilon_{kl} \tag{3.48}$$

where we introduced the contracted product notation of two tensors, represented by the symbol " **:** ", such that **c** = **a** **: b** is equivalent to writing $c_{ij} = a_{ijkl}b_{kl}$.
It is then possible to write the problem in a variationel form (also called weak form). Given the Sobolev space $H^1$ (Ω) made of all the functions which, like their first derivatives within the distributions framework, belongs to $\boldsymbol{L}^2$ (Ω), we can then introduce the whole accepted displacements $S_t$ at a given time $t\in\mathrm{I}$ :

$$S_t = \left\{\mathrm{u}(\mathrm{x},t)\in H^1\left(\overline{\Omega}\right)^{n_d} : \overline{\Omega}\times\mathrm{I}\rightarrow R^{n_d};\ \mathrm{u}(\mathrm{x},t)=\mathrm{g}(\mathrm{x},t) \text{ on } \Gamma_{\mathrm{g}}^{\mathrm{int}}\times\mathrm{I}\right\} \tag{3.49}$$

where **g** is the displacement imposed on the part of the boundary on which Dirichlet boundary conditions are imposed. Let us note $\mathcal{V}$ the space of the acceptable displacements variations (functions test) associated to $S_t$ and defined generally by:

$$\mathcal{V} = \left\{\mathrm{w}(\mathrm{x})\in H^1(\Omega)^{n_d} : \Omega\rightarrow R^{n_d};\ \mathrm{w}(\mathrm{x})=0 \text{ on } \Gamma_{\mathrm{g}}^{\mathrm{int}}\right\} \tag{3.50}$$

We will note that the **w** functions do not depend on time. The variational formulation is then obtained by forming the internal product defined in $\boldsymbol{L}^2$ (Ω) equations described above with the whole accepted variations. By using the divergence theorem, this leads to solve the following problem: given **f**, **g**, **τ** , $\mathbf{u_o}$, $\mathbf{v_o}$, find **u** ( **x** , *t* ) ∈ $S_t$, $\forall t\in\mathrm{I}$, such that $\forall \mathrm{w}\in\mathcal{V}$ :

$$(\mathrm{w},\rho\dot{\mathrm{v}})+a(\mathrm{w},\mathrm{u})=(\mathrm{w},\mathrm{f})+(\mathrm{w},\tau)\Gamma_{\tau}^{\mathrm{int}}+(\mathrm{w},\tau)\Gamma_{abs}^{ext} \tag{3.51}$$

$$(\mathrm{w},\rho\dot{\mathrm{u}})=(\mathrm{w},\rho\mathrm{v}) \tag{3.52}$$

with the initial conditions

$$\left(\mathrm{w},\rho\mathrm{u}(.,t)\big|_{t=0}\right)=(\mathrm{w},\rho\mathrm{u}_0) \tag{3.53}$$

$$\left(\mathrm{w},\rho\mathrm{v}(.,t)\big|_{t=0}\right)=(\mathrm{w},\rho\mathrm{v}_0) \tag{3.54}$$

Where

$$(\mathrm{w},\rho\dot{\mathrm{v}})=\int_{\Omega}\rho\dot{\mathrm{v}}\cdot\mathrm{w}dV;\, a(\mathrm{w},\mathrm{u})=\int_{\Omega}\sigma:\nabla\mathrm{w}dV=\int_{\Omega}\nabla\mathrm{w}:\mathrm{c}:\nabla\mathrm{u}dV \tag{3.55}$$

and

$$(\mathrm{w},\mathrm{f})=\int_{\Omega}\mathrm{f}\cdot\mathrm{w}dV;\;\; (\mathrm{w},\tau)\Gamma_{\tau}^{\mathrm{int}}=\int_{\Gamma_{\tau}^{\mathrm{int}}}\tau\cdot\mathrm{w}d\Gamma;\;\; (\mathrm{w},\tau)\Gamma_{abs}^{ext}=\int_{\Gamma_{abs}^{ext}}\tau\cdot\mathrm{w}d\Gamma \tag{3.56}$$

It will be noted that the given formulation here was written for a linear unspecified case (anisotropic a priori ), the isotropic case will be easily obtained by particularizing the form of the tensor **c** .Also let us note in the foregoing a very important property of the variational form of the problem, and resulting directly from the above mentioned formulation: the contribution of the edges on which a condition in traction is fixed was written in the form $(\mathrm{w},\tau)\Gamma_{\tau}^{\mathrm{int}}$ , where $\tau$ is the traction vector on this border. Therefore, in the particular case of a free surface, the traction on that boundary is null, and the considered term disappears, this condition is thus taken into account automatically.

### 3.4.8 Total energy of the system

At any time in an elastic system, the kinetic energy per unit volume can be written

$$U_c=\frac{1}{2}\rho\left(\frac{\partial u_i}{\partial t}\right)^2 \tag{3.57}$$

and the strain energy density

$$U_p=\frac{1}{2}c_{ijkl}\varepsilon_{ij}\varepsilon_{kl}=\frac{1}{2}\sigma_{ij}\varepsilon_{ij} \tag{3.58}$$

In the absence of an external source, if we introduce non null initial conditions, the total energy contained in the system must be conserved, which results in

$$\int_V (U_c+Up)dV=\text{constante} \tag{3.59}$$

If the behavior is linear elastic, for a homogeneous and infinite medium, and in the absence of source term, a relation even stronger exists, namely that the total kinetic energy and total potential energy are equal .

## 3.5 Various wave types

In the case of wave propagation in an isotropic linear elastic medium, there can exist various types of waves which we will meet in the following development of this thesis. Let us try to describe the principal types. In the following, we will consider the case of an isotropic linear elastic solid.

### 3.5.1 Direct, reflected and refracted waves

In the case of a source placed in an infinite homogeneous medium, two wave types exist, called direct P waves and direct S waves. For a receiver placed in the far field, the P wave arrives first; it travels at the velocity $c_p = \sqrt{(\lambda + 2\mu)/\rho}$ and corresponds to a pure compression. The displacement of the particles is parallel to the direction of propagation (longitudinal wave). The S wave arrives second; it travels at the velocity $c_s = \sqrt{\mu/\rho}$ and corresponds to a pure shearing. The displacement of the particles is perpendicular to the direction of propagation (transverse wave). So now if the field considered is not infinite any more, but limited, when one of the waves hits a border of the field, a coupling between the P and S waves occurs at this border, and in the general case it results two wave types (P and S) for an incidental P or S wave. However, in the case of an incident S wave on an interface, as $c_P$ is always greater than $c_S$, there is a critical angle

$$\theta_c = \arcsin\left(\frac{c_s}{c_p}\right) \tag{3.60}$$

beyond which there is no reflected P wave resulting from the incident S wave. Qualitatively, the same phenomenon occurs when a P wave or an S wave meets a discontinuity in the elastic properties within the medium (interface), this is especially the case of a horizontally layered medium. In such a case, and according to the value of the angle of incidence, an incident P or S wave can give rise to four waves: reflected P, reflected S, transmitted P and transmitted S. This property of mode conversion at the interfaces in a geological model is at the origin of the complexity in the seismic soil structure interaction problems, the number of phases observed which can quickly become very significant.

In the particular case where the incident wave is within a critical angle, for a wave passing from a medium of weaker velocity in a medium of higher velocity, the transmitted wave going through the interface will have an angle of 90 degrees compared to the normal direction. Then the energy travels along the interface with the speed of the fastest medium, and the structures placed beyond a distance called critical distance will be subjected to refracted waves, which are very important to structures and much used in many seismic recordings.

### 3.5.2 Rayleigh, Love and Stoneley waves

When a homogeneous elastic domain is limited by a free surface (corresponding to a condition of null traction on the surface), there is a particular type of waves, highlighted by Lord Rayleigh [88], and corresponds to waves propagating along the surface of the medium, in the vicinity of this one, without however penetrating in the medium (evanescent wave with the depth). These waves are called surface waves, or Rayleigh waves. These waves travel with velocity $c_R$, which is lower than the S wave velocity, and are solution of:

$$\left(\frac{c_R}{c_s}\right)^6 - 8\left(\frac{c_R}{c_s}\right)^4 + 8\left(\frac{c_R}{c_s}\right)^2\left(3 - 2\frac{c_s^2}{c_p^2}\right) - 16\left(1 - \frac{c_s^2}{c_p^2}\right) = 0 \qquad (3.61)$$

As $c_s/c_p$ depends only on the Poisson's ratio, since

$$\frac{c_s}{c_p} = \sqrt{\frac{1-2\upsilon}{2(1-\upsilon)}} \qquad (3.62)$$

the ratio c $_R$ /c $_S$ can be calculated numerically as a function of the Poisson's ratio only.

$$\frac{c_R}{c_s} = \frac{0.862 + 1.14\upsilon}{1+\upsilon} \qquad (3.63)$$

and the following typical values can be given (according to Haskell, [43] ):

| ν | $c_s/c_p$ | $c_R/c_s$ |
|---|---|---|
| 0.00 | 0.707 | 0.862 |
| 0.25 | 0.577 | 0.919 |
| 0.33 | 0.500 | 0.932 |
| 0.40 | 0.408 | 0.941 |
| 0.50 | 0.000 | 0.955 |

Let us note some important properties of Rayleigh waves:

- Rayleigh wave on the surface of a plane homogeneous medium is non-dispersive. The wave will be dispersive only if elastic heterogeneities properties are present in the thickness where the Rayleigh wave propagates, for example in the case of a fine layer having of slow velocity is located on a homogeneous half space of faster velocity.
- In the case of a medium having a curved surface (topography), this one will induce a dispersion of the Rayleigh wave even if the medium is homogeneous. Dispersion is then strongly influenced by the curvature of the topography relative to the wavelength of Rayleigh wave propagating in the medium. Let us note that in the case of a Rayleigh wave meeting a strong curvature of the surface, mode conversions of Rayleigh waves into volume waves (P and S waves) can also occur [90].
- Rayleigh wave is easily recognizable because of its retrograde elliptic polarization in the plan of propagation. A structure placed at the surface of the ground will thus be submitted at the same time to the horizontal component parallel with the direction of propagation, and the vertical component.

Love also showed that a surface wave, oscillating perpendicular to the plan of propagation, can exist when a layer of different elastic properties is located at the surface of a half space. Such a wave is called Love wave. Compared to Rayleigh wave, Love wave cannot exist if the half space is completely homogeneous. Love wave is also always dispersive. These waves are accompanied by a horizontal movement of the ground. A structure placed at the surface of the ground will be then submitted to a horizontal component perpendicular to the direction of propagation.

In the case of an interface between two solids, or a fluid and a solid, an evanescent solution can also exist and propagates along the interface. Such modes are called interface waves, or Stoneley waves. It is however advisable to note that such solutions exist only for much reduced values of the densities and the elastic properties of the materials being in contact. For example, in the case of two solids in contact, it is necessary that ***S*** velocities of the two mediums are close to each other, so that a significant Stoneley wave propagates.

## Chapter 4

# 4. Method of Chebyshev for the wave equations

## 4.1 Introduction

In many practical situation of interest to structural or geotechnical engineers, it is important to be able to simulate the propagation of waves in models including interfaces and/or topography of the surface. In such cases, the use of traditional collocation methods (calling upon Cartesian grids) presents the disadvantage of producing numerical artifacts such as parasitic and noisy diffraction resulting from the discretization at the interfaces and the surface. If the model presents curved interfaces, these artifacts can be attenuated by introducing particular numerical processing for the mesh sampling the interfaces, without however increasing the precision of the discrete diagram in this zone, the discretization remaining always uniform. Moreover, in the particular case of the free surface, it does not seem, that simple means for introducing the correct conditions of free surface into the numerical scheme if the surface is discretized in rectangular grids.

An approach allowing to circumvent these problems, consist in solving the wave equation on a curvilinear grid whose lines coincide with the interfaces. This is conducted classically by solving the wave equation in a Cartesian reference system, and by calling upon the derivation rule to calculate the spatial Cartesian derivatives in the work field. This method has the advantage to take into account curved interfaces, but presents the disadvantage of being more expensive than in the case of a Cartesian grid, because a greater number of spatial derivatives must be evaluated numerically.

A more natural approach, and which makes it possible to avoid this disadvantage, i.e. to preserve the same cost of calculation as in the case of a regular grid, consists in solving the wave equation directly in the curvilinear field. For that, it is necessary to write the wave equation in tensorial form, which by definition is independent of the selected frame of reference. A transformation of co-ordinates makes it possible to bring back the curvilinear grid, whose lines coincide with the interfaces of the model as well with the free surface, to a field of square form. That makes it possible to calculate, in any point of the medium, the metric tensor which appears in the wave equation given in tensorial form. The numerical resolution of the wave equation posed in tensorial form requires the evaluation of the same number of partial derivatives as in the case of a regular grid.

The algebraic method of generation of grids used makes it possible to ensure that lines of the grid follow well the various interfaces of the model, which thus makes it possible to get rid of the parasitic numerical diffractions resulting from the discretization of the interfaces in the case of a regular grid. Moreover, one local refinement of the grid in the vicinity of the various interfaces (in particular in the vicinity of the free surface) makes it possible to increase significantly the precision of the numerical scheme in these zones compared to the case of a Cartesian grid.

It is also possible to discretize such complex domains by using grids which are orthogonal in any point of the domain. That would make it possible to reduce the number of terms appearing in the equations to solve (not-diagonal terms of the metric tensor being then null) but, on the one hand, it is very difficult to generate such grids for realistic models even in the 2D case, and, moreover, as outlined by Thompson et al. [104], the orthogonality of the grid is not the essential point for obtaining a weak error in the numerical calculations. It is much more important that the variation of the size of the meshes of the grid is smooth, which is ensured by the algebraic method that we used.

In this chapter, we sought to use, by improving a traditional modeling technique based on the differential formulation of the equations of elastodynamics and on the use of a polynomial basis of a high order (pseudo-spectral method) for the space resolution. Indeed, in many practical cases soil-structure interaction problems, it is necessary to take into account the layering of the mediums involved, as well as the topography of the surface. The collocation methods, for example the algorithms of pseudo-spectral types or finite differences, are interesting approaches to model the wave propagation in these complex media, in particular because of the relative facility and ease of implementing such algorithms.

However, such methods formulated in Cartesian co-ordinates are not very well suited to the study of models presenting curved interfaces, because owing to the fact that the interfaces and the free surface do not coincide with the Cartesian grid. That led to a rate of weak convergence of which the most visible consequences are the appearance of artifacts such as parasitic and noisy diffraction resulting from the discretization of the interfaces and the free surface by a rectangular grid meshes. Such problems can be avoided by the use of curvilinear grids, of which the lines follow the interfaces and the surface, and of which the density of meshes increases in the vicinity of these interfaces. A possible approach consists in writing the wave equations in Cartesian co-ordinates and using the made up derivation rule to express the Cartesian partial derivatives in terms of the calculated partial derivatives in the curvilinear frame of reference. However, it is more natural to solve directly in the curvilinear frame of reference the wave equation written in tensorial form, after having defined a geometrical transformation making it possible to pass from the curvilinear field to the studied physical field.

The tensorial approach, which by definition is independent of the chosen frame of reference, requires the calculation of the same number of partial derivatives as in the Cartesian case, whereas the approach using the made up derivation rule requires 25 % more calculations in 2D domains, and 50 % more for a 3D case. From the point of view of numerical calculation, however, the tensorial approach requires the use of a greater number of storage tables, therefore consumes more memory from a data-processing point of view. In this chapter, the tensorial approach is validated by comparing the results obtained for Lamb problem to the analytical solution of the problem [60]. A good agreement is found. The numerical calculations carried out on more complex 2D models show then the capacity of this method to model the wave propagation in the presence of interfaces and/or a structure on the surface. Mode conversions, of Rayleigh waves to volume waves, are observed when the surface of the model has a concavity. We also explain in this chapter why the method employed is particularly well suited to soil structure interaction problems computer, and we give an estimate of the performances which we obtained. However, in conclusion of this chapter, we note the limitation of the global differential solution, in particular because of the difficulty in finding, for a realistic model, a regular geometrical transformation between the physical field considered and the field of study. We deduce from it the need for using a finer approach, for example a subdomain type calculation or variational type, when we are interested in the study of really complex models.

## 4.2 Tensorial formulation of the wave equation

### 4.2.1 The wave equation in tensorial form

The wave equation is generally written by using Cartesian co-ordinates. However, the introduction of a particular frame of reference is not really necessary. If we can define a metric, it is possible to use the tensorial formalism to write a system of equations describing the wave propagation in a heterogeneous medium and who is valid in any point of the space independently of the frame of reference. The choice of the co-ordinates particularizes the metric tensor $g_{ij}$ but the equations themselves remain unchanged. In the case of an isotropic linear elastic medium, and by supposing infinitesimal deformations, the general expression of these tensorial equations is the conservation equation of momentum

$$\rho \frac{\partial^2 u_i}{\partial t^2} = \nabla_j \sigma_i^j + \varphi_i \tag{4.1}$$

the strain-displacement relation (within the framework of small strains)

$$\varepsilon_{ij} = \frac{1}{2}\left(\nabla_i u_j + \nabla_j u_i\right) \tag{4.2}$$

and the isotropic linear relation stress-strain (Hooke's law )

$$\sigma_i^j = \lambda g_i^j \varepsilon_k^k + 2\mu \varepsilon_i^j \tag{4.3}$$

where the covariance derivative $\nabla_m$ of a tensor $T_{ij\ldots}^{kl\ldots}$ is given by the following expression

$$\begin{aligned} \nabla_m T_{ij\ldots}^{kl\ldots} &= \partial_m T_{ij\ldots}^{kl\ldots} \\ &\quad - \Gamma_{mi}^{s} T_{sj\ldots}^{kl\ldots} - \Gamma_{mj}^{s} T_{is\ldots}^{kl\ldots} - \ldots \\ &\quad + \Gamma_{ms}^{k} T_{ij\ldots}^{sl\ldots} + \Gamma_{ms}^{l} T_{ij\ldots}^{ks\ldots} + \ldots \end{aligned} \tag{4.4}$$

To improve the numerical calculations, we rewrite the wave equation in the form of stress-velocity. For 2D case, the conservation of momentum is given by

$$\begin{aligned} \rho \frac{\partial \upsilon_\xi}{\partial t} &= \nabla_\xi \sigma_\xi^\xi + \nabla_\eta \sigma_\xi^\eta + \varphi_\xi \\ &= \partial_\xi \sigma_\xi^\xi + \partial_\eta \sigma_\xi^\eta + \Gamma_{\eta\xi}^{\eta} \sigma_\xi^\xi + \Gamma_{\eta\eta}^{\eta} \sigma_\xi^\eta - \Gamma_{\xi\xi}^{\eta} \sigma_\eta^\xi - \Gamma_{\eta\xi}^{\eta} \sigma_\eta^\eta + \varphi_\xi \\ \rho \frac{\partial \upsilon_\eta}{\partial t} &= \nabla_\xi \sigma_\eta^\xi + \nabla_\eta \sigma_\eta^\eta + \varphi_\eta \\ &= \partial_\xi \sigma_\eta^\xi + \partial_\eta \sigma_\eta^\eta + \Gamma_{\xi\xi}^{\xi} \sigma_\eta^\xi + \Gamma_{\xi\eta}^{\xi} \sigma_\eta^\eta - \Gamma_{\xi\eta}^{\xi} \sigma_\xi^\xi - \Gamma_{\eta\eta}^{\xi} \sigma_\xi^\eta + \varphi_\eta \end{aligned} \tag{4.5}$$

the isotropic stress-strain relation is written in the following form

$$\begin{aligned} \dot{\sigma}_\xi^\xi &= \left(\lambda + 2\mu\right) \dot{\varepsilon}_\xi^\xi + \lambda \dot{\varepsilon}_\eta^\eta \\ \dot{\sigma}_\eta^\eta &= \lambda \dot{\varepsilon}_\xi^\xi + \left(\lambda + 2\mu\right) \dot{\varepsilon}_\eta^\eta \\ \dot{\sigma}_\xi^\eta &= 2\mu \dot{\varepsilon}_\xi^\eta \\ \dot{\sigma}_\eta^\xi &= 2\mu \dot{\varepsilon}_\eta^\xi \end{aligned} \tag{4.6}$$

the stress-velocity relation is given by

$$\dot{\varepsilon}_{\xi\xi} = \nabla_\xi \upsilon_\xi = \partial_\xi \upsilon_\xi - \Gamma_{\xi\xi}^{\eta} \upsilon_\eta$$

$$\begin{aligned}\dot{\varepsilon}_{\eta\eta} &= \nabla_{\eta}\upsilon_{\eta} = \partial_{\eta}\upsilon_{\eta} - \Gamma^{\xi}_{\eta\eta}\upsilon_{\xi} - \Gamma^{\eta}_{\eta\eta}\upsilon_{\eta} \\ \dot{\varepsilon}_{\xi\eta} &= \dot{\varepsilon}_{\eta\xi} = \frac{1}{2}(\nabla_{\xi}\upsilon_{\eta} + \nabla_{\eta}\upsilon_{\xi}) = \frac{1}{2}(\partial_{\xi}\upsilon_{\eta} + \partial_{\eta}\upsilon_{\xi}) - \Gamma^{\eta}_{\xi\eta}\upsilon_{\xi} - \Gamma^{\eta}_{\xi\eta}\upsilon_{\eta}\end{aligned} \tag{4.7}$$

and the transformation equation of the strain tensor between its covariance form and its mixed form is as follows

$$\begin{aligned}\dot{\varepsilon}^{\xi}_{\xi} &= g^{\xi\xi}\dot{\varepsilon}_{\xi\xi} + g^{\eta\xi}\dot{\varepsilon}_{\xi\eta} \\ \dot{\varepsilon}^{\eta}_{\eta} &= g^{\xi\eta}\dot{\varepsilon}_{\eta\xi} + g^{\eta\eta}\dot{\varepsilon}_{\eta\eta} \\ \dot{\varepsilon}^{\eta}_{\xi} &= g^{\xi\eta}\dot{\varepsilon}_{\xi\xi} + g^{\eta\eta}\dot{\varepsilon}_{\xi\eta} \\ \dot{\varepsilon}^{\xi}_{\eta} &= g^{\xi\xi}\dot{\varepsilon}_{\eta\xi} + g^{\eta\xi}\dot{\varepsilon}_{\eta\eta}\end{aligned} \tag{4.8}$$

In the above equations, $\xi$ and $\eta$ are the curvilinear co-ordinates, $\lambda$ and $\mu$ are Lamé's constants of the medium, $\rho$ is the density, $v_i$ represents the covariance components of the velocity vector, $\varphi_i$ the covariant source term, $\varepsilon_{ij}$ the covariant strain tensor, $\varepsilon_i^j$ the mixed strain (i.e. having a covariant index and a contra variant index) and $\sigma_i^j$ is the mixed stress tensor. A point above a tensor represents a time derivation. $\Gamma^k_{ij}$ is the affined connection (Christoffel symbols of second type), which can be obtained from the metric tensor by

$$\Gamma^k_{ij} = \frac{1}{2}g^{km}(\partial_i g_{jm} + \partial_j g_{im} - \partial_m g_{ij}) \tag{4.9}$$

Let us note that we use the convention of Einstein's summation, i.e. a summation is implicitly implied when an index appears in a monomial in lower position and upper position at the same time. The symbols $\nabla_{\xi}$ and $\nabla_{\eta}$ represent the covariance derivative, which is equal to the corresponding partial derivative plus a sum of the components of the field itself multiplied by the Christoffel symbols, as shown in equation (4.4). Information on the frame of reference is contained in the metric tensor, $g_{ij}$ represents this tensor in covariance components and $g^{ij}$ this tensor in terms of contra variances components.

It is possible to define a frame of reference which adapts itself to the physical model considered; the equations presented above can be used directly to solve the wave equation in this adapted co-ordinate reference system. This is exactly the same as solving the wave equation on a square grid $(\xi, \eta) \in [-1, 1] \times [-1, 1]$ which may be adapted to the physical space $(x, z)$ considered by a given transformation. As opposed to the method of derivation for which the wave equation is written in Cartesian co-ordinates (i.e. written with the velocity components $v_x$ and $v_z$ and the stress tensor components $\sigma_{xx}$, $\sigma_{zz}$ and $\sigma_{xz}$ for the 2D case) is solved by using the space derivatives calculated in the curvilinear reference frame, the tensorial formulation directly solves the equation in the curvilinear reference frame (i.e. the equation is written directly by using the velocity components $v_{\xi}$ and $v_{\eta}$ and $\sigma_{\xi\xi}$, $\sigma_{\eta\eta}$ and $\sigma_{\xi\eta}$ of the stress tensor components) using the space derivatives calculated in the same curvilinear reference frame.

### 4.2.2 Calculation cost

Although the tensorial approach is more satisfactory, in its philosophy, than the approach using the composed derivation rule, because the equations are written in the same frame of reference as the one in which the calculations are carried out, the cost of calculation of the two approaches must be compared. It is always difficult to compare the costs of calculation of two methods, because of the great number of possible implementations for each method. In the analysis presented here as an example, we suppose relatively similar implementations in which independent time coefficients are stored rather than recomputed with each time step (for example $\Gamma_{ij}^{k}$ in the case of the tensorial approach and $\partial\xi_m/\partial x_i$ in the case of the composed derivation method).

The cost of calculation of a numerical method of direct resolution of the wave equation written in differential form depends mainly on the spatial derivative number, noted $n_\theta$, having to be calculated with each step of time for this method (by supposing that an operator of sufficiently precise discrete derivation is used, for example a pseudo-spectral operator or an operator of finite differences in high order). Thus, we can use the number of space derivations as an indicative measure of its calculation cost, that is

$$\text{calculation cost} \cong \text{constant} \times n_\partial(N) \tag{4.10}$$

where $N$ represents the spatial number.

For the tensorial formulation, the number of spatial derivatives necessary for the calculation of the stress divergence is $N^2$ and the necessary number of derivatives for the calculation of the strain tensor from the displacement is also $N^2$, which gives a total of

$$n_\partial^{tensorial} = 2N^2 \tag{4.11}$$

discrete derivations. That is identical to the number of derivatives necessary in the Cartesian case, which is a particular case of the tensorial approach for which $g_{ij} = \delta_{ij} =$ constant, which means that all the Christoffel symbols are null.

In the approach using the composed derivation rule, we carried out the calculation of the Cartesian derivatives derived in the field work according

$$\frac{\partial f}{\partial x_i} = \frac{\partial f}{\partial \xi_m}\frac{\partial \xi_m}{\partial x_i} \tag{4.12}$$

where $\xi_m$ represents the co-ordinates in the field work and $f$ the field to be derived. The divergence of the stress tensor is calculated using

$$\frac{\partial \sigma_{ij}}{\partial x_i} = \frac{\partial \sigma_{ij}}{\partial \xi_m}\frac{\partial \xi_m}{\partial x_j} \tag{4.13}$$

which implies the calculation of $N^2 \times (N+1)/2$ spatial independent derivatives. In the case of calculation of the deformations by using the composed derivation rule, the most effective method in term of cost calculation consists in calculating and storing the $N^2$ partial derivatives $\partial u_i/\partial \xi_m$, and then using the equation (4.12). Thus, the total number of discrete derivatives which needs to be calculated when using the composed derivation rule is

$$n_\partial^{composed} = N^2\left(\frac{3}{2} + \frac{N}{2}\right) \tag{4.14}$$

It results that the additional calculation cost resulting from the use of the composed derivation rule compared to the tensorial approach can be written

$$\frac{\text{made up cost derivation}}{\text{tensorial cost derivation}} \approx \frac{n_\partial^{composed}}{n_\partial^{tensorial}} = \frac{3}{4} + \frac{N}{4} \equiv \begin{cases} 125\%, & N = 2 \\ 150\%, & N = 3 \end{cases} \tag{4.15}$$

The tensorial approach thus requires a calculation cost similar to the Cartesian case, but more working memory is necessary from a data-processing point of view to store the metric tensor $g^{ij}$ and the Christoffel symbols $\Gamma_{ij}^{k}$ . If we recall that the metric tensor is symmetrical and that the Christoffel symbols are symmetrical in terms of the lower indices, the memory required for storage is $N(N+1)/2$ fields for the metric and of $N^2(N+1)/2$ for the Christoffel symbols. This applies to the general case for which no component of $g^{ij}$ is null. Noting the additional memory necessary for the tensorial approach necessary to store the metric and Christoffel symbols by

$$\Delta M^{tensorial} = \frac{N(N+1)^2}{2} \tag{4.16}$$

In the same way, the use of the derivation composed rule requires the storage of $N^2$ the fields $\partial\xi_m / \partial\xi_i$ compared to the Cartesian case, therefore

$$\Delta M^{composed} = N^2 \tag{4.17}$$

This is lower than the additional memory required by the tensorial approach, the difference between the two is

$$\Delta M^{tensorial} - \Delta M^{composed} = \frac{N(N^2+1)}{2} = \begin{cases} 5 & \text{tables}, \; N = 2 \\ 15 & \text{tables}, \; N = 3 \end{cases} \tag{4.18}$$

The total number of tables necessary to store all the components of displacements, velocity, acceleration, stresses and strains, is about 15 for 2D and 25 for 3D, we can note that the additional cost imposed by the tensorial approach is significant, especially for 3D, and this constitutes the principal disadvantage of this approach. The solution to this problem could be the use of orthogonal grids for which the non-diagonal terms of the metric are null, but such grids are extremely difficult to generate particularly for 3D realistic models.

## 4.3 Grid generation, calculation of the metric and Christoffel symbols

The following model representing a semi-infinite soil medium is represented by a set of points defining the curved interfaces of the layers and the surface of this one. By using an interpolation algorithm based on Hermit's polynomials of degree three, we use a simple method to generate a grid whose horizontal lines follow the interfaces, and whose vertical lines have tangent vectors to these interfaces, as illustrated on figure 4.1.

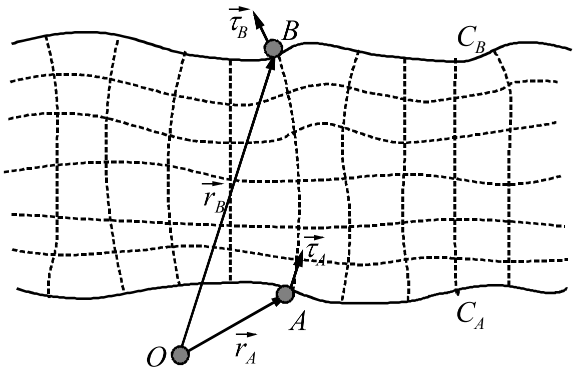

Fig. 4.1 – The algorithm for grid generation, determines a curve connecting points *A* and *B* with the given tangent vectors $\vec{\tau}_A$ and $\vec{\tau}_B$ . These tangent vectors can for example correspond to the normals at points *A* and *B* to the two curves $C_A$ and $C_B$ delimiting a given layer.

It is then possible to define an analytical transformation from a given square field ($\xi$, $\eta$) towards the physical field $\vec{r}(x,z)$, and consequently the transformation function co-ordinates $x = x(\xi, \eta)$ and $z = z(\xi, \eta)$.

In order to get a good precision for the modeling of surface and interface waves, it is often necessary to refine the grid in the vicinity of the various interfaces and the free surface; in order to increase the number of points per wavelength in these zones [90]. The method of grid generation used is interesting from this point of view, because the grid can be refined or stretched in the vicinity of the boundary of a layer, which makes it possible to increase the number of grid points close to the various interfaces and to the free surface, and to decrease this same number of grid points near the absorbing boundaries.

Knowing the transformation functions $x = x(\xi,\eta)$ and $z = z(\xi,\eta)$ that make it possible to go from the work field to the physical space, the basic vectors of the natural reference frame associated with point $\vec{M}$ are given by

$$\vec{e}_i = \frac{\partial \vec{M}}{\partial \xi^i} = \frac{\partial \xi^j}{\partial \xi^i}\vec{e}'_j \tag{4.19}$$

with $x^j \in (x,z)$ and $\xi^i \in (\xi,\eta)$, where $\vec{e}'_j$ are the basic vectors of an orthogonal Cartesian reference frame. That means that the metric tensor in a Euclidean space is given by

$$g_{ij} = \vec{e}_i \cdot \vec{e}_j = \frac{\partial x^k}{\partial \xi^i}\vec{e}'_j \cdot \frac{\partial x^l}{\partial \xi^j}\vec{e}'_j = \frac{\partial x^k}{\partial \xi^i}\frac{\partial x^l}{\partial \xi^j}\delta_{kl} \tag{4.20}$$

since $\vec{e}'_k \cdot \vec{e}'_l = \delta_{kl}$ in the orthogonal Cartesian reference frame.

This expression makes it possible to calculate $g_{ij}$ and $g^{ij}$ in terms of the partial derivatives of the transformation functions. As the functions $x_i = x_i(\xi, \eta)$ are known analytically, it is possible to calculate the metric tensor $g_{ij}$ by using the analytical expressions of the partial derivatives of the transformation functions. The metric tensor can be obviously calculated by using the same operator of the discrete derivation as the one which will be used to solve the wave equations (in our case a Chebyshev operator*). A*lthough this may appear surprising, the work of Thompson et al. [104] showed that the second approach leads to a lower numerical error during the calculation of the partial derivatives in the curvilinear frame. For this reason, we chose to calculate the metric tensor numerically and not analytically. The same operator of discrete derivation is applied to the components $g_{ij}$ in order to calculate Christoffel symbols by using equation (4.9).

# 4.4 Algorithm of resolution

## 4.4.1 Description of Chebyshev algorithm

We use a global pseudo-spectral method based on a base Chebyshev polynomials in order to solve the wave equations written in tensorial form. The various fields are written in terms of finite orthogonal functions which are Chebyshev polynomials. Time extrapolation is conducted using an explicit Runge-Kutta scheme of order four, which gives a stability condition of the type $dt = O(N^{-1})$, where $N$ is the number of grid points in each direction of the grid of calculation. The algorithm using Chebyshev polynomials was selected mainly because it is practically free from any numerical dispersion up to Nyquist frequency .

### Calculation of a space derivative by Chebyshev operator

The calculation field is a square area $(\xi, \eta) \in [-1, 1]$ on which the distribution of the grid points is defined by Gauss-Lobatto-Chebyshev points. Let us show for a *1D* case, what occurs: defining the symbol $\left(\sum\right)'$ as a finite sum of which the first and the last term are divided by two, the field considered $u(\xi)$, $\xi \in [-1, 1]$ is decomposed on the basis of Chebyshev *p*olynomials of $T_n(\xi)$, the collocation points are Gauss-Lobatto-Chebyshev points

$$u(\xi_j) = \left(\sum_{n=0}^{N}\right)' a_n T_n(\xi_j) \tag{4.21}$$

where

$$T_n(\xi_j) = \cos n\theta_j$$

with Gauss-Lobatto-Chebyshev points given by

$$\xi_j = \cos\theta_j, \quad \theta_j = \frac{\pi j}{N}, \quad j = 0, \ldots, N$$

The partial derivative of order $q$ is given by

$$\frac{\partial^q u(\xi)}{\partial \xi^q} = \sum_{n=0}^{N} a_n^{(q)} T_n(\xi)$$

where the coefficients of the derived series are given by

$$c_{n-1} a_{n-1}^{(q)} - a_{n+1}^{(q)} = 2n a_n^{(q-1)}, \quad n \geq 1$$

with

$$c_0 = 2,\ c_n = 1 \quad (n > 0)$$

Thus, by defining $a_n = a_n^{(0)}$ and $b_n = a_n^{(1)}$, the first derivative can be written as

$$\frac{\partial u}{\partial \xi} = \left( \sum_{n=0}^{N} \right)' b_n T_n(\xi) \tag{4.22}$$

where the derived series is given by

$$b_{n-1} = b_{n+1} + 2na_n, \quad n = N,...,1, \quad b_{N+1} = b_N = 0 \tag{4.23}$$

Then we may write

$$u(\xi_j) = \left( \sum_{n=0}^{N} \right)' a_n \cos\frac{\pi nj}{N}$$

and

$$a_n = \frac{2}{N}\left( \sum_{n=0}^{N} \right)' u(\xi_j)\cos\frac{\pi nj}{N}$$

Let us pose $N' = 2N$ , and $u(\xi_j) = 0$ for $j = \frac{N'}{2} + 1,..., N' - 1,$ , and we can write

$$a_n = \frac{a}{N'} \sum_{j=0}^{N'-1} u(\xi_j)\cos\frac{2\pi nj}{N'} \tag{4.24}$$

This is simply the real discrete Fourier transforms (cosine transforms) which can be calculated using an algorithm of fast Fourier transform (FFT*).* Then, we can obtain the *b* $_n$ coefficients of the series from the coefficients of the field using the recurrence formula (equation 4.23). The evaluation of the derivative at Gauss-Lobatto-Chebyshev points is then obtained using equation (4.22), and again using an FFT. One can also show that it is possible to calculate the derivative of the field by applying the product of this one by a matrix of coefficients called derivative matrix, for the analytical expression of this one, and for the Chebyshev polynomials [4] .

## Deformation of the grid "Mapping"

In the case of Gauss-Lobatto-Chebyshev points given by

$$\xi_j = \cos\left( \frac{\pi\, j}{N} \right) \quad j = 0,..., N \tag{4.25}$$

the minimal size of a mesh in the field of study is obtained at the edge of the field, by

$$\Delta\xi_{\min} = \left|1-\cos\left(\frac{\pi}{N}\right)\right| \approx \frac{\pi^2}{2N^2} \tag{4.26}$$

for sufficiently large values of $N$, which is generally the case in practice. It is seen that the size of the smallest mesh decreases as $1/N^2$, where $N$ is the number of points in a direction of the grid. In the case of a conditionally stable time integration diagram, for which the stability criterion will be dictated by the size of the smallest mesh of the grid, this characteristic can quickly become very handicapping, even worse. To circumvent this problem, Gauss-Lobatto-Chebyshev points are reported to the interval $[-1, 1]$ by a non-linear transformation on the edges of the field ("mapping"), allowing a local stretching of the smallest meshes. In the $x$ direction for example, the sampling points are [96]

$$x_j = \frac{x_{\max}}{2}[1-g_x(\xi_j)], \quad j=0,\ldots,N_x$$

with

$$g_x(\xi) = \frac{\arcsin(\gamma\xi)}{\arcsin(\gamma)}$$

a stretching symmetrical function which satisfies $g_x(1) = 1$ and $g_x(-1) = -1$, where $\gamma$ the parameter of stretching is taken very close to 1, about 0.99 in practice. The space derivative is thus given by

$$\frac{\partial u}{\partial x} = \frac{\partial u}{\partial \xi}\frac{\partial \xi}{\partial x} = -\frac{2\arcsin(\gamma)}{\gamma\, x_{\max}}\sqrt{1-\gamma^2\xi^2}\,\frac{\partial u}{\partial \xi}$$

### Time integration scheme

As we used previously, the equations of elastodynamics were rewritten in the form of a first order hyperbolic system in time in stress-velocities that we may note in symbolic form as follows

$$\frac{\partial U}{\partial t} = MU + S$$

where $U$ is the unknown stress-velocity vector, $S$ the source vector, and $M$ a differential operator. For this kind of first order systems, an effective time integration scheme is Runge-Kutta scheme of order four, which is a conditionally stable explicit scheme. That is, if $\Delta t$ is the time step, the solution $U^{n+1}$ at time $(n+1)\Delta t$ is obtained from the solution $U^n$ at time $n\Delta t$ by

$$U^{n+1} = U^n + \frac{1}{6}\Delta t(\delta_1 + 2\delta_2 + 2\delta_3 + \delta_4)$$

where

$$\begin{aligned}
\delta_1 &= MU^n + S^n \\
\delta_2 &= M\left(U^n + \frac{\Delta t}{2}\delta_1\right) + S^{n+1/2} \\
\delta_3 &= M\left(U^n + \frac{\Delta t}{2}\delta_2\right) + S^{n+1/2}
\end{aligned}$$

$$\delta_4 = M\left(U^n + \Delta t \delta_3\right) + S^{n+1}$$

It is seen that four modelings are necessary (application of the differential operator *M* to a given field) for each time step of the Runge-Kutta method of order four. The stability condition of this diagram will be controlled primarily by the size of the smallest mesh of the grid (after stretching by the nonlinear "mapping" function described in the preceding section).

In the case of a point force, the source term $\vec{\varphi}$ of the wave equation (4.5) can be written

$$\vec{\varphi}(\mathrm{x},t) = \delta(\mathrm{x}-\mathrm{x}_s) f(t-\tau)\vec{n} \tag{4.27}$$

where $\delta(\mathrm{x}-\mathrm{x}_s)$ is the Dirac distribution of at the source point $\mathbf{x}_s$, $f(t)$ is a causal function describing the time dependence of the source, τ is the starting time of the simulation, and $\vec{n}$ is an unit vector defining the force source direction . The source term is converted from Cartesian co-ordinates to curvilinear co-ordinates by using

$$\begin{aligned}\varphi_\xi &= \varphi_x \frac{\partial x}{\partial \xi} + \varphi_z \frac{\partial z}{\partial \xi}\\ \varphi_\eta &= \varphi_x \frac{\partial x}{\partial \eta} + \varphi_z \frac{\partial z}{\partial \eta}\end{aligned} \tag{4.28}$$

The time extrapolation scheme is used with zero initial conditions $v(x, t_0) = 0$ and $\sigma(x, t_0) = 0$, the time $t_0 = 0$ corresponds to the beginning of the simulation. The stability time scheme is ensured by a traditional Courant condition

$$\Delta t \left(\frac{\upsilon_P}{\Delta x}\right)_{\max} \le \varepsilon \tag{4.29}$$

where $\Delta x$ is the distance between grid points in the physical field, $v_P$ is the **P** wave velocity in the medium and $\varepsilon$ is the Courant number.

The scheme is practically free of any numerical dispersion until the Nyquist frequency. We ensure this condition by choosing a maximum grid step such that the minimum number of points per wavelength satisfies the following relation

$$n_\lambda^{\min} = \frac{1}{f_{\max}} \left(\frac{\upsilon_S}{\Delta x}\right)_{\min} \ge n_\lambda^{scheme} \tag{4.30}$$

where $\Delta x$ is the distance between grid points in the physical field, $v_S$ is the the S wave velocity in the medium, $f_{max}$ is the maximum frequency of the source, and $n_\lambda^{scheme}$ is the minimum number of points of the grid per wavelength necessary for a correct modeling (about 4 for Chebyshev operator ).

The boundary conditions are of the absorbing type on all the edges of the model except for the free surface. These conditions as well as the free surface condition are implemented in the Chebyshev algorithm by decomposing the field using a paraxial equation according to the perpendicular edge.

### 4.4.2 Inadequacy of finite differences diagrams

Tests were also carried out by using a finite difference method, but the algorithm led to numerical difficulties in the case of strong velocity contrasts at the interface, because of the fact that a grid which is not quincunx is in fact made up of two slightly coupled grids – even worse, completely uncoupled in the case of a regular grid mesh –. Consequently, this approach was abandoned. The finite difference algorithms in quincunx are not well adapted to solve wave equations on a curved grid (using the tensorial formulation or the composed derivation rule), because of the fact that many interpolations must be carried out in this case, which strongly affects and reduces the total precision of the diagram and increases the calculation cost significantly. In the case of the tensorial formulation used on a grid in quincunx, it is necessary to carry out interpolations to calculate the covariant derivative which is equal, in a grid point, to the sum of the partial derivative of the field and components of the field itself multiplied by Christoffel symbols. In the case of use of the composed derivation rule on a grid in quincunx, it is also necessary to carry out interpolations to calculate the Cartesian derivatives of the field, for which it is necessary to sum up in the same grid point the partial derivatives calculated along different axes in the grid of work.

### 4.4.3 Vectorization of the algorithm and performances

As we have shown previously, there are two methods for the calculation of the field derivative using Chebyshev's algorithm that makes use of Gauss-Lobatto collocation points. The first approach consists in calculating the coefficients of the field decomposition in terms of Chebyshev's series using an FFT (equation 2.24), then to calculate the coefficients of the series derived by recurrence, and then to obtain the field derivative from these coefficients by another FFT (equation 4.22). The second method consists in multiplying the field by the derivation matrix directly whose coefficients were calculated once for all.

From the point of view of the number of operations in 2D case, the first approach requires the calculation of $2N$ FFT of length $N$ (2 FFT for each $N$ column, that is a cost in $O(N^2 \log N)$), and $N$ recurrences of length $N$, at a cost in $O(N^2)$. The total cost of the first approach is thus in $O(N^2 \log N)$. The second approach is a simple product of matrices, whose cost is $O(N^2)$ in the 2D case. A first glimpse on the analysis would thus seem to privilege the FFT approach.
Without any doubt, this is the conclusion which would be necessary to draw for the case for a sequential computer code having to be carried out on a workstation. However, in the very frequent case of a powerful personal computer of the vectorial type, it is well-known that a relation of recurrence vectorises badly, even not at all because of the dependences existing between elements of the result vector of this relation of recurrence. In this case, calculation by product of matrix of derivation, although requiring more operations, is appreciably faster. Indeed, a product of matrix is an operation which vectorises well, especially if the size of the grid, therefore the $N$ value, is large. Moreover, the manufacturer of the machine often provides particularly optimized algorithms, called BLAS (Basic Linear Algebra Subroutines), which make it possible to get maximum power benefit from the machine for this type of operations.

## 4.5 Numerical tests in 2D

Numerical tests were undertaken for 2D cases by using two different models, the first model is used to validate the tensorial approach by comparing the results obtained with that of the analytical solution of the problem, and the second making it possible to show the capacity of this approach to take into account the structure model with the free surface of the topography.

### 4.5.1 Validation of the tensorial formulation

In order to validate the method using the tensorial formulation of the wave equation, we compared the results obtained for Lamb's problem, i.e. homogeneous elastic half-space in which a source force is placed in the medium with a normal direction, with the analytical solution of the problem. The grid used is represented on figure 4.2, and has a size of $500m \times 500m$. The medium is homogeneous, the P wave velocity is equal to 3000 $m.s^{-1}$ and the S wave velocity is equal to 1800 $m.s^{-1}$, the density is taken equal to 1000 $kg.m^{-3}$.

The source is a force having a normal direction with the free surface. It is placed at $x_s = 100\ m$, and just below the surface, at a depth of $z_s = 8m$. One of the receivers ($R_1$) is placed on the free surface at $x_{R1} = 200 \quad 1793.3m$ the other receiver ($R_2$) is located in the medium at $x_{R2} = 180\ m$ at a depth of $z_{R2} = 80\ m$. Thus, the first receiver will record mainly a very strong Rayleigh wave, whereas the second receiver records the incident P wave and S wave propagating in the rectangular grid. This will make it possible to validate the tensorial formulation for the three principal wave types propagating in a solid.

Numerical calculation are undertaken for a total duration of 0.875 $s$, i.e. 2500 time steps of duration $\Delta t = 0.35ms$. The length on the mesh sides of the rectangular grid in the physical field varies $\Delta x_{\min} = 1.4m$ to $\Delta x_{\max} = 16.3m$ along the horizontal lines of the grid, and $\Delta z_{\min} = 0.9m$ to $\Delta z_{\max} = 14.1m$ along the vertical lines.

The source function is a second derivative of Gaussian in time, having a central frequency of $f_0 = 20.0$ Hz and a maximum frequency of $f_{max}$=50.0 Hz (defined as the frequency for which the spectral amplitude is equal to about 5 % of its maximum value). The minimum number of grid points per fundamental wavelength (corresponding to the largest meshes) is of 9.7 for the P waves and of 5.6 the S waves.

Snapshots of the velocity vector are presented on figure 4.3, and show the incident P wave, the incident S wave as well as the Rayleigh wave propagating along the free surface. The accelerograms recorded at the two receivers are presented on figure 4.4. A very good agreement is obtained between the analytical solution and the numerical results, at the same time for Rayleigh waves (receiver $R_1$) and for volume waves (receiver $R_2$), which validates the tensorial approach for the elastic wave equations.

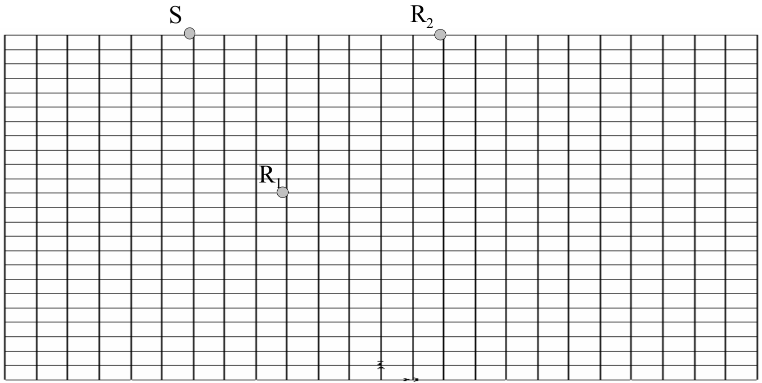

Fig. 4.2: Grid used to validate the tensorial approach compared to the analytical solution of Lamb's problem. The grid size is of 187×187 points. Locations of 2 receivers and the point source is also shown.

### 4.5.2 Simulation in the case of a layered half-space

In order to test the capacity of the tensorial approach to model the elastic wave propagation in layered mediums, we conducted two simulations based on the model presented on figure 4.2. The grid is made up of 187×187 points. A model with two layers is used, the interface is also included. In the upper layer, the density is taken equal to 1000 $kg.m^{-3}$, the P wave velocity to 2800 $m.s^{-1}$ and the S wave velocity to 1820$m.s^{-1}$, with a Poisson's ratio of $\sigma = 0.13$. In the sub-layer, the density is 1500 $kg.m^{-3}$, the P wave velocity to is 3800 $m.s^{-1}$ and the S wave velocity to 2000$m.s^{-1}$, and a Poisson's ratio of $\sigma = 0.30$. Thus, this two layers model presents a strong contrast in terms of velocities and also a strong contrast in terms of Poisson's ratio, which makes it possible to check the behavior of the method for a soil model presenting realistic properties. The characteristics of the source remain the same ones as in the case of Lamb's problem previously studied.

The size of the meshes on the sides of the grid varies between $\Delta x_{\min} = 1.4m$ and $\Delta x_{\max} = 18.6m$ along the horizontal lines of the grid, and between $\Delta z_{\min} = 2.0m$ and $\Delta z_{\max} = 15.6m$ along the vertical lines. It is noted that curved grids may also be used, and in this case the grid is curved, where a straight line in the physical field does not necessarily correspond to a straight line in the field of study. In general, the receivers are not located in grid points and it is necessary to interpolate the field (for example velocity field speed) which one wishes to record. This is carried out by using a bilinear interpolation starting from the known values located at the corners of the mesh.
As previously, numerical calculation are undertaken a duration of propagation of 0.875 $s$, i.e. 2500 steps of time duration $\Delta t = 0.35ms$ each. The minimum number of grid points per wavelength is 7.5 for P wave, and 4.9 for S wave for the two tests.

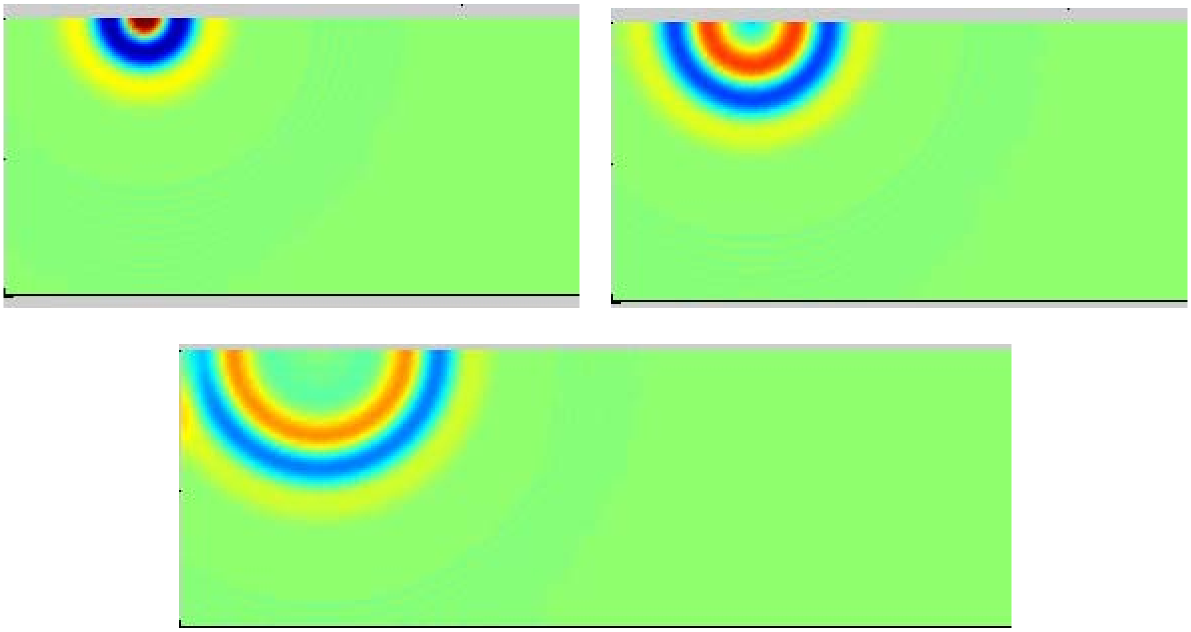

Fig. 4.3 - Instantaneous snapshots of the velocity vector obtained for Lamb's problem. The source $S$ and the two receivers $R_1$ and $R_2$ are as indicated on figure 4.2. The source is placed on the surface, and we can observe the incident P and S waves, along with Rayleigh waves.

- Reflected and refracted waves in a layered half-space.

This is the first test, where the source is a vertical force located at $x_s = 425\ m$ at a depth $z_s = 70\ m$. Fifty equidistant receivers are placed along a horizontal line between $x_r = 25m$ and $x_r = 100\ m$ with a depth $z_r = 20\ m$.

The instantaneous snapshots of the propagation are presented on figure 4.5, and the accelerograms on figure 4.6.

The form of the reflected P and S waves by the layered half-space on the free surface is complex, and triplications occur (see for example the reflected and transmitted waves made by the interface between the two layers and the reflexions made by the excavated part of the soil, where the structure is to be placed ). Wave mode conversion (from P to S and from S to P waves) occur at the free surface, wave mode conversion occurs also at the interface between two layers for the transmitted and reflected waves .

These results clearly illustrate the fact that the tensorial approach is able to model the reflexion and the mode conversion of the P and S waves in a model having layers and/or curved interfaces, including strong velocity contrasts.

- Rayleigh wave on a curved surface

The source force is vertical and placed at $x_s = 660.9m$ at shallow depth (10 *m* depth). The incident P waves and S waves are clearly visible on these snapshots, as well as a strong Rayleigh wave propagating along the free surface with a speed slightly lower than the S waves.

On these instantaneous snapshots, we can also observe a wave which is interpreted as a Rayleigh wave conversion into a volume wave in an area of the free surface where the topography has a strong curve because of the small monticule located in the left part of the model (see the instantaneous snapshots at times $t = 0.280$ *s* and $t = 0.350$ *s*).

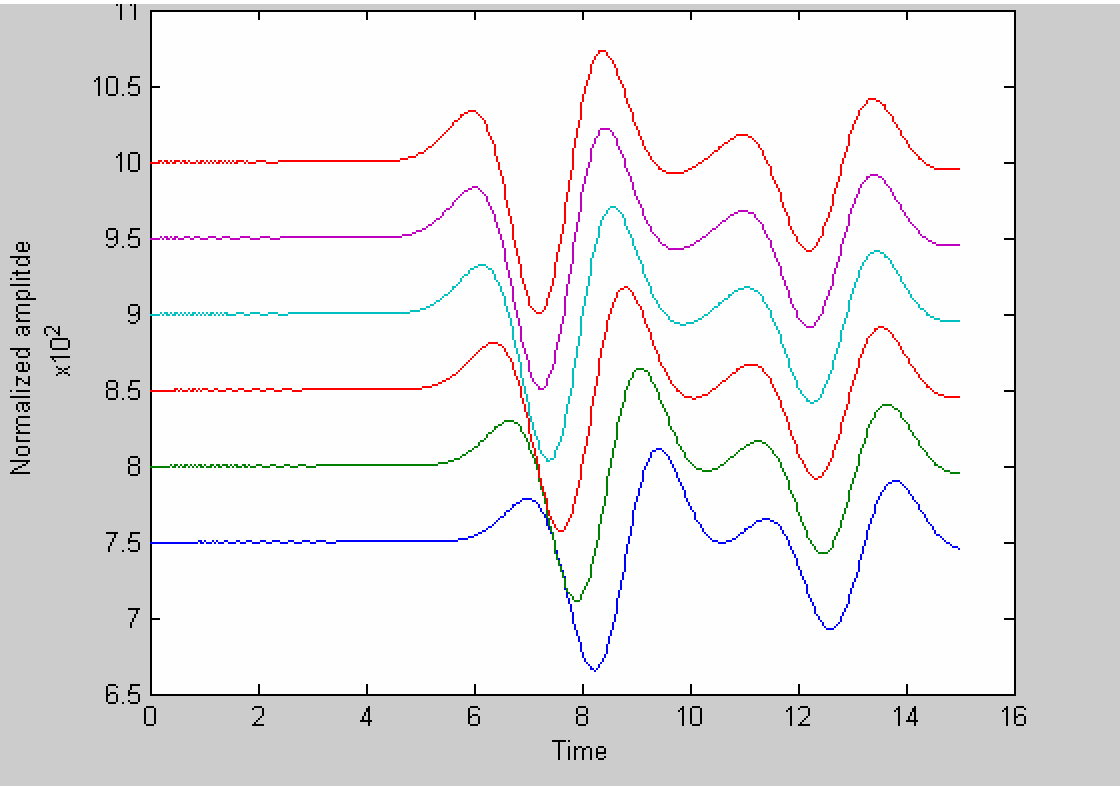

Fig. 4.4–Accelerograms (timehistories) of the horizontal velocity vector component $v_x$ (left) and the vertical component $v_z$ (right) for Lamb's problem of figure 4.3. The top accelerograms correspond to the receiver ($R_1$) located at shallow depth (just under the free surface), and those of the bottom to the receiver ($R_2$) located inside the model. The agreement obtained is excellent, the maximum change between the two solutions is less than 1 %.

The energy part of Rayleigh wave converted into volume waves presents itself in the form of a volume wave which closely follows the incident S wave. It seems that this converted wave was formed at the time of the passage of the Rayleigh wave in the concave part of the soil. This converted wave can be observed clearly on the horizontal component $v_x$ of the velocity recorded on the free surface. These results prove that the tensorial formulation of the wave equations allows the modeling of the propagation of Rayleigh waves in a layerd elastic model even in the presence of a curved surface.

## 4.6 Insufficiency of Chebyshev algorithm for realistic models

We have just seen that a simple solution of pseudo-spectral type can make it possible to solve with precision the wave equations of a complex medium. The introduced tensorial formulation made it possible to reduce significantly the number of calculations to be carried out. Nevertheless, during this study, several difficulties appeared clearly, and showed the intrinsic limitations of the global pseudo-spectral solution based on a differential from of the elastodynamic equations.

- the method is very time consuming (expensive) in a number of operations. The cost of a 2D calculation is in the order of $O(N^3)$, knowing that $N$ is always large, at least 200 for a realistic 2D model. Runge-Kutta algorithm of order four in terms of time is also expensive, since four complete modelings are necessary for each time step.

- to avoid having a stability condition too restrictive in the explicit diagram of Runge-Kutta because of the closeness of Gauss-Lobatto-Chebyshev points on the edges of the domain, a strongly nonlinear mapping must be introduced. It is certain that this one introduces additional truncation errors into the scheme diagram and thus reduces the total precision of the calculation.

- the algorithm is not suited for parallel architectures of modern supercomputers with distributed memory.

- Finally and especially, the fact of having to find a global transformation grid sufficiently regular (smooth) between the studied domain and the square of reference, imposes extremely strong restrictions on the types of models being able to be studied, and decreases the interest of the method for really complicated cases. For example, for an accidental topography, it seems completely illusory to seek a total transformation which is sufficiently regular. It is clear that this argument is even more problematic if one wishes to consider the three-dimensional case.

It is thus now necessary to seek to solve these various problems by other means. The approach that we chose, and which will be described in the following chapters, constitutes the main part of this thesis, is the spectral finite element method, which will make it possible to combine the geometrical flexibility of the variational approach in a weak nature with the precision of the spectral approach.

## 4.7 Conclusions

If one wishes to study a complex soil model, it is advantageous to be able to directly solve the wave equation in deformed grids whose lines coincide with the interfaces of the model which can be layered, and also with the free surface. This will lead to more precise results than if such a model is meshed with regular grids.

A tensorial formulation of the wave equation was presented, which makes it possible to solve the problem without needing to introduce a Cartesian reference frame. Such an approach is more natural than the one largely used, consisting in solving the equation written in Cartesian co-ordinates by calling upon the

composed rule of derivation to calculate the Cartesian derivatives in the curvilinear domain of calculation. Moreover, this tensorial formulation approach results from a numerical point of view in calculating less spatial derivatives than in the case of the composed rule of derivation (exactly the same number as in the Cartesian case), which makes it possible to reduce significantly the total cost of calculation of the method.
A simple algebraic grid generation algorithm makes it possible to define a grid adapting itself to the various interfaces, and which we can refine in a controlled manner in the vicinity of these interfaces and surface. That makes it possible to get rid of the numerical artifacts which would result from the discretization of the interfaces if Cartesian grids were used.

Numerical tests were carried out for a 2D medium by using Chebyshev algorithm that have validated the tensorial approach which also illustrates its capacity to take into account curved interfaces as well as layered soils with non-horizontal surface topography. In the case of Lamb's problem, an excellent agreement with the analytical solution is obtained. In the case of a layered non-horizontal model, complex forms are obtained for the various reflected and converted waves considered, and triplications occur. Moreover, if the source is sufficiently close to surface, Rayleigh wave mode conversions occurs and gives result to volume waves that may be observed when the Rayleigh wave propagates in surface zone having a strong concavity.
From a numerical point of view, we explained why the presented algorithm was particularly suited for supercomputers of the vectorial type, but were not optimal for a parallel architecture. We noted that its cost remained high with 2D, and probably prohibitory with 3D for realistic grid sizes. We have also said that, even if the presented global differential solution is applicable for many problems, it suffered from an intrinsic limitation when the form of the interfaces and free surface became really complicated, and we have deduced the need for a more flexible technique, typically derived from a variational formulation of the $h$ or $h - p$ type problem, that will allows the treatment of realistic cases.

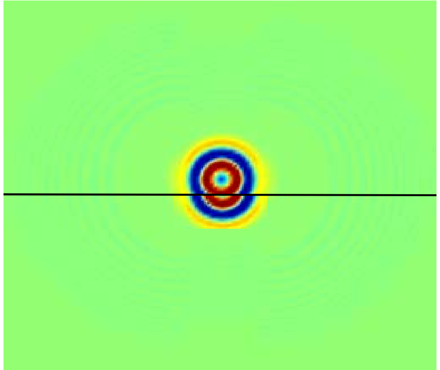

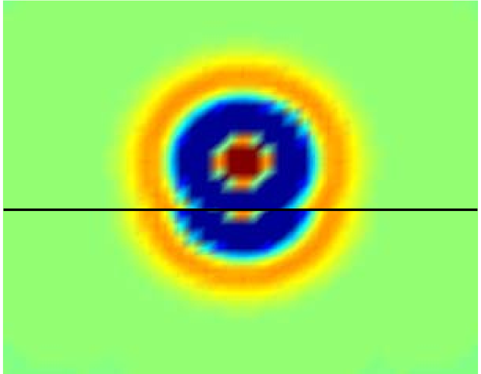

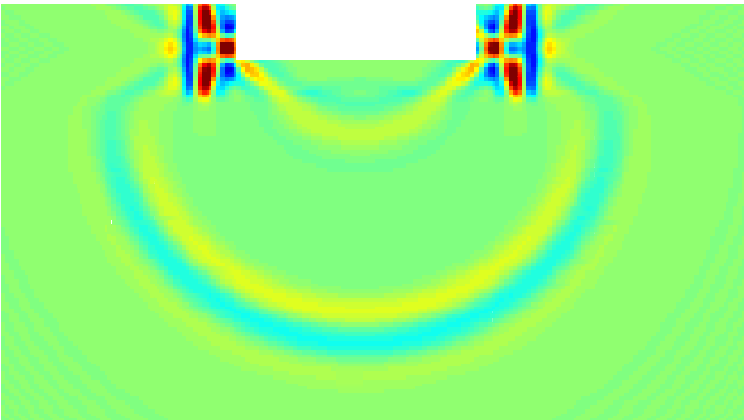

Fig. 4.5 Instantaneous snapshots for a model presenting a layered half-space and an excavated part of the soil at the free surface. The source load is a vertical force placed inside the model, one can observe the complex form of the various waves, for example the transmitted and reflected waves through the interface and from the excavated part of the soil.

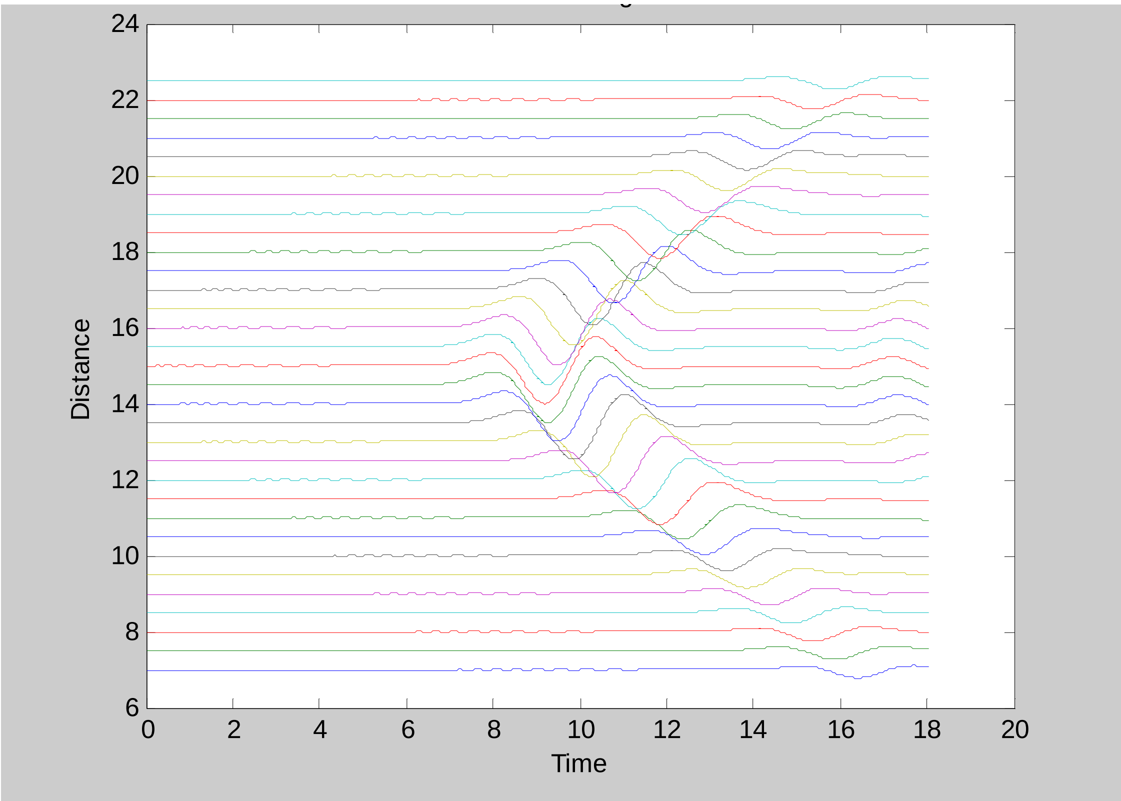

Fig. 4.6 Accelerograms of the above model presenting a layered half-space (figure 4.5).The source is a vertical load located in the model, and the receivers are also located inside the medium.

Chapter 5

# 5. Perfectly matched layers for unbounded domains

## 5.1. Introduction

Solution of wave equations in the presence of unbounded domains is of interest in various fields of engineering and science [110]. Especially, the solution of elastodynamic wave equation finds applications in soil-structure interaction analysis [115] and in the simulation of earthquake ground motion, since the ground beneath a structure of interest can be rationally modelled as an unbounded elastic domain.

The solution of wave equation in the case of an unbounded domain requires the use of a radiation condition in any direction of the unbounded domain, where waves are allowed to radiate outwards from a source or a vibrating structure toward infinity, without spurious wave motions in the reverse direction. Because of the many irregularities in the geometry of the domain or in the physical material, it is generally called upon a numerical solution of the problem, which requires the use of a bounded domain, along with a somewhat artificial boundary that absorbs outgoing waves.

Typical absorbing boundaries belong to one of two main categories:

1) exact, non-local boundaries [99],
2) approximate, local boundaries [44].

The various absorbing boundaries, local or not, have some drawbacks.

The exact rigorous boundaries are highly accurate and thus may be used even with a small bounded domain. However, the small computational cost due to the small size of the domain may be negated by the expensive cost due to not only the non-local nature of such boundaries but also the computation of the boundary terms. Moreover, exact boundaries may not be available for all types of problems. The approximate boundaries, although local and easy to compute, may require larger bounded domains compared to the first ones for satisfactory accuracy, since they absorb incident waves well only over a small range of angles of incidence. Moreover, high order approximate boundaries require the use of special finite elements such spectral finite elements [38] for proper implementation. Many different absorbing layer models [98] surrounding a bounded domain have also been proposed as alternatives to absorbing boundaries; but, obtaining satisfactory results from such models requires careful formulation and implementation, since the change in material properties from the elastic medium to the absorbing layer causes reflection of incident waves. Also interesting are special absorbing boundaries such as the superposition boundary and infinite elements [118]; although based on interesting ideas, use of these boundaries may prove to be cumbersome and computationally expensive.

A perfectly matched layer (PML) is an absorbing layer model for linear wave equations that absorbs, almost perfectly, all propagating waves from all angles of incidence and of all non zero frequencies. The idea of a PML was first introduced by Bérenger [6] in the field of electromagnetic waves. PMLs have been also formulated for other linear wave equations, such the scalar wave equation or the Helmholtz equation [42], the linearised Euler equations [45], the wave equation for poroelastic media [119], and, as discussed below, to the elastodynamic wave equation.

The idea that PMLs could be formulated for the elastodynamic wave equation was first introduced by Chew and Liu [12], they used complex valued coordinate stretching system to obtain the equations governing the PML and presented a proof of the absorptive property of the PML. They also presented a finite difference time domain formulation obtained through field splitting. Later, Liu [64] applied the coordinate stretching idea to the velocity stress formulation of the elastodynamic equation to obtain split field PMLs for time dependent elastic waves in cylindrical and spherical coordinates. Zhang and Ballmann [120] and Collino and Tsogka [16] have also obtained split field, time domain PMLs for the velocity stress formulation and presented finite difference time domain (FDTD) implementations. The latter have also implemented the PML using a two dimensional mixed finite element scheme [5] in which the degrees of freedom of each element are the velocity, the shear stress, and split field components of the axial stresses.

In this thesis the objective of PMLs is twofold:

a) develop the concept of a PML in the context of time harmonic elastodynamics in Cartesian coordinates, utilising some of the insights obtained in the context of electromagnetics [102],

b) develop a new displacement based symmetric spectral finite element method (SFEM) of the PML for time harmonic plane strain to be implemented in the Matlab environment.

The PML concept is first illustrated through the one dimensional example of a rod on elastic foundation and second through the two dimensional example of the anti plane motion of a continuum, governed by the Helmholtz equation. The PMLs for these two systems are studied through analytical and numerical results for the dynamic stiffness of a semi infinite rod on elastic foundation, and through numerical results for the out of plane dynamic stiffness of a semi infinite layer on rigid base. Numerical results are presented for the classical soil structure interaction problems of a rigid strip footing on a half-plane, and a layer on a half-plane, then for a layer on a rigid base.

## 5.2. One dimensional system

### 5.2.1. Semi infinite rod on elastic foundation

For the semi infinite rod on elastic foundation shown on (Fig. 5.1), not subjected to any body forces, but subjected to an imposed displacement $u_0$ exp($i\omega t$) at the left end ($x = 0$), and a radiation condition for $x \to \infty$, with $\omega$ being the frequency of excitation. This excitation causes time harmonic displacements $u(x)$ exp($i\omega t$), which are governed by the following equations:

$$\frac{d\sigma}{dx} - \frac{k_g}{A} u = -\omega^2 \rho u \tag{5.1a}$$

$$\sigma = E\varepsilon \tag{5.1b}$$

$$\varepsilon = \frac{du}{dx} \tag{5.1c}$$

where $\sigma$ and $\varepsilon$ are the axial stress and infinitesimal strain in the rod, $E$ is the Young's modulus of the rod, $A$ its cross-sectional area, $\rho$ its mass density, and $k_g$ the static stiffness per unit length of the foundation.

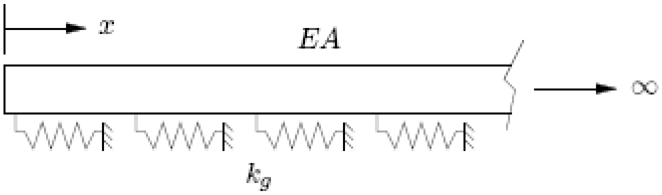

Fig. 5.1. Homogeneous viscous elastic semi infinite rod on elastic foundation.

The frequency response of this system can be expressed in terms of a dimensionless frequency $a_0 = \omega r_0 / c_l$, where $r_0 = \sqrt{EA/k_g}$ is a characteristic length quantity and $c_l = \sqrt{E/\rho}$ is the wave velocity in the rod. For $a_0 < 1$, Eq. (5.1) admits rightward and leftward evanescent wave solutions of the form

$$u(x) = \exp\left[-\sqrt{1-a_0^2}\,\frac{x}{r_0}\right] \quad \text{and} \quad u(x) = \exp\left[+\sqrt{1-a_0^2}\,\frac{x}{r_0}\right] \tag{5.2}$$

and admits rightward and leftward propagating wave solutions of the form

$$u(x) = \exp\left[-i\sqrt{a_0^2-1}\,\frac{x}{r_0}\right] \quad \text{and} \quad u(x) = \exp\left[+i\sqrt{a_0^2-1}\,\frac{x}{r_0}\right] \tag{5.3}$$

for $a_0 > 1$, with $a_0 = 1$ the cutoff frequency of the system; the radiation condition allows only the rightward modes in the system. The dynamic stiffness at $x = 0$, which is the axial force $-\sigma A$ required in the positive $x$-direction at $x = 0$ to maintain $u_0 = 1$, can be obtained using Eqs. (5.1*b*), (5.1*c*) and Eqs. (5.2a), (5.3a) as

$$S^{\infty}(a_0) = K^{\infty}\sqrt{1-a_0^2} \tag{5.4}$$

where $K^{\infty} = \sqrt{EAk_g}$ is the static stiffness coefficient of the system. The dimensionless dynamic stiffness, corresponding to $K_1 = 1$, is defined as

$$\bar{S}^{\infty}(a_0) := \sqrt{1-a_0^2} \tag{5.5}$$

For the case of the motion of a viscous elastic system, where material damping is introduced using the correspondence principle, may also be described by the above equations, but with complex valued material moduli $E^* = E(1+2i\varsigma)$ and $k_g^* = k_g(1+2i\varsigma)$ in place of the real moduli $E$ and $k_g$, $\zeta$ being the hysteretic damping ratio. The introduction of such complex moduli values results in a complex valued wave speed $c_l^* = c_l\sqrt{1+2i\varsigma}$ and complex valued dimensionless frequency $a_0^* = a_0/\sqrt{1+2i\varsigma}$.

The solutions in terms of the displacement and dynamic stiffness of the semi infinite rod are obtained analytically by solving Eq. (5.1) on the unbounded domain [0, 1] using appropriate boundary conditions. The numerical solution of this unbounded domain problem requires the solution of Eq. (5.1) on a bounded domain increased by an artificial absorbing boundary or layer; the PML is well suited as an absorbing layer model that can be used for this purpose.

## 5.2.2. Perfectly matched medium

For a given system of equations of the same form as Eq. (5.1), but with $x$ replaced by a stretched coordinate $\tilde{x}$, defined as

$$\tilde{x} := \int_0^x \lambda(x)\,ds \tag{5.6}$$

where $\lambda$ is a nowhere zero, continuous complex valued coordinate function. By the continuity of $\lambda$,

$$\frac{d\,\tilde{x}}{dx} = \lambda(x) \tag{5.7}$$

which formally implies

$$\frac{d}{d\,\tilde{x}} = \frac{1}{\lambda(x)}\frac{d}{dx} \tag{5.8}$$

Thus this aforementioned system of equations can be defined as

$$\frac{1}{\lambda(x)}\frac{d\sigma}{dx} - \frac{k_g}{A}u = -\omega^2 \rho\, u \tag{5.9a}$$

$$\sigma = E\varepsilon \tag{5.9b}$$

$$\varepsilon = \frac{1}{\lambda(x)}\frac{du}{dx} \tag{5.9c}$$

as a modification of Eq. (5.1), where the constitutive relation, Eq. (5.9b), remains the same as in the elastic medium. A perfectly matched medium (PMM) for a rod on elastic foundation is defined to be a medium where the field variable *u* is governed by Eq. (5.9). The viscoelastic medium is a special PMM, where $\lambda(x) \equiv 1$.

Equation (5.9) is only motivated by, but defined independently of Eq. (5.8); using the latter to derive the PMM equations from Eq. (1) would involve issues of complex differentiability, all of which are avoided by the independent definition of the PMM. The assumption of continuity on $\lambda$ could be dropped, by considering one-sided derivatives, or possibly even weak derivatives, in Eq. (5.7); such technical issues are avoided by this convenient assumption. Note that the assumption of a continuous $\lambda$ is not restrictive in the least, the stretching function is specified a priori, and is not a physical quantity that is intrinsically discontinuous.

As is to be expected from the coordinate stretching motivation, Eq. (5.9) admits solutions similar in form to those in Eqs. (5.2) and (5.3) admitted by the elastic medium, but with *x* replaced by $\tilde{x}$. Evanescent wave type solutions are of the form

$$u(x) = \exp\left[-\sqrt{1-a_0^2}\,\frac{\tilde{x}}{r_0}\right] \quad \text{and} \quad u(x) = \exp\left[+\sqrt{1-a_0^2}\,\frac{\tilde{x}}{r_0}\right] \tag{5.10}$$

for $a_0 < 1$, and propagating wave type solutions are of the form

$$u(x) = \exp\left[-i\sqrt{a_0^2-1}\,\frac{\tilde{x}}{r_0}\right] \quad \text{and} \quad u(x) = \exp\left[+i\sqrt{a_0^2-1}\,\frac{\tilde{x}}{r_0}\right] \tag{5.11}$$

for $a_0 > 1$; that these are solutions of Eq. (5.9) can be shown by utilising the continuity of $\lambda$ through Eq. (5.7). An interesting property of these PMMs is that if two PMMs having different λ are placed adjacent to each other, with the functions $\lambda$ such that they match at the interface of the two media, then a wave type motion will pass through the interface without generating any reflected waves; this is the perfect matching property of the PMM. Without loss of generality, consider two PMMs: one is defined on $(-\infty, 0)$ with $\lambda(x) := \lambda(x)^{lt}(x)$, and the other on $(0, \infty)$ with $\lambda(x) := \lambda(x)^{rt}(x)$, with the stretching functions such that $\lambda(x)^{lt}$

$(0) = \lambda\ (x)^{rt}\ (0)$. These two PMMs can be considered as only one PMM but with a continuous $\lambda$ defined piecewise on $(-\infty,\ 0)$ and $(0, \infty)$; thus, there is no interface, precluding the possibility of the generation of any reflected waves. The perfect matching property holds for both solutions in Eq. (5.11) as well as for those in Eq. (5.10), i.e., it is independent of the wave type, of the direction of propagation, and of the frequency $a_0$.

Another special property of the PMMs is that for suitable choices of $\lambda$, the solutions in the PMM take the form of the corresponding elastic medium solution but with an imposed spatial attenuation. Consider, for $a_0 > 1$, $\lambda$ defined in terms of a real valued, continuous function $f$ as

$$\lambda(x) := 1 - i\frac{f(x)}{\sqrt{a_0^2 - 1}} \tag{5.12}$$

Then

$$\frac{\tilde{x}}{r_0} = \frac{x}{r_0} - i\frac{\bar{F}(x/r_0)}{\sqrt{a_0^2 - 1}} \tag{5.13}$$

where

$$\bar{F}(\bar{x}) := \int_0^{\bar{x}} \bar{f}(\bar{\xi})\,d\bar{\xi} \tag{5.14}$$

with $\bar{\xi} = \xi/r_0$ and $\bar{f}(\bar{\xi}) = f(r_0\bar{\xi}) = f(\xi)$. On substituting for $\tilde{x}$ from Eq. (5.13) into Eq. (5.11a), the solution is obtained as

$$u(x) = \exp\left[\bar{F}(x/r_0)\right]\exp\left[-i\sqrt{a_0^2 - 1}\,\frac{x}{r_0}\right] \tag{5.15}$$

Thus, if $\bar{F}(x/r_0) > 0$, then $u(x)$ is a rightward propagating wave that is attenuated in that direction, with the attenuation independent of the frequency due to the choice of $\lambda(x)$; the function $f$ is termed the attenuation function. Furthermore, for $a_0 < 1$, $\lambda$ is defined as

$$\lambda(x) := 1 + \frac{f(x)}{\sqrt{1 - a_0^2}} \tag{5.16}$$

then Eq. (5.10) is transformed to

$$u(x) = \exp\left[-\bar{F}(x/r_0)\right]\exp\left[-\sqrt{1 - a_0^2}\,\frac{x}{r_0}\right] \tag{5.17}$$

i.e., an evanescent wave with additional attenuation. The above choices for the stretching function are only illustrative choices that exploit prior knowledge of the solution. A more realistic choice for $\lambda$ would be in terms of two non negative attenuation functions $f^{\mathrm{e}}$ and $f^{\mathrm{P}}$, as

$$\lambda(x) := \left[1 + \frac{f^e(x)}{a_0}\right] - i\frac{f^P(x)}{a_0} \tag{5.18}$$

This function does not assume knowledge of the frequency equation of the system, nor does a priori distinguish between evanescent and propagating waves. This choice for $\lambda$ imposes a frequency dependent attenuation and a phase change on the rightward propagating wave. Eq. (5.11) is transformed into

$$u(x)=\exp\left[-\overline{F}^{P}(x/r_0)\sqrt{1-\frac{1}{a_0^2}}\right]\exp\left[-i\sqrt{a_0^2-1}\left(\frac{x}{r_0}+\frac{\overline{F}^{e}(x/r_0)}{a_0}\right)\right] \tag{5.19}$$

where $\overline{F}^{e}$ and $\overline{F}^{P}$ are appropriately defined integrals of $f^{\,e}$ and $f^{\,\mathrm{P}}$, respectively. Using Eq. (5.18) imposes an attenuation and a harmonic mode on evanescent waves. Eq. (5.10) transforms to

$$u(x)=\exp\left[-\overline{F}^{e}(x/r_0)\sqrt{\frac{1}{a_0^2}-1}\right]\exp\left[-i\overline{F}^{P}(x/r_0)\sqrt{\frac{1}{a_0^2}-1}\right]\exp\left[-\sqrt{1-a_0^2}\,\frac{x}{r_0}\right] \tag{5.20}$$

Thus, $f^{e}$ imposes an attenuation on evanescent waves and $f^{p}$ on propagating waves.

### 5.2.3. Perfectly matched layer

The special properties of the PMM can be used to define an absorbing layer adjacent to a bounded domain such that the layer and the domain together model the unbounded domain.
Forr the system shown in Fig. 5.2(a): $\Omega_{\mathrm{BD}}$ (:= [0, L] ) is the bounded domain governed by Eq. (5.1), and $\Omega_{PM}^{\infty}(:=(L,\infty))$ is the unbounded PMM, governed by Eq. (5.9). The stretch $\lambda$ is taken to be of the form given in Eq. (5.12) for $a_0 > 1$ and Eq. (5.16) for $a_0 < 1$, with $f$ chosen such that $f(L) = 0$. Alternatively, $\lambda$ can be chosen as in Eq. (5.18) for all $a_0$, with the attenuation functions such that $f^{\,\mathrm{e}}(L) = f^{\,\mathrm{P}}(L) = 0$. Since the medium in $\Omega_{\mathrm{BD}}$ is a special PMM, with $\lambda \equiv 1$, and since the admissible choices of attenuation functions impose that the functions $\lambda$ for the two domains are matched at the interface, all waves propagating outwards from $\Omega_{\mathrm{BD}}$ are completely absorbed into and then attenuated in $\Omega_{PM}^{\infty}$. Thus, the displacements of this system in $\Omega_{\mathrm{BD}}$ are exactly the same as the displacements of the semi infinite rod in $\Omega_{\mathrm{BD}}$.
If the waves are attenuated enough in a finite distance, $\Omega_{PM}^{\infty}$ can be terminated with a fixed boundary condition at that distance without any significant reflection of the waves. Shown in Fig. 5.2(b), this bounded [PMM $\Omega_{\mathrm{PM}}$ (:= ($L$; $L$+$L_{\mathrm{P}}$ ] is termed the perfectly matched layer (PML). If the wave reflection from the fixed boundary is not significant, the displacements of the entire bounded system $\Omega(:= \Omega_{\mathrm{BD}} \cup \Omega_{\mathrm{PM}})$ in $\Omega_{\mathrm{BD}}$ should be almost the same as the displacements of the semi infinite rod in $\Omega_{\mathrm{BD}}$.

### 5.2.4. Effect of fixed-end termination of the PML

The effect of fixed-end termination in a given domain on the PMM is considered, first by calculating the reflected waves from the fixed boundary conditions and then by investigating the effects of $L$, $L_{\mathrm{P}}$ and $f$ on the dynamic stiffness $\overline{S}(a_0)$ of $\Omega$ at $x = 0$.
The reflected wave amplitude is calculated by considering a PMM defined on [0, $L_{\mathrm{P}}$ ] with an imposed displacement $u(L_{\mathrm{P}}) = 0$. The stretch is chosen as in Eq. (5.12) for $a_0 > 1$ and as in Eq. (5.16) for $a_0 < 1$. A rightward propagating wave ($a_0 > 1$) with a unit amplitude as it enters the PML, along with a wave reflected back from the fixed boundary, can be represented

$$u(x)=\exp\left[-i\sqrt{a_0^2-1}\,\frac{\tilde{x}}{r_0}\right]+R\exp\left[+i\sqrt{a_0^2-1}\,\frac{\tilde{x}}{r_0}\right] \tag{5.21}$$

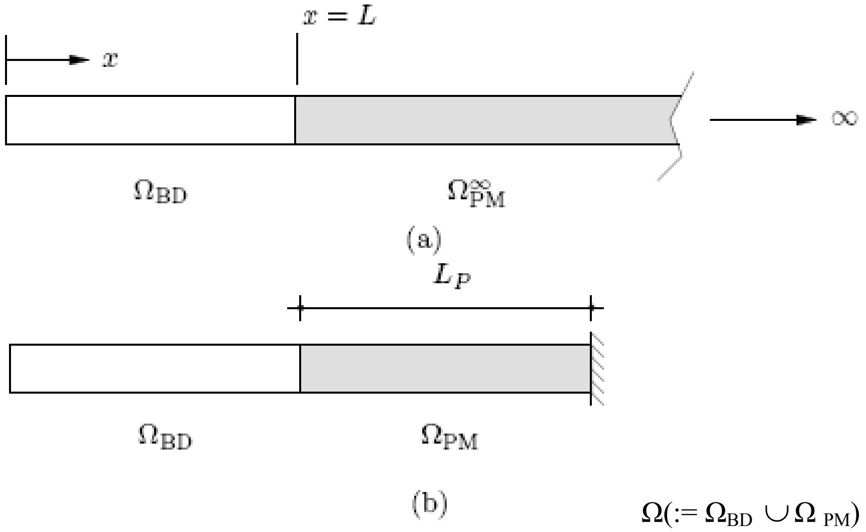

Fig. 5.2. (a) Perfectly matched medium; (b) perfectly matched layer, adjacent to the bounded domain for the semi infinite rod on elastic foundation.

Imposing $u(L_{\mathrm{P}}) = 0$ gives

$$|R| = \exp[-2\overline{F}(L_P/r_0)] \tag{5.22}$$

which is the amplitude of the reflected wave as it exits the PML. A similar calculation for evanescent waves using Eq. (5.16) shows that $|R|$ in Eq. (5.22) is the additional attenuation imposed by the PML on the reflected evanescent wave. This reflection coefficient $|R|$ due to the PML is controlled by the choice of the parameters $f$ and $L_{\mathrm{P}}/r_0$, independently of the size of the bounded domain to which the PML is adjacent. This suggests that if displacement and stress quantities near $x = 0$ for the semi infinite elastic medium are the quantities of interest in the analysis, the bounded domain may be restricted to the region of interest, thus lowering the computational cost, if the parameters of the PML are chosen appropriately.
A choice of $\lambda$ as in Eq. (5.18) leads to

$$|R| = \exp\left[-2\overline{F}^{P}(L_P/r_0)\sqrt{1-\frac{1}{a_0^2}}\right] \tag{5.23}$$

for $a_0 > 1$, and

$$|R| = \exp\left[-2\overline{F}^{e}(L_P/r_0)\sqrt{\frac{1}{a_0^2}-1}\right]\exp\left[-2\sqrt{1-a_0^2}\,\frac{L_P}{r_0}\right] \tag{5.24}$$

for $a_0 < 1$; an additional attenuation is imposed upon evanescent waves.

The dynamic stiffness of $\Omega$ at $x = 0$ is calculated as follows:
1) assume a solution of the form

$$u(x) = B_1 \exp\left[-\sqrt{1-a_0^2}\,\frac{\widetilde{x}}{r_0}\right] + B_2 \exp\left[+\sqrt{1-a_0^2}\,\frac{\widetilde{x}}{r_0}\right] \tag{5.25}$$

in terms of constants $B_1$ and $B_2$, with imaginary square roots for $a_0 > 1$, and $\lambda$ in $\widetilde{x}$ defined as

$$\lambda(x) \equiv 1 \text{ for } x \in [0, L] \tag{5.26a}$$

and, following Eqs. (5.16) and (5.12), in terms of a non-negative attenuation function *f* as

$$\lambda(x) = \begin{cases} 1 + f(x-L)/\sqrt{1-a_0^2} & \text{if } \mathrm{a}_0 < 1, \\ 1 - f(x-L)/\sqrt{a_0^2 - 1} & \text{if } \mathrm{a}_0 < 1, \end{cases} \quad \text{for } x \in (L,\, L+L_P] \tag{5.26b}$$

2) impose boundary conditions $u(0) = 1$ and $u(L + L_\mathrm{P}) = 0$ to calculate $B_1$ and $B_2$, and
3) compute the dynamic stiffness as $-(\sigma A)\big|_{z=0}$ using Eqs. (5.9b) and (5.9c). The dimensionless dynamic stiffness of Ω is thus obtained as

$$\bar{S}(a_0) = \bar{S}^{\infty}(a_0)\frac{1 + |R|\exp\left[-2\sqrt{1-a_0^2}\,(L+L_P)/r_0\right]}{1 - |R|\exp\left[-2\sqrt{1-a_0^2}\,(L+L_P)/r_0\right]} \tag{5.27}$$

with $\bar{S}^{\infty}(a_0)$ given by Eq. (5.5), |R| given by Eq. (5.22). Here $\bar{S}(a_0) \to \bar{S}^{\infty}(a_0)$ as |R|→0, i.e., the dynamic stiffness of the entire bounded domain is a good approximation to that of the unbounded domain if the reflection coefficient is suitably small.

If $\lambda$ is chosen as

$$\lambda(x) = \left[1 + \frac{f^e(x-L)}{a_0}\right] - i\,\frac{f^P(x-L)}{a_0} \tag{5.28}$$

in [L, $L$+$L_\mathrm{p}$], following Eq. (5.18), then the dynamic stiffness for all $a_0$ is still given by Eq. (5.27), but with |R| replaced by

$$\exp\left[-2\bar{F}^e(L_P/r_0)\sqrt{\frac{1}{a_0^2}-1}\right]\exp\left[2i\bar{F}^P(L_P/r_0)\sqrt{\frac{1}{a_0^2}-1}\right]$$

The accuracy of the bounded domain approximation is thus controllable by $f^{\mathrm{e}}$ for evanescent waves and by $f^{\mathrm{P}}$ for propagating waves.

### 5.2.5. PML parameters effect on results accuracy

Equations (5.27), and (5.22), are used to investigate the effect of the PML parameters $L_\mathrm{P}/r_0$ and *f* on the dynamic stiffness $\bar{S}(a_0)$, represented in terms of frequency dependent stiffness, $k(a_0)$, and damping, $c(a_0)$, coefficients given by the relation

$$\bar{S}(a_0) = k(a_0) + i a_0 c(a_0) \tag{5.29}$$

This approximation to the stiffness of the unbounded medium is compared against the exact stiffness $\bar{S}^{\infty}(a_0)$, also decomposed into stiffness and damping coefficients.

The attenuation function is chosen to be of the form

$$f(x) := f_0\left(\frac{x}{L_P}\right)^m \tag{5.30}$$

which gives

$$\overline{F}(L_P/r_0) = \frac{f_0 L_P/r_0}{m+1} \tag{5.31}$$

Thus the reflection coefficient |R| in Eq. (5.22) depends on the maximum value of the attenuation function, $f_0$ [$= f(L_P)$], the depth of the PML, $L_P / r_0$, and the polynomial degree of the attenuation function, $m$. Equation (5.31) suggests that the accuracy will be related directly to $f_0$ and to $L_P / r_0$, but inversely to $m$.

It is demonstrated that it is the depth $L_P / r_0$ of the PML that is significant, rather than the size $L / r_0$ of the bounded domain. Figure 5.3(a) shows that if $L_P / r_0$ is not large enough, then increasing $L / r_0$ does not improve the accuracy of the results. However, as shown in Fig. 5.3(b), for a sufficiently large PML ($L_P / r_0 = 1$), the size of the bounded domain does not affect the results, there is no difference between either approximate result and the exact one.

Figure 5.4 shows the effect of the choice of the attenuation function on the accuracy of results.

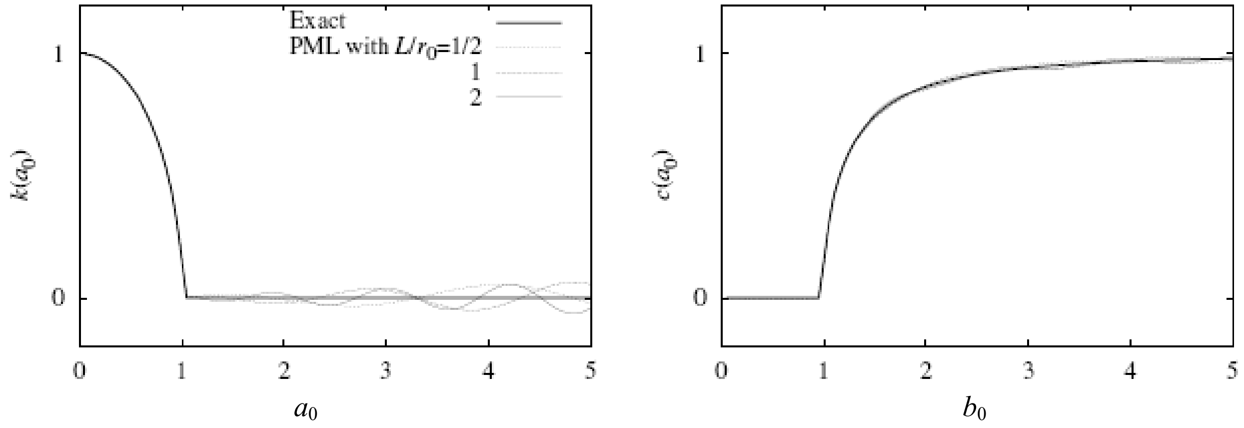

(a) $L_p / r_0 = 1 / 2$

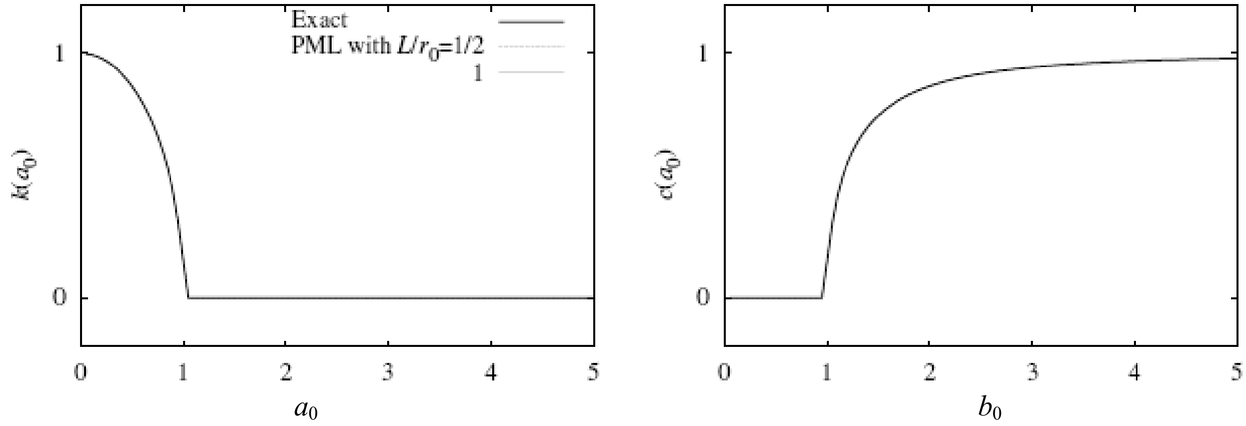

(b) $L_p / r_0 = 1$

Fig. 5.3. Size effect of bounded domain on the accuracy of dynamic stiffness of the elastic rod for two different depths of the PML; $f_0 = 10$, $m = 1$.

As was predicted from Eq. (5.31), increasing $f_0$ increases the accuracy of results, but increasing $m$ leads to less accurate results. This suggests that the attenuation function should be chosen as a linear polynomial and that the accuracy should be controlled through $f_0$. An adequate value of $f_0$ can be established through a rudimentary trial-and-error procedure; it is not appropriate to choose a value of $f_0$ by choosing an adequate value of |R| in e.g., Eq. (5.22), because adequacy of the |R| value is equivalent to adequacy of the $f_0$ value. If the dynamic stiffness of the bounded domain is calculated for $\lambda$ in the PML given by Eq. (5.28) with $f^{e}$

$= f^{\mathrm{p}} = f$, then the effects of $L / r_0$, $L_{\mathrm{P}} / r_0$, $f_0$ and $m$ on the dynamic stiffness is qualitatively similar to their effects for λ in the PML given by Eq. (5.26b), shown in Figs. 5.3 and 5.4. In fact, a highly accurate dynamic stiffness is still obtained by choosing the parameter values $L / r_0 = 1 / 2$, $L_{\mathrm{P}} / r_0 = 1$, $f_0 = 10$ and $m = 1$.

## 5.2.6. Finite element method

The non homogeneous viscoelastic medium is interpreted as a perfectly matched medium, which is then implemented using standard displacement based finite elements [47]. As is known, the displacement formulation is well established, therefore only the salient steps of the implementation are presented. Equation (5.9) is rewritten in the form of Equation (5.9a) multiplied by $\lambda(x)$, and $\varepsilon$ in Eq. (5.9c)

$$\frac{d\sigma}{dx} - \frac{k_g}{A}\lambda(x)u = -\omega^2 \rho \lambda(x) u \tag{5.32a}$$

$$\sigma = E\frac{1}{\lambda(x)}\varepsilon \tag{5.32b}$$

$$\varepsilon = \frac{du}{dx} \tag{5.32c}$$

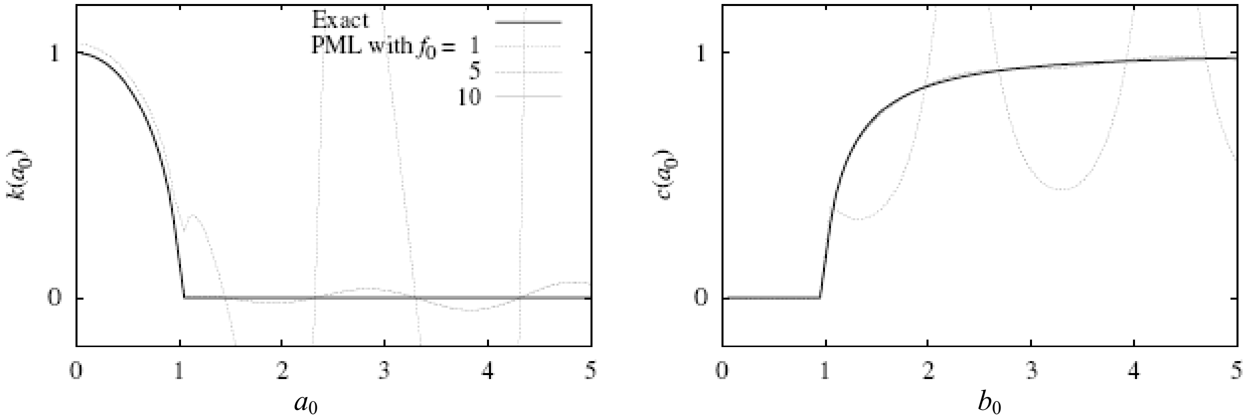

(a) $m = 1$

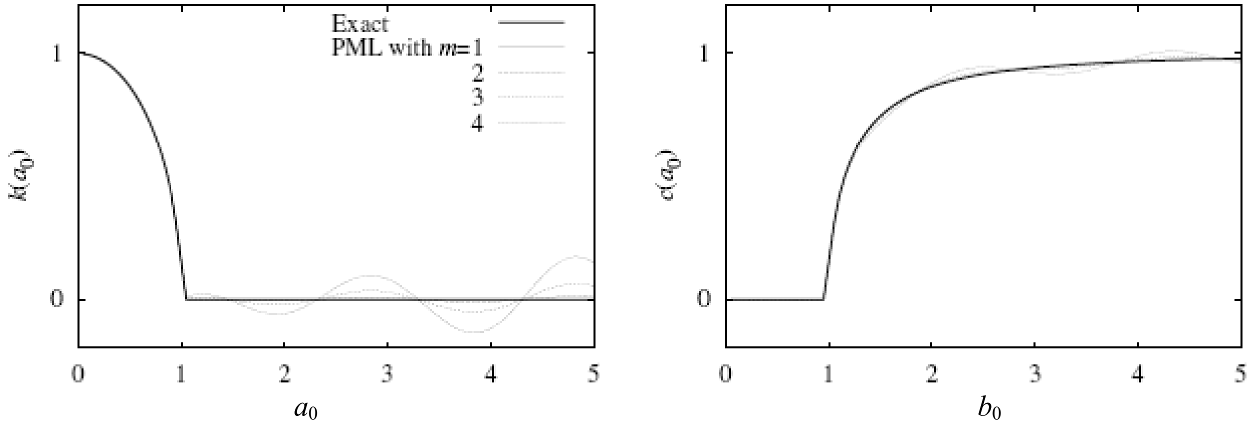

(b) $f_0 = 10$

Fig. 5.4. Effect of attenuation function on the accuracy of dynamic stiffness of the elastic rod; $L / r_0 = 1/2$, $L_{\mathrm{P}} / r_0 = 1$. is redefined as $\varepsilon \leftarrow \lambda(x)$ to obtain an equivalent system of equations

The coordinate stretch is transformed into a change in the material parameter properties; this PMM can therefore be interpreted as a non homogeneous elastic medium.

Then, the weak form of Eq. (5.32a) will be derived as follows: first, the equation is multiplied by an arbitrary weighting function, *w*, in an appropriate admissible space, and then integrated using integration-by-parts to obtain

$$\int_{\Omega}\frac{d\omega}{dx}\sigma d\Omega+\int_{\Omega}\frac{k_g}{A}\lambda(x)\omega u d\Omega-\omega^2\int_{\Omega}\rho\lambda(x)\omega u d\Omega=\left(\omega\sigma\right)\Big|_{\partial\Omega} \tag{5.33}$$

The functions *u* and *w* are interpolated by element in terms of nodal quantities using ***N***, a vector of nodal shape functions, then Eqs. (5.32b) and (5.32c) are substituted into the integrals on the left hand side of Eq. (5.33). Limiting the integrals to $\Omega^e$, the element domain, will give the stiffness and mass matrices for a PML element:

$$k_{IJ}^{e}=\int_{\Omega^e}\frac{dN_I}{dx}E\frac{1}{\lambda(x)}\frac{dN_J}{dx}d\Omega+\int_{\Omega^e}\frac{k_g}{A}\lambda(x)N_IN_Jd\Omega \tag{5.34a}$$

$$m_{IJ}^{e}=\int_{\Omega^e}\rho\lambda(x)N_IN_J\,d\Omega \tag{5.34b}$$

$m_{IJ}^{e}$ and $k_{IJ}^{e}$ are the nodal sub matrices of the whole element matrices $\mathbf{m}^{e}$ and $\mathbf{k}^{e}$, with *I* and *J* the node numbers and $N_I$ the shape function corresponding to node *I*. In Eq. (5.34), λ is defined globally on the computational domain. The obtained element mass and stiffness matrices are symmetric, but are complex valued and frequency dependent because of the choice for λ [Eq. (5.12) or (5.18)]. Therefore, the system matrices for Ω will be complex, symmetric, and banded, the PML contributions to which will have to be computed for each frequency.

# 5.3. Anti-plane motion

## 5.3.1. Elastic domain

For the case of a two-dimensional homogeneous isotropic elastic domain undergoing time harmonic anti-plane displacements and in the absence of body forces. For such motion, if the $x_3$-direction is pointing out of the plane, only the 31- and 32-components of the three-dimensional stress and strain tensors are non-zero. The displacements in terms of $u(x)\exp(i\omega t)$, with ω being the excitation frequency are governed by the following equations ($i \in 2$ {1, 2}):

$$\sum_i\frac{\partial\sigma_i}{\partial x_i}=-\omega^2\rho u \tag{5.36a}$$

$$\sigma_i=\mu\varepsilon_i \tag{5.36b}$$

$$\varepsilon_i=\frac{\partial u}{\partial x_i} \tag{5.36c}$$

where ρ is the mass density and μ the shear modulus of the medium; $\sigma_i$ and $\varepsilon_i$ represent the 3*i*-components of the stress and strain tensors.

For an unbounded domain, Eq. (5.36) admits only plane shear wave solutions of the following form

$$u(x)\exp[-i\,k_s x\,.\,p] \tag{5.37}$$

where the wave-number is given by $k_s=\omega/c_s$, with the wave velocity $c_s=\sqrt{\mu/\rho}$, and *p* is a unit vector representing the propagation direction. In addition, consider the domain shown in Fig. 5.5, where a layer of thickness $d$ and material constants $\mu_l$ and $\rho_l$, and a traction free surface at $x_1 = -d$, supported by a half plane having material constants $\mu_h$ and $\rho_h$. For such a domain, Eq. (5.36) Love wave solutions are given by the following

$$u(x) = (B_1 e^{-i\beta_l x_1} + B_2 e^{+i\beta_l x_1})e^{-ik_v x_2} \text{ in the layer} \tag{5.38a}$$

$$u(x) = B_3 e^{-\beta_h x_1} e^{-ik_v x_2} \text{ in the half-plane} \tag{5.38b}$$

if $c_s^h > c_s^l$, where $c_s^h$ and $c_s^l$ are the shear wave velocities in the half-plane and the layer respectively. In Eq. (5.38), $B_1$, $B_2$ and $B_3$ are constants, $\beta_l^2 = (k_s^l)^2 - k_v^2$ and $\beta_h^2 = k_v^2 - (k_s^h)^2$, with , $k_s^h = \omega / c_s^h$, $k_s^l = \omega / c_s^l$ and $k_v = \omega / c_v$ ; $c_v$ is the wave velocity in the $x_2$-direction, satisfying $c_s^l < c_v < c_s^h$, and governed by the following equation

$$\mu_h \beta_h - \mu_l \beta_l \tan(\beta_l d) = 0 \tag{5.39}$$

An elastic medium, with damping introduced through the correspondence principle, can also be described using the above equations, but with a complex valued shear modulus $\mu^* = \mu(1 + 2i\zeta)$, $\zeta$ being the hysteretic damping ratio, leading to a complex valued wave velocity $c_s^* = c_s\sqrt{1+2i\zeta}$ and wavenumber $k_s^* = k_s\sqrt{1+2i\zeta}$

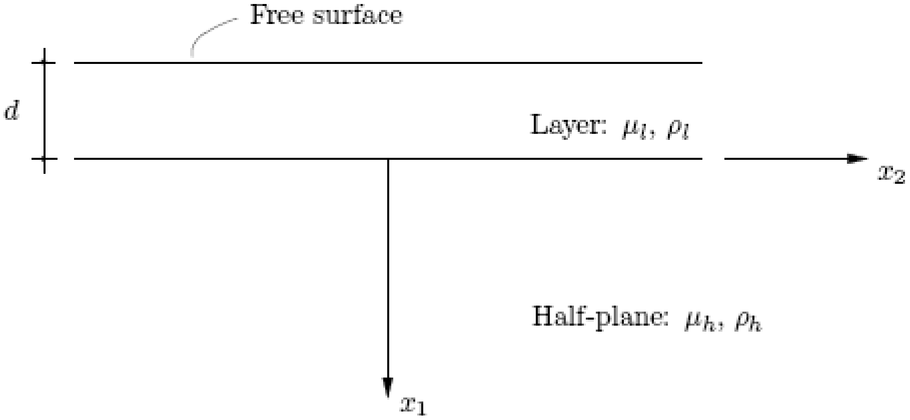

Fig. 5.5. Layer with a free surface supported on a half-plane; this geometry admits Love wave motion.

## 5.3.2. Perfectly matched medium

For a given system of equations of the same form as Eq. (5.36), but with $x_i$ replaced by stretched coordinates $\tilde{x}_i$, defined as

$$\tilde{x}_i := \int_0^{x_i} \lambda_i(s)ds \tag{5.40}$$

where $\lambda_i$ are nonzero, continuous, complex valued coordinate stretching functions. This coordinate stretching formally implies that

$$\frac{\partial}{\partial \tilde{x}_i} = \frac{1}{\lambda_i(x_i)} \frac{\partial}{\partial x_i} \tag{5.41}$$

this system of equations can be expressed by

$$\sum_i \frac{1}{\lambda_i(x_i)} \frac{\partial \sigma_i}{\partial x_i} = -\omega^2 \rho u \tag{5.42a}$$

$$\sigma_i = \mu \varepsilon_i \tag{5.42b}$$

$$\varepsilon_i = \frac{1}{\lambda_i(x_i)} \frac{\partial u}{\partial x_i} \tag{5.42c}$$

which a modification of Eq. (5.36), where the constitutive relation [Eq. (5.42b)] remains the same as for the case of the elastic medium. For the case of a two dimensional elastic continuum, the PMM for anti plane motion is governed by Eq. (5.42); an elastic viscous medium corresponds to $\lambda_i(x_i) \equiv 1$. Eq. (5.42) is then defined independently, but motivated by the definition of $\tilde{x}_i$; this is similar to the definition of Eq. (5.9) for the one dimensional PMM.

For the continuity of $\lambda_i$, the forms of the solutions admitted in the PMM are similar to those given by Eqs. (5.37) and (5.38) for the case of the elastic medium, but with $x_i$ replaced by $\tilde{x}_i$. Then, for an unbounded domain, Eq. (5.42) admits plane wave type solutions of the following equation

$$u(x) = \exp\left[-ik_s \tilde{x} \cdot p\right] \tag{5.43}$$

In addition, for the domain shown in Fig. 5.7 given by $\lambda_1(x_1) \equiv 1$, Eq. (5.42) admits Love wave type solutions of the following equation

$$u(x) = (B_1 e^{-i\beta_l x_1} + B_2 e^{+i\beta_l x_1}) e^{-ik_v \tilde{x}_2} \text{ in the layer} \tag{5.44a}$$

$$u(x) = B_3 e^{-\beta_h x_1} e^{-ik_v \tilde{x}_2} \text{ in the half-plane} \tag{5.44b}$$

where $\beta_l$, $\beta_h$, $k_v$ etc., defined for the elastic medium.

The exact matching property of these PMMs is that: if two PMMs having different $\lambda_i$ are placed adjacent to each other, and with the $\lambda_i$ functions for the two media such that they match at the interface, then a propagating wave will pass through the interface without generating any reflected waves. To clearly show this property, it is implicitly assumed in the definition of the PMM that $\lambda_i$ is a function of $x_i$ only, which means that, the coordinate stretches are uncoupled. Consider the $x_1 - x_2$ plane, with two PMMs defined on it; one on the left half plane (:= {($x_1$, $x_2$)| $x_1 < 0$}) with $\lambda_i(x_i) := \lambda_i^{lt}(x_i)$, and another on the right half plane (:= {($x_1$, $x_2$)| $x_1 \geq 0$}) with $\lambda_i(x_i) := \lambda_i^{rt}(x_i)$. If $\lambda_2^{lt} = \lambda_2^{rt}$, and if $\lambda_1^{lt}(0) = \lambda_2^{rt}(0)$, then the two PMMs can be considered as one PMM, where a continuous $\lambda_1$ is defined piecewise on the two half planes, and each $\lambda_i$ is a function of $x_i$ only; thus there is no interface to generate any reflected waves. This perfect matching property holds for any wave solution admitted by the PMM. In particular, for a plane wave type solution as in Eq. (5.43), the matching is independent of the direction of propagation $p$ and of the wave number $k_s$. A good choice of $\lambda_i$ imposes an attenuation on the wave solutions to Eq. (5.42). Again for the plane wave type solution in Eq. (5.43), if the functions $\lambda_i$ are defined in terms of real valued, continuous attenuation functions $f_i$ by the following equation

$$\lambda_i(x_i) := 1 - i\frac{f_i(x_i)}{k_s} \tag{5.45}$$

where

$$\widetilde{x}_i = x_i - i\frac{F_i(x_i)}{k_s} \tag{5.46}$$

and

$$F_i(x_i) := \int_0^{x_i} f_i(\xi)d\xi \tag{5.47}$$

Substitution of Eq. (5.46) into Eq. (5.43) gives the following

$$u(x) = \exp\left[-\sum_i F_i(x_i)p_i\right]\exp\left[-ik_s x \cdot p\right] \tag{5.48}$$

Therefore, if $F_i(x_i) > 0$ and $p_i > 0$, then $u(x)$ is attenuated as $\exp[-F_i(x_i)p_i]$ in the $x_i$-direction, and the attenuation is independent of the frequency.

In addition, consider the Love wave-type solution in Eq. (5.44); if $\lambda_2$ for the layer and for the half plane are chosen as in Eq. (5.45), as follows

$$\lambda_2^l(x_2) := 1 - i\frac{f_2(x_2)}{k_s^l} \tag{5.49a}$$

for the layer, and

$$\lambda_2^h(x_2) := 1 - i\frac{f_2(x_2)}{k_s^h} \tag{5.49b}$$

for the half-plane, then the $\exp(-ik_v\widetilde{x}_2)$ term in Eq. (5.44), which represents a wave propagating in the positive $x_2$-direction, is transformed to the following

$\exp\left[-F_2(x_2)\frac{c_s^l}{c_v}\right]e^{-ik_v x_2}$ for the layer, and

$\exp\left[-F_2(x_2)\frac{c_s^h}{c_v}\right]e^{-ik_v x_2}$ for the half plane.

Since $c_v$ depends on $\omega$ through Eq. (5.39), the attenuation is not independent of frequency for the choices of $\lambda_2$ given above. The use of $k_v$ in place of $k_s^l$ and $k_s^h$ in Eq. (5.49) would, of course, make the attenuation independent of frequency, but would require the solution of Eq. (5.39) to determine $k_v$. In a PMM for an elastic medium, with damping incorporated through the correspondence principle, the complex wavenumber $k^*_s$ may be used in place of $k_s$, even in the stretching function, such, in Eq. (5.45).

## 5.3.3. Perfectly matched layer

For a given wave of the form in Eq. (5.37) propagating in an unbounded elastic domain, the $x_1$-$x_2$ plane, governed by Eq. (5.36). Then, the main idea of defining a PML is to simulate this wave propagation by using a corresponding bounded domain. For the replacement of the unbounded domain by $\Omega_{BD} \cup \Omega_{PM}^{\infty}$ as shown in Fig. 5.8(a), where $\Omega_{BD}$ is a bounded truncated domain, governed by Eq. (5.36), and $\Omega_{PM}^{\infty}$ is the unbounded PMM, governed by Eq. (5.42), with $\lambda_1$ of the form in Eq. (5.45), satisfying $f_1(0) = 0$, and $\lambda_2 \equiv 1$. Because the medium in $\Omega_{BD}$ is a special PMM [$\lambda_i(x_i) \equiv 1$, no summation], and the functions $\lambda_i$ for the two media are chosen to be matched at the interface, all waves of the form in Eq. (5.37) propagating outwards from $\Omega_{BD}$ (waves having $p_1 > 0$) are completely absorbed and then attenuated in the $x_1$-direction in $\Omega_{PM}^{\infty}$. Thus the displacements in $\Omega_{BD}$ due to an outward propagating wave are exactly the same as the displacements of the original unbounded elastic medium in $\Omega_{BD}$ due to the same wave. If this outward propagating wave is attenuated enough in a finite distance, then $\Omega_{PM}^{\infty}$ can be truncated by a fixed boundary without any significant wave reflections. The layer $\Omega_{PM}$ of the PMM shown in Fig. 5.8(b) is termed the PML. If wave reflections from the fixed boundary are not significant, then the displacements of the system ($\Omega_{BD} \cup \Omega_{PM}$) into $\Omega_{BD}$ should be the same as those of the unbounded elastic domain into $\Omega_{BD}$. Similarly, a PML for the system given in Fig. 5.5 can be constructed by using a vertical layer consisting of two different PMMs with material properties matching the physical layer and the half-plane.

Next, the effect of domain truncation in the PMM is analysed by studying the plane wave reflections by fixed boundary conditions. Shown in Fig. 5.6(b), is the incident plane wave at an angle $\theta$ and of unit amplitude as it enters the PML, is reflected from the fixed boundary.

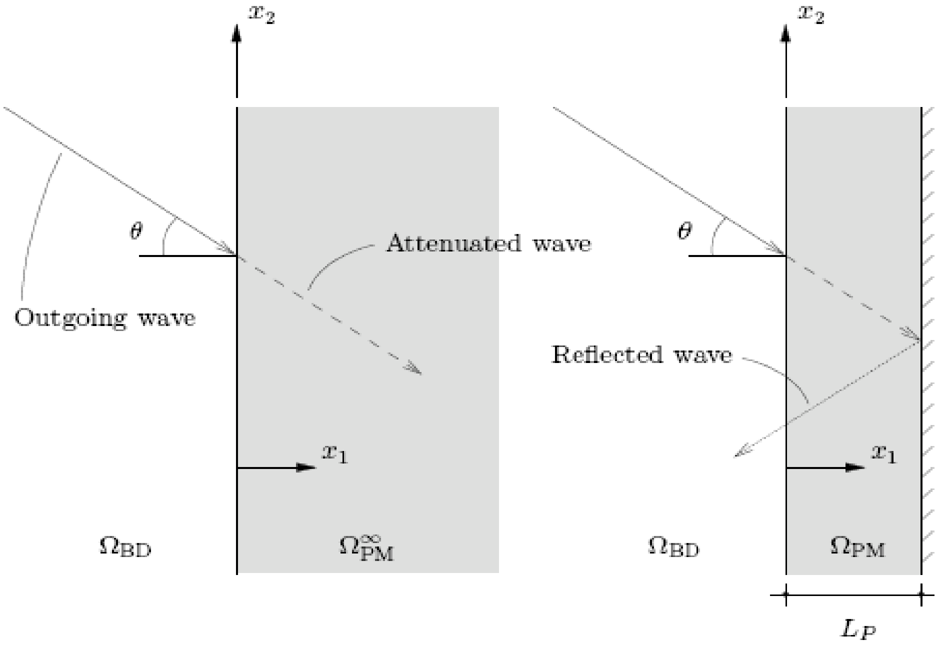

(a) (b)

Fig. 5.6. (a) A PMM adjacent to a bounded truncated domain attenuates an outgoing plane wave; (b) a PML with a fixed edge also reflects the wave back towards the bounded domain.

Then, the total wave motion may be expressed by the following equation

$$u(x) = \exp\left[-ik_s\tilde{x} \cdot p^{(I)}\right] + R\exp\left[-ik_s\tilde{x} \cdot p^{(R)}\right] \tag{5.50}$$

where, $p^{(I)}$ and $p^{(R)}$ are the propagation directions of the incident and reflected waves respectively. Fixing $u(x) \equiv 0$ for $x_1 = L_P$ and for all $x_2$, and substituting $p_1^{(I)} = \cos\theta$, will result in

$$|R| = \exp\left[-2F_1(L_p)\cos\theta\right] \tag{5.51}$$

which is the amplitude of the reflected wave as it exits the PML. This reflection coefficient is mainly controlled by the choice of the parameters $f_1$ and $L_P$ independently of the size of the bounded domain to which the PML is adjacent and is influenced by the angle of incidence. This suggests that the bounded domain may be restricted to the region of interest in the analysis, thus lowering considerably the computational cost, if the parameters and the orientation of the PML are chosen accordingly.

### 5.3.4. Interpretation of the PMM

Given below is another interpretation of the anti plane PMM as an anisotropic, non homogeneous elastic medium, obtained by simply transforming the coordinate stretch into a change in the constitutive relation. In the plane, consider two rectangular Cartesian coordinate systems as follows:
1) an $\{x_i\}$ system, with respect to an orthonormal basis $\{e_i\}$,
2) an $\{x'_i\}$ system, with respect to another orthonormal basis $\{e'_i\}$, with the two bases related by the rotation of basis matrix $Q$, with components $Q_{ij} := e_i \,.\, e'_j$ .
Equation (5.42) can also be rewritten differently in terms of the coordinates $x'_i$ just by replacing $x_i$ by $x'_I$ , as no summation is considered (the summation convention is abandoned in this section) representing a PMM where waves are attenuated in the $e'_1$ and $e'_2$ directions, rather than in the $e_1$ and $e_2$ directions as in Eq. (5.42); $\sigma_i^{'}$ and $\varepsilon_i^{'}$ are the $3i$ components in the basis $\{e'_i\}$ of the stress and strain tensors.

$$\sum_i \frac{1}{\lambda_i(x_i^{'})}\frac{\partial \sigma_i^{'}}{\partial x_i^{'}} = -\omega^2 \rho\, u \tag{5.52a}$$

$$\sigma_i^{'} = \mu \varepsilon_i^{'} \tag{5.52b}$$

$$\varepsilon_i^{'} = \frac{1}{\lambda_i(x_i^{'})}\frac{\partial u}{\partial x_i^{'}} \tag{5.52c}$$

Multiplying Eq. (5.52a) with $\lambda_1\{x'_1\}\lambda_2\{x'_2\}$ and knowing that $\lambda_i$ is a function of $x'_i$ only, Eq. (5.52) can be rewritten as

$$\nabla^{'} \cdot (\widetilde{\Lambda}^{'} \sigma^{'}) = -\omega^2 \rho \left[\lambda_1(x_1^{'})\lambda_2(x_2^{'})\right] u \tag{5.53a}$$

$$\sigma^{'} = \mu \varepsilon^{'} \tag{5.53b}$$

$$\varepsilon^{'} = \Lambda^{'} \cdot (\nabla^{'} u) \tag{5.53c}$$

where

$$\sigma^{'} := \begin{Bmatrix} \sigma_1^{'} \\ \sigma_2^{'} \end{Bmatrix}, \quad \varepsilon^{'} := \begin{Bmatrix} \varepsilon_1^{'} \\ \varepsilon_2^{'} \end{Bmatrix}, \quad \nabla^{'} := \begin{Bmatrix} \dfrac{\partial}{\partial x_1^{'}} \\ \dfrac{\partial}{\partial x_2^{'}} \end{Bmatrix} \tag{5.54}$$

and

$$\widetilde{\Lambda}^{'} := \begin{bmatrix} \lambda_2(x'_2) & \cdot \\ \cdot & \lambda_1(x'_1) \end{bmatrix}, \quad \Lambda^{'} := \begin{bmatrix} 1/\lambda_1(x'_1) & \cdot \\ \cdot & 1/\lambda_2(x'_2) \end{bmatrix} \tag{5.55}$$

The primed quantities in Eq. (5.53) can be transformed to the basis $\{e_i\}$ to obtain

$$\nabla \cdot (\widetilde{\Lambda} \sigma) = -\omega^2 \rho \left[\lambda_1(x'_1)\lambda_2(x'_2)\right] u \tag{5.56a}$$

$$\sigma = \mu \varepsilon \tag{5.56b}$$

$$\varepsilon = \Lambda(\nabla u) \tag{5.56c}$$

where

$$\sigma := \begin{Bmatrix} \sigma_1 \\ \sigma_2 \end{Bmatrix} = Q\sigma', \quad \varepsilon := \begin{Bmatrix} \varepsilon_1 \\ \varepsilon_2 \end{Bmatrix} = Q\varepsilon', \quad \nabla := \begin{Bmatrix} \dfrac{\partial}{\partial x_1} \\ \dfrac{\partial}{\partial x_2} \end{Bmatrix} = Q\nabla' \tag{5.57}$$

and

$$\widetilde{\Lambda} = Q\widetilde{\Lambda}'Q^T, \quad \Lambda = Q\Lambda'Q^T \tag{5.58}$$

The tensors $\widetilde{\Lambda}$ and $\Lambda$ are called the left and right stretch tensors. In addition, because these stretch tensors are diagonal in the basis $\{e'_i\}$, this basis is called the characteristic basis of the PMM. Redefining $\sigma$ as $\sigma \leftarrow \widetilde{\Lambda}\sigma$ and ε as $\varepsilon \leftarrow \Lambda^{-1}\varepsilon$ in Eq. (5.56), and defining

$$f_m := \lambda_1(x_1')\lambda_2(x_2') \tag{5.59}$$

will result in an equivalent system of equations:

$$\nabla \cdot \sigma = -\omega^2 \rho f_m u \tag{5.60a}$$

$$\sigma = \mu \mathrm{D} \varepsilon \tag{5.60b}$$

$$\varepsilon = \nabla u \tag{5.60c}$$

where

$$\mathrm{D} := \widetilde{\Lambda}\Lambda = Q\widetilde{\Lambda}'\Lambda'Q^T \tag{5.61}$$

Coordinate stretching in the PMM, represented by $\widetilde{\Lambda}$ and $\Lambda$ in Eq. (5.56), has been transformed into a change in the constitutive relation, thus leading to an interpretation of this PMM as an anisotropic, non homogeneous elastic medium. This interpretation of the PMM is similar to the non homogeneous media interpretation of the one dimensional PMM presented above.

## 5.3.5. Finite element implementation

The anisotropic non homogeneous medium form of the PMM, given by Eq. (5.60), is next implemented using standard displacement based finite elements. The weak form of Eq. (5.60a) is derived by multiplying it with an arbitrary weighting function *w* in an appropriate admissible space, and then integrating over the whole computational domain using integration by parts and the divergence theorem to get the following

$$\int_\Omega \nabla\omega \cdot \sigma d\Omega - \omega^2 \int_\Omega \rho f_m \omega u d\Omega = \int_\Gamma \omega\sigma \cdot n d\Gamma \tag{5.62}$$

where Γ : = ∂Ω is the boundary of Ω and *n* is a unit normal to Γ. Assuming element interpolations of *u* and *ω* in terms of nodal shape functions *N*, imposing Eqs. (5.60b) and (5.60c) point in Eq. (5.62), and restricting the domain integrals to the element domain $\Omega = \Omega^e$ will result in the stiffness and mass matrices for a PML element. For nodal sub matrices, these are

$$k_{IJ}^e = \int_{\Omega^e} (\nabla N_I)^T \mu D (\nabla N_J) d\Omega \tag{5.63a}$$

$$m_{IJ}^e = \int_{\Omega^e} \rho f_m N_I N_J d\Omega \tag{5.63b}$$

where *I* and *J* denote node element numbers.

In Eq. (5.63), the functions $\lambda_i$ in D and in $f_m$ are globally defined on the computation domain. We note that a finite element implementation of Eq. (5.56) would also have resulted in the stiffness and mass matrices in Eq. (5.63), because the coordinate stretch model of the PMM [Eq. (5.56)] is similar to the anisotropic medium model [Eq. (5.60)]. These element matrices are symmetric, but intrinsically complex valued and frequency dependent. Therefore, the system matrices for Ω will be complex, symmetric, and banded, the PML contributions have to be computed for each given frequency.

# 5.4. Conclusions

Perfectly matched layers have been developed in the context of time harmonic elastodynamics by utilising insights obtained from the electromagnetic fields. This new concept has been developed and implemented into a Matlab computer code and later on will be implemented in the spectral finite element Matlab code through the presentation of perfectly matched media for three different systems:

1) a rod on elastic foundation,
2) a continuum undergoing anti plane motion,
3) a continuum undergoing plane strain motion.

The PML concept is resumed as a perfectly matched medium (PMM) defined as one governed by a modification of the equations for the elastic medium, with the modification motivated by a continuous, complex valued, uncoupled coordinate stretching. The PMM solutions are of the form of those admitted by an elastic medium, but with the stretched coordinates replacing the real coordinates. PMMs exhibit the perfect matching property; if the stretching functions of two adjacent PMMs match at their interface, then the interface is invisible to all wave type solutions and no reflected waves are generated when a wave travels from one PMM to the other. This property holds for any direction of propagation and for any frequency. In addition, if choices of the stretching functions are appropriate, the solutions in the PMM take the form of the corresponding elastic medium solution, but with an imposed spatial attenuation, the imposed attenuation is spatial; it is not imposed through a temporal attenuation, or damping, employed in earlier absorbing layer models [98].

Perfect matching and attenuation properties of the PMM are used to build an absorbing layer the perfectly matched layer around a bounded domain such that the layer absorbs and attenuates outward propagating waves of all non tangential angles of incidence and of all non zero frequencies. Ending the layer by a fixed boundary causes reflection of the waves back towards the bounded domain, with the amplitude of reflected waves controllable; independently of the size of the bounded domain by the choice of the PML parameters:

a) the depth of the layer,
b) the attenuation profile.

Therefore, wave propagation in an unbounded domain can be modelled through a bounded domain that is restricted to the region of interest, and a PML surrounding it. The one dimensional problem of the semi infinite rod on elastic foundation has been used to analytically study a bounded domain PML model. The function expressing the stretching is given in terms of an attenuation function, which controls the reflection due to the finite depth of the PML. Then, the reflection coefficient is directly related to the dynamic stiffness of the rod, and it is shown that the dynamic stiffness of the PML model approaches that of the unbounded domain system as the reflection coefficient approaches zero. Analytically speaking, the attenuation function should be chosen to increase linearly from zero at the bounded domain PML interface to a maximum value at the end of the layer, and that this maximum value, as well as the depth of the layer, should be used to control the accuracy of results; this conclusion is validated through analytical results. It is expected that a rudimentary trial and error procedure should be sufficient to establish an adequate maximum value of the attenuation function. Also proposed is a realistic choice of the stretching function that does not employ prior knowledge of the frequency equation of the system, but is adequate for both evanescent and propagating waves; this adequacy is confirmed through analytical and numerical results.

It has been shown that the one dimensional and the anti plane PMM, although formulated through coordinate stretching, can also be interpreted as anisotropic, non homogeneous elastic media. Equivalent interpretations have then been used to obtain symmetric finite element (FE) implementations of these PMMs, with the implementation of the anti plane PMM matching those presented in earlier works [25] [41]. The PMM for plane strain or two dimensional motion is not amenable to a similar equivalent interpretation; however, a new displacement based, symmetric FE implementation of this PMM is obtained, by expressing the PMM equations in a tensorial form. The obtained FE matrices are symmetric, but complex valued and frequency dependent. Thus the system matrices for the bounded domain are complex, symmetric and banded, the PML contributions to which have to be computed for each new frequency.

These FE implementations have been applied to the following canonical problems:

1) one dimensional semi-infinite rod on elastic foundation,
2) anti plane motion of a semi in finite layer on rigid base,
3) classical plane strain soil structure interaction problems
    i) half plane,
    ii) layer on a half plane,
    iii) layer on a rigid base.

Very accurate results have been obtained from PML models using small bounded domains; the computational cost of the PML models was seen to be similar to that of comparable viscous dashpot models, and the inaccuracy of results from these dashpot models emphasized the small size of these bounded domains. Notably, accurate PML results have been obtained even for the waveguide system of a layer on a rigid base, undergoing either anti plane or plane strain motion, where evanescent modes are significant. This is achieved through the realistic choice of the stretching function proposed in the one dimensional analysis; such a stretching function is thus seen to be adequate even for systems with many evanescent modes. Numerical investigations of the mesh density effect on the accuracy of results suggest that the mesh density in the PML should be chosen to be similar to that of the bounded domain [42].

In this research, PMLs are presented for isotropic, homogeneous or discretely non homogeneous media. The same motivation of complex valued coordinate stretching is used for all three systems to define the PMM corresponding to the elastic medium. Consequently

1) all three PMMs exhibit perfect matching property,
2) propagating harmonic waves in the elastic medium are transformed to attenuated waves in the PMM,
3) the constitutive relation is not affected by the coordinate stretching, i.e., the constitutive relation in the PMM is the same as that in the elastic medium.

The PMMs presented in this research, as well as any extensions, could be seen as verifications of an assertion made by Teixeira and Chew [102]. They give a geometric interpretation of the PML concept, as a change in the metric of the coordinate space, and state: ". . . the PML concept does not depend on the particular form of field equations and is applicable to any linear wave phenomena."

Chapter 6

# 6. Spectral finite element method

## 6.1 Introduction

A first approach making it possible to model the wave propagation in complicated structures consists in solving the wave equations written in differential form, for example by using finite element method, boundary element method, hybrid methods combining FEM and BEM or a pseudo-spectral method. Although this approach can be used successfully in certain cases, it presents the major disadvantage to be limited if a total transformation of sufficiently smooth grid can be found between the studied physical field and the square field in which calculations are carried out, which is seldom the case when one considers realistic models.

An approach much more natural, making it possible to solve this problem, consists in using the variational formulation of the wave equation on a grid adapted to the geometrical constraints of the model. Classically, this will lead to the finite element method by Hughes [48]. One attempt to use this method in geophysics were carried out by Lysmer and Drake [71] but, because of the weak approximation order which is usually used in order to reduce the cost of calculation of such schemes, the precision of the results often appeared disappointing [75].

Taking account of these developments, and with an aim of increasing the precision of modeling while maintaining a reasonable low calculation cost, we use in this chapter a spectral element method [83] [4] [105] [30] which, during the last decade, proved its effectiveness primarily in the field of fluid mechanics [94] [95]. Such a method makes it possible to solve the equation of the elastic waves in complicated mediums, presenting for example a curved topography and interfaces, while keeping the high degree of accuracy of the pseudo-spectral methods. The wave equation is written in a weak formulation, the grid being made up of curved 2D quadrangles or curved 3D hexahedrons. In the 2D case, each element is brought back to the square $[-1, 1] \times [-1, 1]$, and to the cube $[-1, 1] \times [-1, 1] \times [-1, 1]$ for the 3D case, on which tensorial products of Lagrange polynomials associated with Gauss-Lobatto-Legendre integration points are used as polynomial bases. A fundamental consequence of this particular choice is that the system mass matrix is diagonal by construction, which leads to a completely explicit diagram and makes easy the inversion of this matrix. We use for the time integration an explicit-implicit diagram predictor-multicorrector of the Newmark type based either on a traditional formulation in terms of acceleration by Hughes [48], or on a formulation based on the speed written in conservative form by Simo [97]. Three types of boundary conditions can be used: a free surface condition (Neumann), a rigid edge condition (Dirichlet) or an absorbing condition allowing simulating an extending infinite medium. The latter is introduced by solving a first order paraxial equation in time domain on the boundary. In this chapter, the precision of the introduced method is shown for two traditional problems (problem of Lamb, problem of Garvi) by comparing the solution calculated by using a low number of points per wavelength (approximately 5) with the analytical solution of the problems considered. An excellent agreement is found. The flexibility and the robustness of the method will be then proven in the following by studying more realistic models in 2D as 3D. The heterogeneous structural analysis by a spectral finite element method constitutes, to our knowledge, a new approach in the field of SSI problems.

We also show the implementation of the method into a MATLAB computer program called `SFEM2D` (Appendix C), this by itself constitute a major contribution that had never been undertaken before and we show that it is possible to reach very interesting performances.

# 6.2 Spacial discretization and Galerkin approximation

As we know, it is possible to write the equations governing the elastic wave propagation in variational form. The advantages which one can get from such an approach are (geometrical flexibility allowing to treat really complex models, easy implementation of the natural boundary conditions, in particular the free surface boundary condition …). However, in order to be able to solve numerically the problem for the different boundary conditions thus formulated, it is necessary to reduce the size of the dynamic system of infinite extent to a system of manageable finite size. This is generally carried out in three steps:

1. Spatial discretization: the geometrical field $\Omega$ is discretized in a family of sub-fields not overlapping $\{\Omega_e\}$ , $e$ =1, $n_{el}$. This enables us to introduce the restriction $w^e$ of w to $\Omega^e$, i.e. the field defined on $\Omega_e$ and which coincides with w on this finite support.
2. Galerkin approximation: the subspace containing the phases of infinite size $S$ x $V$ is replaced by a subspace of finite size via a Galerkin projection. This is carried out by introducing the space of the polynomials functions per pieces, and a projection operator on the grid of collocation defined by the integration points. This boundary problem with initial conditions is now formulated in the form of an ordinary linear differential equations resulting from the discretization of the variational form of the equations, taking account of the local form of the constitutive equations.
3. Discretization in time domain: the system of ordinary linear differential equations introduced above describes the evolution in time of the discrete degrees of freedom. A discretization in time and the introduction of a time evolution algorithm are then necessary to be able to calculate the displacement fields, speed and acceleration at any moment of the time interval considered.

## 6.2.1 Space discretization

The studied physical field is first discretized in non-overlapping elements: $\Omega = \bigcup_{e=1}^{e=n_{el}} \Omega_e$. At 2D, the elements are quadrangles (in the general case, their sides may be curved). For the 3D, they are hexahedrons. This field partition must satisfy the traditional finite element condition, that consists to make sure that for all $e \neq e'$ the intersection $\Omega \cap \Omega_{e'}$ must be either empty or made up of a node, a side or a common face. For each element $\Omega_e$ of the field, the field $w^e = w \big|_{\Omega e}$ is defined as the restriction of w on the spatial finite support $\Omega_e$.
Let us note □ the area of reference in the space $\xi$ (for example a closed square of $R^2$ in 2D: $\square = \Lambda \times \Lambda$ , where $\Lambda = [-1, 1]$, and a closed cube of $R^3$ in 3D: $\square = \Lambda \times \Lambda \times \Lambda$ ). For each element $\Omega_e$, we can define a regular diffeomorphism $\mathcal{F}_e: \square \rightarrow \Omega_e$ such that:

$$\mathbf{x}(\xi) = \mathcal{F}_e(\xi) \tag{6.1}$$

A traditional way to build $\mathcal{F}_e$ , following Gordon and Hall [39], consists to start the parameterization from the four curved sides $\Gamma_i^e (i = 1,...,4)$ constituting the border $\partial\Omega_e$ of the element $\Omega_e$. That is, if $\mathbf{a}_j$ ($j$=1,…,4) are the tops of $\Omega_e$, let us suppose given four regular functions $f_i$ from [ – 1 , 1] in $R^2$ [4]:

$$f_1([-1,1]) \cap f_2([-1,1]) = f_1(-1) = f_2(-1) = a_2$$

$$
\begin{aligned}
f_2([-1,1])\, 4\, f_3([-1,1]) &= f_2(1) = f_3(-1) = \mathrm{a}_3 \\
f_3([-1,1])\, 4\, f_4([-1,1]) &= f_3(1) = f_4(1) = \mathrm{a}_4 \\
f_4([-1,1])\, 4\, f_1([-1,1]) &= f_4(-1) = f_1(1) = \mathrm{a}_1
\end{aligned}
\tag{6.2}
$$

Then the application $\mathcal{F}_e$ of $\Lambda^2$ in $\mathrm{R}^2$ can be written in the form

$$
\begin{aligned}
\mathsf{F}_2(r,s) = {} & \frac{1+s}{2} f_3(r) + \frac{1-s}{2} f_1(r) \\
& + \frac{1+r}{2}\left( f_4(s) - \frac{1+s}{2} f_4(1) - \frac{1-s}{2} f_4(-1) \right) \\
& + \frac{1-r}{2}\left( f_4(s) - \frac{1+s}{2} f_2(1) - \frac{1-s}{2} f_2(-1) \right)
\end{aligned}
\tag{6.3}
$$

It is then advisable to make sure that the jacobien $J_e$ of the transformation $\mathcal{F}_e$ thus defined is not null everywhere. Another traditional way to define such a transformation (see figure 6.1) consists in considering the 1D Lagrange polynomials of order $n, l_i^n, 1 \le i \le n+1$, finite on $\Lambda$ starting from the geometrical nodes used to discretetize the segment. One can then simply define the geometrical transformation $\mathcal{F}_e$ by writing (example for a 2D case):

$$
\mathrm{F}_2(\xi,\eta) = \sum_{k=1}^{n_{en}} N_k(\xi,\eta)\mathrm{a}_k \tag{6.4}
$$

where $\mathbf{a}_k$, $k = 1, \ldots, n_{en}$ are the geometrical nodes defining the element. For a quadratic parameterization on each side of the element (corresponding to a 2D transformation controlled by eight nodes), the functions $\mathrm{N}_k$, called shape functions in finite element terms, are, for the nodes belonging to the corners of the element:

$$
\begin{aligned}
N_1(\xi,\eta) = l_1^2(\xi) l_1^2(\eta) \quad &; \quad N_2(\xi,\eta) = l_3^2(\xi) l_1^2(\eta) \\
N_3(\xi,\eta) = l_3^2(\xi) l_3^2(\eta) \quad &; \quad N_4(\xi,\eta) = l_1^2(\xi) l_3^2(\eta)
\end{aligned}
\tag{6.5}
$$

and for the nodes in the middle

$$
\begin{aligned}
N_5(\xi,\eta) = l_2^2(\xi) l_1^1(\eta) \quad &; \quad N_6(\xi,\eta) = l_2^1(\xi) l_2^2(\eta) \\
N_7(\xi,\eta) = l_2^2(\xi) l_2^1(\eta) \quad &; \quad N_8(\xi,\eta) = l_2^2(\xi) l_1^1(\eta)
\end{aligned}
\tag{6.6}
$$

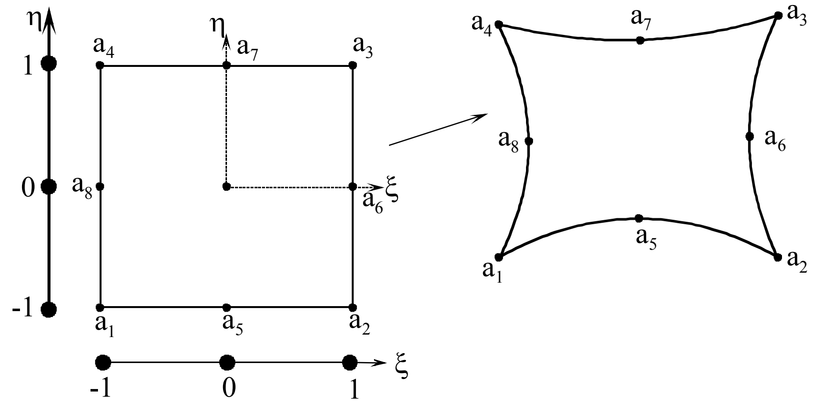

Fig. 6.1. Example of a quadratic geometrical transformation between the deformed field and the area of reference.

The analytical expression of these 2D shape functions having eight nodes is given in Dhatt and Touzot [27].

The case of a 3D element can be described by elements having 20 nodes for which the analytical expression of the shape functions is somewhat difficult to write. In order to ensure the condition of non-overlapping of the elements of the grid, it is necessary to check that the jacobien $J_e$ of the transformation thus defined is non-null everywhere.

## 6.2.2 Galerkin Approximation

The subspace of phases of infinite size $S \times V$ is replaced by a subspace of finite size $S_N^h \times V_N^h$ by using a Galerkin approximation and an operator of polynomial interpolation. The index h is referred to as the association of $S^h$ and $V^h$ with the grid, i.e. the spacial discretization of the field Ω, which can be parameterized by a characteristic scale length *h*. In relation with the space discretization, let us consider for $N \in \boldsymbol{N}$, the approximation of finite size of $S$ defined as follows (with $n_d$ being the dimension of the physical space considered):

$$\left\{S_N^h = \mathrm{u}^h \in S : \mathrm{u}^h \in L^2(\Omega)^{n_d} \quad \text{and} \quad u^h\middle|\Omega_e \circ F_e \in \left[P_N(\text{弈})\right]^{n_d}\right\} \tag{6.7}$$

and for the space of the acceptable variations $V$

$$\left\{V_N^h = \mathrm{w}^h \in V : \mathrm{w}^h \in L^2(\Omega)^{n_d} \quad \text{and} \quad \mathrm{w}^h\middle|\Omega_e \circ F_e \in \left[P_N(\text{弈})\right]^{n_d}\right\} \tag{6.8}$$

where $\boldsymbol{P}_N$ (□ ) is the space of the polynomials of degree ≤ $N$ defined on the domain of reference. This defines a polynomial approximation per pieces on each element $\Omega_e$.

Galerkin approximation of the considered problem can then be formulated as follows:

Given $f$, $g$, $\tau$, $\mathrm{u}_0$, $\mathrm{v}_0$ find $\mathrm{u}_N^h(\mathrm{x},t) \in \mathrm{S}_{N,t}^h \quad \forall \mathrm{t} \in \mathrm{I}$ such that $\forall \mathrm{w}_N^h \in V_N^h$ :

$$\begin{gathered}\left(\mathrm{w}_N^h, \rho\, \dot{\mathrm{v}}_N^h\right) + a\left(\mathrm{w}_N^h, \mathrm{u}_N^h\right) = \left(\mathrm{w}_N^h, \mathrm{f}\right) + \left(\mathrm{w}_N^h, \tau\right)\Gamma_\tau + \left(\mathrm{w}_N^h, \tau\left(\mathrm{u}_N^h\right)\right)\Gamma_{abs}^{ext} \\ \left(\mathrm{w}_N^h, \rho\, \dot{\mathrm{u}}_N^h\right) = \left(\mathrm{w}_N^h, \rho\, \mathrm{v}_N^h\right)\end{gathered} \tag{6.9}$$

with

$$\left(\mathrm{w}_N^h, \rho\, \mathrm{u}_N^h(.,t)\big|_{t=0}\right) = \left(\mathrm{w}_N^h, \rho\, \mathrm{u}_0^h\right)$$

$$\left(\mathrm{w}_N^h, \rho\, \mathrm{v}_N^h(.,t)\big|_{t=0}\right) = \left(\mathrm{w}_N^h, \rho\, \mathrm{v}_0^h\right) \tag{6.10}$$

All integrations appearing in the formulas above must now be approximated by numerical integrations. Thanks to the geometrical transformation $\mathcal{F}_e$ previously defined, we can transform each integral on an elementary field in the physical space into an integral in the area of reference (that is to say the square or the cube □ previously introduced, according to whether one works with 2D or 3D). Then, the integrals can be calculated in an approximate way by means of a numerical integration method (square rule) which can be defined on the domain of reference. The square rule that we use is the Gauss-Lobatto-Legendre. For 1D, the Gauss-Lobatto-Legendre integration points $\xi_j$, $0 \le j \le \mathrm{N}$, are defined as the zeros of the polynomial $(1-\xi^2)\, L_{N'}'$ where $L_{N'} \in \boldsymbol{P}_N(\Lambda)$ is the Legendre polynomial of degree $N$ defined on Λ. The square rule in higher dimension (2D or 3D) is obtained by simple tensorisation of the 1D squaring rule. For example in the 3D case, we can detail this stage of space discretization. One associates each elementary field $\Omega_e$ a grid of integration $\Xi_N^e = \{(\xi_i,\eta_j,\gamma_k); 0 \le i \le N, 0 \le j \le N, 0 \le k \le N\}$ including $(N+1)^3$ points which can be defined in the domain of reference □ (see figure 6.2):

$$\begin{aligned} a_N(\mathrm{w}_N^h,\mathrm{u}_N^h) &= \sum_{e=1}^{n_{el}}\sum_{i=0}^{N}\sum_{j=0}^{N}\sum_{k=0}^{N}\sigma^h(\xi_i,\eta_j,\gamma_k):\tilde{\nabla}\mathrm{w}_N^h\Big|_{\Omega_e}(\xi_i,\eta_j,\gamma_k)\Big|J_e(\xi_i,\eta_j,\gamma_k)\Big|\rho_i\rho_j\rho_k \qquad (6.11)\\ &= \sum_{e=1}^{n_{el}}\sum_{i=0}^{N}\sum_{j=0}^{N}\sum_{k=0}^{N}\tilde{\nabla}\mathrm{w}_N^h\Big|_{\Omega_e}(\xi_i,\eta_j,\gamma_k):\mathrm{c}(\xi_i,\eta_j,\gamma_k):\tilde{\nabla}\mathrm{u}_N^h\Big|_{\Omega_e}(\xi_i,\eta_j,\gamma_k)\Big|J_e(\xi_i,\eta_j,\gamma_k)\Big|\rho_i\rho_j\rho_k \end{aligned}$$

$$(\mathrm{w}_N^h,\mathrm{f})_N = \sum_{e=1}^{n_{el}}\sum_{i=0}^{N}\sum_{j=0}^{N}\sum_{k=0}^{N}\mathrm{w}_N^h\Big|_{\Omega_e}(\xi_i,\eta_j,\gamma_k)\mathrm{f}\Big|_{\Omega_e}(\xi_i,\eta_j,\gamma_k)\Big|J_e(\xi_i,\eta_j,\gamma_k)\Big|\rho_i\rho_j\rho_k \qquad (6.12)$$

where $\rho_j > 0$ are the weights associated with the squaring rule and $\tilde{\nabla}$ the gradient operator in the domain of reference □:

$$\nabla_x\mathrm{w}_N^h\Big|_{\Omega_e} = \tilde{\nabla}\mathrm{w}_N^h\Big|_{\Omega_e}(\xi) = \mathrm{F}_e^{-1}(\xi)\nabla_\xi\mathrm{w}_N^h\Big|_{\Omega_e} \qquad (6.13)$$

where $\mathrm{F}_e(\xi) = \partial_\xi \mathsf{F}_N(\xi)$ represents the gradient of the geometrical transformation.

In order to define the polynomial approximation in pieces $\mathrm{w}_N^h$ of the field w, we use the integration grid of Gauss-Lobatto $\Xi_N^e$, defined for each elementary field $\overline{\Omega}_e$, as well as the local geometrical transformation $\mathcal{F}_e$. In the elementary field $\overline{\Omega}_e$, we introduce the Lagrange interpolation operator associated with the grid of Gauss-Lobatto defined on the domain of reference □ : for restrictions $\mathrm{w}\big|_{\Omega_e}$, $\boldsymbol{I}_N\left(\mathrm{w}\big|_{\Omega_e}\right)$D is the single polynomial of $\boldsymbol{P}_N$(□) which coincides with $\mathrm{w}\big|_{\Omega_e}$ at $(N+1)^3$ points of $\Xi_N^e$.

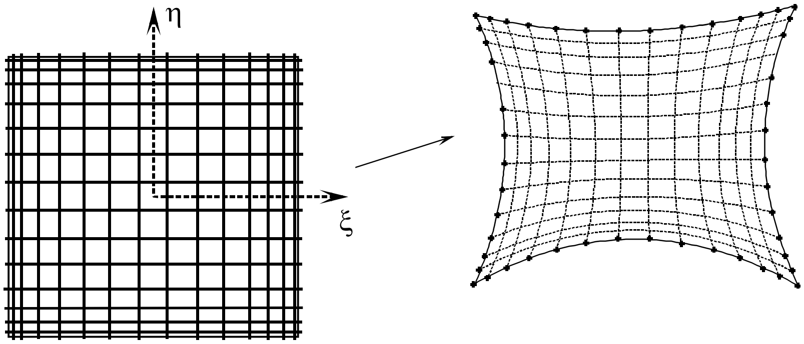

Fig. 6.2. Grid points of Gauss-Lobatto-Legendre in the domain of reference for the 2D case, and in the corresponding curved element.

Let $l_i^N(\xi)$ be the Lagrange polynomial of degree $N$ associated with point $i$ of Gauss-Lobatto-Legendre in the 1D squaring formula (see figure 6.3). The Lagrange polynomials $l_i^N \otimes l_j^N \otimes l_k^N$ define a base of $\boldsymbol{P}_N$(□) and thus:

$$\mathrm{u}_N^h\Big|_{\Omega_e}(x,y,z) = I_N\left(\mathrm{u}\big|_{\Omega_e}\right) = \sum_{i=0}^{N}\sum_{j=0}^{N}\sum_{k=0}^{N} l_i^N(\xi)\, l_j^N(\eta)\, l_k^N(\gamma)\, u_{ijk}^e \tag{6.14}$$

with $\mathbf{x} = \mathcal{F}_e(\xi)$ and $u_{ijk}^e = \mathrm{u}_N^h\big|_{\Omega_e} \circ \mathcal{F}_e(\xi_i, \eta_j, \gamma_k)$.

One notes $\Xi_N$ the global collocation grid which is the assemblage of collocation grids defined on each elementary field:

$$\Xi_N = \bigcup_{e=1}^{n_{el}} \Xi_N^e \tag{6.15}$$

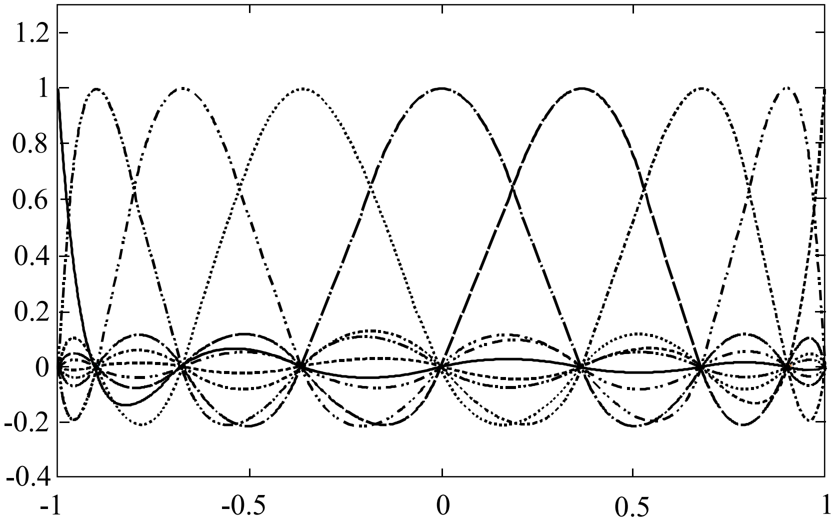

Fig. 6.3. 1D Lagrange polynomials associated to Gauss-Lobatto-Legendre points of order $N$=8.

### 6.2.3 Matrix form of the problem with initial semi-discrete values:

The discretization procedure described above leads to a coupled system of ordinary linear differential equations written in conservative form:

$$\left.\begin{aligned} \dot{\mathrm{p}}(t) &= \mathrm{F}^{ext}(t) - \mathrm{F}^{\mathrm{int}}(d(t)) \\ \dot{\mathrm{d}}(t) &= \mathrm{M}^{-1}\mathrm{p}(t) \equiv \mathrm{v}(t) \end{aligned}\right\} \quad \text{for} \quad t \in \mathbf{I} \tag{6.16}$$

subjected to the initial condition $(\mathrm{d},\mathrm{p})\big|_{t=0} = (\mathrm{d}_0,\mathrm{p}_0)$. If $n_{node}$ is the total number of nodes of the global collocation grid $\Xi_N$, note **d** as the global displacement vector having $n_{node}$ degrees of freedom, and **p** the global momentum vector having also $n_{node}$ degrees of freedom:

$$\mathrm{P}(t) = \mathrm{M}\dot{\mathrm{d}}(t) \tag{6.17}$$

Noting $l^N \otimes l^N \otimes l^N$ as the tensorized base for the 3D case, corresponding to the usual notation $l_i^N(\xi) l_j^N(\eta) l_k^N(\gamma)$ in the elementary Gauss-Lobatto-Legendre grid, one can define the mass matrix **M** by:

$$\mathrm{M} = \underset{e=1}{\overset{n_{el}}{\mathrm{A}}} \int_{\Omega_e} (l^N \otimes l^N \otimes l^N) \otimes (l^N \otimes l^N \otimes l^N) \rho dV \tag{6.18}$$

where $\mathrm{A}_{e=1}^{n_{el}}[\cdot]$ is the assembly operator, as in the finite element method for example, on the total number of spectral elements $n_{el.}$ The use of the squaring rule of Gauss-Lobatto, as well as the Lagrange polynomials, has the fundamental advantage to lead to a diagonal mass matrix. One also notes $\mathbf{F}^{ext}$ the vector of the external forces (imposed nodal forces):

$$\mathrm{F}^{ext} = \underset{e=1}{\overset{n_{el}}{\mathrm{A}}} \left[ \int_{\Omega_e} (l^N \otimes l^N \otimes l^N) \mathrm{f} dV + \int_{\Gamma_T} (l^N \otimes l^N \otimes l^N) \tau \, d\Gamma \right] \tag{6.19}$$

and $\mathbf{F}^{int}$ the total vector of the interior forces:

$$\mathrm{F}^{\mathrm{int}} = \underset{e=1}{\overset{n_{el}}{\mathrm{A}}} \left[ \int_{\Omega_e} \nabla (l^N \otimes l^N \otimes l^N) : c : \nabla \mathrm{u}_N^h \Big|_{\Omega_e} dV - \int_{\Gamma_{abs}} (l^N \otimes l^N \otimes l^N) \tau(\mathrm{u}_N^h) \, d\Gamma \right] \tag{6.20}$$

In the case of a distribution of moments $m(x, t) = m_0(x) \, g(t - t_0)$, we can write:

$$\mathrm{F}^{ext} = \underset{e=1}{\overset{n_{el}}{\mathrm{A}}} \left[ \int_{\Omega_e} \nabla (l^N \otimes l^N \otimes l^N) : m(x,t) dV \right] \tag{6.21}$$

The particular case where $m = m_0 \, I$, with $I$ the identity tensor, corresponds to an impulsive source force.

# 6.3 Time integration algorithms

We present here two diagrams which we used for the discretization in time of the problem to the initial values semi-discrete.

## 6.3.1 Newmark schemes

The evolution in time is defined by the semi-discrete equation of conservation of momentum that have to be checked at time $t_{n+1}$, associated with Newmark formulas [47]:

$$\begin{aligned} \mathrm{Ma}_{n+1} &= \mathrm{F}_{n+1}^{ext} - \mathrm{F}^{\mathrm{int}}(\mathrm{d}_{n+1}, \mathrm{v}_{n+1}) \\ \mathrm{d}_{n+1} &= \mathrm{d}_n + \Delta t \, \mathrm{v}_n + \Delta t^2 \left[ \left( \frac{1}{2} - \beta \right) a_n + \beta a_{n+1} \right] \\ \mathrm{v}_{n+1} &= \mathrm{v}_n + \Delta t \left[ (1-\gamma) a_n + \gamma a_{n+1} \right] \end{aligned} \tag{6.22}$$

Some interesting properties of this family of diagrams can be quoted in [84]:

- These diagrams are unconditionally stable in the linear case for $\beta \geq \gamma \geq 1/2$, and conditionally stable for $\gamma \geq 1/2$ and $\beta < 1/2$. A detailed study of the stability of such diagrams is available in Hughes [47].
- These diagrams are of the second order if and only if $\gamma = 1/2$.

- The only member of this family which ensures the conservation of the total angular momentum is the method of the centered explicit finite differences ($\beta = 0$ and $\gamma = 1/2$ ).
- The trapezoidal rule associated to Newmark diagram, ($\gamma = 1/2$ and $\beta = 1/4$), does not have this property of conservation of the total angular momentum. However, this diagram has good properties ensuring the conservation of the total momentum, and defines an algorithm of temporal discretization depending on acceleration. On the other hand, the acceleration field predicted by this algorithm is known to be disturbed.

## 6.3.2 Newmark algorithms in terms of speed in conservative form

In this case, the conservation equation of the total momentum is written in conservative form at time $t_{n+\alpha}$ [97], which gives the following speed algorithm:

$$\frac{1}{\Delta t}\mathrm{M}(\mathrm{v}_{n+1} - \mathrm{v}_n) = \mathrm{F}^{ext}_{n+\alpha} - \mathrm{F}^{\mathrm{int}}(\mathrm{d}_{n+\alpha}, \mathrm{v}_{n+\alpha})$$

$$\mathrm{d}_{n+1} = \mathrm{d}_n + \Delta t\left[\left(1 - \frac{\beta}{\gamma}\right)\mathrm{v}_n + \frac{\beta}{\gamma}\mathrm{v}_{n+1}\right] + \Delta t^2\left(\frac{1}{2} - \frac{\beta}{\gamma}\right)\mathrm{a}_n$$

$$\mathrm{a}_{n+1} = \frac{1}{\gamma\Delta t}\left(\mathrm{v}_{n+1} - \mathrm{v}_n\right) + \left(1 - \frac{1}{\gamma}\right)\mathrm{a}_n \tag{6.23}$$

$$\mathrm{d}_{n+\alpha} =\& \alpha\mathrm{d}_{n+1} + \left(1-\alpha\right)\mathrm{d}_n \tag{6.24}$$

where

$$\mathrm{F}^{ext}_{n+\alpha} =\& \alpha\,\mathrm{F}^{ext}_{n+1} + (1-\alpha)\mathrm{F}^{ext}_n \tag{6.25}$$

and

We can mention some interesting properties of this type of diagrams:

- The exact conservation of the total angular momentum is obtained for $\alpha = \beta / \gamma = 1/2$, which corresponds to the medium point rule written in conservative form. These values of the parameters define an algorithm of evolution in time independent of acceleration.
- A precision of the second order is obtained if and only if $\alpha = 1/2$ . The particular case $\alpha = \beta / \gamma = 1/2$ and $\gamma = 1$, often used in practice, gives the formula a posteriori $\mathbf{a}_{n+1} = ( \mathbf{v}_{n+1} - \mathbf{v}_n ) / \Delta t$. The stability of these diagrams is studied in Hughes [48] and Simo [97].

## 6.3.3 Predictor-multicorrector algorithms

The two diagrams presented can be rewritten in the form of an iterative algorithm of predictor-multicorrector type which can make it possible to improve their properties in certain cases. A traditional implementation of this type is given below for the family of Newmark diagrams written in acceleration terms:
$i = 0$ (iteration index)
Prediction phase

$$\mathrm{d}^{(i=0)}_{n+1} = \tilde{\mathrm{d}}_{n+1}$$

$$\mathrm{v}^{(i=0)}_{n+1} = \tilde{\mathrm{v}}_{n+1}$$

$$\mathrm{a}_{n+1}^{(i=0)} = 0 \tag{6.26}$$

Resolution phase

$$\begin{aligned} \Delta \mathrm{F}_{n+1}^{(i)} &= \mathrm{F}_{n+1}^{ext} - \mathrm{F}^{\mathrm{int}}\left(\mathrm{d}_{n+1}^{(i)}, \mathrm{v}_{n+1}^{(i)}\right) - \mathrm{Ma}_{n+1}^{(i)} \\ \mathrm{M}\Delta\ \mathrm{a} &= \Delta \mathrm{F}_{n+1}^{(i)} \end{aligned} \tag{6.27}$$

Correction phase

$$\begin{aligned} \mathrm{a}_{n+1}^{(i+1)} &= \mathrm{a}_{n+1}^{(i)} + \Delta a \\ \mathrm{v}_{n+1}^{(i+1)} &= \tilde{\mathrm{v}}_{n+1} + \Delta t \gamma\, \mathrm{a}_{n+1}^{(i+1)} \\ \mathrm{d}_{n+1}^{(i+1)} &= \tilde{\mathrm{d}}_{n+1} + \Delta t^2 \beta\, \mathrm{a}_{n+1}^{(i+1)} \end{aligned} \tag{6.28}$$

where the predictors are defined by:

$$\begin{aligned} \tilde{\mathrm{d}}_{n+1} &= \mathrm{d}_n + \Delta t\ \mathrm{v}_n + \Delta t^2 \left(\frac{1}{2} - \beta\right) \mathrm{a}_n \\ \tilde{\mathrm{v}}_{n+1} &= \mathrm{v}_n + \Delta t\ (1-\gamma)\mathrm{a}_n \end{aligned} \tag{6.29}$$

For a scheme posed in terms of speed in conservative form, we can write:

$i = 0$ (iteration index)
Prediction phase

$$\begin{aligned} \mathrm{d}_{n+1}^{(i=0)} &= \tilde{\mathrm{d}}_{n+1} \\ \mathrm{v}_{n+1}^{(i=0)} &= 0 \\ \mathrm{a}_{n+1}^{(i=0)} &= \tilde{\mathrm{a}}_{n+1} \end{aligned} \tag{6.30}$$

Resolution phase

$$\frac{1}{\Delta t} \mathrm{M}\Delta \mathrm{v}^{(i)} = \Delta \mathrm{F}_{n+\alpha}^{ext} - \mathrm{F}^{\mathrm{int}}\left(\mathrm{d}_{n+\alpha}^{(i)}\right) - \frac{1}{\Delta t} \mathrm{M}\left(\mathrm{v}_{n+1}^{(i)} - \mathrm{v}_n\right)$$

Correction phase

$$\begin{aligned} \mathrm{v}_{n+1}^{(i+1)} &= \mathrm{v}_{n+1}^{(i)} + \Delta v^{(i)} \\ \mathrm{d}_{n+1}^{(i+1)} &= \tilde{\mathrm{d}}_{n+1} + \Delta t \frac{\beta}{\gamma} \mathrm{v}_{n+1}^{(i+1)} \\ \mathrm{a}_{n+1}^{(i+1)} &= \tilde{\mathrm{a}}_{n+1} + \frac{1}{\Delta t} \mathrm{v}_{n+1}^{(i+1)} \end{aligned} \tag{6.31}$$

where the predictors are defined by:

$$\begin{aligned} \tilde{\mathrm{d}}_{n+1} &= \mathrm{d}_n + \Delta t \left(1 - \frac{\beta}{\gamma}\right) \mathrm{v}_n + \Delta t^2 \left(\frac{1}{2} - \frac{\beta}{\gamma}\right) \mathrm{a}_n \\ \tilde{\mathrm{a}}_{n+1} &= -\frac{1}{\gamma \Delta t} \mathrm{v}_n + \left(1 - \frac{1}{\gamma}\right) \mathrm{a}_n \end{aligned} \tag{6.32}$$

with by definition

$$\begin{aligned} \mathrm{d}_{n+\alpha}^{(i)} &= (1-n)\mathrm{d}_n + \alpha\, \mathrm{d}_{n+1}^{(i)} \\ \mathrm{v}_{n+\alpha}^{(i)} &= (1-n)\mathrm{v}_n \end{aligned}$$

$$F_{n+\alpha}^{ext} = (1-\alpha)F_{n}^{ext} + \alpha\, F_{n+1}^{ext}$$

# 6.4 Implementation of the algorithm

After space and temporal discretization, we have seen that we are led to solve for each step of time a system of the type (6.16). Let us note that the 2D expressions differ from the 3D expressions by their number of terms, but not by their structure because of the use of a tensorized base at the elementary level, because of this the reasoning will hold for both cases. From an algorithmic point of view, we can describe the essential calculation phases (in the order in which it is necessary to carry out these operations within each step of time):

1. Calculation of the interior forces on the level of each element.
2. Assembly of the interior forces at boundary of the neighboring elements.
3. Calculation of the external forces at the global level.
4. Inversion of the linear system (6.16) to obtain at the global level the speed or acceleration field starting from the sum of the calculated forces, and the mass matrix.
5. Updates of the speed and displacement fields thanks to the calculated acceleration field, by using the relations (6.22) .

For the 2D case, the calculation of the interior forces at the local level can be done by multiplication of the displacement field by local derivation matrices (calculation of the gradient), then numerical integration of the resulted quantities, again by a simple matrix multiplication at the local level. We also show that the calculation of the external forces is commonplace, and that the mass matrix is rigorously diagonal because of the base choice. From these very significant properties of the formulation suggested, we can draw the following conclusions:

- The calculation of the interior forces at the local level, corresponding to a succession of products by matrices of calculated coefficients once for all, has a cost in $O\,(N^3)$ in the 2D case, and in $O\,(N^4)$ for the 3D case, $N$ being the number of Gauss-Lobatto points used in each direction within the element of reference, which corresponds to a polynomial degree of $N-1$. This cost is thus moderated, in particular for 3D, the magnitude order of the number of points $N$ being 10.

- The summation of the contributions between close elements, for the global calculation of the interior forces, utilizes the tops, edges and faces common for several elements, but not the interior points within each element. So the quantity of information to exchange remains limited to the only boundaries of the close elements, and thus remains weak within the framework of the field decomposition.
- The calculation of the external forces is of a negligible cost.
- Lastly, the mass matrix is exactly diagonal, we have a really explicit method because the inversion of this matrix is immediate, which is a very strong property compared to a traditional finite element method.

Of these various conclusions, which had already been established in the field of fluid mechanics a few years ago [32], one can establish that in the case of linear elastodynamic equations, the cost of total calculation of the method will be primarily controlled by the cost of calculation of the interior forces. This cost is weak at the local level, to pass at the global level it is necessary to sum up the contributions between ends of the close elements (phase "of assembly" in the finite element language, or phase of "send-get" or even "gather-scatter" in the language of parallel calculation). The cost of this operation of assemblage is not easily calculable, because it strongly depends on the structure of the calculator being used. However, on a parallel calculator and within the framework of using an algorithm of field decomposition [32], making it possible to distribute the data on the various processors by ensuring a balance of their load and making it possible to minimize communication times by supporting the locality of data, this operation is natural for a grid made up of hexahedrons. The number of information to be summed up remains limited to the boundary of the neighboring (close) elements, typically, on a parallel calculator, this phase will include mainly communication data, but will require very little CPU time. On the Connection Machine, by using the programming Parallel Data model, it is not necessary to call explicitly upon a decomposition of domain to distribute the data on the various processors, indeed this organization is dealt with by the compiler and optimized routines are provided by the manufacturer.

Contrary, such an algorithm will lead itself relatively bad to an implementation on a supercomputer of the vectorial type, indeed, the polynomial order remaining always relatively low within an element (typically 10), all the vectorial operations at the local level will apply to vectors of very low length, which is always penalizing for this type of architectures. So, the algorithm will function but its effectiveness on this kind of architecture will be rather average.

## 6.5 Validation for 2D Lamb problem

The problem of Lamb is a traditional test which is often used to measure the precision of a method of modeling of the elastic wave propagation. One considers an elastic homogeneous half-space, with a force source placed in the medium, or on the surface of this one. There is an analytical solution with this problem. The problem of Lamb thus makes it possible to validate the algorithm for a source of the external force type colloqued in a point of the grid. If the source is placed in volume, a direct P wave and a direct S wave will be propagated, and reflexions and conversion of modes will occur on the free surface. If the source is placed just under the surface, or exactly on the surface, the principal event will be a Rayleigh wave [88] which will propagate along the surface. In this case, Rayleigh wave is nondispersive, because the medium is homogeneous and its surface is plane. Thus, the problem of Lamb constitutes an excellent test of the precision of a numerical modeling technique, since the three types of elastic waves (P wave, S wave and Rayleigh wave) must be correctly modeled. A detailed numerical analysis of this problem is available in Khun [58].

### 6.5.1 Source inside the model

In this first example, the source is placed inside the model, the free surface is plane, the medium has a P wave speed of 3200 m/s, an S wave speed of 1847.5 m/s and a density of 2200 kg/m$^3$. The studied model has a width of 4000 m and a 2000 m height. Absorbing conditions are used on the left, right and lower boundaries in order to simulate a semi-infinite medium. The grid is composed of 50 × 30 elements, and one uses a polynomial degree of 8 in each direction of an element. This value of 8 was selected because it is close to the optimum for a spectral element method approach [96]. Indeed, if a higher order polynomial is used, and because of the densification of Gauss-Lobatto points on the edges of the element, one does not gain much in precision whereas the cost of calculation grows significantly at the elementary level. If on the other hand a weaker order polynomial is taken, one tends towards a traditional finite element method, and the precision of the diagram is quickly degraded.

The grid that we use is thus composed of 96 641 points. In order to have very precise results in this numerical experiment of which the goal is to compare the calculated results with the exact solution of the problem, a small time step $\Delta t = 0.25$ ms is used. If we define the Courant number by

$$n_0 = \left( \frac{c\Delta t}{\Delta x} \right)_{\max} \tag{6.33}$$

such a time step corresponds for the smallest mesh of the grid in a number of Courant of 0.25, that is to say approximately 40 % of the limit of stability which corresponds to a Courant number of approximately 0.60 (this value being empirically given).

The time diagram used is the predictor-corrector algorithm of Newmark type, that we choose purely explicit ($\beta = 0$ and $\gamma = 1/2$). The total number of time steps is 6000. The position of the source is $(x, z)$ = (2000 , 1400) m and the line of receivers goes from (600, 1700) to (3400, 2200) m. The source is a force, of the Ricker type (second Gaussian derivative) having a central frequency of 14.5 Hz. Such a frequency corresponds, for the grid used, to a sampling of approximately 5 points for smaller wavelength S in the model, on average on a spectral element.

Let us recall that, for a Ricker of central frequency $f_0$, if we define the maximum frequency $f_{\max}$ of this Ricker as the frequency for which the amplitude of the spectrum is 5 % of its maximum value, then we have

$$f_{\max} \approx 2.5 f_0 \tag{6.34}$$

The smallest wavelength S in the heterogeneous model is then

$$\lambda_{s_{\min}} = \left( \frac{c_s}{f_{\max}} \right)_{\min} \tag{6.35}$$

and one will be always placed, in a situation such as this smaller wavelength is sampled by approximately 5 points within a spectral element, which, after test, seems to be the limit of sampling, in which, point numbers below 5 points will cause numerical problems. Wave propagation snapshots corresponding to the problem of Lamb are presented on figure 6.4. As subsequently, all over this thesis, on snapshots the source is represented by a small cross and the line of receivers by two rhombuses connected by a dotted line. One can observe the P and S waves, as well as the converted and reflected waves on the free surface. The displacements recorded by the line of receivers placed in the model are shown on figure 6.5, and the comparison with the analytical solution for receivers 75 and 100 is also shown on figure 6.5. On the figure showing the comparison with the analytical solution, the numerical solution was drawn as well as the residues compared to the analytical solution, represented on the same scale after multiplication by a factor 10. The real amplitudes were compared (without standardization). We obtain a very good agreement, the maximum error relative being less than 1 %. This value is close to the limit of resolution of the analytical code, indeed the analytical solution is obtained after numerical convolution with the temporal function of the source, which introduces in fact a small numerical error into the reference solution (it would be thus preferable to speak about a semi - analytical solution). It is interesting to note that, as it will be often the case in the numerical tests which we will present in the following, the principal source of numerical error comes from the stray reflections on the absorbent boundaries, because owing to the fact that to simulate these absorbing boundaries, a paraxial approximation was used, this approximation being exact for an incidental wave according to the normal at the boundary, and its effectiveness degrades as the incidence angle of the wave deviates from the normal.

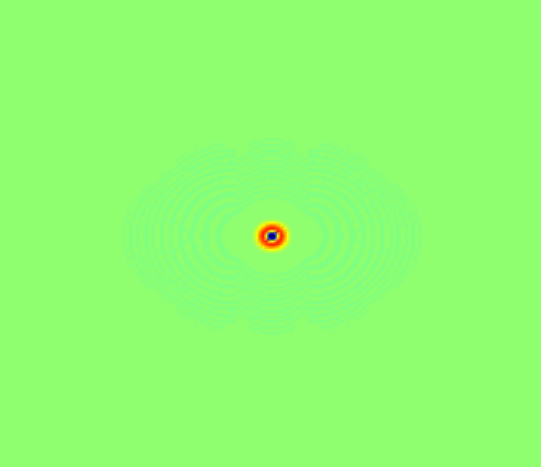

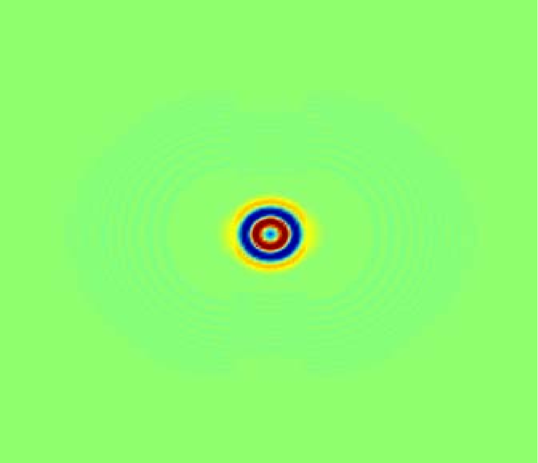

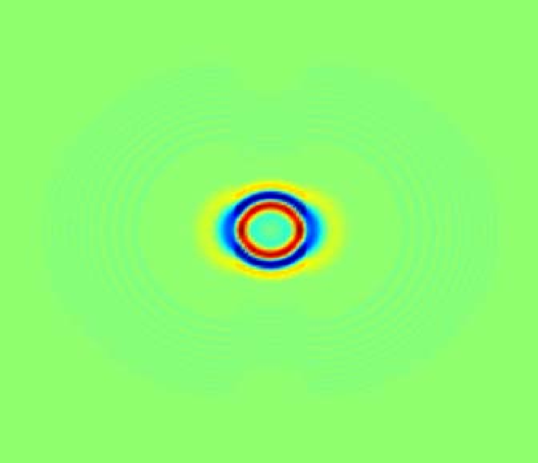

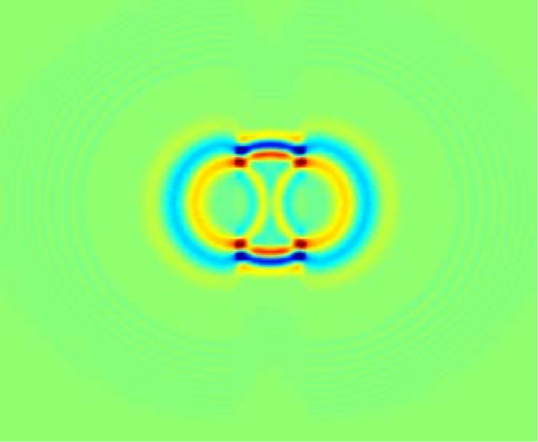

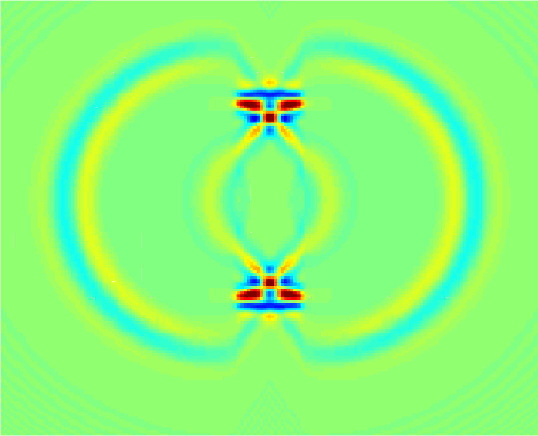

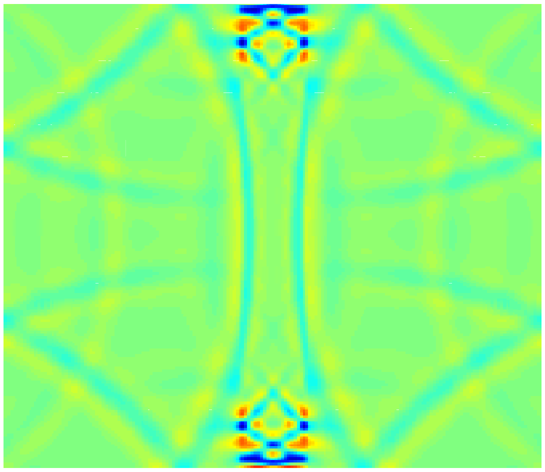

Fig. 6.4. Snapshots obtained for Lamb problem with a source force placed inside the model. One can observe the P and S waves, as well as the reflections and the mode conversions which occur on the free surface.

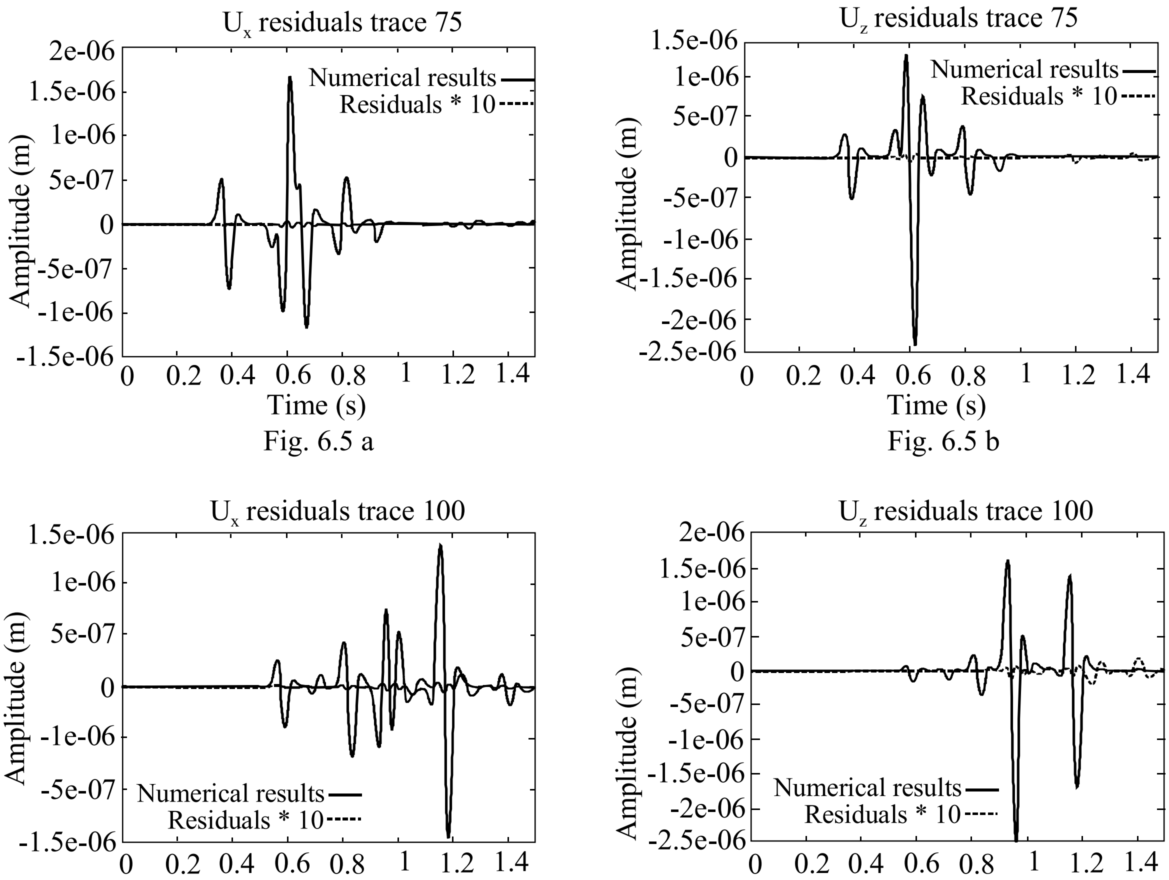

Fig. 6.5 a

Fig. 6.5 b

Fig. 6.5 c

Fig. 6.5 d

Figs. 6.5 (a, b, c and d) : Snapshots recorded by receivers 75 and 100 of Lamb problem with a source load placed inside the model. The residues compared to the analytical solution, drawn on the same scale after multiplication by a factor 10, are also represented. A very good agreement is obtained, the maximum relative error is less than 1 %. The small artifacts on the right are noise reflections coming from absorbing boundaries.

### 6.5.2 Source on the surface

In this second example, the model and the source are the same ones as previously, but the source is now placed exactly on the free face, in $x_s = 1720$ m, as well as the line of receivers. So those will record mainly a strong non-dispersive Rayleigh wave. Such a simulation constitutes an excellent test of the precision of the numerical free surface condition. The corresponding snapshots are introduced on figure 5.6, where the strong Rayleigh wave can be clearly observed, with its elliptic characteristic polarization. The wave refracted on the surface ("head wave") appears also clearly. A diagram of the various wave fronts appearing in such a case is presented on figure 6.7. The displacements recorded by the receivers are shown on figure 6.8 and the comparison with the analytical solution for receivers 75 and 100 is also represented on the same figure. The real amplitudes were compared (without standardization). Again, we find a very good agreement with the reference solution, the maximum relative error being about 1 %. Note that for this simulation, the distance from the source to receiver 100 corresponds to approximately 20 fundamental Rayleigh wavelengths, and 50 minimal Rayleigh wavelengths.

One observes few numerical artifacts, which constitutes a significant advantage related to the use of a variational formulation, into which the free surface condition is introduced in a natural way, to solve the problem - the introduction of the numerical free surface condition being a difficult point in certain traditional numerical methods, for example if high order finite differences or differential pseudo-spectral methods are used [59] [93] [94]-. On the traces presented on figure 6.8, we can observe that the amplitude of the Rayleigh wave remains constant while propagating along the surface, as is required by theoretical calculations in the case of a simulation in plane deformations (corresponding to an infinite source line in the third direction, see for example Garvin [36] ).

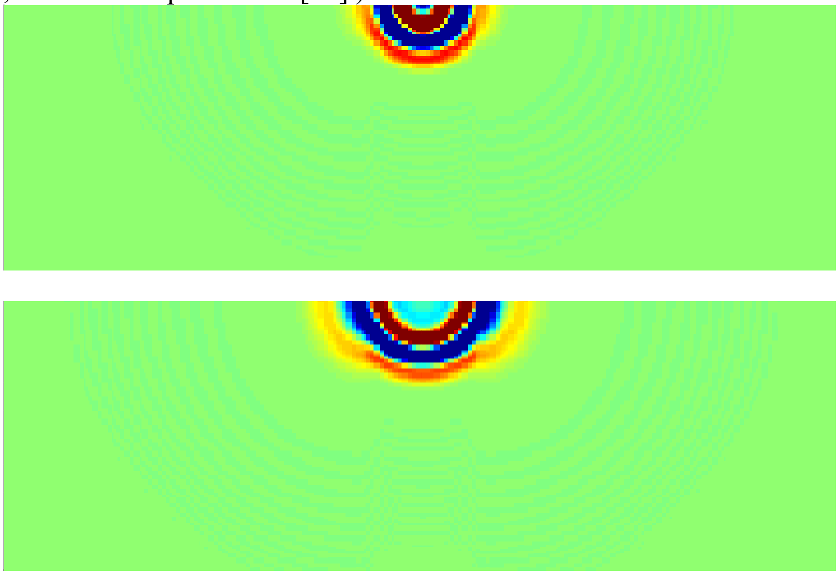

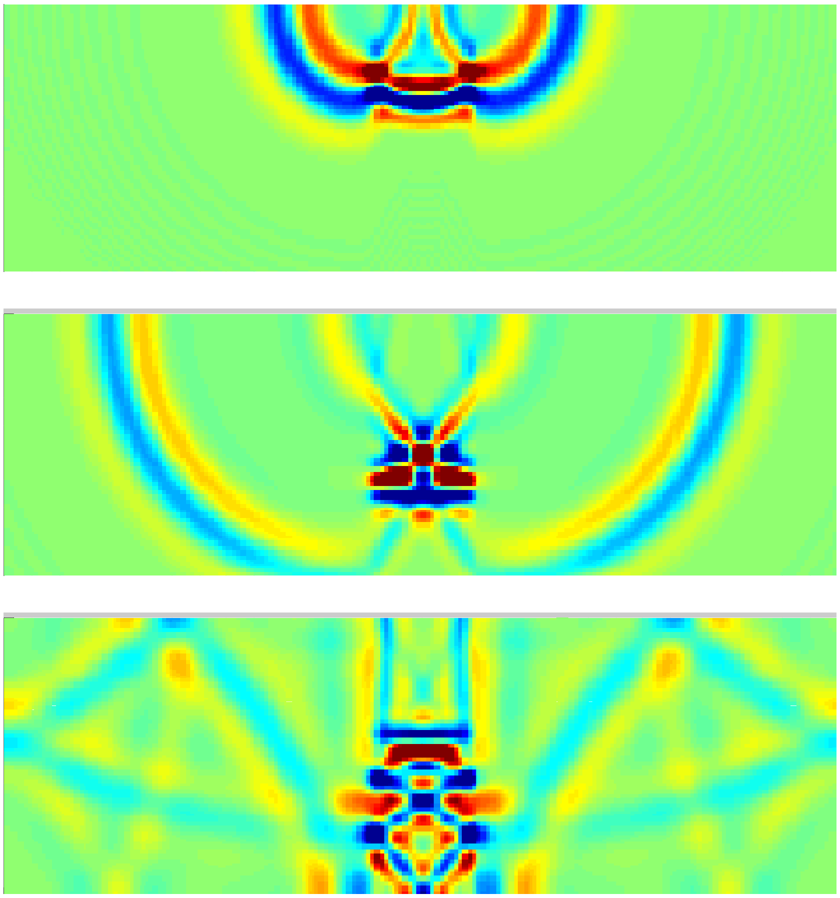

Fig. 6.6: Snapshots recorded by receivers 75 and 100 of Lamb problem with a source load placed at the free surface of the model. The residues compared to the analytical solution, drawn on the same scale after multiplication by a factor 10, are also represented. A very good agreement is obtained; the maximum relative error is less than 1 %. The small artifacts on the right are noise reflections coming from absorbing boundaries.

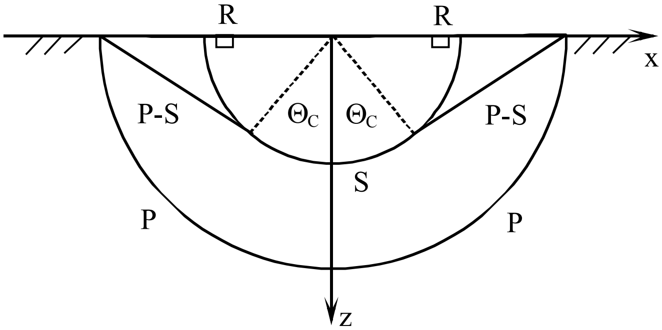

Fig. 6.7 : Diagram showing wave types appearing in Lamb problem when the source is placed on the free face. One can distinguish the P wave, the S wave, the of Rayleigh (R) wave and the P-S wave "head-wave". $\Theta_c$ is the critical angle.

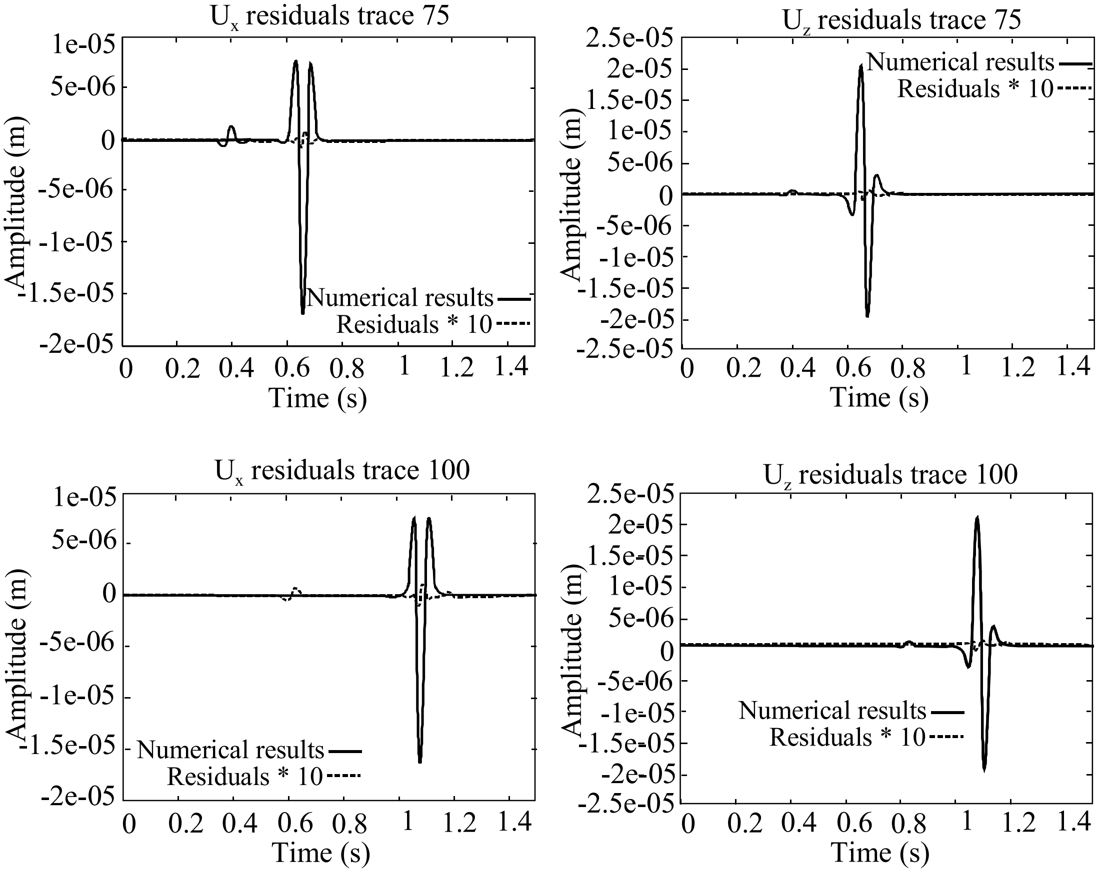

Fig. 6.8: Traces recorded by receivers 75 and 100 for Lamb problem when the source force is placed exactly on the free surface. The residues compared to the analytical solution of the problem are also drawn on the same scale, after multiplication by a factor 10. The agreement is excellent, almost no numerical dispersion is observed, the maximum relative error being about 1%. The amplitude of the Rayleigh wave remains constant during the propagation, which is correct in the case of a calculation in plane deformations.

### 6.5.3 Behaviour on a random grid

In this example, we show that the numerical method suggested remains very precise even if the grid employed is disturbed. The physical model that we consider is the same one as in the preceding case when the source was placed in the volume, but now we use a random grid to solve the problem. The disturbance of the position of the grid points compared to their original position (see figure 6.9), in which the size of the meshes was about 80 m, is drawn randomly between 0 and ± 22 m along the x axis , and between 0 and ± 20 m along the y axis , which represents significant maximum disturbances compared to the original size of the meshes.

The corresponding snapshots are presented on figure 6.9, and the comparison with the analytical solution for receivers 75 and 100 on figure 5.10. Again, we obtain a very good agreement with the analytical solution, which proves that the method remains very precise even when a very disturbed grid is used. The maximum relative error is again about 1 %.

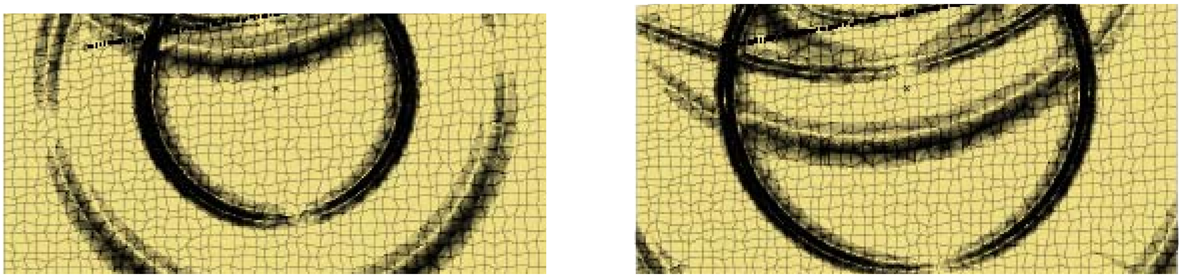

Fig. 6.9: Instantaneous snapshots for Lamb problem using a random grid, with a source placed inside the model. In spite of the use of this strongly disturbed grid, we observe the same phenomena as on figure 6.5. A weak noise reflection coming from the absorbing edge is also visible on the lower edge of the model.

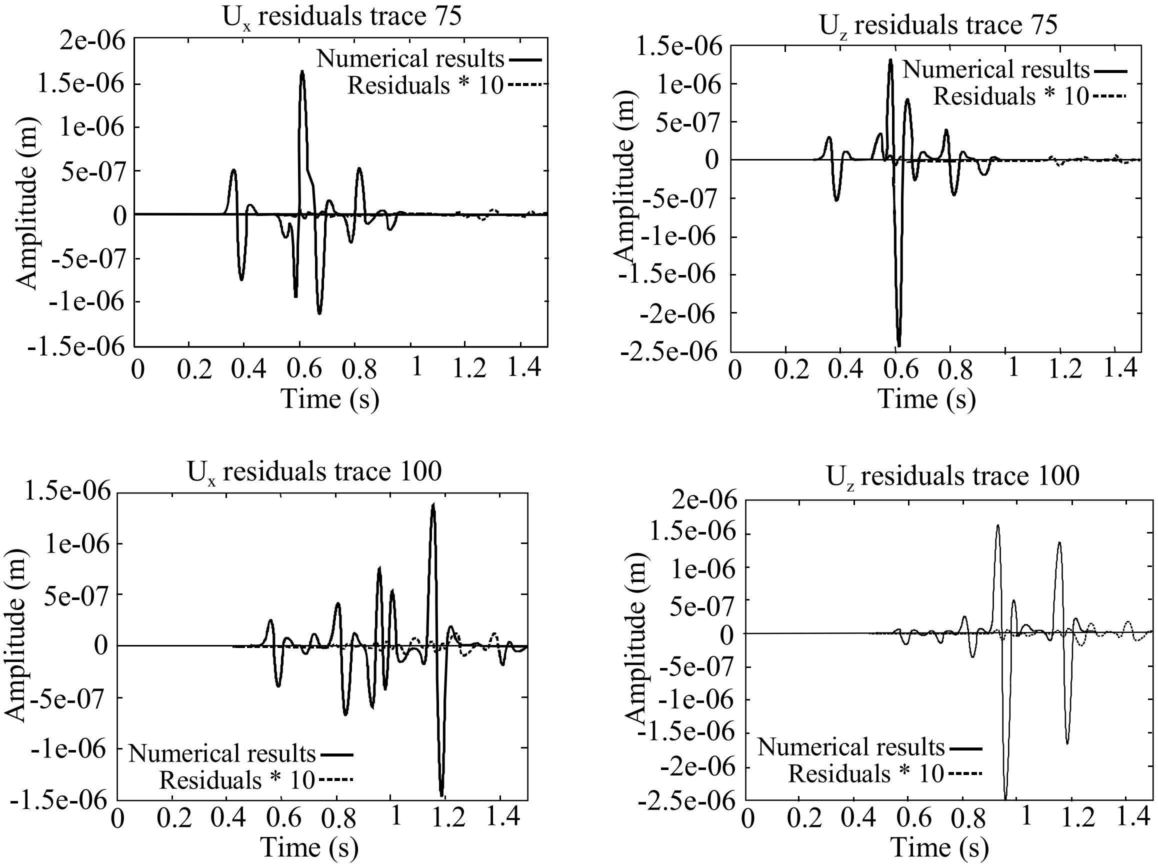

Fig. 6.10: Snapshots recorded by receivers 75 and 100 for Lamb problem using a random grid, the source is placed inside the model. The residues compared to the analytical solution of the problem are also drawn on the same scale after multiplication by a factor 10. A very good agreement is obtained even by using this strongly disturbed grid; the maximum relative error is about 1 %. The weak artifacts on the line are noise reflections coming from the absorbents boundaries.

## 6.6 Stability and dispersion of the numerical method

### 6.6.1 Numerical checking of the stability of the method

It is fundamental to have an idea of the stability and dispersion properties of the algorithm proposed. Let us note immediately that such a study, in the general case of a medium with a non-regular grid, is extremely difficult to carry out (traditional techniques of analysis of stability for example, use a regular Cartesian grid). Thus, we were constrained to limit our study to the stability of the diagram using a series of numerical experiments.

The first experiment was undertaken for Lamb problem previously exposed, by using an explicit Newmark diagram in time ( $\beta = 0$ and $\gamma = 1/2$ ). All other parameters are identical to the cases used above at the time of comparisons to the analytical solution of the problem. However, in order to preserve exactly the total energy contained in the dynamic system considered, we use free boundaries on the four sides of the grid, and not of the absorbent boundaries. We test numerically the stability of the diagram by calculating the total kinetic energy at each time step, the total potential energy, and their sum, which is the total energy present in the medium. If the numerical diagram is stable, the total energy must remain constant during simulation. The explicit Newmark diagram being conditionally stable, we carry out same simulation for several values of time steps ( $\Delta t =$ 0.50 ms , $\Delta t =$ 0.75 ms , $\Delta t =$ 0.80 ms and $\Delta t =$ 0.81 ms ). The value $\Delta t$ = 0.50 ms corresponds, for the smallest mesh, to a maximum Courant number of approximately 0.38, and the value $\Delta t$ = 0.81 ms with a number of maximum Courant slightly higher than 0.60. The results obtained (see figure 6.11 are identical for the first three time step values, and the total energy remains constant during simulation of 3000 time steps, which means that the diagram is stable. The value $\Delta t$ = 0.81 ms is slightly beyond the limit of stability, because we note numerically that after a certain number of time steps, the diagram becomes unstable. The number of maximum Courant corresponding to the limit of stability is thus approximately 0.60 in this case.

The second numerical experiment was undertaken for the same model as previously (only the position of the source being slightly different), but now by using successively the three numerical temporal discretization diagrams that we have, namely:

1. Explicit Newmark diagram in time ( $\beta = 0$ and $\gamma = 1/2$ ). This diagram, is equivalent to a of finite differences centered diagram of order two, is conditionally stable.

2. Newmark implicit-explicit diagram ( $\beta = 1/4$ and $\gamma = 1/2$ in equations 6.22), written in the form predictor/multicorrector (see equations 6.29). This iterative diagram is also conditionally stable .

3. Algorithm written in terms of velocity in conservative form ($\alpha = 1/2$, $\beta = 1/2$ and $\gamma = 1$ in equations (6.23), with a diagram of the predictor/multicorrector type. This diagram is conditionally stable [97].

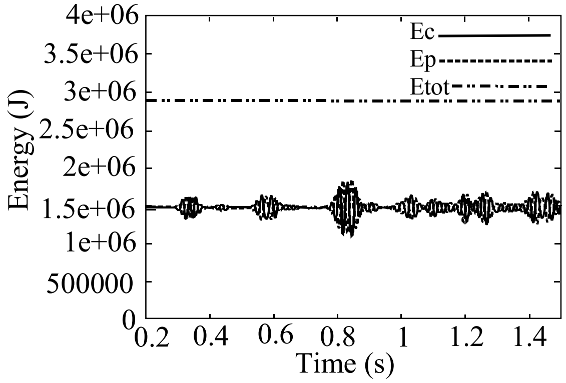

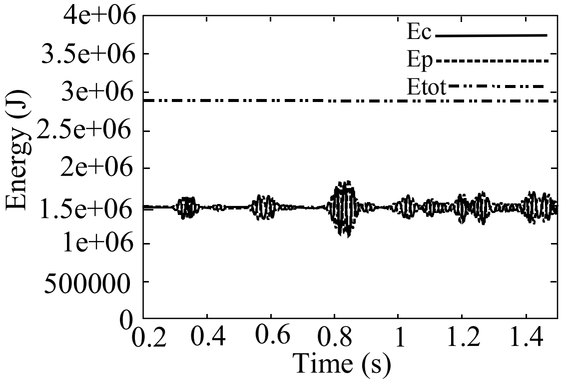

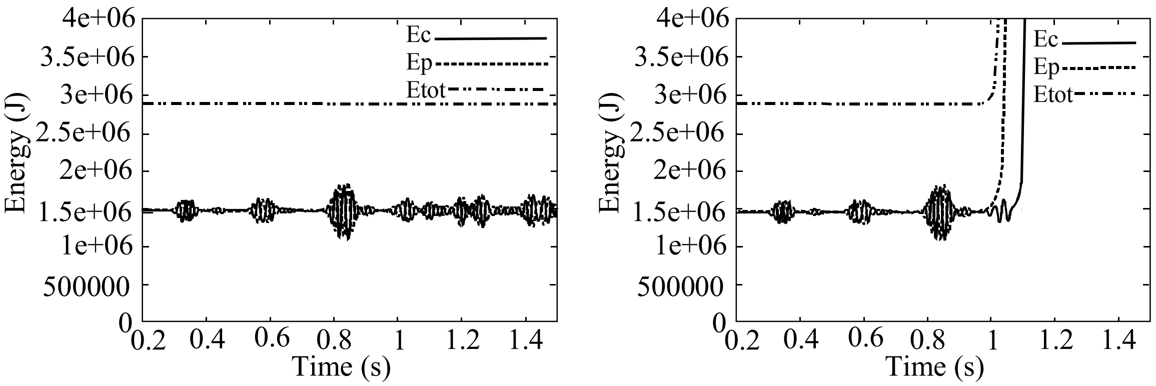

Fig. 6.11: Stability of Newmark diagram for the case of Lamb problem. The four tests correspond to a time step value of (from left to right and from top to bottom) from $\Delta t = 0.50$, 0.75, 0.80 and 0.81 ms respectively. Total energy remains constant during 3000 time steps, proving the stability of the diagram, except for $\Delta t = 0.81$ ms, for which the diagram explodes because the limit of stability was exceeded.

### 6.6.2 Numerical dispersion of the method

As soon as one is interested in a numerical diagram to solve the elastic wave propagation problem in a medium, it is important to ask about the dispersion properties of the diagram being used. The spectral element methods present a very weak numerical dispersion. The analytical study of this numerical dispersion is very hard in the general case (deformed grid). For regular grids, the non-uniformity of the Gauss-Lobatto collocation points makes the analysis rather heavy. In the case of a uniform grid and for polynomial degree $N = 3$ , the collocation points, in each space direction, are divided into several types of nodes repeating itself periodically, with periodicity h , the size of the element: the end node of a segment and two interior nodes. Fourier analysis of the approximation leads to a system of three 1D equations and 2D equations. The solution of this system compared with the Fourier transform of the solution of the continuous system provides an estimate of the error of the space approximation and numerical dispersion. This problem was recently analyzed in the case of the acoustic equation by Cohen et al. [17] and Tordjman [105]. The analysis is rather long. The principal results, for a spectral approximation of order $N = 3$ , are:

- the error of the space approximation is of order $O(h^6)$ for the end nodes and $O(h^5)$ for the interior nodes, which indicates properties of super convergence (one would expect intuitively an error in $O(h^4)$);
- dispersion is controlled by the maximum eigenvalue of the discrete dynamic matrix.

For spectral elements of order 2, this eigenvalue is given by ($k$ being the wave number)

$$\lambda^1(k) = h^2k^2\left(1 - \frac{h^4k^4}{1440} + o(h^6k^6)\right) \tag{6.36}$$

and for spectral elements of order 3 by

$$\lambda^1(k) = h^2k^2\left(1 - \frac{h^6k^6}{302400} + o(h^8k^8)\right) \tag{6.37}$$

One can deduce that numerical dispersion for the semi-discrete problem, for particular solutions of the form :

$$u(x, y, t) = \exp i\,(k_1 x + k_2 y - \omega t) \qquad k_1,\ k_2 \in \mathrm{R} \quad \omega \geq 0 \tag{5.38}$$

is given by

$$q_h(K,\phi) = \frac{\omega_h}{\omega} = \frac{\sqrt{\lambda^1(K\cos(\phi)) + \lambda^1(K\sin(\phi))}}{2\pi K} \tag{5.39}$$

where $q_h(K,\phi)$ is the adimensional phase speed, with $\omega_h$ the numerical pulsation and $\omega$ the physical pulsation, $K = \frac{hk}{2\pi} = \frac{1}{N}$ where $N$ corresponds to the number of elements per wavelength, and $\phi$ the angle between the $x$ axis and the direction of propagation.

The corresponding dispersion curves are given on figure 6.12 for spectral elements of order two and order three. It is clear according to the curves presented that, even for polynomial orders relatively low, the spectral element method has a very weak numerical dispersion in comparison with finite difference methods of order 2 or order 4 (see the dispersion analysis of such methods for example in Rodrigues, [90] ).

These properties can be better for higher polynomial orders ( $N > 3$ ). The complete study for the elastodynamic case is in hand, and should confirm the preceding results obtained for the acoustic case.

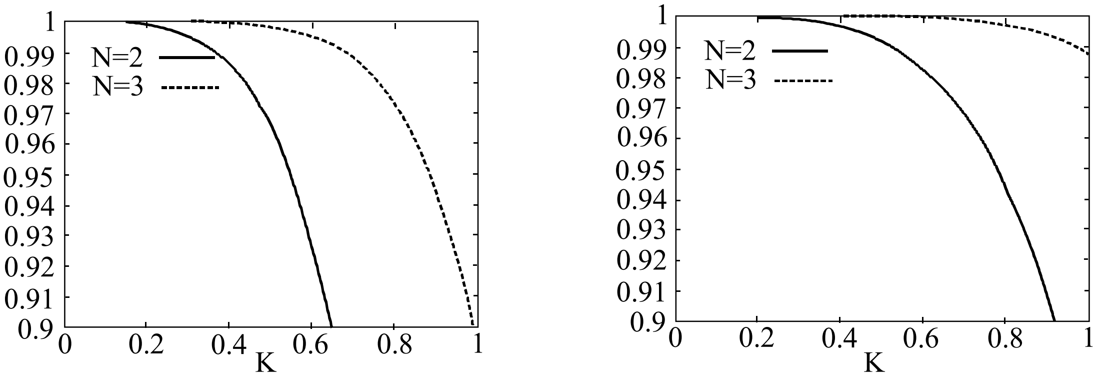

Fig. 6.12: Adimensional phase speed according to the inverse of the element number per wavelength $K$ for the case of the spectral elements of order two and three. The left side curves correspond to Φ= 0°, the right side curves to Φ = 45°.

# 6.7 Effectiveness of the absorbents boundaries

We have seen in the simulations of Lamb problem (see section 6.5) in which it was necessary to introduce on the three sides of the grid absorbent boundaries in order to be able to simulate a semi-infinite medium. The implementation of such absorbent boundaries calls upon paraxial conditions posed in weak form. The equations used being exact only for an incident normal wave for the boundary considered, it is interesting to investigate the effectiveness of these conditions. For that, we again consider the case of Lamb problem studied previously, but we use now absorbent boundaries on the four sides of the grid, in order to simulate an infinite homogeneous medium. Thus, if the absorbing conditions had a perfect effectiveness, we should see that the total energy contained in the system decreases as the waves emitted by the point source reach the boundaries of the field.

The obtained curve for total energy is given on figure 6.13, the second curve being a zoom of an interesting zone of the first curve. Even if the general shape of the curve is correct, and shows as awaited a fast decrease of the total energy contained in our numerical system, a zoom carried out on the final part of the curve shows that it remains a residue of energy even when all the waves should have left the field. This residual energy corresponds to spurious reflections on the absorbent boundaries, for waves emitted by the point source and whose incidence angle is not normal at the boundary considered. Even if this residual energy corresponds only to some ten-thousandth of total energy, in displacement, this can correspond to parasitic waves whose amplitude is about some percents of the direct wave. These parasitic waves are superimposed on the calculated solution in the model, and can lead to significant errors on the calculated signal.

As we have already announced previously, the parasitic reflections coming from the absorbent boundaries will often constitute, in the simulations presented in this thesis, the principal source of numerical noise, and it would be advisable in the future to improve the effectiveness of these absorbing boundary conditions. Another problem which it would be advisable to tackle is the inconsistency between absorbing condition and free surface condition in the higher corners of the model, when a half space is considered. Indeed, in this case, the higher edge is a free surface, imposing a null traction in the higher corners of the grid, condition which is incompatible with the fact that these corners also belong to the absorbent lateral boundaries. In the current approach, this problem has not been solved; the two corners diffract parasitic energy which comes to pollute the numerical solution calculated in the model.

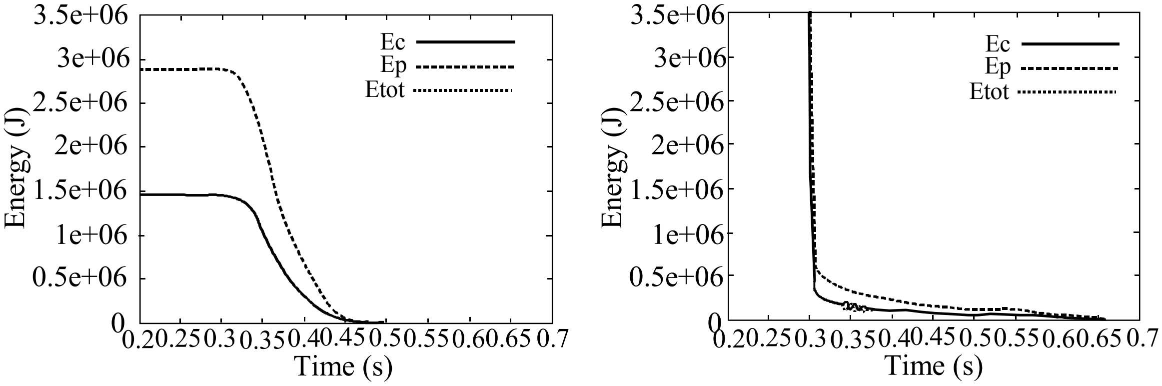

Fig. 6.13: Energy residue in the case of a homogeneous medium having with four absorbents boundaries. The residual value means that, for a non perpendicular incident waves, noise reflections are present in the model. These noisy reflections cause a conversion between kinetic energy and potential energy on the boundary (see for example to $t = 0.8$ s on the of right-hand side figure). The noisy reflections are absorbed after having been propagated in the grid (around $t = 1.3$ s). Calculation was carried out using Newmark algorithm with $\beta = 0.25$ and a time step $\Delta t = 0.50$ ms.

## 6.8 Validation for the 2D Garvin problem

The problem of Garvin [29] is another traditional test making it possible to check the precision of a code of the elastic wave propagation. A homogeneous elastic half space is considered again, but the source is now an explosion. There is an analytical solution for this problem. If the source is placed inside the medium, only a direct P wave is propagated, and a P wave reflection as well as a P-S wave conversion occurs on the free surface. If the source is placed right under the surface, the principal event will be the propagation of a Rayleigh wave along this one. The Rayleigh wave is in this case non-dispersive, because the medium is homogeneous and its surface is plane we simulate the wave propagation by using a grid whose surface is inclined (the Jacobean matrix is thus not diagonal). The receivers record the normal and tangential components (compared to surface) of the displacement field, then the analytical solution given by Garvin can be used.

### 6.8.1 Source inside the model

In this first example, the medium has a P wave speed of 3200 m/s, an S wave speed of 1847 m/s and a density of 2200 kg/m$^3$. The studied physical model has a width of 4000 m and a 2000 m height. Absorbing conditions are used on all the boundaries of the model except for the free surface, in order to simulate a semi-infinite medium. The grid is composed of 50 × 30 elements, a polynomial degree of 8 being used in each direction of an element. The total number of grid points is 96 641. The time step used is again $\Delta t = 0.25$ ms (corresponding to a Courant number of 0.25) in order to obtain very precise results in this simulation of which the goal is to compare the calculated solution with the exact solution of the problem. The total number of time steps is 6000. The position of the source is $(x, z) = (1850, 1380)m$ and the line of receivers extends from (600, 2200) to (3400, 1700)$m$. The source is a Ricker having a central frequency of 14.5 Hz. The corresponding snapshots are introduced on figure 6.14. We can observe the direct P wave, the reflected P wave as well as the converted P-S wave. The comparison with the analytical solution for receivers 55 and 80 is shown on figure 6.15. We find a very good agreement between the two solutions; the maximum relative error is about 1 %, which is the order of magnitude of the precision of the analytical solution, in which the numerical convolution with the source signal introduces a light numerical noise. Again, the spurious reflections coming from the absorbent boundaries constitute the principal source of numerical error.

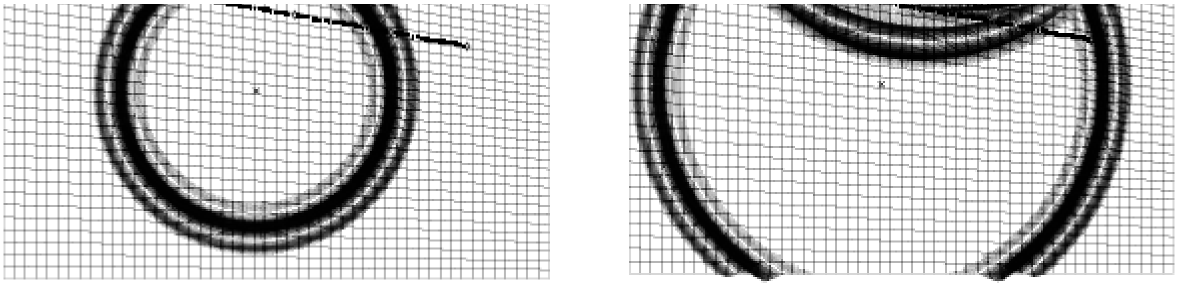

Fig. 6.14: Snapshots for Garvin problem with a compressive wave source (explosion) placed inside the model. The P wave, the reflected P wave as well as the converted P-S wave can be observed.

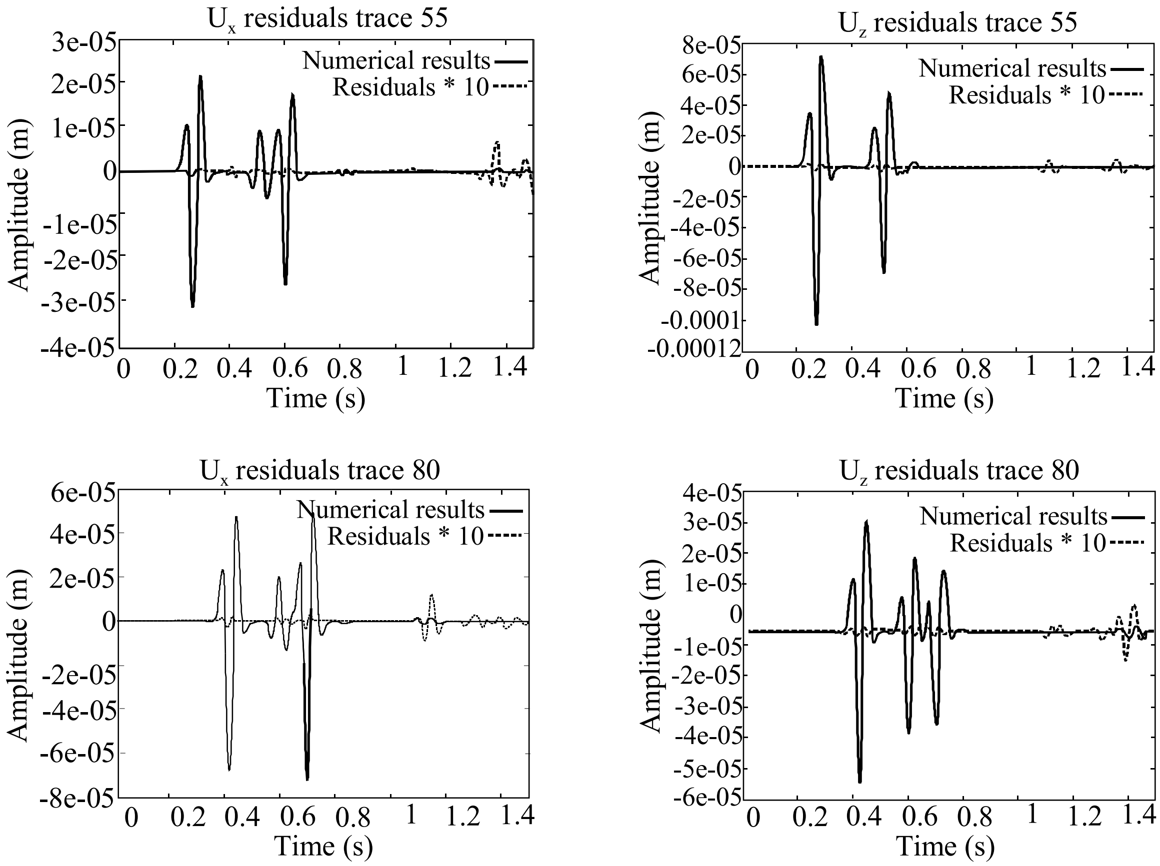

Fig. 6.15: Traces recorded by receivers 55 and 80 for *Garvin* problem when the explosive source is placed inside the model. The numerical solution is represented, as well as the residues compared to the analytical solution, are drawn on the same scale after multiplication by a factor 10. The agreement obtained is very good; the maximum relative error is about 1 %. The weak artifacts on the line are noisy reflections coming from the absorbents boundaries.

### 6.8.2 Source on the surface

The impulsive source is now placed exactly on the free surface. In this case, the principal event is a strong non-dispersive Rayleigh wave propagating along the surface; its amplitude remains constant in a plane strain simulation. The corresponding snapshots are introduced on figure 6.16, the receivers being placed on the surface. We can observe the direct P wave, the Rayleigh wave with its typical elliptic polarization, and the refracted wave ("head wave"). The comparison with the analytical solution for receivers 75 and 100 is represented on figure 6.17. The agreement obtained is very good, the maximum relative error being again about 1 %. We can notice on the snapshots that almost no energy is emitted in the form of P wave in the normal direction with the surface, the source being placed exactly on the free surface. It can thus appear preferable in certain cases to place more in-depth impulsive (explosive) source in order to illuminate all the medium, the principal disadvantage in this case being the presence of a strong wave reflected from the free surface (wave called "phantom wave" or "ghost wave" in oil industry) which comes to superimpose, with a small shift, with the direct wave.

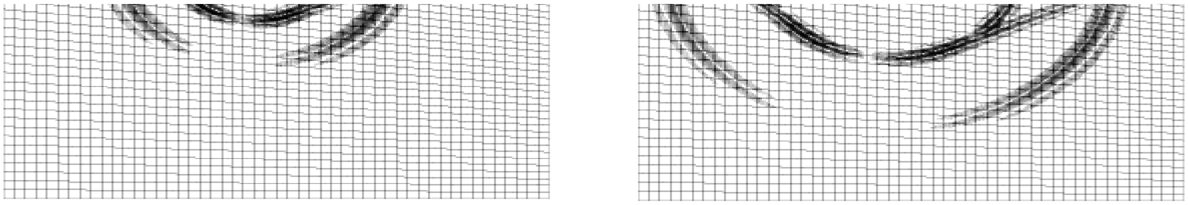

Fig. 6.16: Snapshots Garvin problem when the explosive source is placed exactly on the free surface. The Rayleigh wave, with its typical elliptic polarization, is clearly recognizable, as well as the "head-wave". In this case, almost no energy is emitted in the form of P wave in the direction perpendicular to the slope.

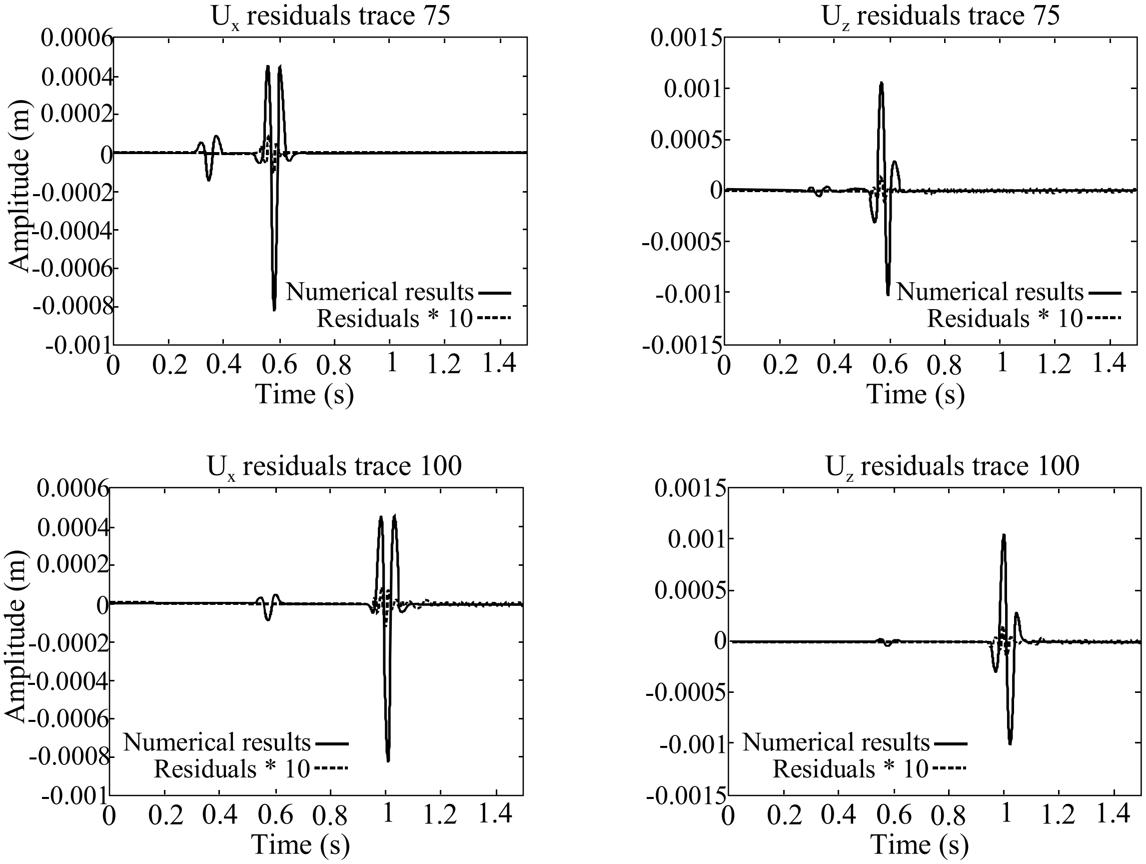

Fig. 6.17: Traces recorded by receivers 75 and 100 for Garvin problem when the explosive source is placed exactly on the free surface. The numerical solution is represented, as well as the residues compared to the analytical solution, drawn on the same scale after multiplication by a factor 10. The agreement is very good; the maximum relative error is about 1 %.

## 6.9 Conclusions

In many cases of elastodynamic problems, it is important to be able to simulate the elastic wave propagation in models containing plan interfaces and/or layered topography. The use of a variational formulation of the wave equation makes it possible to naturally take into account these complex geometries.

We showed that it was possible to use a spectral element method in order to solve the wave equations of such complex mediums for both 2D as 3D cases. The precision of the method was shown by solving two traditional 2D problems (Lamb problem and Garvin problem) and by comparing the calculated solution by using a low number of points per wavelength (about 5) with analytical solutions. An excellent agreement was found, which made it possible to validate the introduced numerical method.

The stability of the suggested method was checked numerically, and the effectiveness of the boundary conditions was discussed. We also noted that the spectral element method was very well adapted to the modern computer architectures, and that very interesting performances could be obtained from a data-processing point of view.

Chapters 4 and 6 of the present thesis reviewed methods of soil structure interaction (SSI) problem analysis and the coupling of finite element analysis with spectral element methods. Emphasis has been put on the spectral finite element method (SFEM), which is claimed to provide reliable results. As already stated in Chapter 4, there has been little research of SFEM related to SSI, and no reliability study at all. Chapter 6 and the next chapter of this research aims at applying SFEM to SSI problems and making comparisons and evaluations with respect to more classical approaches such as FEM, BEM and hybrid methods FEM-BEM. As already discussed in chapter 6, SFEM is well established for linear problems so far. Thus elastic two-dimensional mechanical problems have been chosen for the present study. The conclusions of the study should be understood only in this context. It is reminded that both the boundary element method and the finite element methods can be and have already been applied to general non-linear problems (including large strains, plasticity) as well as dynamics. These approaches have a much larger scope than SFEM, at least in its present stage of development. However, in the case when all these approaches are applicable (i.e. for linear problems), the present study will give some new lights about their respective advantages and shortcomings.

## Chapter 7

# 7. 2-D spectral finite element analysis

## 7.1 Introduction

In this chapter, we will show the flexibility of the of the spectral element method by simulating the wave propagation in 2-D models having more realistic structures than those used in the preceding chapter (heterogeneous mediums, layered mediums presenting a discontinuity of the free surface, or wave types reputed difficult to model by using more traditional numerical methods, like the refracted waves or Stoneley waves). Such models are often encountered in practice. For example when a seismic soil structure interaction analysis is undertaken in order to assess the vulnerability of existing or newly designed structures, or a seismic zoning campaign in zones presenting high seismic risk, such discontinuities of the free surface, presence of faults or interfaces in highly contrasted mediums, where wave mode conversion from surface waves into volume waves can take place. In this chapter, we will analyze the results provided by the of the spectral element method on a certain number of complicated models corresponding to such situations. We finish this study by calculating soil structure interaction effects in 2-D structures, for which reference solutions exist .

## 7.2 Modeling of the refracted waves

The correct calculation of the refracted waves on an interface in a heterogeneous medium is fundamental in all seismic refraction experiments. To model this phenomenon, we consider a medium made up of two elastic half spaces of different properties in contact, an explosive source being placed in one of them. An incident P wave will be propagated, and will be partly reflected and partly transmitted at the interface. A converted P-S wave will be also generated in each half space. But the most interesting phases, and most difficult to model, are certainly the refracted waves which will be propagated along the interface, and which will be recorded by the receivers.

The grid is divided horizontally into two parts having different elastic properties. Absorbing conditions are used on all the edges of the grid. The lower medium has a P velocity of 3400 $m.s^{-1}$, an S velocity of 1963 $m.s^{-1}$ and a density of 2600 $kg.m^{-3}$. The upper medium has a P velocity of 2500 $m.s^{-1}$, an S velocity of 1558 $m.s^{-1}$ and a density of 1500 $kg.m^{-3}$. The physical model considered has a width of 4000*m* and a height of 3000*m*. The grid is composed of 40 × 30 elements, an 8 degree polynomial is used in each direction of an element. Thus, the total number of the grid points is 77361. The time step used is again $\Delta t$ = 0.25*ms* (corresponding to a maximum Current number of 0.25), and the total number of time steps is 6000. The position of the source is $( x, z )$ = (1042, 1570)*m* and the line of receivers extends from (500, 1920) to (3900,1920)*m*. the source is an explosion, its time dependence is a Ricker of a central frequency of 14 Hz. The corresponding instantaneous snapshots are represented on figure 7.1. We can observe the incident P wave, the reflected and converted waves at the interface.

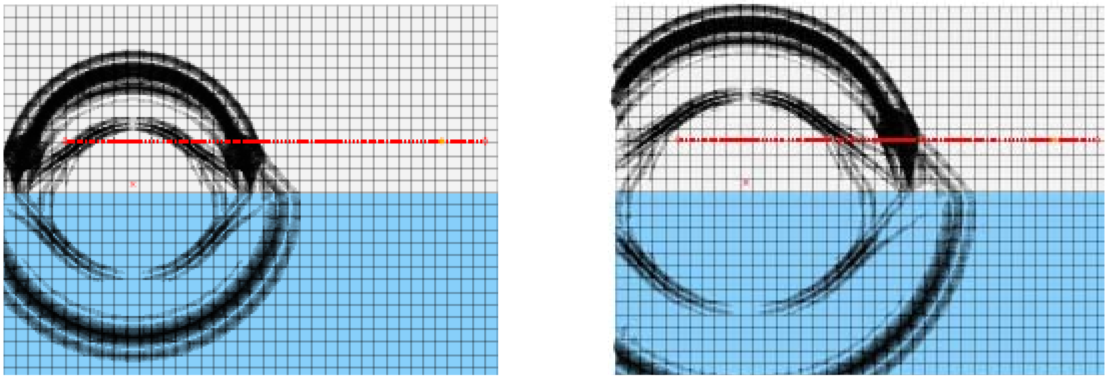

Fig. 7.1 – Instantaneous snapshots obtained in the case of two layer elastic medium. We can observe the incident P-wave, the reflected and converted waves on the interface.

## 7.3 Dispersive Rayleigh wave

In the case of a fine layer of low velocity (for example, a surface layer having a thickness of few meters only) located on a homogeneous elastic half space, Rayleigh waves are highly dispersive. Such a phenomenon is frequently observed into seismic terrestrial prospecting. Let us consider a homogeneous elastic half space having a P velocity of 3000 $m.s^{-1}$, an S velocity of 1500 $m.s^{-1}$ and a density of 2000 $kg.m^{-3}$, covered with a fine elastic layer of 63.2$m$ thickness, having a P velocity of 2000 $m.s^{-1}$, an S velocity of 1200 $m.s^{-1}$ and a density of 1000 $kg.m^{-3}$. There is no analytical solution with this problem, but a certain number of numerical studies are available [87]. The physical model considered has a width of 3200m and a height of 2400m. The grid is composed of 50 × 38 elements, a polynomial degree of 8 being used in each direction of an element. The total number of points of the grid is 122305.

The time step used is $\Delta t = 0.4ms$, and the total number of time steps is 3800. The position of the source is $(x, z) = (1100, 2383)m$ and the line of receivers is placed on the free surface between $x = 1200$ and $x = 2900m$. The source is an explosion, with a Ricker time dependence having a central frequency of 13 Hz. The instantaneous correspondents are given on figure 7.2. The predominant event is a Rayleigh dispersive wave, accompanied by the incident P wave as well converted waves in the zone of low velocity. The recorded accelerograms by the receivers are presented on figure 7.3, where we can identify multiple P waves, generated in the zone of low velocity, as well as the dispersive Rayleigh waves.

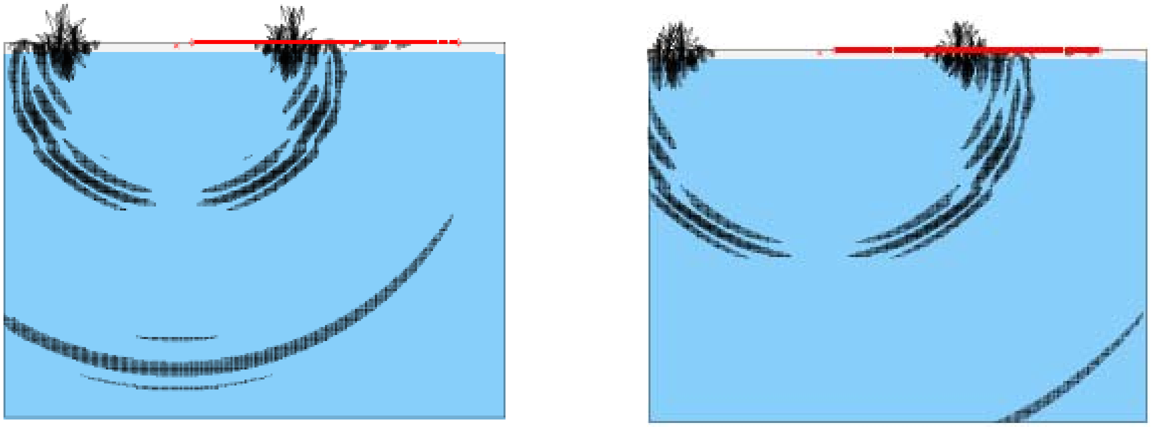

Fig. 7.2 : Instantaneous snapshots obtained in the case of a dispersive Rayleigh wave in a double-layered elastic medium. We can observe the dominant phase which is the dispersive Rayleigh wave, as well as the incident P wave and the multiples (reflected and converted waves in the zone of low velocity).

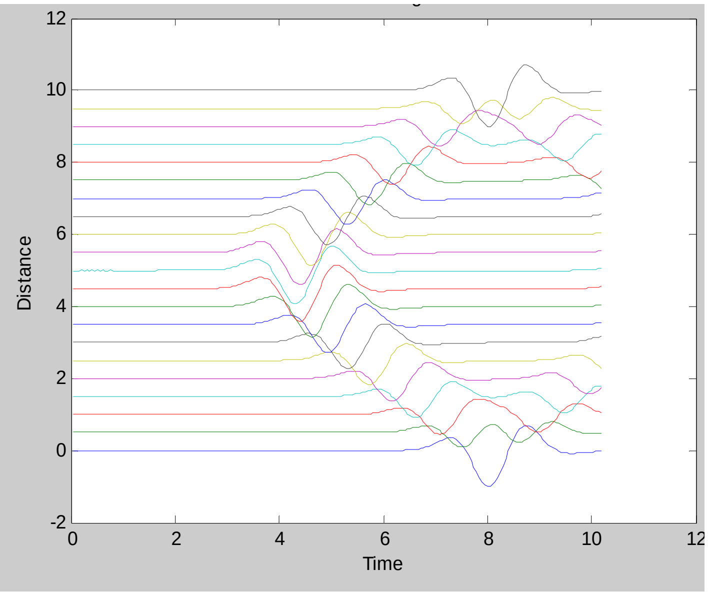

Fig. 7.3: Recorded accelerograms in the case of two elastic half-spaces in contact. We can observe the incident P wave, the reflected and the converted waves at the interface, and various types of refracted waves. Because of the low amplitude of the refracted waves compared to the incident wave, the amplitudes were represented with a strong saturation, which reveals a little numerical noise and parasitic reflections coming from the edges of the model.

## 7.4 Discontinuity at the free surface

In this example, we study the behavior of a Rayleigh wave meeting a discontinuity on the free surface, for example a discontinuity in the form of stair. This problem was the subject of a theoretical study and of an experimental study [26]. It is representative of a soil model whose surface has a clear discontinuity, like a cliff for example. The source is a vertical force placed right under the upper free surface. Absorbing conditions are used on the left edge and the lower edge of the grid. The medium has a P velocity of 3200 $m.s^{-1}$, an S velocity of 1847.5 $m.s^{-1}$ and a density of 2200 $kg.m^{-3}$. The studied physical model has a width of 4000$m$, and a height of 2400$m$. The grid is composed of 50 × 30 elements, a polynomial degree of 8 being used in each direction of an element. The total number of grid points is 96641. The time step used is $\Delta t = 0.50ms$, and the total number of time steps is 5000. The position of the source is $( x, z ) = (2440, 2340)m$ and the receivers are placed on the free surface on both sides of the corner. The normal and tangential displacement components are recorded by the receivers on two surfaces. The source is a colloced force, its time dependence is a Ricker having a central frequency of 14.5 Hz. The corresponding instantaneous snapshots are shown on figure 7.4. We can observe a strong Rayleigh wave which is propagating along the upper edge of the model, and which is partially reflected and partially transmitted by the corner. We can observe the transmitted Rayleigh wave going down along the flat rim from the model. The corner behaves like a diffracting point, and gives rise to spherical P and S waves which can be clearly observed on the second instantaneous snapshot. The accelerograms recorded by the receivers placed on both sides of the corner are shown on figure 7.5.

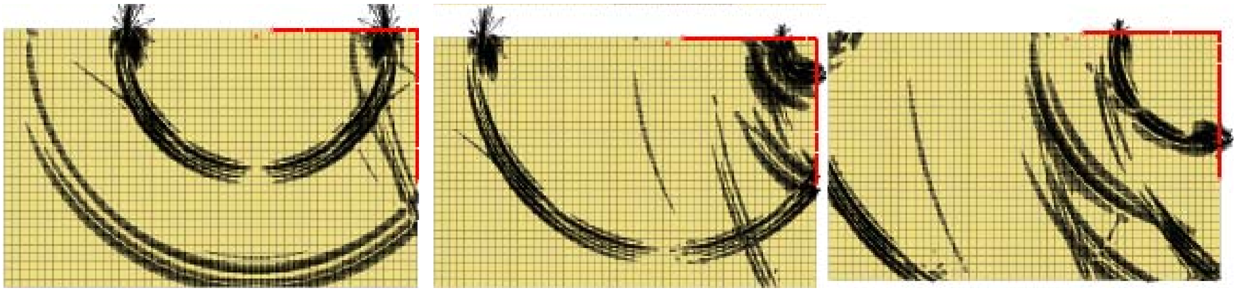

Fig. 7.4:Snapshots of the displacement vector in which the corner is touched by a Rayleigh wave. We can observe a strong Rayleigh wave propagating along the higher border of the model, which is partly reflected and partly transmitted by the corner. We can observe the transmitted Rayleigh wave propagating In its way down along the flat rim from the model. The corner acts like a diffracting point, and gives rise to spherical P and S waves.

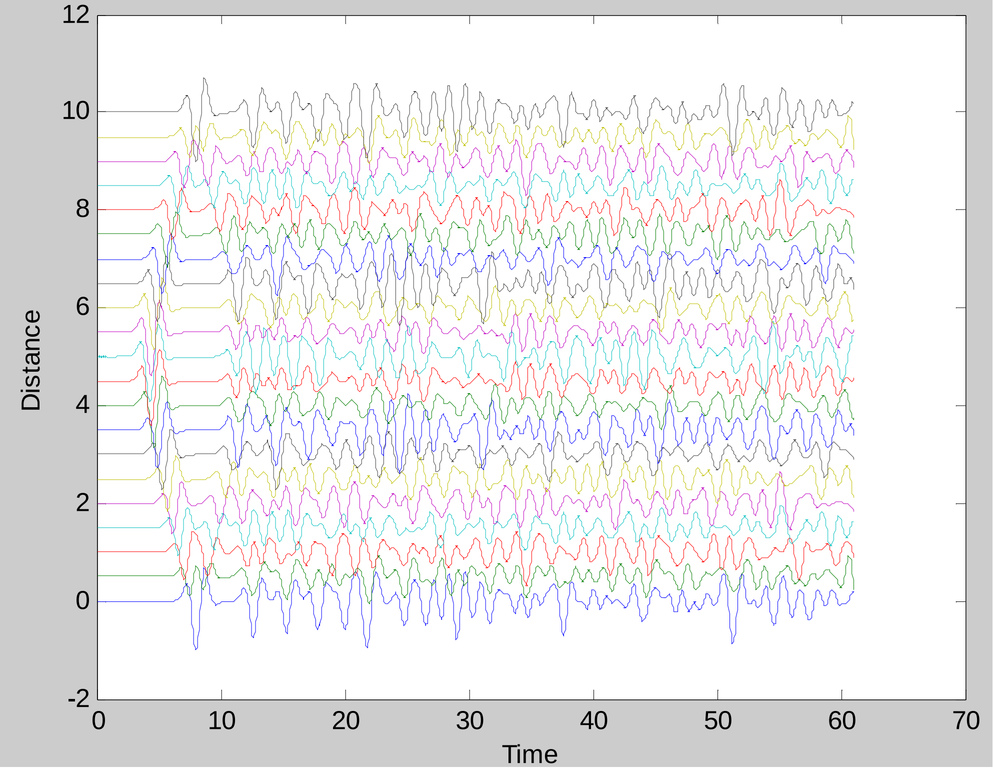

Fig. 7.5: Accelerograms recorded in the case of a corner of the model hit by a Rayleigh wave. We can observe a strong Rayleigh wave propagating along the upper surface, which is partly reflected and partly transmitted by the corner. The corner acts like a diffracting point, and gives rise to spherical P and S waves.

## 7.5 Wave propagation in the presence of multi-story buildings

In this section we present the through soil wave-propagation to calculate the seismic response of multistory buildings, founded on a layered soil media and subjected to vertically propagating shear waves. Buildings are modeled as an extension of the layered soil media by considering each story as another layer in the wave-propagation path. The seismic response is expressed in terms of wave travel times between the layers and wave reflection and transmission coefficients at layer interfaces. Accounts is made of the filtering effects of the concentrated foundation and floor masses. Compared with commonly used vibration formulation, the wave-propagation formulation provides several advantages, including simplicity, improved accuracy, better representation of damping, the ability to incorporate the soil layers under the foundation, and providing better tools for identification and damage detection from seismic records.

### 7.5.1 Wave propagation in buildings

Figure (7.6) shows a multistory building resting on a layered soil medium and subjected to vertically propagating shear waves. The seismic waves propagating through the soil and the building can be separated into the upgoing and the down-going components, as shown in the figure. Whenever the up-going and downgoing waves cross a layer interface they are partly reflected and partly transmitted into the next layer. The reflections and transmissions are characterized by the reflection and transmission coefficients. This is schematically shown in Fig. 7.7(b), where $u$ denotes the upgoing wave, and $R_u$ and $T_u$ denote the reflection and transmission coefficients for the upgoing wave, respectively. Similarly, $d$ denotes the down-going wave, and $R_d$ and $T_d$ denote the corresponding reflection and transmission coefficients for the downgoing wave, respectively.

We derive the wave-propagation equations by using the discrete-time formulation that is commonly used by researchers in oil exploration. Consider the three consecutive layers, layers $j-1$, $j$, and $j+1$, as schematically shown in Fig. 7.7(b). Let $u_j(t)$ and $d_j(t)$ represent the amplitudes at discrete time t of the upgoing wave at the top and the downgoing wave at the bottom, respectively, of layer $j$. We can show from Fig. 7.7(b) that the upgoing wave $u_l(t)$ in layer $j$ is composed of the reflected portion of the downgoing wave from the bottom, plus the transmitted portion of the upgoing wave from the layer below. This relationship can be expressed by the following equation:

$$u_j(t) = R_{d.j-1}.d_j(t-\tau_j) + T_{u.j-1}.u_{j-1}(t-\tau_j) \tag{7.1 }$$

where $R_{d.j-1}$ and $T_{u.j-1}$ denote the reflection coefficient for the downgoing waves and the transmission coefficient for the up-going waves, respectively, at interface $j-1$. $\tau_j$ is the one-way

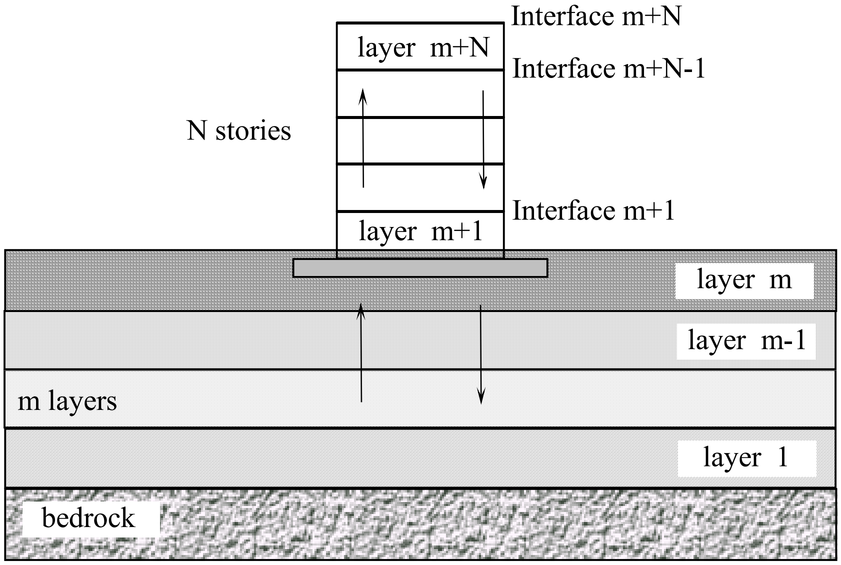

(a)

Fig. 7.6 : Bedrock-soil-building system: (a) Layers, interfaces, and upgoing and downgoing waves.

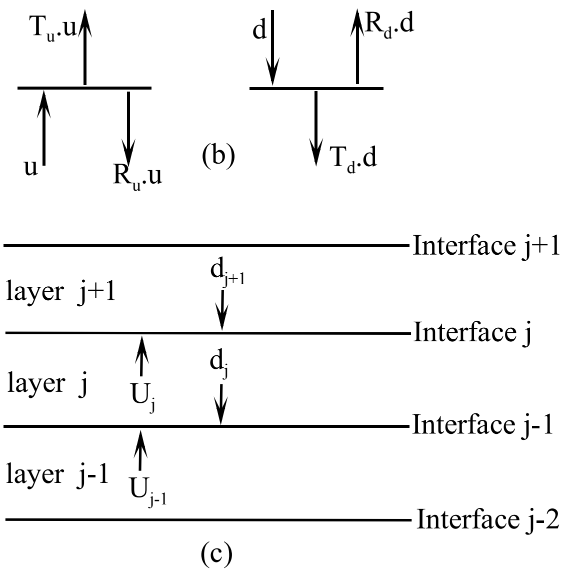

Fig. 7.7 . (b) Reflection and transmission of upgoing and downgoing waves; (c) Three consecutive layers with upgoing and downgoing waves.

travel time of the waves in layer *j*. Similarly, we note that the downgoing wave $d_j(t)$ in layer *j* is composed of the reflected portion of the upgoing wave from the top, plus the transmitted portion of the downgoing wave from the layer above. This can be expressed by

$$d_j(t) = R_{u.j}.u_j(t-\tau_j) + T_{u.j}.d_{j+1}(t-\tau_j) \qquad (7.2\ )$$

Where R $_{u,j}$ , and $T_{d,j}$ denote the reflection coefficient for the upgoing waves and the transmission coefficient for the down-going waves, respectively, at interface *j*. eqs. (7.1) and (7.2) are valid for all intermediate soil and building layers. For the first and the last layers, we modify the equations to incorporate the boundary conditions. For the first layer, which is the bottom soil layer next to the bedrock [Fig. (7.7)], we can show that

$$u_1(t) = R_{d,0}.d_1(t-\tau_1) + T_{u,0}.x_0(t-\tau_1) \qquad (7.3\ )$$

$$d_1(t) = R_{u,1}.u_1(t-\tau_1) + T_{d,1}.d_2(t-\tau_1) \qquad (7.4\ )$$

where $x_0$(t) = input seismic wave at the bedrock-soil interface. It is assumed that there are no reflections from the bottom of bedrock. For the last layer [layer $m + N$ in Fig. (7.1)], which is the top story of the building, we note that there are no downgoing waves transmitted from the layer above. Thus

$$u_{m+n}(t) = R_{d,m+N-1}.d_{m+N}(t-\tau_{m+N}) + T_{u,m+N-1}.u_{m+N-1}(t-\tau_{m+N}) \qquad (7.5\ )$$

$$d_{m+N}(t) = R_{u,m+N}.u_{m+N}(t-\tau_{m+N}) \qquad (7.6\ )$$

Eqs. (7.1) - (7.6) provide a complete description of the wave propagation in a soil-building system.

The actual response of any floor in the building, or any interface in the soil medium, can be calculated by combining the upgoing and downgoing waves. For interface $j$ in the building, for example, the response at the top and the bottom of the floor slab is

$$y_{j,top}(t) = u_{j+1}(t - \tau_{j+1}) + d_{j+1}(t) \tag{7.7 }$$

$$y_{j,bot}(t) = u_j(t) + d_j(t - \tau_j) \tag{7.8 }$$

The continuity of displacements at the floor slab requires that $y_{j,top}(t) = y_{j,bot}(t)$; therefore, either (7.7) or (7.8) can be used to represent the motions of the floors.

If the sampling interval of the incident bedrock motion $x_0(t)$ is small enough such that the travel times $\tau_j$ in the layers are integer multiples of the sampling interval, the wave-propagation equations all become finite-difference (i.e., discrete-time filtering) equations. The soil-building system is defined in the equations by the wave travel times in the layers, and the wave reflection and transmission coefficients at the layer interfaces, which can all be determined uniquely from the physical characteristics of the building and the soil (we will add the damping in the equations later). For a given soil-building system and the bedrock motion, the equations can be solved recursively starting from the bedrock [i.e., with eq.(7.3)] and continuing upward. Note that the initial values of $u_j(t)$ and $d_j(t)$ are zero until the first arrival of the waves in layer $j$. That is

$$u_j(t) = 0 \quad \text{for} \quad t < \sum_{k=1}^{j} \tau_k \tag{7.9 }$$

$$d_j(t) = 0 \quad \text{for} \quad t < \tau_j + \sum_{k=1}^{j} \tau_k \tag{7.10 }$$

We should mention that in the wave-propagation formulation either accelerations, velocities, or displacements can be used as input. Calculated response is of the same type as the input, and the response in the building represents the absolute response, not the relative response with respect to ground.

## 7.5.2 Wave travel times in buildings

Wave travel times in the layers are calculated by simply dividing the layer thickness with the wave velocity in each layer. The shear-wave velocities for soil are generally determined by field tests and are available in the literature for a large number of different soil types. Theoretically, the 1D shear-wave velocity $\upsilon_S$, in an elastic soil medium is $\upsilon_S = \sqrt{G/\rho}$, where $G$ and $\rho$ are the shear modulus and the mass density, respectively, of the soil. In buildings, if we assume that the vertical segment between the two floor slabs is fairly uniform (in terms of its mass and stiffness), we can approximate the shear-wave velocity $\upsilon_b$ in that story as $\upsilon_b = \sqrt{Sh/\gamma}$ [15], where $S$, $h$, and $\gamma$ are the shear stiffness, height, and the mass per unit length of the story, respectively. $\gamma$ represents the mass per unit length of the vertical segment between the floors but does not include any of the concentrated floor masses at the top or the bottom of the story. If a vertical segment between the floors is not uniform (e.g., a large window opening, a sharp stiffness change at mid-story, etc.), we can always divide it into smaller vertical segments until each segment is approximately uniform. In other words, we represent such stories with more than one layer.

More precise methods of estimating shear-wave velocities in reinforced concrete frame buildings can be found in Trifunac and Todorovska [109].

## 7.5.3 Wave reflection and transmission coefficients

When the upgoing and downgoing waves cross from one layer to another, their amplitudes and phases are altered because of the reflections at the layer interface. These alterations are characterized by the reflection and transmission coefficients and are different for upgoing and downgoing waves. If the interface has no concentrated mass, such as the bedrock-soil or soil-soil interfaces, the coefficients are constants. When the interface has a concentrated mass, such as the foundation or the building floors, the coefficients become functions of frequency.

To derive the equations for the reflection and transmission coefficients, we subject the layer interface to an incident plane wave of a specified frequency and calculate its reflected and transmitted components by using the conditions that the displacements above and below the interface are equal and the shear forces are in equilibrium. The inertia forces acting on the concentrated masses of the foundation and the building floors should be included in the shear equilibrium equations for those interfaces. More detail of these calculations can be found in [15]. The coefficients for all interfaces can be summarized by the following equations:

$$R_{u,j} = \frac{I_j - I_{j+1} - i.2\pi\, f.m_j}{I_j + I_{j+1} + i.2\pi\, f.m_j}, \quad T_{u,j} = 1 + R_{u,j} \tag{7.11 }$$

$$R_{d,j} = \frac{I_{j+1} - I_j - i.2\pi\, f.m_j}{I_j + I_{j+1} + i.2\pi\, f.m_j}, \quad T_{d,j} = 1 + R_{d,j} \tag{7.12 }$$

where $I_j$ = impedance of layer *j;* and $m_j$ denotes the concentrated mass at interface *j.* For soil layers, $I_j = \rho_j \upsilon_j$, where $\rho_j$ and $\upsilon_j$ are the mass density and the shear-wave velocity in the layer, respectively; and $m_j \equiv 0$. For building layers, $I_j = \gamma_j \upsilon_j$, with $\gamma_j$ and $\upsilon_j$ denoting the mass per unit length and the wave velocity, respectively, in layer *j.* At the soil-foundation interface [interface *m* in Fig. (7.1)], we take $I_m = \rho_m\, \upsilon_m\, A_{fn}$, where $A_{fn}$ is the contact area of the foundation. Note for the bedrock-soil and soil-soil interfaces that since $m_j \equiv 0$ the reflection and transmission coefficients are constants. For the foundation and the building floors the coefficients are frequency dependent because $m_j \neq 0$.

The amplitude and the phase of the reflection coefficients for upgoing and downgoing waves at the soil-foundation interface for typical bounds of $a = I_{m+1} / I_m$ and $b = m_f / I_m$ are calculated. For small *a* and *b* values (i.e., small first-story stiffness, small foundation mass, large contact area, or hard soil) the amplitude and the phase of the reflection coefficient for the upgoing waves approach one and zero, presence of the building does not influence the motions at the top of the soil layer, and they are practically equal to those at a free field. For large a values, the reflection coefficient becomes much less than one at low frequencies and, depending on the value of *b,* gradually approaches one as the frequency increases. In other words, the low frequency components are transmitted to the building, while most of the high-frequency components are blocked.

For the amplitude and the phase of the reflection coefficients in a building floor for typical bounds of $a = I_{j+1} / I_j$ and $b = m_j / I_j$, the concentrated floor masses have the effect of a low-pass filter on the upgoing and downgoing waves crossing the interface.

The reflection and transmission coefficients derived above are for shear waves, because we assumed that the building deforms mainly in shear. If the bending deformations are significant, we have to use the reflection and transmission coefficients calculated for flexural waves. Flexural waves include four terms, two complex-valued propagating terms (same as the shear waves) plus two real-valued ringing terms. Four coefficients require four equations to determine the reflection and transmission coefficients. The equations are obtained by writing the equality of the displacements and rotations and the equilibrium of the shear forces and the bending moments at the interface.

## 7.5.4 Damping

Damping gives a measure of energy loss per cycle and is present in all oscillatory systems. For soils the energy loss due to damping can be represented by the following simple attenuation equation [3]:

$$A_s(f) = e^{-\pi\tau f/Q} \qquad (7.13\ )$$

where $A_S(f)$ represents the reduction in the amplitude of a sinusoidal wave of frequency $f$ when it travels a distance of travel time $\tau$. The damping is defined by $Q$, known as the quality factor. l/$Q$ gives the measure of energy loss per cycle and can be assumed to be independent of frequency for many cases. The logarithmic decrement (i.e., the natural logarithm of the ratio of amplitudes of two successive maxima) for the solid friction model is $\pi / Q$. By comparing this with the logarithmic decrement of free vibrations under viscous damping, we can show that $\xi = 1/ 2Q$, where $\xi$ is the viscous damping ratio. The exponent of the attenuation function for viscous damping is proportional to $f^2$, whereas for solid friction it is proportional to $f$, as seen in eq.(7.13). In this paper, the damping in each soil layer will be defined by its $Q$ value.

For buildings, the damping has generally been assumed to be of viscous type and proportional to the mass or the stiffness of the building. The assumption of proportionality is mainly for mathematical convenience so that we can have real-valued frequencies and mode shapes when using modal analysis. In the wave-propagation formulation, these assumptions are not needed because we can specify the damping independently for each story. Experiments show that for cyclically stressed materials, the energy loss per cycle is independent of frequency and proportional to the square of vibration amplitude [15]. This type of damping is called the structural damping and is represented by the structural damping factor $\lambda$. The attenuation function for structural damping is identical to that for solid friction; except for notation, we use A instead of 1/$Q$ in the exponent of eq.(7.13). It can be shown by comparing the resonance amplitudes of an oscillator under harmonic loads that at the resonance frequency the structural damping factor is equal to twice the viscous damping factor. It should be remembered, however, that for viscous damping the energy loss per cycle depends on the frequency, whereas for structural damping it is independent of frequency.

The simplest way to incorporate damping in the equations is to make shear stiffnesses of the layers complex quantities. For soil layers, we can approximate the damping by multiplying the wave velocities with $(1 - 0.5\, i /Q)$. For building layers, we make the stiffness complex by multiplying the original stiffness with $(1 + i.\, \lambda\, )$ in each layer. Complex stiffnesses result in complex wave velocities.

## 7.5.5 Solution of wave propagation equations

As stated earlier, for a given building and bedrock motion, the wave propagation equations [(7.1) - (7.6)] can be solved recursively starting from the bedrock [i.e., with eq.(7.3)] and continuing upward. The initial values of $u(t)$ and $d(t)$ to start the recursion are given by eqs (7.9) and (7.10). If we choose to incorporate the damping in the equations by making the shear stiffnesses complex, the wave velocities and the travel times all become complex resulting in finite-difference equations with complex time shifts. A frequency-domain technique might be more appropriate to solve such equations. The frequency-domain solution methods will be the subject of another paper. In this paper, we will solve the equations by using recursive, discrete-time domain methods, which are simpler and easier to program than the frequency-domain methods.

First, we need to write the damped version of the wave-propagation equations given by eqs. (7.1) - (7.6). To incorporate damping, we multiply the upgoing and downgoing waves in each layer with the corresponding attenuation function for damping in the layer. When this is done, the equations for layer *j* become

$$u_j(t) = A_j(f).[R_{d,j-1}.d_j(t-\tau_j) + T_{u,.j-1}.u_{j-1}(t-\tau_j)] \tag{7.14 }$$

$$d_j(t) = A_j(f).[R_{u,j}.u_j(t-\tau_j) + T_{d,.j}.d_{j+1}(t-\tau_j)] \tag{7.15 }$$

where $A_j(f)$ denotes the attenuation function for layer *j*. Although these equations are in the discrete-time domain, the reflection and transmission coefficients for the foundation and the building, as well as the attenuation function due to damping, are all frequency dependent. Therefore, to solve the equations recursively in the time domain, we should first convert the frequency-dependent parameters into discrete-time filters.

Because the reflection and transmission coefficients, given by eqs (7.11) and (7.12), include the term $i(2\pi f)$ explicitly, they can easily be converted into discrete-time filters by using the bilinear transformation [1]. To do this we simply replace $i(2\pi f)$ with

$$i(2\pi\, f) = \frac{2}{\Delta}\cdot\frac{1-q^{-1}}{1+q^{-1}} \tag{7.16 }$$

where Δ = sampling interval in seconds; and $q^{-1}$ = backward-shift operator, defined as $q^{-1}\, x(t) = x\,(t-j)$. With the transformation, we can write each reflection and transmission coefficient as a first-order discrete-time filter. For example, $R_{u,j}(q)$, the discrete-time equivalent of $R_{u,j}(f)$, is

$$R_{u,j}(q) = \frac{\beta_{0j} + \beta_{1j} q^{-1}}{1+\alpha_{1j} q^{-1}} \tag{7.17 }$$

where the filter coefficients $\beta_{0j}$, $\beta_{1j}$ and $\alpha_{1j}$ are found to be

$$\alpha_{1j} = \frac{\Delta(I_j + I_{j+1}) - 2m_j}{\Delta(I_j + I_{j+1}) + 2m_j}\;;\quad \beta_{0j} = \frac{\Delta(I_j - I_{j+1}) - 2m_j}{\Delta(I_j + I_{j+1}) + 2m_j}\;;\quad \beta_{1j} = \frac{\Delta(I_j - I_{j+1}) + 2m_j}{\Delta(I_j + I_{j+1}) + 2m_j} \tag{7.18 }$$

Similar conversions can be made for $R_d(f)$, $T_u(f)$, and $T_d(f)$.

The attenuation function for damping [eq.(7.13)] does not have the term $i(2\pi f)$ explicitly. However, it has the form of a low pass filter and can be matched by a simple discrete-time filter of the following form :

$$A(q) = \frac{1-\alpha}{2}\cdot\frac{1+q^{-1}}{1-\alpha\, q^{-1}} \tag{7.19 }$$

where

$$\alpha = \frac{1-\sqrt{1-\cos^2\theta}}{\cos\theta} \quad \text{with } \theta = \ln(2)\frac{Q\Delta}{\tau} \tag{7.20}$$

The parameter $Q$ in eq.(7.20*)* should be replaced with 1/ λ if the layer belongs to the building. By incorporating eqs (7.17, 7.18) and eqs (7.19, 7.20) in eqs (7.14, 7.15), we obtain the discrete-time forms of the wave-propagation equations as follows:

$$u_j(t) = \sum_{k=1}^{2} A_{1k} u_j(t-k) + \sum_{l=0}^{2} A_{2l} d_j(t-\tau_j - l) + \sum_{s=0}^{2} A_{3s} u_{j-1}(t-\tau_j - s) \tag{7.21 }$$

$$d_j(t) = \sum_{k=1}^{2} B_{1k} d_j(t-k) + \sum_{l=0}^{2} B_{2l} u_j(t-\tau_j - l) + \sum_{s=0}^{2} B_{3s} d_{j+1}(t-\tau_j - s) \tag{7.22 }$$

The coefficients $A_{1k}$,…, $B_{3s}$ can all be calculated in terms of the coefficients of the filters given by eqs (7.17, 7.18) and eqs (7.19, 7.20). Similar discrete forms can be written for the first and the top layers.
There are several software packages with routines to convert frequency domain filters into discrete-time filters [e.g., the m-file `invfreqz.m` in MATLAB's Signal Processing Toolbox]. The utilization of such routines greatly simplifies the calculations.

## 7.6 Conclusions

In the preceding chapter, we have described and validated the spectral element method to solve the elastic wave propagation problem on some classical models having an analytical solution that may be used as reference solution. In this chapter, we showed also, that the method may be applied to many real 2D cases (of which some are considered difficult to study). In particular we showed that the method may also be used for the study of wave propagation along an elastic interface, and the modeling of Stoneley wave propagation, and allowed also to take into account a non-plane surface topography, even having a discontinuity. Moreover, we were able to study some 2D site effects, for which we found the expected effects described in the literature. It seems now natural to try to extend this reasoning to the coupled soil structure interaction problems, which we will try to make in the next chapter.

Chapter 8

# 8. Parametric study

## 8.1 Introduction

In the following, a parametric study is performed in order to investigate SSI effects for the case of a structure subjected to an incident wave field.

In practice, a general assessment of the wave propagation induced vibration is based on simple rules, expressing the decay of vibrations from the free field to the basement, as well as the attenuation of the vibration energy as it propagates through the structure and the amplification due to resonance of floors or other structural members. The dynamic soil characteristics as well as the structural parameters such as the foundation type and the used materials are expected to importantly affect the wave propagation in the soil and the vibration levels in the free field and the structure. In the case of particular, sensitive structures such as a micro-electronics lab, a concert hall, a hospital, etc., a detailed study of the dynamic SSI problem using a FE model of the structure is also advised. For such projects, it is customary to perform free field vibration measurements on the future building site, especially if the latter is located in the vicinity of busy roads or tracks.

Detailed studies are not always possible, especially not in small-scale projects, and the simple design rules are unreliable, a first calculation using a simplified numerical prediction model where no dynamic SSI is accounted for would be very useful. Therefore, a parametric study on the effect of dynamic SSI is performed in this chapter. A simple structure representing an ordinary type buiding is studied.

Because all parameters can be changed, the structure is referred to as a parametric building in the following. The response of this structure is computed for the passage of a wave field on a halfspace. As the effects of structural parameters are important, the results of three cases where the structure is founded on a slab foundation, a strip foundation and a box foundation are compared, accounting for or neglecting the effects of dynamic SSI.

If SSI is neglected, the motion of the foundation is derived from the incident wave field assuming a rigid or a flexible kinematic behaviour of the foundation. In addition, the parametric study also investigates the influence of the stiffness of the soil. The acquired knowledge within the frame of this parametric study will provide guidance and technical basis for the development of national or international vibration norms and guidelines as well as for the evaluation of the efficiency of vibration isolation measures.

## 8.2 Problem outline

### 8.2.1 Introduction

The response of a parametric building due to the passage of a wave front field on a halfspace is considered. Figure 8.1 shows the plan view of the foundation and the soil-structure system. Three cases are compared, where the building is founded on a slab foundation, a strip foundation and a box foundation. The different foundation types and the layout of the structure are given in figure 8.2.

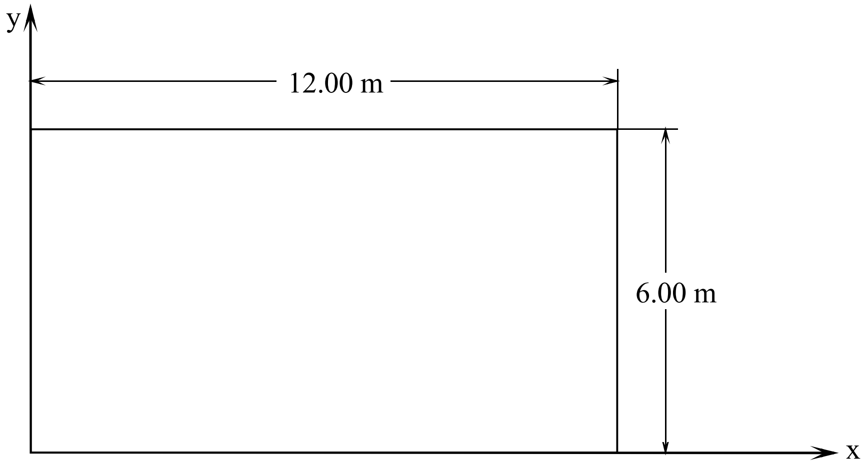

Fig. 8.1: Plan view of the soil-structure system.

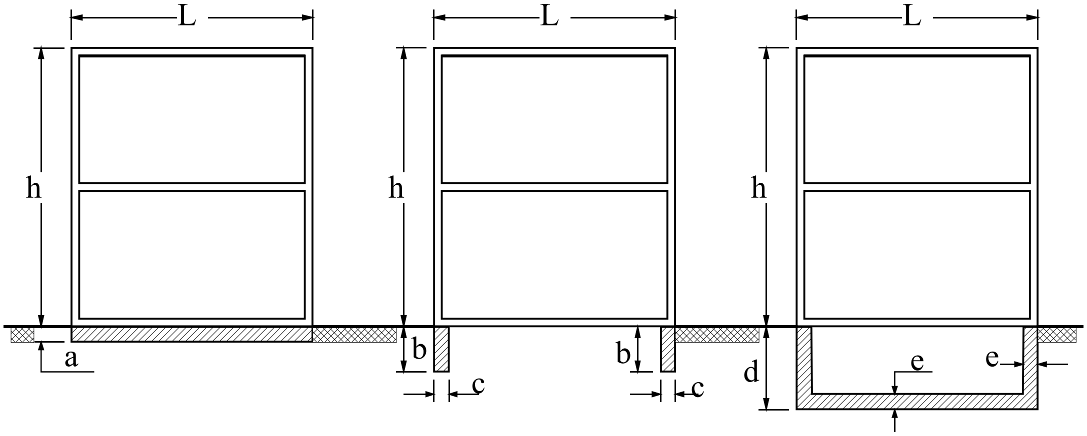

a. Slab foundation. b. Strip foundation. c. Box foundation.

Fig. 8.2: Geometry of the (a) slab, (b) strip and (c) box foundation.

The analysis of the parametric building is based on the Craig-Bampton substructure technique, developed earlier. As mentioned before, this method is advantageous due to the possibility of decoupling the foundation from the superstructure. If changes are made in the structural properties a new BE analysis is not required. Only a new FE analysis in order to obtain the modes $\underline{\Psi}_a$ of the superstructure and a new assembly and solution of the problem are required. The computation of the new dynamic stiffness matrix $\mathbf{K}_s$ of the soil and the load vector $f_f$ on the interface $\sum$ due to the incident wave field using a BEM are time-consuming. Therefore, the method used in the parametric study is preferable to the one used in the validation where modes of the total structure are introduced in the modal decomposition. In spite of all that, a new BE analysis has to be performed in some cases like changes in the length $L_x$ or the width $L_y$ of the structure or in the material characteristics of the foundation.

## 8.2.2 The source model

The aim of this parametric study is to investigate the dynamic soil structure interaction (DSSI) effect and the influence of the foundation type on the structural response. Therefore, the parametric study has intentionally been limited to the passage of a wave field with known characteristics at a single frequency on a halfspace fixed at its base. Figure 8.3 shows the halfspace sine-shaped ramp with a length l = 1:2m. The foundation has a width of 2B = 4 m. The properties of the foundation section, are as given in table 8.1. The foundation is supported by a homogeneous halfspace with a shear wave velocity $C_s$ = 200 m/s, a density $\rho$ = 1800 kg/m$^3$, a Poisson's ratio $\nu$ = 1/3 and a material damping ratio $\beta$ = 0.025.

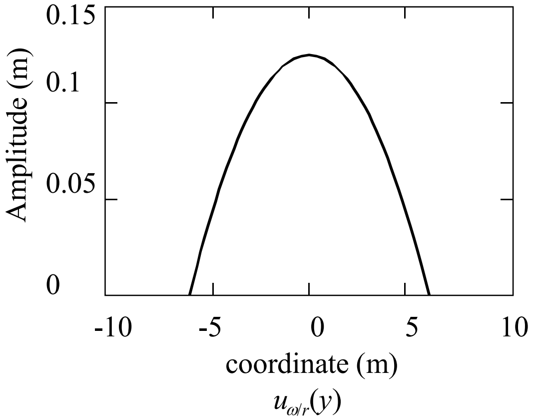

Fig. 8.3: Sine-shaped ramp as a function of the coordinate $y$ along the base of the halfspace.

The resulting free field displacements at the interface between the foundation and the soil are used as an input for the SSI calculation. Figure 8.4 shows the free field vertical velocity in a receiver point at $x$ = 0m, $y$ = 3m and $z$ = 0m.
The time history shows four peaks corresponding to the wave front over the two ramps. The frequency content of the free field velocity is concentrated below 30 Hz.

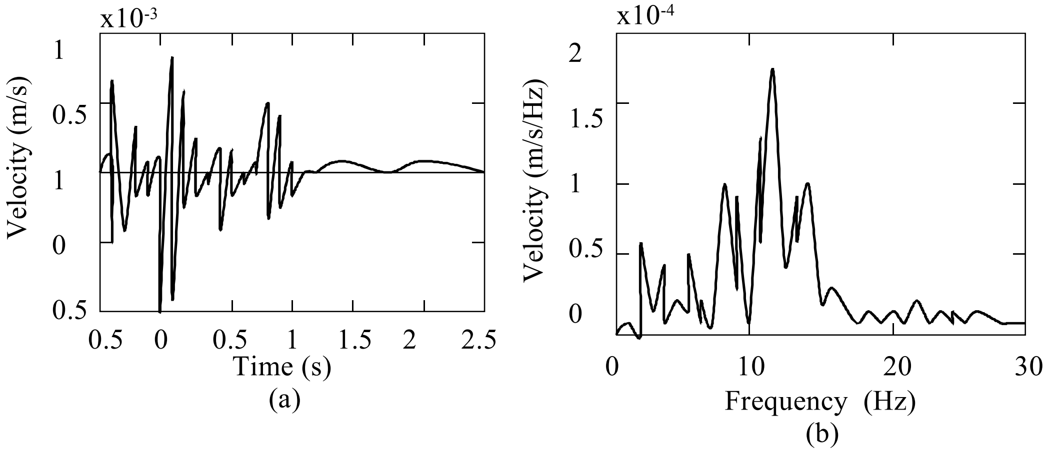

(a)

(b)

Fig. 8.4: (a) Time history and (b) frequency content of the free field vertical velocity in the point at $x$ = 0 m , $y$ = 3m and $z$ = 0m due to a Sine-shaped ramp load applied at the base of the halfspace.

## 8.2.3 The receiver model

### 8.2.3.1 The foundation

As mentioned earlier, three different foundation types are considered for the parametric building. Figure 8.2 shows the geometry of a structure with a concrete slab foundation, an embedded concrete strip foundation and an embedded concrete box foundation. The foundation has a length $L_x$ = 12m and a width $L_y$ = 6m. The thickness of the slab foundation is equal to 0.3 m, while the bottom slab of the embedded box foundation has a thickness of 0.3 m and the thickness of the foundation walls is also equal to 0.3 m. The embedment of the box foundation is equal to 2 m. The width of the strips is equal to 0.3 m and the embedment equals 1 m. The slab and box foundation are modelled using 4-node shell elements with 6 DOF per node (3 translational DOF and 3 rotational DOF). As the slabs and the walls have no stiffness around the normal axis, this rotational degree of freedom is eliminated.

As the building is supposed to be constructed in a row of adjacent houses, it is then assumed that displacements in the global $y$-direction are prevented and only motions in the global $x$- and $z$-direction occur. This assumption does not affect the overall structural behaviour of the building and results only in a reduction of the number of degrees of freedom. The following material properties for concrete are used: a Young's modulus $E = 33300\text{x}10^6$ N/m$^2$, a Poisson's ratio $\nu = 1/3$ and a density $\rho = 2500$ kg/m$^3$. In order to model the strip foundation, the 4-node shell elements are extruded into 8-node brick elements with the same material properties and 2 translational DOF per node as the displacements in the global $y$-direction are prevented. The element size is determined by the minimum wavelength in the soil, which is equal to $\lambda_{\min}$ = 4m corresponding to a shear wave velocity $C_s$ = 200 m/s and the maximum frequency $f_{\max}$ = 30 Hz that is considered in the analysis. Furthermore, in order to represent accurately the minimum wavelength $\lambda_{\min} = \sqrt{2\pi}\sqrt[4]{D/\rho d}\big/\sqrt{f_{\max}}$ in the structure, where $D = Ed^3\big/(12(1-\nu^2))$ is the bending stiffness and $d$ is the slab thickness, a condition is imposed on the element length that is used in the FEM. The minimum wavelength is equal to $\lambda_{\min}$ = 6m for the foundation. A FE model with a rectangular mesh is proposed, where $N_e$ = 12 elements per wavelength are chosen. This results in $n_{ex}$ = 24 and $n_{ey}$ = 12 elements in the $x$- and $y$-direction, respectively. The number of elements in the $z$-direction is chosen equal to $n_{ez}$ = 5 for the embedded box foundation and $n_{ez}$ = 4 for the embedded strip foundation. As the minimum wavelength in the soil is smaller than the minimum wavelength in the building, an accurate BE analysis of the soil requires a finer mesh. However, the same element length of 0.5 m is used on the interface in the horizontal as well as the vertical direction in order to limit the computational effort. The element length of 0.5 m corresponds to $N_e$ = 8 elements per wavelength, which is larger than the advised minimum value $N_e$ = 6 [91].

### 8.2.3.2 The structure

Figure 8.5 represents the parametric building with $n_s$ stories and a story height $H_s$ =3 m. The properties of the model are given in table 7.1. A modal damping ratio $\xi = 0.02$ is used for each mode. Based on the size of the elements of the foundation, $n_{ex}$ = 24 and $n_{ey}$ = 12 elements in the $x$- and $y$-direction are used. The number of elements in the $z$-direction is chosen equal to $n_{ez}$ = 5. This results in a rectangular mesh.

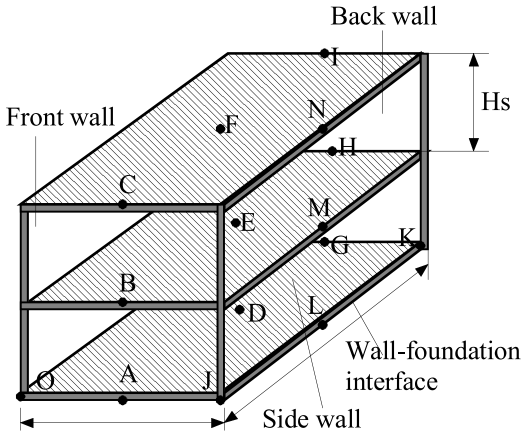

Fig. 8.5: Parametric building with two stories.

The front and the back walls are modelled using 4-node shell elements. The presence of window and door openings generally reduces the stiffness of the walls. Using the principle of conservation of strain energy, the internal brick walls are modelled without openings using shell elements with an equivalent reduced thickness.

**Table 8.1**: The parameters of the building.

| layer type | D (m) | $\upsilon$ | $\rho$ (kg/m$^3$) | E (x10$^6$ N/m$^2$) |
|---|---|---|---|---|
| Front and back massonry walls | 0.20 | 0.15 | 1200 | 10500 |
| Side massonry walls | 0.30 | 0.15 | 1200 | 10500 |
| Reinforced concrete | 0.20 | 0.20 | 2500 | 15000 |

Only the internal brick walls are assumed to contribute to the structural stiffness, whereas the mass of the external walls is accounted for using an equivalent density for the masonry. As expected, the out-of-plane stiffness of the wall is negligible. The degrees of freedom of the front and back walls are determined by the global response of the structure. The structural motion is limited to a displacement in the $x$- and $z$-direction and a rocking motion around the $y$-axis.

In the present study, the inner walls are not modelled. However, the influence of the presence of the inner walls on the behaviour of the structure and especially of the slabs can be large. In fact, a change in span seriously affects the resonance frequency of a slab. Craig [19] provide an analytical expression for the generalised mass and stiffness matrix of a simply supported slab based on sine-shaped displacement modes in two directions:

$$\psi(x,y)=\sin\frac{\pi x}{L_x}\sin\frac{\pi y}{L_y} \tag{8.1}$$

where $L_x$ and $L_y$ denote the span in the $x$- and $y$-direction, respectively. The generalised mass and stiffness matrix are given by:

$$\begin{aligned}
m^* &= \int_0^{L_x}\int_0^{L_y} m(x,y)\psi(x,y)^2\,dxdy \\
k^* &= \int_0^{L_x}\int_0^{L_y}\left\{\left[\frac{\partial^2\psi(x,y)}{\partial x^2}+\frac{\partial^2\psi(x,y)}{\partial y^2}\right]^2\right. \\
&\quad \left. -2(1-\nu)\left[\frac{\partial^2\psi(x,y)}{\partial x^2}\frac{\partial^2\psi(x,y)}{\partial y^2}-\left(\frac{\partial^2\psi(x,y)}{\partial x\partial y}\right)^2\right]\right\}dxdy
\end{aligned} \tag{8.2}$$

where $m(x, y)$ is the mass per unit of surface, $D=Ed^3/(12(1-\nu^2))$ is the bending stiffness, $d$ is the slab thickness and $\nu$ is the Poisson's ratio. The influence of the span on the eigenfrequency $\omega=\sqrt{k^*/m^*}$ can be obtained evaluating equations (8.2), which results into:

$$\omega=\pi^2\sqrt{\frac{D\left(L_x^4+L_y^4+2L_x^2L_y^2\right)}{\overline{m}L_x^4L_y^4}} \tag{8.3}$$

where a constant mass distribution $m$ over the surface is used.

The slabs have the same degrees of freedom as the walls and an additional rocking degree of freedom around the $x$-axis. The degrees of freedom are depicted in figure 8.5 using arrows for the displacements and double arrow-heads for the rocking motion. All floors are simply supported, corresponding to hinged joints at the slab edges.

### 8.2.3.3 Kinematics of the structure

For the three foundation types, the modes of the structure clamped (fixed) at the base and the quasi-static transmission of the foundation modes into the structure is calculated. Figure 8.6 illustrates some of these modeshapes. The first two modes of the structure fixed at the base are local bending modes of the floors at 11.58 Hz and 11.71 Hz. The following modes up to mode 6 are all local bending modes of the floors. Mode 7 at 32.75 Hz is a global deformation of the structure.

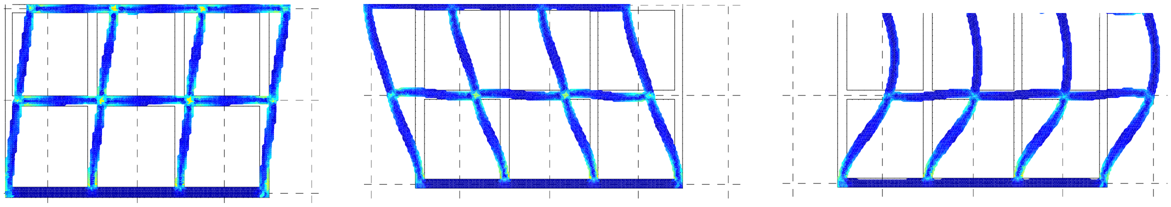

Fig. 8.6: Some snapshots of the modeshapes for the slab foundation type.

For the slab foundation, the first four foundation modes with free boundary conditions on the interface are rigid body modes, followed by bending modes of the foundation at 7.84 Hz and 9.99 Hz. The modes of the structure that incorporate a wall deformation are not likely to occur given the low frequency content of the excitation. Therefore, two situations can be expected. If the building is resting on a soft soil, no deformation of the walls occurs and the global motion of the building is dominated by rigid body kinematics. In the case of a structure resting on a stiff soil, the walls deform in a quasi-static way, following the ground motion. In addition to this, the presence of a (stiff) foundation prohibits the walls to deform.

For the strip and the box foundation, similar conclusions can be drawn concerning the modeshapes and eigenfrequencies (Figures 8.7 and 8.8). The eigenfrequencies of the structure fixed at the base are different, due to the presence of a floor at ground level and the implementation of the connection between the structure and the foundation.

In fact, 4-node shell elements with 4 DOF per node are used to model the box foundation and the superstructure, whereas the strip foundation is modelled using 8-node brick elements with 2 DOF per node. Only the translational DOF can therefore be coupled in the case of a strip foundation. Lysmer's criterion [73], which suggests to employ all modes with an eigenfrequency lower than 1.5 times the highest excitation frequency, can only be applied if the modes of the total structure (superstructure and foundation) are used.

20 modes for the foundation and 20 modes for the building clamped at the base (40 modes in total) are sufficient to have a similar accuracy as in a calculation using 20 modes of the total structure (20 in total). For both alternatives, 20 modes are considered in the SSI calculation for the determination of the soil stiffness. At first, the benefits of the Craig-Bampton substructuring technique seem to be negligible. However, as the computational effort for the SSI calculation is very large, the Craig-Bampton analysis is a good alternative to a modal analysis using the total structural modes as it does not require a new SSI calculation if a property (e.g. the number of stories) is changed.

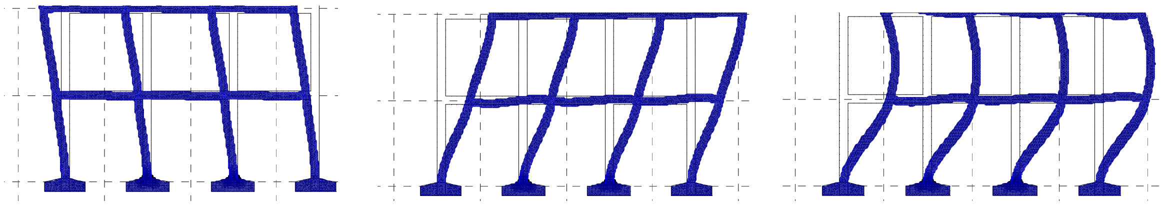

Fig. 8.7: Some snapshots of the modeshapes for the strip foundation type.

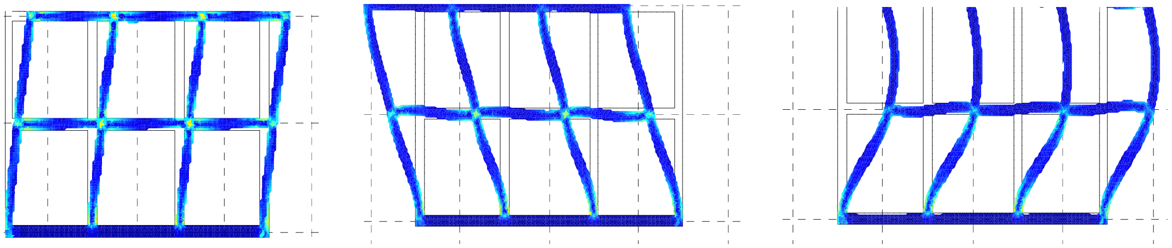

Fig. 8.8: Some snapshots of the modeshapes for the box foundation type.

The eigenfrequencies of the slab foundation are much lower than those of the strip and the box foundation. However, this does not necessarily mean that the slab foundation is flexible. The stiffness of the slab foundation is influenced by the stiffness of the superstructure, which is stiff due to the presence of the side walls, on the interface between the superstructure and the foundation. Furthermore, the behaviour of the foundation largely depends on the stiffness of the soil.

### 8.2.3.4 The impedance matrix of the soil

Embedded foundations may suffer from the fictitious eigenfrequencies depending mainly on the characteristics of the foundation and the soil. In order to check wether the fictitious eigenfrequencies occur in the frequency range of interest, the eigenfrequencies of the excavated part of the soil with Dirichlet conditions on the boundary $\sum$ and free boundary conditions along the free surface $\Gamma_{so}$ are computed for both a box and a strip foundation. A FE model consisting of linear 8-node brick elements, which material properties correspond to the excavated soil, is investigated.
For the box foundation, the first vertical displacement mode **M**1 occurs at the dimensionless frequency $a_0$=5. As the latter is below the maximum dimensionless frequency amax $a_0^{\max}$ = 7.5 corresponding to the frequency of 50 Hz, fictitious eigenfrequencies are likely to occur for the box foundation. A dimensionless coupling constant $\overline{\alpha} = i/a_0^{\max} = 0.13$ is therefore introduced. The hypersingularity in the boundary integral equation is avoided using a finite difference approximation of the mixed boundary integral equation. A dimensionless distance $\overline{h}$ = 1 is used in the present calculations.
In the case of the strip foundation, the first vertical displacement mode **M**1 occurs at the dimensionless frequency $a_0$ = 50.9, which is much larger than for the box foundation. As this frequency exceeds the maximum dimensionless frequency $a_0^{\max}$ = 7.5, problems are not expected.

## 8.3 The importance of SSI for different foundation types

### 8.3.1 The results in different points in the structure

The response of the structure with the three foundation types is calculated by means of the spectral finite element method . Taking fully accounts for SSI effects. In the following, this calculation is denoted as the SSI calculation. As an alternative, the response of the structure is calculated neglecting SSI, which will be referred to as the no-SSI calculation.
The effect of SSI on the amplitude of the structural response is twofold. The peak response, which occurs at the eigenfrequency of the corresponding dynamic system, shifts to lower frequencies due to a decrease in the stiffness of the soil, while the geometrical damping (radiation damping) in the unbounded soil generally causes a decrease in amplitude.
In the no-SSI calculation, the response of the foundation is found using finite element method of the incident wave field on the soil-structure interface. The behaviour of a structure subjected to an incident wave field depends on the difference in stiffness between the structure and the soil. In this procedure, the

number of foundation modes used for this approximation is varied. Besides the calculation of the response using all foundation modes (no-SSI-FF calculation) (FF:Flexible Foundation), the response is estimated using only the rigid body modes of the foundation (no-SSI-RF calculation) (RF:Rigid Foundation).
The first choice results in a good correspondance between the incident wave field and the foundation displacement as would be the case for a relatively rigid soil, while the second results in a rigid body motion of the foundation that is the spatial average of the incident wave field.
The difference in the SSI, the no-SSI-RF and the no-SSI-FF calculation is first investigated using the vertical displacement of the edge between the wall and the foundation for the three foundation types (line JK in Figure 8.5) at succesive points in time.

Figure 8.9 shows the results of the SSI, the no-SSI-FF and the no-SSI-RF calculation for the slab foundation. The incident wave field, which is indicated too in Figure 8.9, is approximated properly by the linear combination of 20 foundation modes with free boundary conditions in the no-SSI-FF calculation. Due to the wall stiffness, no wall deformation modes appear in the frequency range of interest.
Rather than following the soil displacements of the incident wave field, the motion of the wall is dominated by rigid body kinematics. If the building is resting on a soft soil, no deformation of the walls occurs and the global motion of the building is dominated by rigid body kinematics. In the case of a structure resting on a stiff soil, the walls deform in a quasi-static way, following the ground motion. In addition to this, the presence of a (stiff) foundation prohibits the walls to deform.
The no-SSI-FF calculation gives rise to an unphysical deformation of the walls and unsatisfactory results. A no-SSI-RF calculation is a solution to this problem, as the rigid body kinematics of the foundation do not deform the walls. The resulting displacements of the wall-foundation edge better approximate the displacements of a SSI calculation than the no-SSI calculation using all foundation modes. A no-SSI-FF calculation results in a foundation displacement that is close to the incident wave field.
Figure 8.10 shows the results of the SSI, the no-SSI-FF and the no-SSI-RF calculation for the strip foundation. The incident wave field is approximated properly by the linear combination of 20 foundation modes with free boundary conditions in the no-SSI-FF calculation.
Figure 8.11 for the box foundation shows that this number of foundation modes is insufficient to approximate the incident wave field at the edge by means of the least squares approximation, because the box foundation mode shapes are dominated by bending modes of the bottom slab. Especially for the box foundation, the SSI calculation results in a linear vertical displacement of the wall-foundation edge.

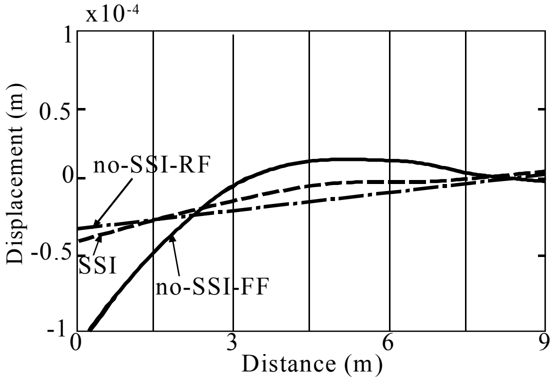

Fig. 8.9 : Vertical displacement of the foundation-structure interface JK at t = -0.35s for the slab foundation.

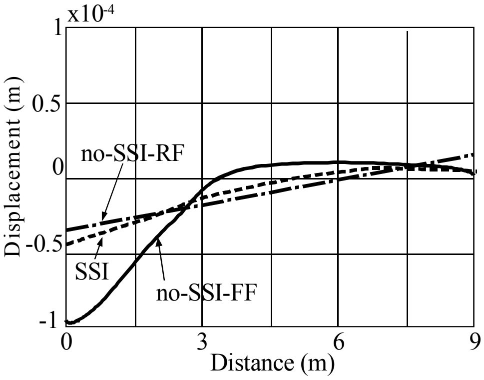

Fig. 8.10 : Verticaldisplacement of the foundation-structure interface JK at t = -0.33 s for the strip foundation.

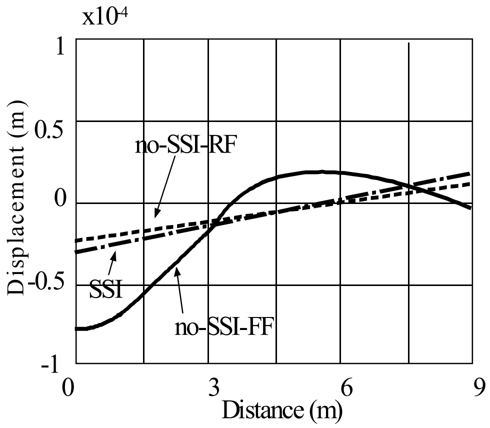

Fig. 8.11: Vertical displacement of the foundation-structure interface JK at t = -0.31s for the box foundation.

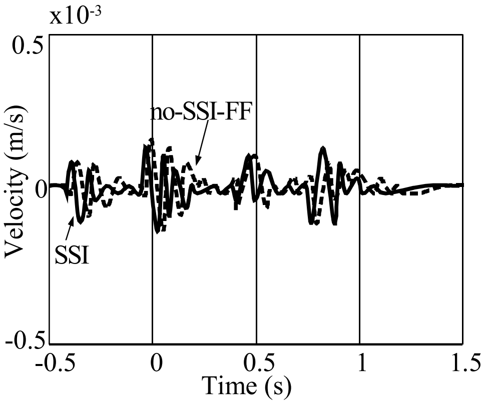

Fig. 8.12 : Time history of the horizontal response in point A (front wall-foundation edge) for the slab foundation.

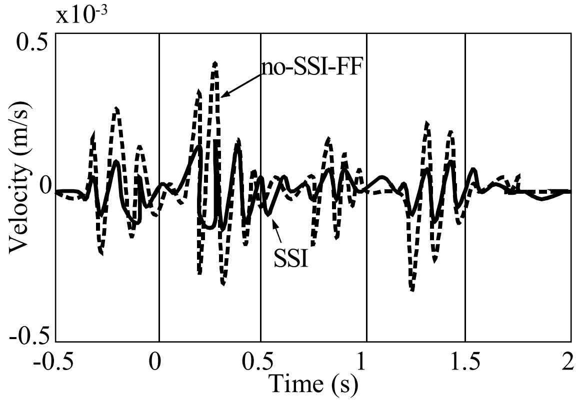

Fig. 8.13 : Time history of the horizontal response in point A (front wall-foundation edge) for the strip foundation.

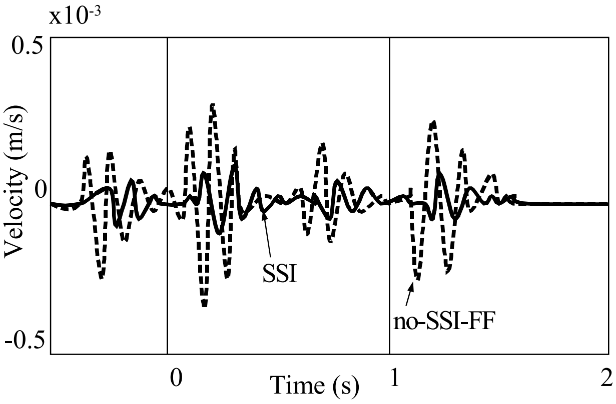

Fig. 8.14: Time history of the horizontal response in point A (front wall-foundation edge) for the box foundation.

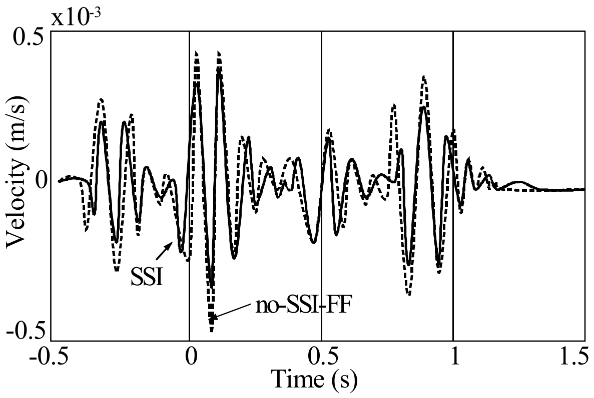

Fig. 8.15 : Time history of the horizontal response in point C, for the slab foundation.

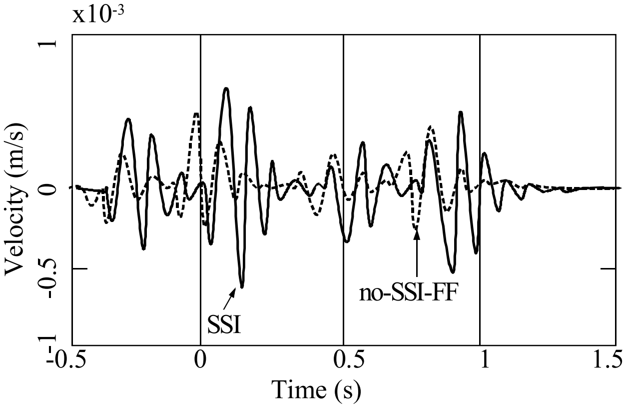

Fig. 8.16 : Time history of thehorizontal response in point C, for the strip foundation.

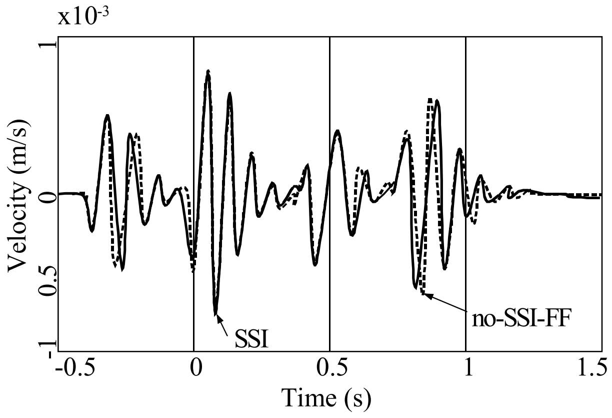

Fig. 8.17 : Time history of the horizontal response in point C, for the box foundation.

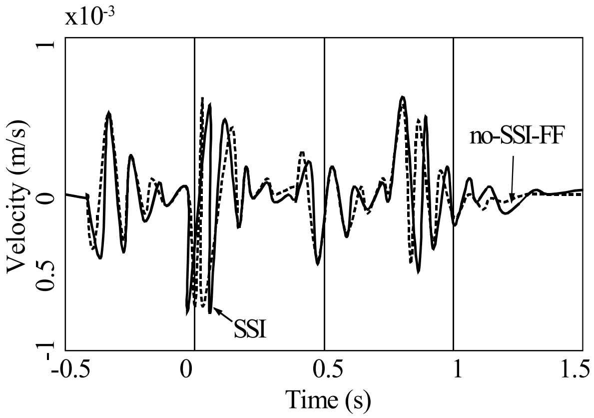

Fig. 8.18 : Time history of the vertical response in point A, for the slab foundation.

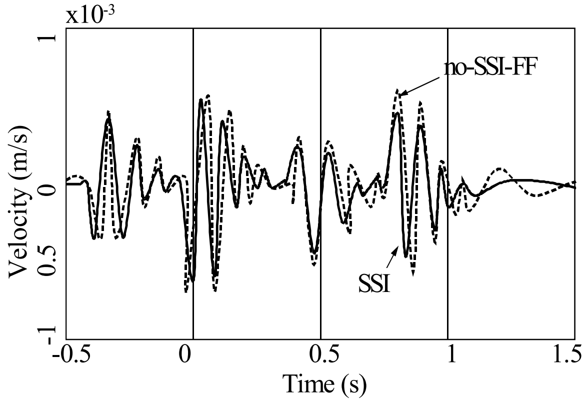

Fig. 8.19 : Time history of the vertical response in point A, for the strip foundation.

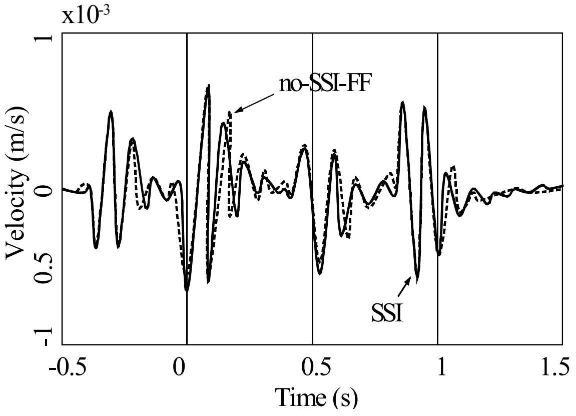

Fig. 8.20 : Time history of the vertical response in point A, for the box foundation.

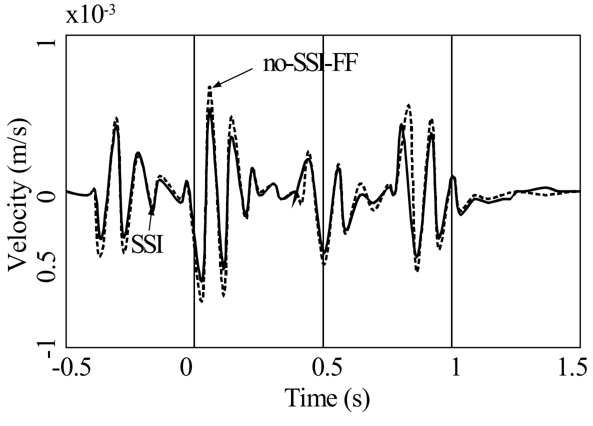

Fig. 8.21 : Time history of the vertical response in point C, for the slab foundation.

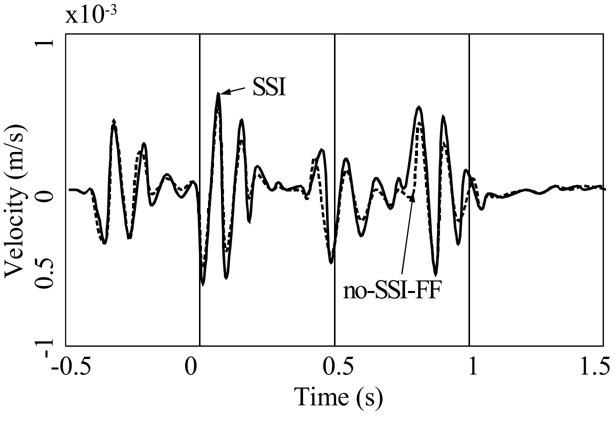

Fig. 8.22: Time history of the vertical response in point C, for the strip foundation.

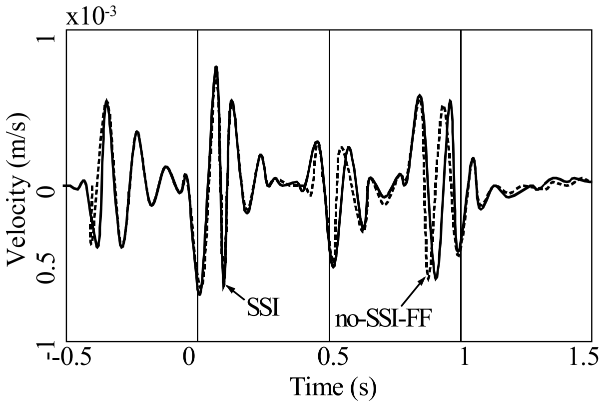

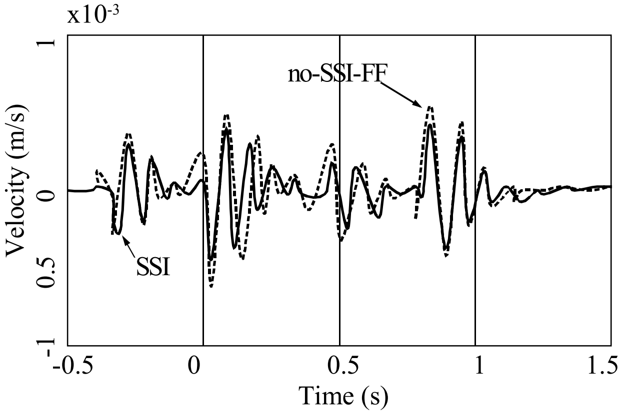

Fig. 8.23 : Time history of the vertical response in point C, for the box foundation.

Fig. 8.24 : Time history of the vertical response in point G, for the slab foundation.

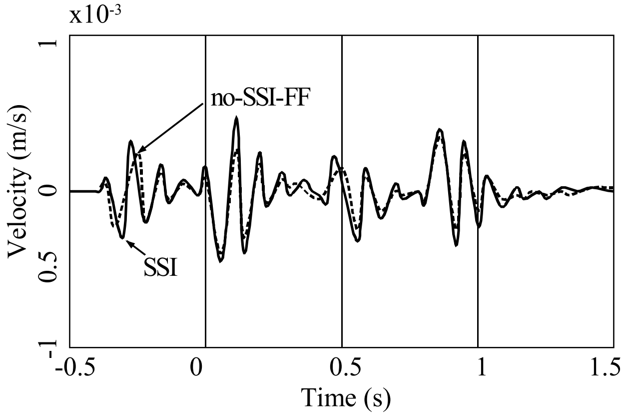

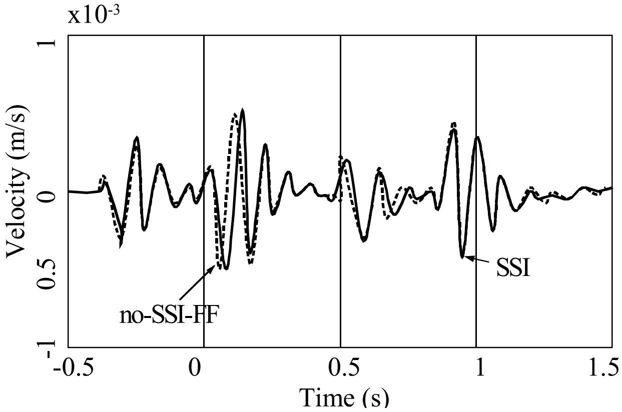

Fig. 8.25 : Time history of the vertical response in point G, for the strip foundation.

Fig. 8.26 : Time history of the vertical response in point G, for the box foundation.

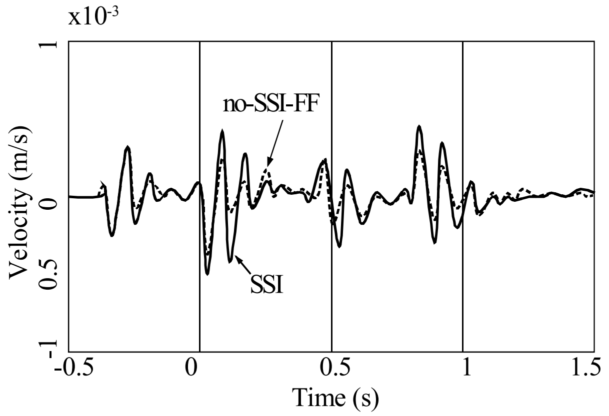

Fig. 8.27 : Time history of the vertical response in point D, for the slab foundation.

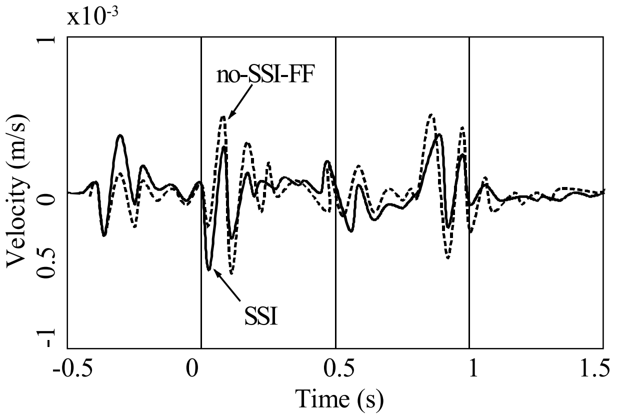

Fig. 8.28 : Time history of the vertical response in point D, for the box foundation.

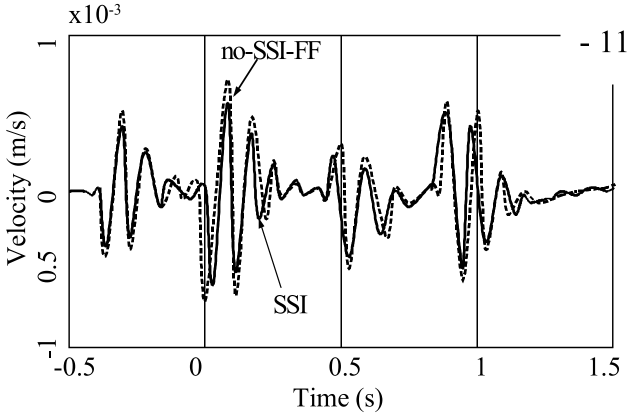

Fig. 8.29 : Time history of the vertical response in point B, for the slab foundation.

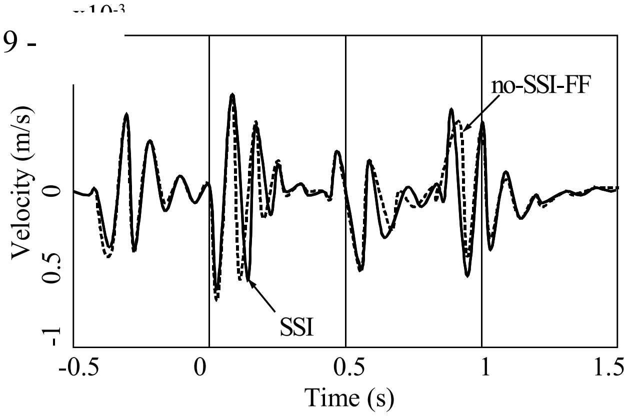

Fig. 8.30 : Time history of the vertical response in point B,for the strip foundation.

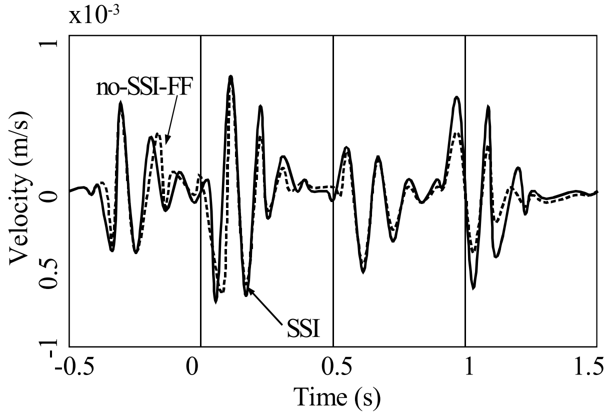

Fig. 8.31 : Time history of the vertical response in point B, for the box foundation.

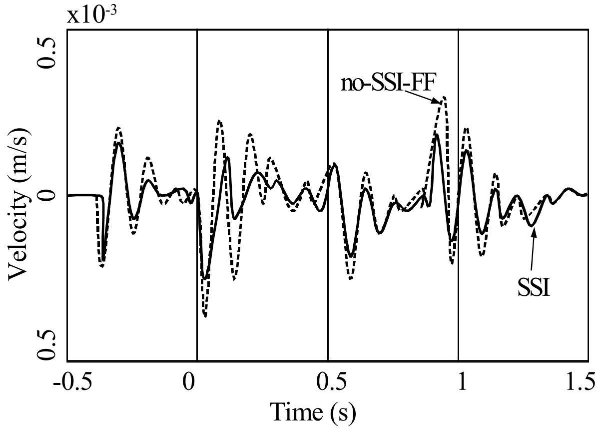

Fig. 8.32 : Time history of the vertical response in point M, for the slab foundation.

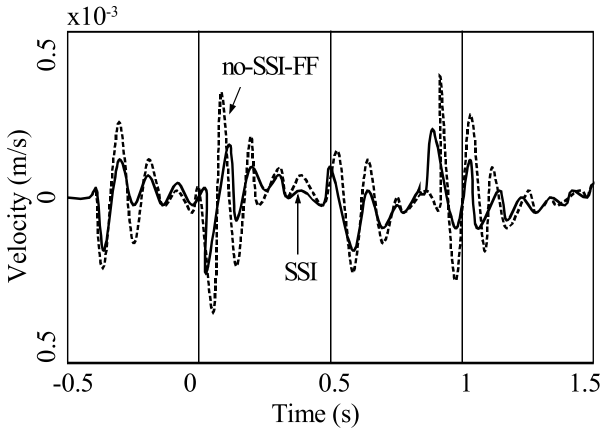

Fig. 8.33 : Time history of the vertical response in point M, for the strip foundation.

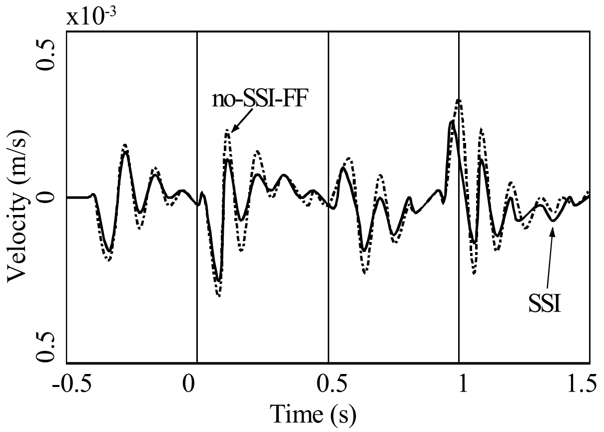

Fig. 8.34 : Time history of the vertical response in point M, for the box foundation.

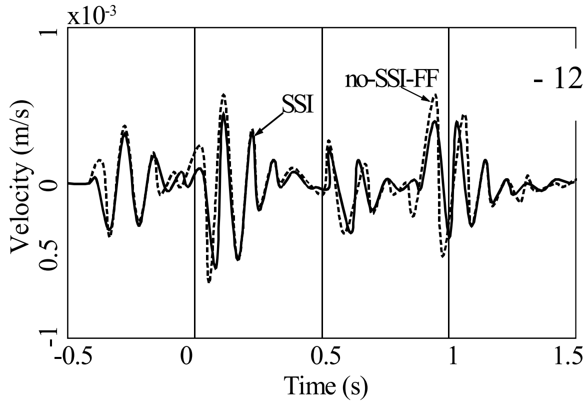

Fig. 8.35 : Time history of the vertical response in point H, for the slab foundation.

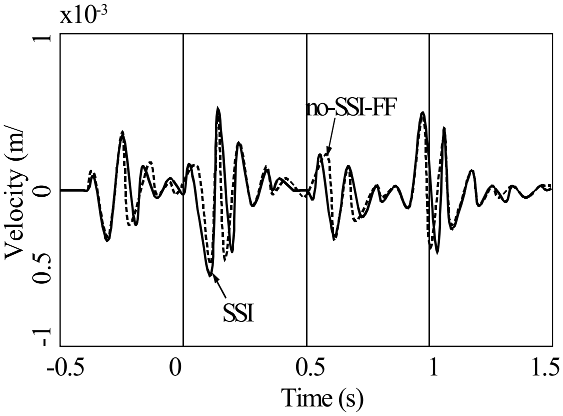

Fig. 8.36 : Time history of the vertical response in point H, for the strip foundation.

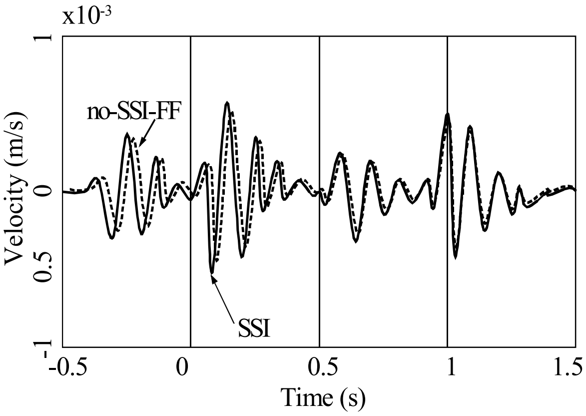

Fig. 8.37 : Time history of the vertical response in point H, for the box foundation.

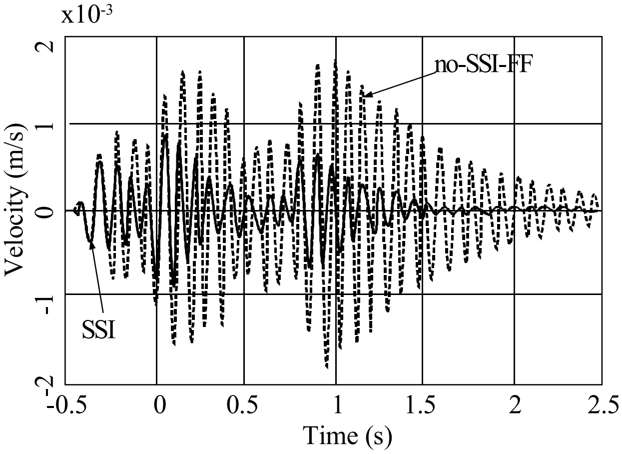

Fig. 8.38 : Time history of the vertical response in point E, for the slab foundation.

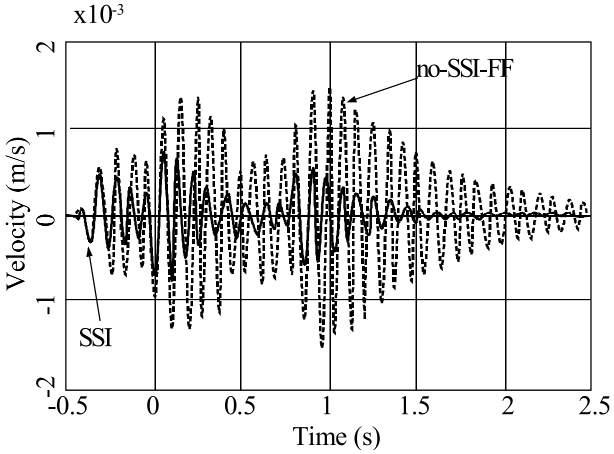

Fig. 8.39 : Time history of the vertical response in point E, for the strip foundation.

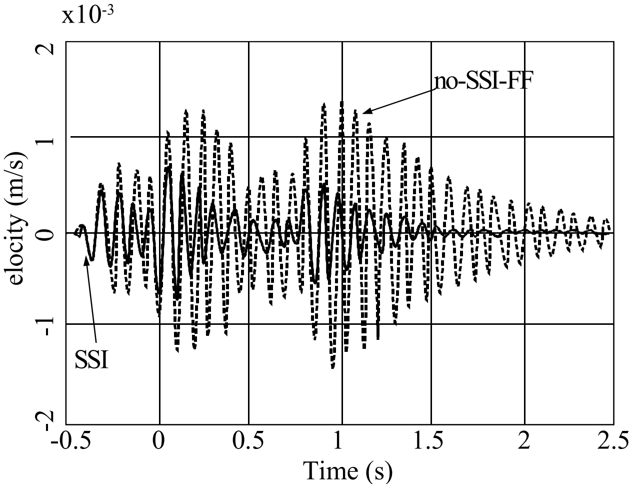

Fig. 8.40 : Time history of the vertical response in point E, for the box foundation

Figures 8.12 up to 8.17 show the time history and the frequency content of the horizontal velocity in the points A and C for the SSI, the no-SSI-FF a RF calculation (Figure 8.5). As expected, the horizontal response in point A is larger for th due to the rocking component that arises for an embedded structure. This effect is less pronounced for the strip foundation as the embedment is small. Bending effects of the structure around the *y*-axis increase to a large extent the response in the horizontal direction in point C in comparison with point A.

Figures 8.18 up to 8.26 show the time history and the frequency content of the vertical velocity in the points A, C and G. The response in the vertical direction is almost the same in the points A and C due to the high structural stiffness in the vertical direction. In point A, the incident wave field is only weakly affected by the presence of the building. The response in point G is more affected by the rigid body motion of the walls, since the wave front is disturbed by the presence of the building as it travels from point A to point G. In the low frequency range, the no-SSI-RF calculation is a good approximation for the response of the building in a calculation using SSI.

Figures 8.27 and 8.28 show the time history and the frequency content of the vertical response for both the slab and the box foundation in point D. Due to the flexibility of the slab foundation with respect to the stiffness of the soil, the response of the centre of the foundation is close to the incident wave field. The assumption of a rigid foundation yields an underestimation of the response of the foundation. The box foundation is more rigid, and follows the global rigid body kinematics of the entire building. Therefore, the effect of SSI is more important in the latter case.

The problem of excessive vibrations is often related to the slab. Figures 8.29 up to 8.37 show the time history and the frequency content of the vertical velocity in the points B, M and H along the boundary of the slab (Figure 8.5). As there is a difference between the results in points located on the edges of the slab, a plate model of this slab, that is excited by a non-uniform input motion along its boundary is required.

Figures 8.38, 8.39 and 8.40 shows the time history and the frequency content of the vertical response in point E positioned in the centre of the first floor. The frequency content is dominated by a peak at 11.58 Hz, corresponding to the first eigenmode (Figures 8.6, 8.7 and 8.8) of the structure clamped at the base. The difference between both SSI and no-SSI calculations is explained as follows. The incident wave field adds an amount of energy to the structure through the soil-structure interface. In a calculation without SSI, the structure can be referred to as a closed system after the incident wave has passed. All energy is dissipated through material damping in the structure.

In contrast to this, the energy can be dissipated through radiation damping in the soil in a SSI calculation. The response on the oors is dominated by the local floor modes, resulting in a resonance of the floors. Due to the presence of radiation damping, the effect of SSI results in an increased attenuation of the floor response (Figures 8.38, 8.39 and 8.40). In contrast to points on the slab, the difference between the SSI and the no-SSI calculation is smaller for the walls.

It is generally assumed that the effect of dynamic SSI increases the more flexible the soil is and the stiffer the structure is. The parametric building has a stiff superstructure, which predominantly acts as a rigid body. The same holds for the strip foundation and especially for the box foundation. A good approximation of the structural behaviour in stiff points is therefore obtained using a no-SSI-RF calculation. However, in points located on the slab foundation (point D) or on the other slabs (points E and F) resonance of the floors is attenuated more rapidly due to radiation damping and a SSI calculation is therefore advisable.

A modal damping ratio $\xi = 0.02$ is used for each mode. The damping ratio that is estimated from the logaritmic decrement of the peak response in point E measured over consecutive cycles (the free vibration decay method), is equal to $\xi = 0.0188$ for the no-SSI-RF, $\xi = 0.0184$ for the no-SSI-FF and $\xi = 0.0325$ for the SSI calculation for a structure with a slab foundation. As expected, the damping ratio increases taking the SSI effect into account. The small deviation of the damping ratio for the no-SSI-RF and the no-SSI-FF calculation is due to reading errors using the plot of the peak amplitudes and a ruler.

# 8.4 Variation of the numbe

In this section, the effect of the number of stories in dynamic SSI problems is illustrated by means of the parametric building with a slab foundation and four stories.

Figure 8.41 shows the modeshapes of the 4-story building. The first eigenfrequency at 11.34 Hz of the structure clamped at the base is near the first eigenfrequency at 11.58 Hz of the building with two stories. Figure 8.42 shows the vertical response in point **C**. The results for the no-SSI-FF calculation are comparable, whereas the results for the SSI calculation show a large difference. The peak amplitude decreases and the frequency content shifts to lower frequencies. This phenomenon can be attributed to the mass. As the mass of the 4-story structure is larger than the mass of the 2-story structure, the effect of SSI is more important. Figure 8.43 shows the horizontal response in point **C**. Besides a shift to the lower frequency range, the peak amplitude seriously increases as bending effects of the structure around the *y*-axis increase to a large extent the response in the horizontal direction in a 4-story building in comparison with a 2-story building. This example clearly demonstrates that the SSI effect is very important for taller structures and cannot be omitted using an easier no-SSI calculation.

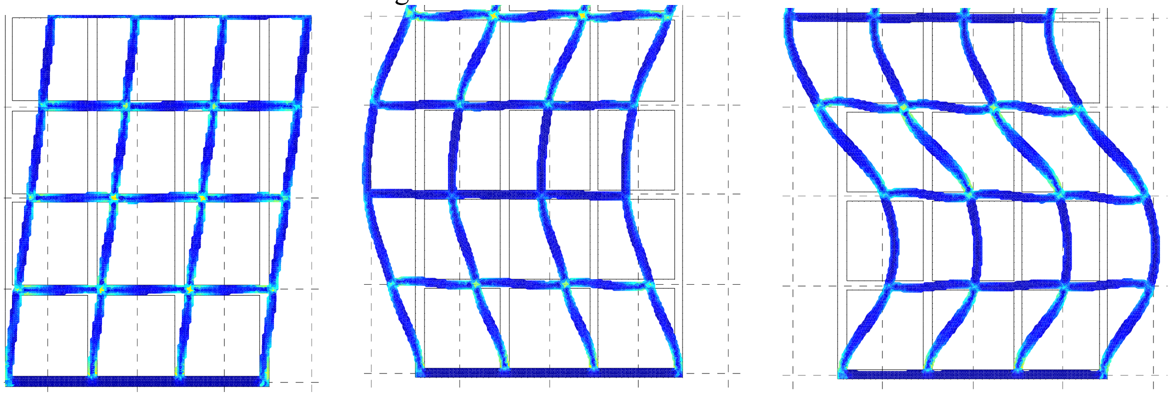

Fig. 8.41: Some snapshots of the modeshapes of the 4-story building for the strip foundation type.

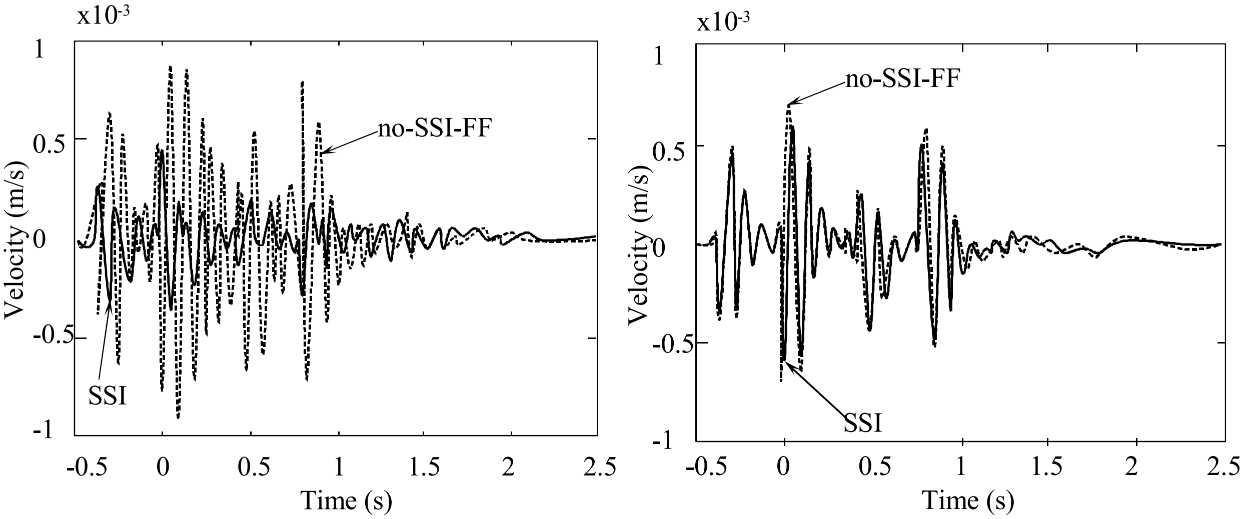

(a) 4 stories structure (b) 2 stories structure

Fig. 8.42 : Time history of the vertical response in point **C** on the front wall-second floor edge.

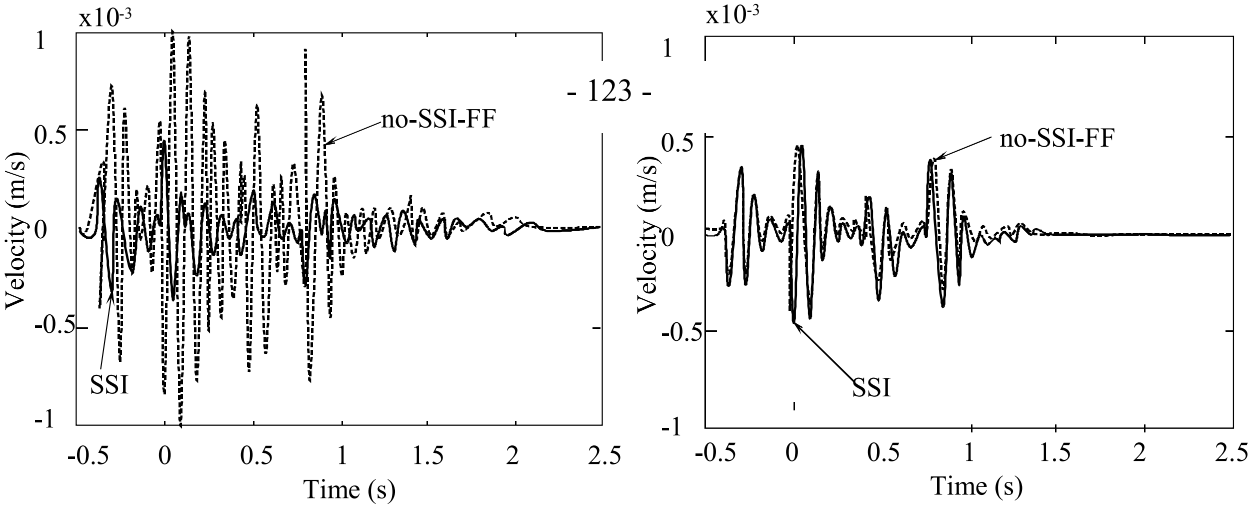

(a) 4 stories structure (b) 2 stories structure

Fig. 8.43 : Time history of the horizontal response in point **C** on the front wall-second floor edge.

## 8.5 Variation of the soil properties

Only qualitative statements on the effect of the stiffness of the soil on the SSI problem are possible at this stage, as the parameters related to the soil have not been varied yet. If the effect of the stiffness of the soil on the response of the structure is investigated, a decrease in stiffness of the soil can reduce or increase the structural response depending on the excitation frequency. In general, the peak response is smaller for a structure founded on a softer soil. However, the incident wave field increases if the stiffness of the soil decreases. Therefore, the effect of the stiffness of the soil on the dynamic SSI problem should be examined thoroughly. The response of the parametric building founded on a softer soil is investigated. A homogeneous halfspace with a shear wave velocity $C_s$ = 100 m/s, a density $\rho$ = 1750 kg/m$^3$, a Poisson's ratio $\nu$ = 1/3 and a material damping ratio $\beta$ = 0.025 in deviatoric and volumetric deformation is considered. This soil will be denoted as a soft soil in the following, whereas the soil with a shear wave velocity.

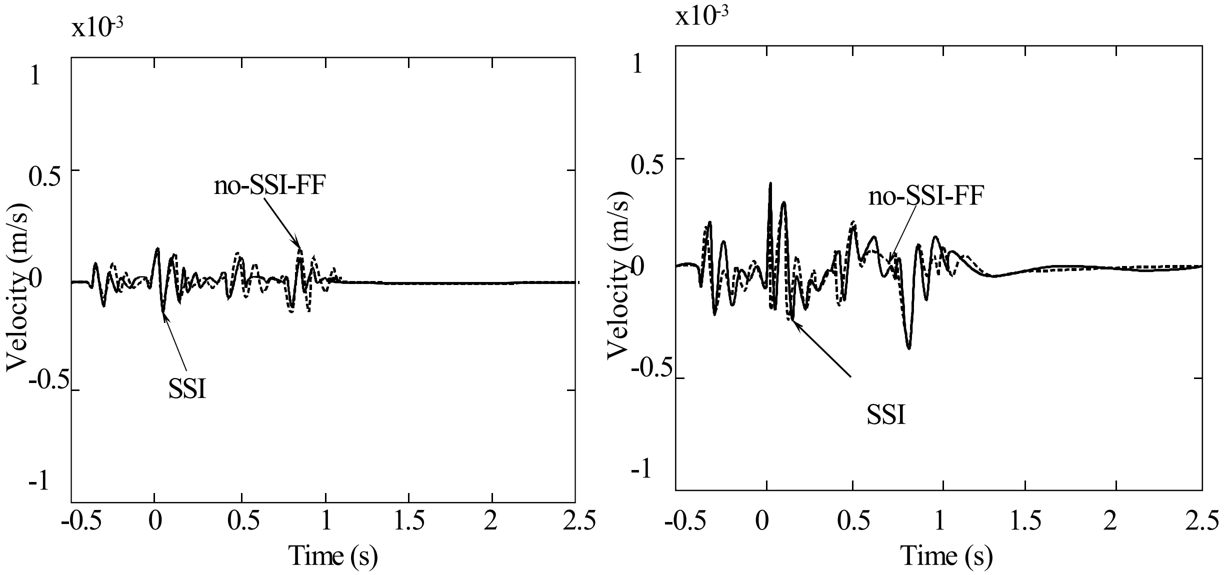

(a). Soft soil.

(b). Stiff soil.

Fig. 8.44 : Time history of the horizontal response in point A on the front wall-foundation edge.

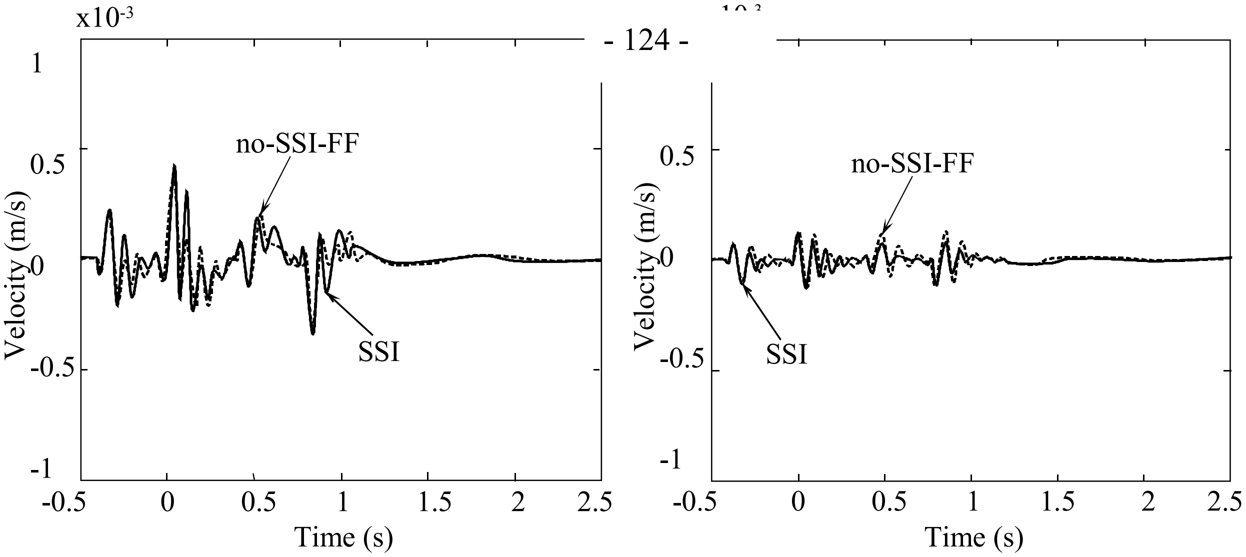

(a). Soft soil.

(b). Stiff soil.

Fig. 8.45 : Time history of the horizontal response in point **C** on the front wall-second floor edge.

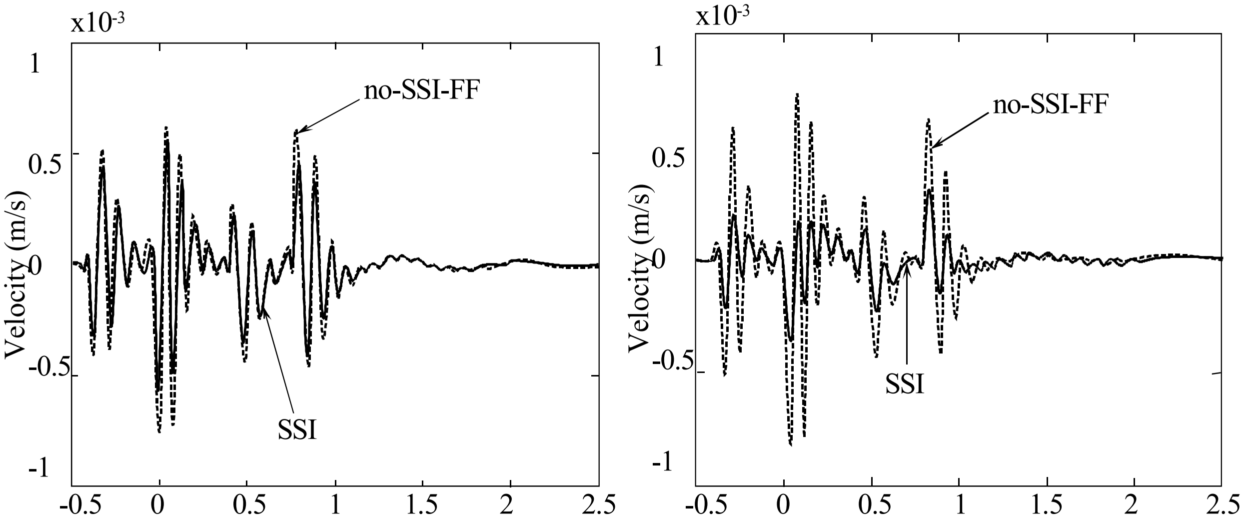

(a). Soft soil. (b). Stiff soil.

Fig.8.46 : Time history of the vertical response in point A on the front wall-foundation edge.

Figures 8.44 and 8.45 show the time history and the frequency content of the horizontal response in the points **A** and **C**. As the vibration level of the incident wave is approximately a factor of four larger for the soft soil, the same phenomenon is observed in the point A in the structure. An increasing horizontal response in the point **C** is observed in figure 8.46 due to the flexibility of the structure and the rocking motion around the *y*-axis. For the softer soil ($C_s$ = 100 m/s) the frequency content in the frequency range below 8 Hz is largely amplified, whereas, beyond the frequency of 8 Hz, only a slight difference in vibration level in comparison with the stiffer soil ($C_s$ = 200 m/s) is visible.

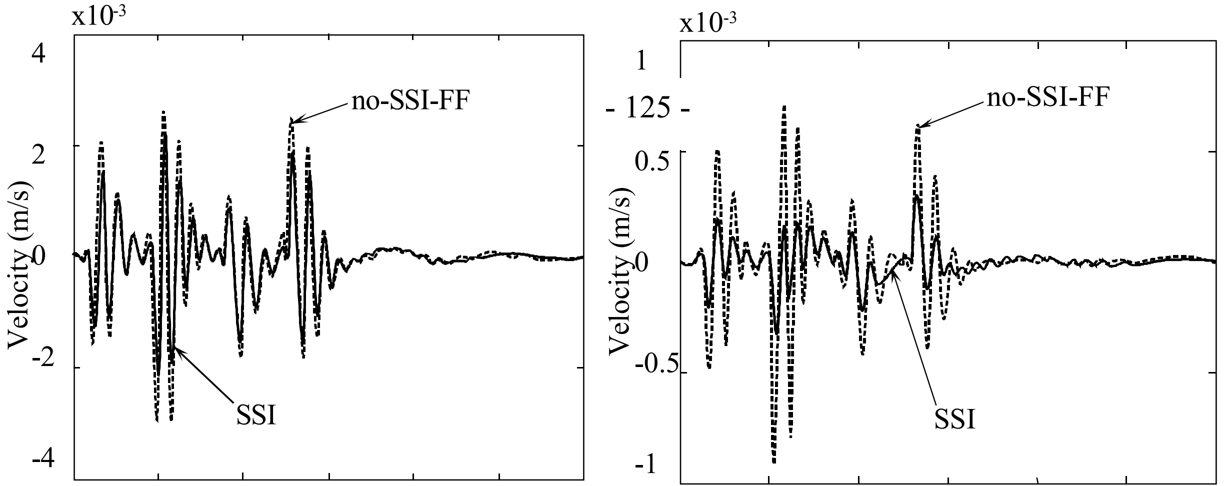

(a). Soft soil. (b). Stiff soil.

Fig. 8.47 : Time history of the vertical response in point D on the centre of the ground floor.

The same trend is observed in Figures 8.46 and 8.47 for the response in the vertical direction in the points **A** and **D**. Note that a different vertical scale is chosen for the vertical response. A decrease in stiffness of the soil shifts the frequency content to lower frequencies. In spite of the increasing peak amplitude related to the higher incident wave field, the amplification factor on the response in the structure is smaller than the amplification factor of four on the free field response due to the flexibility of the soil. Figures 8.44 to 8.47 show large deviations between the SSI and the no-SSI calculations. If the response of heavy structures founded on a soft soil is considered, it is crucial to take the SSI effect into account. Omitting the SSI effect may result in an overestimation of the response and an expensive structural design.

Figure 8.33 shows the time history and frequency content of the vertical response in point F. The peak in the frequency content due to resonance of the slab at a frequency of 10 Hz is amplified. However, the increase in the maximum amplitude of the incident wave field is much larger. Due to the flexibility of the soil, energy in the slab can be radiated more easily than for a structure founded on a stiff soil.

Figure 8.49 shows the time history of the energy in the structure for the SSI calculation. As the incident wave field for a structure founded on a soft soil is larger than for a stiff soil, the energy in the structure is much larger.

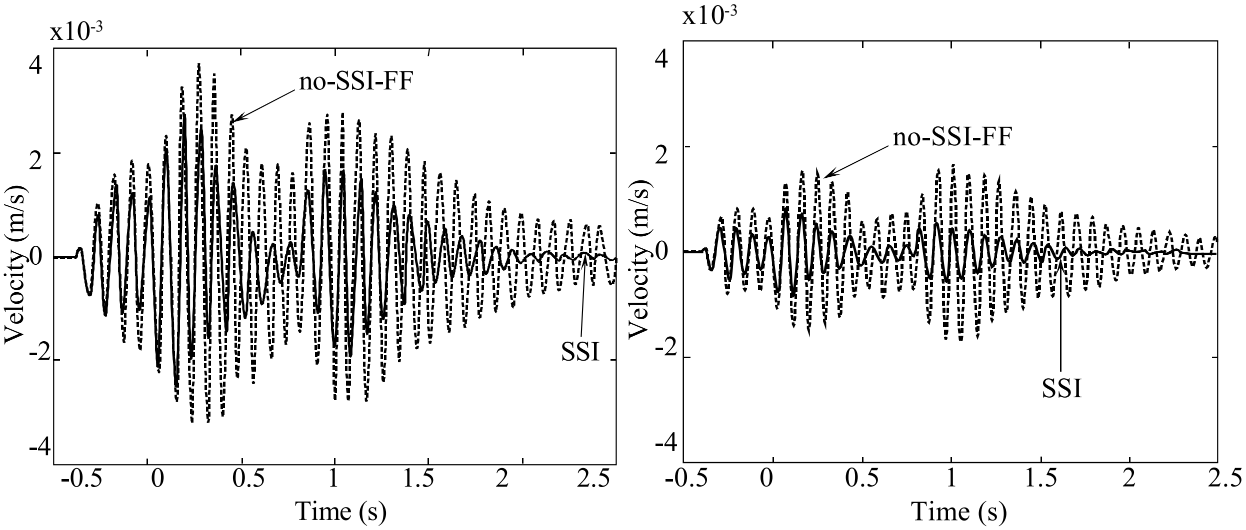

(a). Soft soil.

(b). Stiff soil.

Fig. 8.48 : Time history of the vertical respon the centre of the second floor.

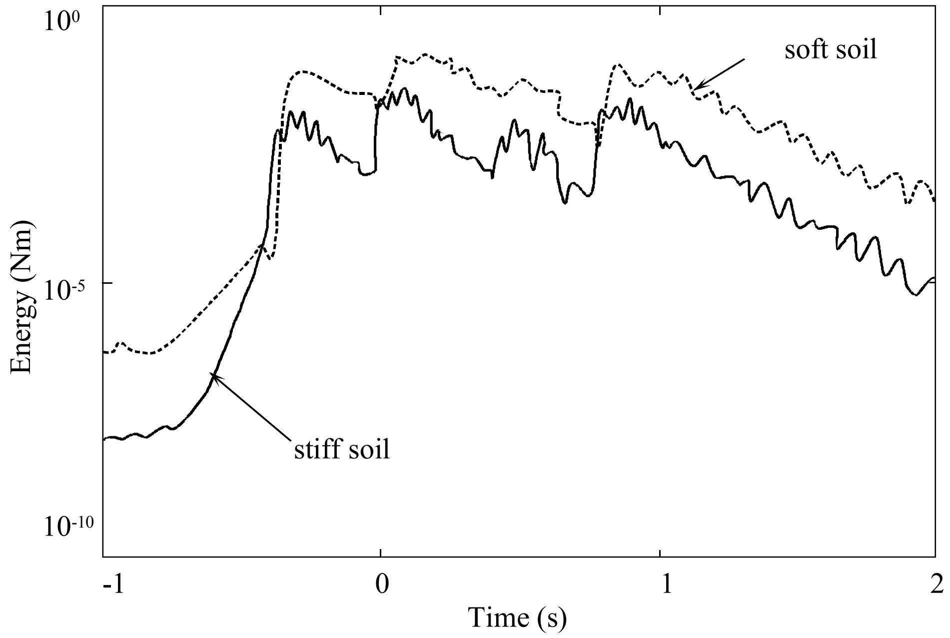

Fig. 8.49 : The time history of the total energy in the structure for the SSI calculation for a stiff soil (solid line) and a soft soil (dashed line).

## 8.6 Spectral finite element analysis of a real 2-D soil structure system

This section is intented to evaluate the effects of soil-structure interaction (SSI) on the modal characteristics and on the dynamic response including stresses of a real structure Figure 8.50. From the above studies, the stress was on the overall behaviour of SSI systems, and it was not possible from a pratical point of vue to study a full 3-D SSI system. In fact a simple 3-D five storey reinforced concrete structure building typically encountered in Algeria including a finite extent of a soil domain limited by a simple viscous type boundary conditions, will have several hundreds of thousands of degrees of freedom. The PC used, an Intel Pentium 4 with a 2.40GHz processor having a 512 Mo memory, becomes very slow and crashes from time to time. That is why, the study was limited to a 2-D SSI sytem, which is the most used method in real life studies in most pratical situations. Unstead of the homogeneous halfspace used in the parametric building of section 8.2.2, a bounded Mohr-Coulomb soil model is used.

The unbounded nature of the soil medium requires special Boundary Conditions (BC) that do not reflect seismic waves into the soil-structure system. Various models of BC exist that enable the energy transmission [72], the most commonly used in the FEM are of the viscous type. The position of the local viscous boundaries should be far away from the structure in order to obtain realistic results. From recent studies it is recommended that the location of the transmitting boundary to be selected far away 8-10 times of the foundation base width [91].

The BC used in this study are based on the method described by Lysmer and Kuhlmeyer [72].

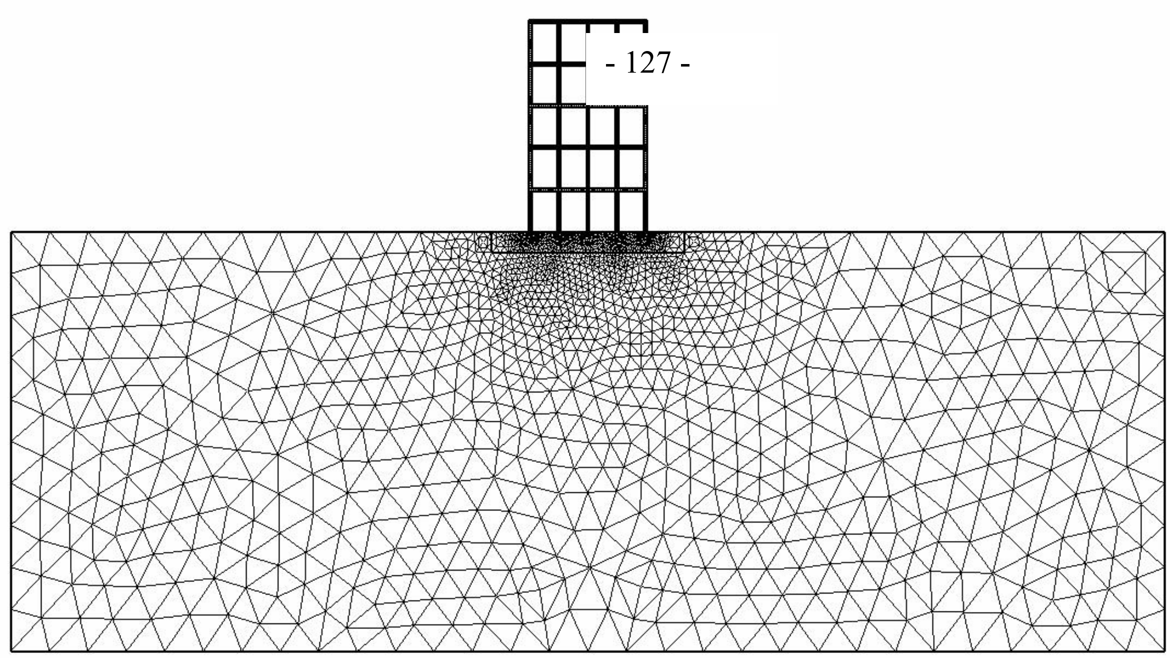

Fig. 8.50 : Finite element discretization of the Soil-Structure System.

### 8.6.1 Characteristics of soil-structure model

In order to investigate the soil-structure-interaction of regular type reinforced concrete (R/C) buildings with isolated footings response due to earthquake ground motion, 48 models of the 5 storey building have been examined. Table 8.2 shows the dynamic properties and the geometry of the 5-storey R/C building model.

**Table 8.2**. Dynamic characteristics and geometry of 5-storey model.

| Structural properties | Shear Wave Velocity Vs (m/s) | Depth of Soil Layer H (m) | | |
|---|---|---|---|---|
| <u>Superstructure</u><br>Exterior Footing=1.5 x 1.5(m); thickness=0.36m<br>Interior Footing=2.1 x 2.1(m); thickness=0.51m<br>Area of cross-section of members = 0.3x0.3m$^2$<br>storey height = 4.08m with a bay of 4.20m.<br>Poisson's ratio = 0.20<br>mass of each storey = 40.21 KN/m<br>mass of roof = 26.38 KN/m<br>critical damping ratio =10%<br>modulus of elasticity= 24821129 KN/ m$^2$<br>mass density=2.40 KN/m$^3$<br><u>Soil</u><br>Poisson's Ratio of soil = 0.20<br>mass density=1.70 KN/m$^3$<br>critical damping ratio =10% | | 30 | 50 | 100 |
| | $V_S$ | Fundamental Period of Vibration $T_1$ (sec) | | |
| | 50 | 2.54055 | 2.74284 | 2.73103 |
| | 400 | 0.81089 | 0.84031 | 0.88972 |
| | 1200 | 0.80314 | 0.81222 | 0.81214 |
| | Fixed Base Condition (i.e., without SSI) | 0.79038 | | |

Since the dynamic response of this soil-structure on the frequency content of the input motion and its variation through the soil layers, the interaction between foundation and it's underneath soil layers has been studied. Three different types of soil layers with different depths 30, 50 and 100m have been considered. In each analytical model different shear wave velocities ranging from 50 to 1200m/s simulating soft to hard soil conditions have been used.

The dynamic characteristics of three types of soil layers will be considered, simulating soft, medium and hard soil conditions (table 8.2.). To study the dynamic response of soil-structure interaction, the 5-storey building model is submitted to El Centro earthquake ground motion.

## 8.6.2 Discussions of results

For the real 5-storey R/C structure mentioned above a comparison of the results is undertaken in order to evaluate the effects of SSI, initially, in terms of fundamental periods (table 8.2). One limits our presentation and analyzes of results for three types of ground only (Vs = 50, 400, 1200m/s) representing soft, medium and hard soil conditions respectively.

As expected, soft soil condition amplify structural response and elongates natural periods, as opposed to hard soil, where for increasing values of shear wave velocities, we approach the fixed base condition (fixed base condition represents a theoretical case of a surface soil having an infinite rigidity). The severity of damages will be amplified when the frequency content of the earthquake input motion will be near the fundamental mode of vibration of the soil – structure system.

When the depth of the soil layer increases and its stiffness decreases, the period of the soil-structure system will increase and in these cases the adjacent soil stiffness plays very important role in decreasing or increasing the base shear for the type of structure considered. One of the aims of this study is the necessity to explicitly consider the occurrence of one or more nonlinearities (geometric and material); i.e., allowing for the structure to slide and uplift at the foundation interface.

It is interesting to compare the behaviour of the building that is not allowed to uplift nor slide with the behaviour of the same building that is allowed to uplift and slide (table 8.3). By allowing the uplifting and the sliding of the foundations the lateral displacement at the top of the structure has not changed significantly (displacement and acceleration time histories are given in figures 8.51 and 8.52 respectively). However, allowing foundation uplifting reduces significantly the base shear (–74,0%) and overturning moments (table 8.4).

In addition of the insight gained from SSI analysis it improves our understanding of the behaviour of real structures. As a result of this understanding, design and construction practices can be modified so that future earthquake damage is minimized. As reported in the literature SSI analysis is seldom performed for ordinary structures. Even, when SSI effects are negligible in terms of loads, they do affect structural stability in terms of large deflection and nonlinear response; this is rarely investigated.

It is possible to investigate such effects, by first creating a model that represents the real structure and then perform a sensitivity analysis as for different support conditions allowing for the structure to uplift and slide.

**Table 8.3**. Summary of Results for Building allowed to Uplift and slide submitted to El Centro Earthquake $\xi$=0.05

| Cases considered | Shear Wave Velocity Vs (m/s) | Max. lateral Displacement at top of Bldg. (cm) | Max. Axial Force (KN) | Max. Base Shear (KN) | Max. Base Moment (KN.m) |
|---|---|---|---|---|---|
| Model A* | Encastré | 11.1 | 575.5 | 440.8 | 108.3 |
| Model B* | 50 | 16.9 | 617.6 | 327.0 | 0.0 |
| | 400 | 9.6 | 575.8 | 114.5 | 106.9 |
| | 1200 | 10.0 | 575.0 | 431.2 | 103.4 |

* Model A: structure fully fixed at base, i.e., w

* Model B: Nonlinear SSI, taking into account possible uplift and slide of foundation.

**Table 8.4 .** Summary of Results for Building allowed to Uplift and slide (in terms of percent difference) submitted to El Centro Earthquake $\xi$=0.05

| Cases considered | Shear Wave Velocity Vs (m/s) | Percent Difference % | | | |
|---|---|---|---|---|---|
| | | Max. lateral Displacement at top of Bldg | Max. Axial Force | Max. Base Shear | Max. Base Moment |
| Model A & | 50 | +43% | +6.8% | -25.8% | -99.9% |
| Model B | 400 | +1% | 0% | -74.0% | -1.2% |
| | 1200 | 0% | 0% | -2.2% | -4.4% |

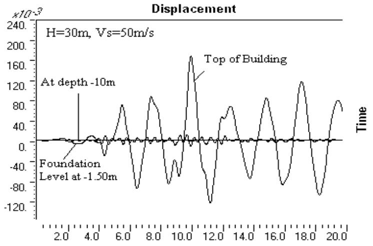

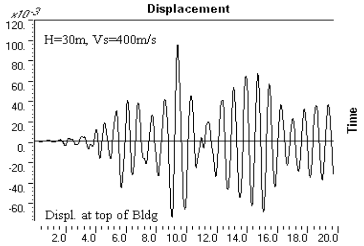

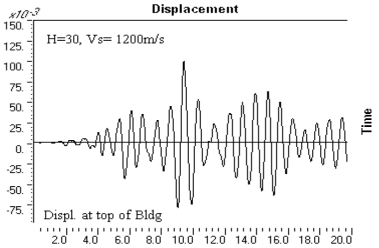

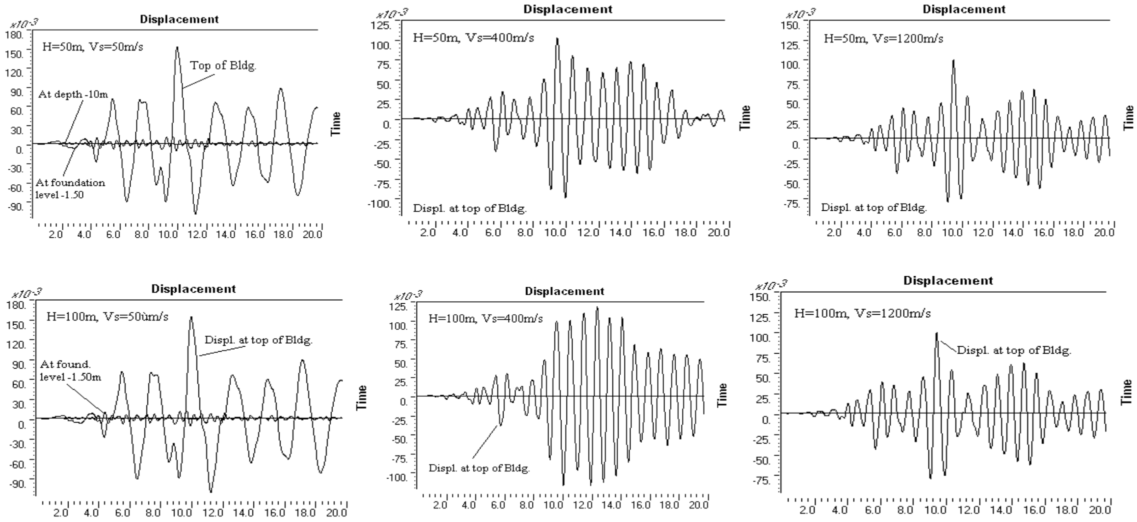

Fig. 8.51 : Displacement time history plots for H=30, 50 and 100m; Vs= 50, 400 and 1200m/s.

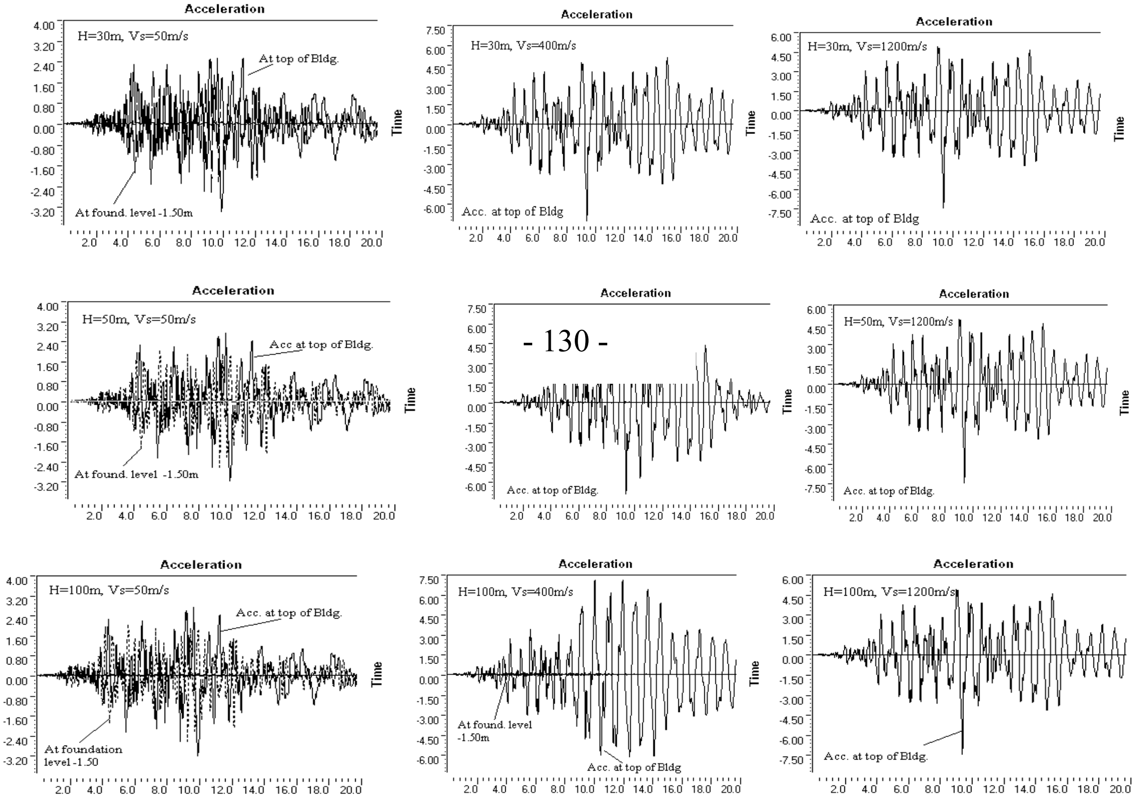

Fig. 8.52 : Acceleration time history plots for H=30, 50 and 100m; Vs= 50, 400 and 1200m/s.

## 8.7 Conclusions

In this chapter, a parametric study on the determining factors for wave induced vibrations in buildings has been performed. The response of a parametric building due to the passage of a wave field has been calculated for a slab, a strip and a box foundation. The second study was for a real 5 storey R/C building. The importance of SSI for the three foundation types as well as the influence of the number of stories in the dynamic SSI problem has been investigated. The stiffness of the soil has also been varied. The conclusions from the investigation of the modes of the structure and the response in different points in the structure and from an energy perspective are summarized as follows:

1. For the calculation of the response of the structure, a decomposition of the displacement vector of the structure into the modes of the superstructure clamped at the base and the quasi-static transmission of the free foundation modes into the superstructure is performed. Because of the rigidity of the walls, the free foundation modes do not properly represent the kinematics of the foundation, which is prevented to deform along the connection between the foundation and the walls. Therefore, a sufficiently high number of modes of the foundation (20) must be used. Accounting for the additional 20 modes of the superstructure, the total number of modes is twice. However, the number of modes used for the calculation of the soil impedance is the same in both cases. Therefore, the Craig-Bampton substructure method, that distinguishes between the modes of the foundation and the superstructure, is a valuable alternative to a modal decomposition based on the modes of the total structure, as it does not require a new dynamic SSI calculation when the properties of the structure are changed.

2. Due to the stiffness of the walls, no wall deformation modes appear in the frequency range of interest. In general, two situations may occur: (1) if the building is resting on a soft soil, no deformation of the walls occurs and the global motion of the building is dominated by rigid body kinematics; (2) in the case of a structure resting on a stiff soil, the walls deform in a quasi-static way, following the ground motion. Additionally, the presence of a stiff foundation prevents wall deformations. This has important consequences for vibration induced damage to buildings: wall cracking, caused by excessive deformations, is more likely to occur in the case where there is a quasi-static transmission of the ground motion into the walls.

3. The influence of the stiffness of the so[illegible]se in the free field and the structure is examined. The stiffness of the soil seriously affects the free field response. Higher vibration levels occur in the case of a soft soil.

4. When no dynamic SSI is accounted for, the assumption that the motion of the foundation is equal to the incident wave field results in unrealistic wall deformations when the structure is relatively rigid with respect to the soil. Allowing only for a rigid body motion of the foundation as a spatial average of the incident wave field, results in a better approximation of the wall displacements. When dynamic SSI is accounted for, the loss of energy due to radiation damping in the soft soil is benefficial. In general, the peak amplitudes decrease and the frequency content shifts to lower frequencies. The importance of a SSI calculation for structures founded on a soft soil is demonstrated by this example.

5. The response of the floors is dominated by the local bending modes. Dynamic SSI results in an increased attenuation of the floor response due to radiation damping in the soil.

6. The importance of the foundation flexibility has been investigated. The slab foundation is flexible with respect to the stiffness of the soil. The eigenfrequency of the first flexible eigenmode of the slab is close to the frequency range of interest. Therefore, the response of the centre of the foundation is close to the incident wave field. The box foundation is more rigid and follows the global rigid body kinematics of the entire building. Therefore, the effect of dynamic SSI is more important in the latter case.

7. The height of a building seriously influences the horizontal response. Bending effects of the structure increase to a large extent the horizontal motion. The SSI effect increases due to the

higher mass. The peak amplitude decreases and the frequency content shifts to lower frequencies. This example shows the importance of a SSI calculation for tall structures.

8. When no SSI is accounted for, energy has to be dissipated through material damping in the structure. The total energy in the structure is large, especially if the motion of the foundation is derived from the incident wave field assuming a flexible behaviour of the foundation. If SSI is accounted for, the total energy in the structure is smaller as energy can be dissipated through radiation damping in the soil. The energy in the structure is attenuated more rapidly.

9. The results of the parametric study have shown that the influence of the type of foundation is small. The highest vibration levels occur in the structure with a box foundation, although, the difference with the other types of foundations is not significant. As the stiffness of the structure with a box foundation is larger, the loss of energy due to radiation damping in the soil is smaller. The effect of the difference in mass for the three types of foundations on the SSI effect cannot be observed in the present example.

10. The results of the second study, it was found that, by allowing the uplifting and the sliding of the foundations the lateral displacement at the top of the structure has not changed significantly. However, allowing foundation uplifting reduces significantly the overturning moments and base shear up to –74,0%.

The results of this study allow estimating vibration in new-built and existing situations and may aid to develop effcient and cost-effective vibration isolation solutions.

Chapter 9

# 9. Conclusions and recommendations for further research

## 9.1 Conclusions

A numerical model for the prediction of wave induced vibrations in buildings has been developed and a MATLAB Toolbox is elaborated, which includes different methods, that is, FEM, BEM, FEM-BEM and the new method SFEM, which is recently introduced to SSI problems.

The coupling of a source model for the prediction of free field wave induced vibrations to the receiver model is emphasized. Both models are based on a subdomain formulation for dynamic SSI problems, while the direct formulation may also be easily imlemented. The formulation used is not novel, in a sense that it has been applied before, especially to the seismic analysis of structures. However, a substantial contribution of this work is the application to foundation wave induced vibrations. This is novel and not trivial, necessitating the mitigation of fictitious eigenfrequencies when a BEM is used for the computation of the impedance of embedded foundations. The basic procedure that is used in seismic engineering to solve dynamic SSI problems is extended, taking measures against the occurrence of fictitious eigenfrequencies.

First the numerical model for the prediction of vibrations in buildings due to wave propagation is elaborated. A dynamic foundation-soil interaction problem is solved to compute the incident wave field, which is subsequently applied to the structure.

The response in the structure is calculated using a subdomain formulation. A FEM is applied for the structure, whereas the unbounded soil domain is computed using a pseudo-spectral approach for the calculation of the wave propagation into a homogeneous or layered halfspace.

Very good correspondence with the results published in the literature is obtained with a constant dimensionless imaginary coupling parameter inversely proportional to the maximum dimensionless frequency that is considered and a unit dimensionless distance. As the results of this parametric study have proven that spurious non-zero displacements in the interior domain due to fictitious resonances disappear almost completely when these parameters are used, this solution procedure is subsequently used in the numerical model for wave induced vibrations in buildings with an embedded foundation.

Next, the computer Matlab program of the numerical prediction model for foundation wave induced vibrations accounting for dynamic SSI at the source and the receiver is successfully elaborated. The source model is subsequently coupled with the receiver and the incident wave field is applied to the structure. A spectral finite element method is used for the soil-structure model. An attempt has been made to trace the propagation of waves through the soil, the interaction with the building and the amplification in the structure.

The results of the numerical model are very satisfactory and show that the prediction model describes the essential physical phenomena, while meeting a reasonable accuracy. The numerical prediction model is a valuable tool in the calculation of the stresses under the dynamic behaviour of the structure.

Finally, the numerical prediction model is used in a parametric study as to elucidate the effect of dynamic SSI for three types of foundations. The response of a two and five story buildings due to the passage of a wave front field are considered. The results of three cases where the structure is founded on a slab foundation, a strip foundation and a box foundation are compared, accounting for or neglecting the effects of dynamic SSI. If SSI is disregarded, the motion of the foundation is found as the least squares approximation of the incident wave field assuming a rigid kinematic behaviour of the foundation. This assumption results in a rigid body motion of the foundation which is the spatial average of the incident wave field and is a valuable alternative for the SSI calculation. It is concluded that the effect of dynamic SSI on the response of this type of structure can be disregarded if the foundation is assumed to behave as a rigid body. Accounting for the dynamic SSI effect results in an increased attenuation of the floor response due to radiation damping in the soil.

The results of the parametric study have shown that the influence of the type of foundation is relatively small. The SSI effect is more important for tall structures. The coupled source-receiver model has proven to be a valuable tool in the prediction of wave induced vibrations and an important help to study the relevant physical phenomena. The present work contributes to a large extent to the latest developments in the area of dynamic SSI analysis. However, this prototype version of the numerical prediction model has to be translated into a practically-oriented toolbox that is applicable for design purposes, for the study of cases were vibration nuisance occurs or to predict the effect of vibration isolation measures.

An improved elements based on spectral element method allows to reduce complex SSI models to simpler and precise models taking into account absorbent boundary conditions. The numerical model described above has been implemented into a MATLAB toolbox. The calculation of the Green's functions of the horizontally layered halfspace is performed separately within the existing computer program SFEM2D.

## 9.2 Recommendations for further research

### 9.2.1 A further refinement of the soil model

The foregoing discussion of the prediction model allows to indicate a few points where the model can be refined:

- The loss of contact between the foundation and the soil or non-linear characteristics can be accounted for if a non-linear SSI model is used.
- The use of a plate model for the foundation instead of a beam model allows to account for the flexibility of the foundation's cross section. This refinement is important as far as the foundation's response is considered. Its influence on the free field response is limited to the high frequency contribution where the wavelength in the soil is small with respect to the width of the foundation.
- In the present model, it is assumed that the foundation is located at the soil's surface. The discussion on the numerical simulation results compared to literature results shows, that the embedment of the foundation has a considerable influence on the free field wave propagation. The importance of these refinements, is estimated to be relatively high compared to the impact of parameters as the dynamic soil characteristics.
- More elaborated work may be undertaken to improve the numerical methods used, that is, FEM, BEM, FEM-BEM and the new method SFEM. As each one of these constitute a specialized domain by itself.

### 9.2.2 A source-receiver model for wave induced vibrations

More than refining the soil model, the further study of wave induced vibrations requires the development of a model that allows to predict the dynamic response of nearby buildings. If it is assumed that the dynamic soil-structure interaction problems at the source and at the receiver can be uncoupled, a solution in two stages can be applied. First, the present source model is used to predict the incident wave field. Next, the interaction of the incident wave field with the structure is considered. The uncoupling of the source and the receiver is a wide-spread assumption in the field of earthquake engineering and is valid when the distance between the source and the receiver is much larger than the dominant wavelength in the soil. The main focus in further research should therefore go to the development of such a source-receiver model.

For the experimental validation of this model, it is advantageous to set up experiments where the building response as well as the free field response are measured simultaneously. This enables a rigorous validation at the different stages of the prediction model. In order to usefully apply this model for design purposes, it is important to indicate how the uncertainty on the various input parameters affects the prediction of the structural response. Such an approach results in the prediction of the probability of exceeding a given vibration level during a certain period of time. The source-receiver model allows to address a wider range of problems related to wave induced vibrations:

- The prediction of the building response provides insight in the factors that determine the vibration levels in buildings. The attenuation of the vibrations at the foundation level, the vertical resonance of flexible floors and the amplification of the horizontal vibrations over the height of the building are important phenomena that should be investigated in detail.
- Predictions of building vibrations can be combined with fatigue laws of brittle materials to study the occurrence of structural damage due to wave propagation induced vibrations.
- In problem situations where wave induced vibrations lead to structural damage, the model can be used to identify the causes.
- Numerical simulations under Matlab or others, allow to evaluate the efficiency of vibration isolating measures at the source, at the receiver or on the transmission path of the vibrations.
- For the design of important structures, such as micro-electronics laboratories or concert halls, where wave induced vibrations are of great concern, the model can be used in a design phase.
- For small structures, such as single story structures, the model can be used to formulate simplified guidelines. In practical guidelines, minimum eigen-frequencies for floors or other structural building parts can be advised.

## Appendix A

# A. Boundary Element Method

The BEM uses the Boundary Integral Equation (BIE) in elastodynamics, which is based on the dynamic reciprocity theorem that specifies the relationship between a pair of elastodynamic states. It is the dynamic extension of the classical reciprocity theorem of Betti-Rayleigh in elastostatics [48].

Consider a volume Ω with boundary ∑. The Betti-Rayleigh theorem in the frequency domain between two states can be written as:

$$\begin{aligned}&\int_{\Sigma} t_{1j}(\mathrm{x})u_{2j}d\Sigma + \int_{\Omega}\rho b_{1j}(\mathrm{x})u_{2j}(\mathrm{x})d\Omega \\ &= \int_{\Sigma} t_{2j}(\mathrm{x})u_{1j}d\Sigma + \int_{\Omega}\rho b_{2j}(\mathrm{x})u_{1j}(\mathrm{x})d\Omega\end{aligned} \tag{A.1}$$

where $u_{1j}$(x) and $u_{2j}$ (x) are elastodynamic displacement fields with the corresponding tractions $t_{1j}$ (x) and $t_{2j}$ (x). $\rho b_{1j}$ (x) and $\rho b_{2j}$ (x) denote the body forces.

The Green's displacements $u_{ij}^{G}(\xi,\mathrm{x})$ and tractions $t_{ij}^{G}(\xi,\mathrm{x})$ are introduced as one of the states in the dynamic reciprocity theorem (A.1). The second-order Green's tensor $u_{ij}^{G}(\xi,\mathrm{x})$ represents the displacement components in the direction $\mathbf{e}_j$ in the point ξ due to a Dirac load $\rho_s b_j(\mathrm{x}) = \delta(\mathrm{x}-\xi)\delta_{ij}\mathrm{e}_i$ in the direction $\mathbf{e}_j$ at the point ξ where the Kronecker delta $\delta_{ij}$ is given by:

$$\delta_{ij} = \begin{Bmatrix} 0 & i \neq j \\ 1 & i = j \end{Bmatrix} \tag{A.2}$$

The second-order Green's tensor $t_{ij}^{G}(\xi,\mathrm{x})$ represents the components of the traction vector in the direction $\mathbf{e}_j$ in the point **x** for the same load. On a boundary with a unit outward normal vector $n_k$, these tractions are equal to $\sigma_{jk}^{Gi}(\xi,\mathrm{x})n_k$, with $\sigma_{jk}^{Gi}(\xi,\mathrm{x})$ the stress tensor.

The Green's tensors $u_{ij}^{G}(\xi,\mathrm{x})$ and $t_{ij}^{G}(\mathrm{u})(\xi,\mathrm{x})$ show singularities of the order $r^{-1}$ and $r^{-2}$, respectively, for points ξ located on the boundary ∑. Therefore, the dynamic reciprocity theorem is not immediately applicable and a regularisation procedure has to be applied. A spherical extension with centre ξ and radius $\varepsilon$ of the interior domain $\Omega_s^{\mathrm{int}}$ is introduced and the radius $\varepsilon$ is taken to the limit, i.e. $\varepsilon \to 0$. This finally results in the boundary integral equation for the unbounded soil domain $\Omega_s^{ext}$ :

$$c_{ij}(\xi)u_i(\xi) = \int_{\Sigma} t_j(\mathrm{u})(\mathrm{x})u_{ij}^{G}(\xi,\mathrm{x})d\Sigma - \int_{\Sigma} t_{ij}^{G}(\xi,\mathrm{x})u_j(\mathrm{x})d\Sigma \tag{A.3}$$

with $c_{ij}$ (ξ) = 0 if $\xi \in \Omega_s^{\mathrm{int}}$, $c_{ij}$ (ξ) = 1/2 if $\xi \in \Sigma$ for a locally smooth boundary and a locally homogeneous domain at the point ξ, and $c_{ij}$ (ξ) = 1 if $\xi \in \Omega_s^{\mathrm{ext}}$.

The second integral is the Cauchy Principal Value (CPV) integral. This integral equation formulation is called a direct formulation as the unknowns have a physical meaning such as displacements or tractions.

If the BIE is based on the Green's functions for a horizontally layered halfspace, only a discretisation into elements of the interface ∑ between the soil and the structure is required and the number of unknowns is drastically reduced. The interface $\sum = \cup_{e=1}^{n_e} E_e$ is discretised into $n_e$ boundary elements $E_e$.

A collocation method is used where the displacements $u_j$ (x) and tractions $t_j$ (x) are interpolated from the value at the centre of gravity of each element:

$$u_j(\mathrm{x}) \approx \hat{u}_j(\mathrm{x}) = \sum_{l=1}^{n_e} \underline{u}_{jl} N_l(\mathrm{x}) \tag{A.4}$$

$$t_j(\mathrm{x}) \approx \hat{t}_j(\mathrm{x}) = \sum_{l=1}^{n_e} \underline{t}_{jl} N_l(\mathrm{x}) \tag{A.5}$$

where $\underline{u}_{jl}$ and $\underline{t}_{jl}$ are the displacements and the tractions at the element *l*. The element based shape functions $\mathrm{N}_l$(x) are equal to 1 on the element *l* and zero elsewhere. The discretisation of the displacements $u_j$ (x) and the tractions $t_j$ (x) according to equations (A.4) and (A.5) is introduced into the boundary integral equation (A.3) and is evaluated on the boundary ∑:

$$c_{ij}(\xi)\sum_{l=1}^{n_e} \underline{u}_{jl} N_l(\xi) = \sum_{l=1}^{n_e} \underline{t}_{jl} \int_{E_e} N_l(\mathrm{x}) u_{ij}^G(\xi,\mathrm{x})\, d\Sigma - \sum_{l=1}^{n_e} \underline{u}_{jl} \int_{E_e} t_{ij}^G(\xi,\mathrm{x}) N_l(\mathrm{x})\, d\Sigma \tag{A.6}$$

As the interpolation functions $N_l$(x) are equal to 1 on the element *l* and zero elsewhere, equation (A.6) becomes:

$$\sum_{l=1}^{n_e}\left( c_{ij}(\xi)\delta_{ij} + \int_{E_e} t_{ij}^G(\xi,\mathrm{x})\, d\Sigma \right) \underline{u}_{jl} = \sum_{l=1}^{n_e} \int_{E_e} u_{ij}^G(\xi,\mathrm{x})\, d\Sigma\, \underline{t}_{jl} \tag{A.7}$$

The boundary integral can be evaluated numerically for each element resulting in a fully-populated non-symmetrical system of 3 × $n_e$ algebraical equations:

$$\mathrm{H}\underline{\mathrm{u}} = \mathrm{G}\underline{\mathrm{t}} \tag{A.8}$$

where $\underline{\mathrm{t}}$ and $\underline{\mathrm{u}}$ are the nodal traction and displacement vectors. The elements of the fully populated and non-symmetric matrices **G** and **H** that represent the Green's displacement and traction tensor, respectively, are calculated as follows:

$$G_{ij} = \int_{E_e} u_{ij}^G(\xi,\mathrm{x})\, d\Sigma \tag{A.9}$$

$$H_{ij} = c_{ij}(\xi)\delta_{ij} + \int_{E_e} t_{ij}^G(\xi,\mathrm{x})\, d\Sigma \tag{A.10}$$

The calculation of the elements of the matrices **G** and **H** involves the evaluation of $n_e - 1$ regular integrals when the point ξ is located outside the element where the integral is evaluated and one singular integral if the point ξ coincides with the centre of gravity of the element. A regularisation technique is therefore applied [37].

# Appendix B

# B. Computation of the loading term due to a free field incident wave field

The loading term due to the incident wave field is computed on the boundary ∑ of the unbounded exterior soil domain $\Omega_s^{ext}$ using a BEM. This loading term $\mathbf{f}_\mathrm{b}$ due to an incident wave field applied on the structure is defined as:

$$\mathrm{f_b} = -\int_\Sigma \mathrm{N}_b^{\mathrm{T}} \mathrm{t}_s(\mathrm{u}_{\mathrm{inc}} + \mathrm{u}_{d0}) d\Sigma \tag{B.1}$$

The BIE for the locally diffracted wave field $u_{d0}$ defined on the boundary ∑ of the unbounded exterior soil domain $\Omega_s^{ext}$ is equal to:

$$c_{ij}(\xi)u_{d0i}(\xi) = \int_\Sigma t_j(u_{d0})(\mathrm{x})u_{ij}^G(\xi,\mathrm{x})d\Sigma - \int_\Sigma t_{ij}^G(\xi,\mathrm{x})u_{d0j}(\mathrm{x})d\Sigma \tag{B.2}$$

with $c_{ij}(\xi) = 1/2$ for $\xi \in \Sigma$ for locally smooth boundary and a locally homogeneous domain at the point ξ. The BIE (B.2) for the locally diffracted wave field $u_{d0}$ is defined on the boundary ∑ of the unbounded exterior soil domain $\Omega_s^{ext}$ with the unit outward normal vector $n_i^{ext}$ (figure B.1).

As the loading term due to the incident wave field is computed on the exterior soil domain $\Omega_s^{ext}$ using a BEM, the unit outward normal vector $n_i^{ext}$ is also preferred for the definition of the BIE for the incident wave field $\mathbf{u}_{\mathrm{inc}}$ on the boundary ∑, which is equal:

$$c_{ij}(\xi)u_{\mathrm{inc}i}(\xi) = \int_\Sigma t_j(u_{\mathrm{inc}})(\mathrm{x})u_{ij}^G(\xi,\mathrm{x})d\Sigma + \int_\Sigma t_{ij}^G(\xi,\mathrm{x})u_{\mathrm{inc}j}(\mathrm{x})d\Sigma \tag{B.3}$$

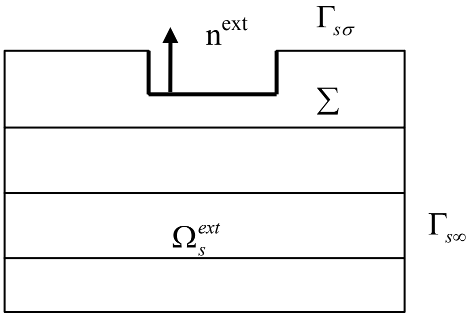

**Figure B.1**: The exterior soil domain $\Omega_s^{ext}$

Subtraction of equations (B.2) and (B.3) results into:

$$\begin{aligned} c_{ij}(\xi)(u_{d0i}(\xi)-u_{\mathrm{inc}i}(\xi)) &= \int_{\Sigma}(t_j(u_{d0})(\mathrm{x})+t_j(u_{\mathrm{inc}})(\mathrm{x}))u_{ij}^{G}(\xi,\mathrm{x})d\Sigma \\ &\quad -\int_{\Sigma}(t_{ij}^{G}(\xi,\mathrm{x})+u_{d0j}(\mathrm{x})+u_{\mathrm{inc}j}(\mathrm{x}))d\Sigma \end{aligned} \tag{B.4}$$

The displacement field $\mathbf{u}_0$ is decomposed into an incident wave field $\mathbf{u}_{\mathrm{inc}}$ and a locally diffracted wave field $\mathbf{u}_{d0}$ from which follows:

$$\mathrm{u}_{d0}(\xi)-\mathrm{u}_{\mathrm{inc}}(\xi)=\mathrm{u}_0(\xi)-2\mathrm{u}_{\mathrm{inc}}(\xi) \tag{B.5}$$

Equation (B.4) can then be elaborated as:

$$c_{ij}(\xi)(u_{0i}(\xi)-2u_{\mathrm{inc}i}(\xi))=\int_{\Sigma}(t_j(\mathrm{u}_0)(\mathrm{x})u_{ij}^{G}(\xi,\mathrm{x})d\Sigma-\int_{\Sigma}(t_{ij}^{G}(\xi,\mathrm{x})u_{0j}(\mathrm{x})d\Sigma \tag{B.6}$$

As $\mathbf{u}_0 = 0$ on the interface $\sum$ and with $c_{ij}$ ($\xi$) = 1/2 for $\xi \in \Sigma$ for a locally smooth boundary and a locally homogeneous domain at the point $\xi$, equation (B.6) reduces to:

$$-u_{\mathrm{inc}i}(\xi)=\int_{\Sigma}t_j(\mathrm{u}_0)(\mathrm{x})u_{ij}^{G}(\xi,\mathrm{x})d\Sigma \tag{B.7}$$

The tractions $t_j$ ($\mathbf{u}_0$)(x) in equation (B.7) are calculated in the centre of gravity of each element of the discretised boundary $\sum$. The loading term $\int_{\Sigma}\mathrm{N}_b^{\mathrm{T}}\mathrm{t}_s(\mathrm{u}_0)d\Sigma$ (equation B.1) due to the incident wave field is subsequently computed.

## Appendix C

# C. Matlab Code Implementation

MATLAB is a high-level technical computing language and interactive environment for algorithm development, data visualization, data analysis, and numerical computation. It allows one to solve technical computing problems faster than with traditional programming languages, such as C, C++, and Fortran. Add-on toolboxes (collections of special-purpose MATLAB functions) extend the MATLAB environment to solve particular classes of problems. You can integrate your MATLAB code with other languages and applications.

## C.1. The MATLAB Language

The MATLAB language supports the vector and matrix operations that are fundamental to engineering and scientific problems. It enables fast development and execution. With the MATLAB language, you can program and develop algorithms faster than with traditional languages because you do not need to perform low-level administrative tasks, such as declaring variables, specifying data types, and allocating memory. In many cases, MATLAB eliminates the need for ‘for’ loops. As a result, one line of MATLAB code can often replace several lines of C or C++ code. At the same time, MATLAB provides all the features of a traditional programming language, including arithmetic operators, flow control, data structures, data types, object-oriented programming (OOP), and debugging features.

## C.2. Object-oriented implementation in Matlab

In order to carry out the comparisons mentioned above, numerical tools had to be implemented. The Matlab environment was chosen for this purpose. The first reason is the ease of implementation due to the numerous toolboxes for numerical analysis provided by Matlab. The second reason is the ability of developing software within the object-oriented paradigm. Matlab possesses some special features (e.g. structures, cell arrays) that allow to pack information into some kinds of objects. Having adopted this way of programming, it should not be a hard task to transfer the Matlab code into a true object-oriented language like C++ and Fortran 90 or 95. In this sense, the computer code produced for the present study can be viewed as a paste-up for later more robust implementation in C++ or Fortran.

The first objective is to compare analysis methods for elastic two-dimensional mechanical problems. Precisely, two methods have been implemented, the simulated samples of the buildings carrying out a deterministic finite element analysis of the mechanical problem, and finally, the SFEM method is applied followed by the post-processing.

The second objective is rather the implementation of the Spectral Finite Element Method (SFEM) in the Matlab environment. In order to be able to compare a broad spectrum of methods, attention has been focused on elastic two-dimensional problems, even though more elaborated soil models (Mohr-Coulomb) is given and may be implemented in SFEM at a later stage. Object-oriented programming was aimed at, first to allow a versatile utilization of the code, second to build a base for later implementation in a true object-oriented language like C++. The different programs were applied to SSI problems in a large parametric study (chap6.). As far as is concerned, SFEM methods provide good results, when perfectly matched layers are used as boundary conditions. SFEM can give fair results and better insight for SSI problems, at a cost much lesser than that of the direct FEM or BEM methods.

For this purpose, different routines grouped in different repertories have been developed under the Matlab environment, and they may be looked at, as my contribution for SSI related problems:

- A random wave field discretization program called WAVE.
- A finite element code called FEM.
- A boundary element code called BEM.
- A hybrid code called FEM-BEM.
- A dynamic soil structure Interaction code called Dynamic_SSI.
- A BEM wave code called BEM-WAVE.
- A FEM wave code called FEM-WAVE.
- A Green's functions code called Greens_Function.
- A soil model code called Soil_Models
- a software implementing the SFEM method.

Due to limited space only few Matlab routines are given at the end of this section.

# C.3. SFEM Software

## C.3.1 History and credits

The main part of the elastic-isotropic solver was written in the mid 90's by Dimitri Komatitsch. The elastic-anisotropic solver and several significant improvements to the isotropic code were added by this research, the code was almost completely rewritten in a more object-oriented style in preparation to the implementation of higher level functionalities, such as multigrid, subcycling, adaptivity and multiscale coupling. While the extensive use of object-oriented features can degrade performance this is not critical in 2D simulation, the emphasis has been rather in code reusability and expandibility.

A simultaneous development for the simulation of earthquake dynamics was undertaken and is the main new feature of the current toolbox. Spontaneous rupture along multiple non-planar faults can be currently modelled. Although there is no intrinsic limitation on applying different friction laws, only linear slip weakening friction is implemented. Dynamic source simulations using methods that discretize the bulk, such as finite difference, finite element and spectral element methods, are more prone to high frequency numerical noise than boundary element methods.

## C.3.2 Overview

The SFEM package is a set of tools for the simulation and analysis of the seismic response of soil-structure systems as well as dynamic earthquake ruptures. Its core is SFEM2D, an explicit Spectral Element solver for the 2D elastic wave equation. The general flow of a simulation project is:

1. Mesh generation: SFEM2D works on an initial mesh made of quadrangles (basically a Q4 or Q9 finite element mesh).
2. Mesh quality verification, eventually return to previous step.
3. Numerical simulation.
4. Post-processing and visualization of the output.

This is a research code, and is still under development and provided "as is", and therefore it should not be considered by the user as a 100 % bug-free software package. We welcome comments, suggestions, module contributions and bug reports.

### C.3.3 The solver SFEM2D

Based on a mesh of quadrangular spectral elements and a set of material properties, sources and receivers SFEM2D solves the elastic wave equation applying a Spectral element method in space and a second-order explicit Newmark scheme in time. The SFEM, first introduced in Computational fluid dynamics, can be seen as a domain decomposition version of Pseudo-spectral methods or as a high order version of the Finite element method. It inherits from its parent methods the accuracy (spectral convergence) and the geometrical exibility and natural implementation of mixed boundary conditions, respectively.

### C.3.4 Installation

- Just put SFEM2D package in Matlab toolbox directory
- Launch Matlab, Add a new directory path to the list of included directories.

To do so use the Matlab addpath function, by using the **Set Path** dialog box. Select **Set Path** from the **File** menu in the MATLAB desktop by using the following **Syntax** addpath('SFEM2D'). For more details refer to MATLAB Function Reference book or the website: http://www.mathworks.com

## C.4 Conclusion

As a conclusion, it is noted that the present study is the first attempt to compare SFEM methods to FEM or BEM methods for a given SSI application. Throughout the description of the implementation, it has been seen that these methods have more in common than what the different research communities involved in their development sometimes think, at least from a computational point of view. Of course, three building type examples cannot be used to draw general conclusions of the superiority of some methods over others, but it gives at least a new light on their respective advantages and shortcomings.

# Bibliography

[1] Apsel R.J. and Luco J.E. On the Green's functions for a layered half-space. Part II. Bulletin of the Seismological Society of America, 73:931- 951, 1983.

[2] Aubry D. and Clouteau. D. A subdomain approach to dynamic soil-structure interaction. In V. Davidovici and R.W. Clough, editors, Recent advances in Earthquake Engineering and Structural Dynamics, 251-272. Ouest Editions/AFPS, Nantes, 1992.

[3] Awojobi A.O. Harmonic rocking of a rigid rectangular body on a semi-infinite elastic medium. Journal of Applied Mechanics, Transactions of the ASME, 88:547- 552, 1966.

[4] Azaiez M., Dauge M. et Y. Maday. Méthodes spectrales et des éléments spectraux. Rapport technique, Institut de Recherche Mathématique de Rennes, Université de Rennes I. 1994.

[5] Bécache E., Joly P., Tsogka C. Fictitious domains, mixed finite elements and perfectly matched layers for 2-D elastic wave propagation, Journal of Computational Acoustics 9 (3) 1175–1201, 2001.

[6] Bérenger JP. A perfectly matched layer for the absorption of electromagnetic waves. Journal of Computational Physics; 114(2):185-200, 1994.

[7] Bespalov A. On the usage of a regular grid for implementation of boundary integral methods for wave problems. Russian Journal of Numerical Analysis and Mathematical Modeling 15, 469–488, 2000.

[8] Biot M.A. Theory of propagation of elastic waves in a fluid-saturated porous solid. I. low frequency range. Journal of the Acoustical Society of America, 28(2):168 -178, 1956.

[9] Blume J.A. The Building and Ground Vibrator, Chapter 7 in “Earthquake Investigations in California 1934-1935”, U.S., Dept. of Commerce, Coast and Geoletic Survey, Special Publication No. 201, Washington, D.C. 1936.

[10] Bonnet M. Boundary Integral Equation Methods for Solids and Fluids. John Wiley and Sons, England, 1995.

[11] Celebi M. and Okawa I. Proc. UJNR Workshop on Soil Structure Interaction, Menlo Park, California, September 22-23, 1998, Open File Report 99-142, U.S. Geological Survey. 1999.

[12] Chew W. C. and Liu Q. H. Perfectly matched layers for elastodynamics: A new absorbing boundary condition, Journal of Computational Acoustics 4 (4) 341–359, 1996.

[13] Clouteau D. MISS, Manuel de validation, Impédance de fondations superficielles, rigides et non-pesantes. Laboratoire de Mécanique des Sols, Structures et Matériaux, Ecole Centrale de Paris, 2000.

[14] Clouteau D. MISS, Manuel de validation, Impédance de fondations enfouies, rigides et non-pesantes. Laboratoire de Mécanique des Sols, Structures et Matériaux, Ecole Centrale de Paris, 2003.

[15] Clough R.W. and Penzien J. Dynamics of structures. McGraw-Hill, New York, second edition, 1975.

[16] Collino F. Tsogka C. Application of the perfectly matched absorbing layer model to the linear elastodynamic problem in anisotropic heterogeneous media, Geophysics 66 (1) 294–307, 2001.

[17] Cohen G., Joly P. and Tordjman N. Construction and analysis of higher order finite elements with mass lumping for the wave equation. Proceedings of the SIAM conference, 152-160. Delaware, June 1993.

[18] Craig R. Structural Dynamics. An Introduction to Computer Methods. John Wiley & Sons 1981.

[19] Craig R. J. and Bampton M. Coupling of substructures for dynamic analyses. AIAA Journal, 6(7):1313-1319, 1968.

[20] Crouse C.B., Hushmand B. and Martin G.R. Dynamic Soil-Structure Interaction of a Single-Span Bridge, Earthquake Eng. and Structural Dynamics, 15, 711-729. 1987.

[21] De Barros F.C.P. and Luco J.E. Moving Green's functions for a layered visco-elastic half-space. Technical report, Department of Applied Mechanics and Engineering Sciences of the University of California, La Jolla, 1992.

[22] Degrande G., De Roeck G., Van den Broeck P. and Smeulders D. Wave propagation in layered dry, saturated and unsaturated poroelastic media. International Journal of Solids and Structures, 35(34-35):4753- 4778, 1998. Poroelasticity Maurice A. Biot memorial issue.

[23] Degrande G. A spectral and finite element method for wave propagation in dry and saturated poroelastic media. PhD thesis, Department of Civil Engineering, Katholieke Universiteit Leuven, 1992.

[24] Degrande G. and De Roeck G. A spectral element method for two-dimensional wave propagation in horizontally layered saturated porous media. Computers and Structures, 44(4):717-728, 1992.

[25] Degrande G., De Roeck G., Van den Broeck P. and Smeulders D. Application of a direct stiffness method to wave propagation in multiphase poroelastic media. Meccanica, 32(3):205-214, 1997.

[26] Desmet W. A wave based prediction technique for coupled vibroacoustic analysis. Ph. D. thesis, K.U.Leuven, division PMA, Leuven, 1998.

[27] Dhatt G. and Touzot G. The finite element method displayed. New York : John Wiley and sons. 1984.

[28] Dominguez J. Boundary Elements in Dynamics. Co-published by Computational Mechanics Publications, Southampton, Boston and Elsevier Applied Science London, New York, 1993.

[29] Erdik M. and Gülkan P. (1984). Assessment of Soil-Structure Interaction Effects on Prefabricated Structures, Proc. 8th World Conf. On Earthquake Eng., Vol. III, 913-920.

[30] Faccioli E., Maggio F., Quarteroni A. and Tagliani A.. Spectral-domain decomposition methods for the solution of acoustic and elastic wave equations. Geophysics 61(4), 1160-1174. 1996.

[31] Farhat C., Harari I. and Hetmaniuk U. A discontinuous Galerkin method with Lagrange multipliers for the solution of Helmholtz problems in the mid-frequency regime. Computer methods in applied mechanics and engineering 192, 1389–1419, 2003a.

[32] Farhat C. H. A simple and efficient automatic FEM domain decomposer. Rapport technique, University of Colorado, Boulder, Colorado. 1987.

[33] Farhat C., Wiedemann-Goiran P. and Tezaur R. A discontinuos Galerkin method with plane waves and Lagrange multipliers for the solution of short wave exterior Helmholtz problems on unstructured meshes. Wave Motion 39, 307–317, 2004.

[34] Fisher P., Ho L. W., Karniadakis G. E., Rønquist E. M. and Patera A. T. Recent advances in parallel spectral element simulation of unsteady incompressible flows. Computers and Structures 30, 217-231. 1988.

[35] Frazer L.N. and Gettrust J.F. On a generalization of Filon's method and thecomputation of the oscillatory integrals of seismology. Geophysical Journal of the Royal Astronomical Society, 76:461- 481, 1984.

[36] Garvin W. W. Exact transient solution of the buried line source problem. Proc. R. Soc. London Ser. A 234, 528-541. 1956.

[37] Gazetas G. and Mylonakis G. 1998. Seismic soil-structure interaction: new evidence and emerging issues. Geotechnical Earthquake Engineering and Soil Dynamics III ASCE, eds. P. Dakoulas M. K. Yegian, and R. D. Holtz, Vol. II, 1119-1174.

[38] Givoli D. High-order non reflecting boundary conditions without high-order derivatives, Journal of Computational Physics 170 (2) 849–870, 2001.

[39] Gordon W. J. and Hall C. A. Geometric aspects of the finite element method, with applications to partial differential equations, 769-784. Academic Press. A. K. Aziz editor. 1972.

[40] Gupta V.K. and Trifunac M.D. A Note on Contributions of Ground Torsion to Seismic Response of Symmetric Multistoried Buildings, Earthquake Eng. and Eng. Vibration, 10(3),27- 40. 1990.

[41] Guzina B.B. and Pak R.Y.S. On the analysis of wave motions in a multilayered solid. Quarterly Journal of Mechanics and Applied Mathematics, 54(1):13-37, 2001.

[42] Harari I., Slavutin M., and Turkel E. Analytical and numerical studies of a finite element PML for the Helmholtz equation, Journal of Computational Acoustics 8 (1) 121–137, 2000.

[43] Haskell N.A.. The dispersion of surface waves on multilayered media. Bulletin of the Seismological Society of America, 73:17- 43, 1953.

[44] Higdon R. L. Absorbing boundary conditions for elastic waves, Geophysics 56 (2) 231–241, 1991.

[45] Hu F. Q. On absorbing boundary conditions for linearized Euler equations by a perfectly matched layer, Journal of Computational Physics 129 (1) 201–219, 1996.

[46] Hudson D.E. Dynamic Tests of Full-Scale Structures. Chapter 7 in “Earthquake Engineering”, edited by R. Wiegel, Prentice Hall, New Jersey. 1970.

[47] Hughes T. J. R. and Marsden J. E. Classical elastodynamics as a linear symmetric hyperbolic system. Journal of Elasticity 8(1), 97–110. 1978..

[48] Hughes T.J.R. The finite element method: linear static and dynamic finite element analysis. Prentice-Hall, Englewood Cliffs, New Jersey, 1987.

[49] Housner G.W. Interaction of Building and Ground During an Earthquake, Bull Seism. Soc. Amer., 47, 179-186. 1957.

[50] Housner G.W. and McCann G.D. The Analysis of Strong-Motion Earthquake Records with the Electric Analog Computer, Bull. Seism. Soc. Amer., 39, 47-56. 1949

[51] Iguchi M. and Luco J.E. Vibration of Flexible Plate on Viscoelastic Medium. J. of Engng. Mech., ASCE, 108(6), 1103-1120. 1982.

[52] Iguchi M. and Yasui Y. Soil-Structure Interaction Researches Relating to Recent Strong Earthquakes in Japan, UJNR Workshop on Soil-Structure Interaction, Sept. 22-23, 1998, Open File Report 99-142, Paper 1, 1-17. 1999.

[53] Jirousek J. Basis for development of large finite elements locally satisfying all field equations. Computer methods in applied mechanics and engineering 14, 65–92, 1978.

[54] Kausel E. and Roësset J.M. Stiffness matrices for layered soils. Bulletin of the Seismological Society of America, 71(6):1743-1761, 1981.

[55] Jirousek J. and Wroblewski W. T-elements: State of the Art and Future Trends. Archives of Computational Methods in Engineering -State of the art reviews 3, 323–434,1996.

[56] Kausel E. and Roesset J.M. Semi-analytical hyper-element for layered strata. Journal of the Engineering Mechanics Division, Proceedings of the ASCE, 103(EM4):569-588, 1977.

[57] Kita E. and Kamiya N. Trefftz method: an overview. Advances in Engineering Software 24, 3–12, 1995.

[58] Khun, M. J. A numerical study of Lamb’s problem. Geophys. Prosp. 33, 1103-1137. 1985.

[59] Kosloff D., Reshef M. and Loewenthal D. Elastic wave calculations by the Fourier method. Bull. Seis. Soc. Am. 74, 875-891. 1984.

[60] Lamb H. On the propagation of tremors over the surface of an elastic solid. Phil. Trans. R. Soc. London. Ser. A 203, 1- 42. 1904.

[61] Lee U., Kim J. and Leung A. The spectral element method in structural dynamics. The Shock and Vibration Digest 32, 451–465. 2000.

[62] Lee U. and Lee J. Dynamic analysis of one- and two-dimensional structures using spectral element method. In N. Ferguson, H. Wolfe, and C. Mei (Eds.), International Conference on Recent Advances in Structural Dynamics, Southhampton, UK, 1997.

[63] Lee V.W. Investigation of Three-Dimensional Soil-Structure Interaction, Dept. of Civil Eng. Report No. 79-11, Univ. of Southern California, Los Angeles, California. 1979.

[64] Liu Q. H. Perfectly matched layers for elastic waves in cylindrical coordinates, Journal of the Acoustical Society of America 105 (4) 2075–2084, 1999.

[65] Lombaert G., Degrande G. and Clouteau D. Numerical modelling of free field traffic induced vibrations. Soil Dynamics and Earthquake Engineering, 19(7):473 - 488, 2000.

[66] Lombaert G., Degrande G. and Clouteau D. The influence of the soil stratification on free field traffic induced vibrations. Archive of Applied Mechanics, 71:661- 678, 2001.

[67] Luco J.E. Linear Soil Structure Interaction, in "Seismic Safety Margins Research Program (Phase I)", U.S. Nuclear Regulatory Commission, Washington D.C. 1980.

[68] Luco J.E. and Apsel R.J. On the Green's functions for a layered half-space. Part I. Bulletin of the Seismological Society of America, 4:909-929, 1983.

[69] Luco J.E., Trifunac M.D. and Udwadia F.E. An Experimental Study of Ground Deformations Caused by Soil-Structure Interaction, Proc. U.S. National Conf. On Earthquake Eng., 136-145. 1975.

[70] Luco J.E., Trifunac M.D. and Wong H.L. On the Apparent Change in Dynamic Behavior of a Nine-Story Reinforced Concrete Building, Bull. Seism. Soc. Amer., 77(6), 1961-1983. 1987.

[71] Lysmer J. and Drake L. A.. A finite element method for seismology. Methods in Computational Physics, Volume 11. New York : Academic Press. 1972.

[72] Lysmer J. and Kuhlmeyer R.L. Finite Dynamic Model for Infinite Media. ASCE J. of the Eng. Mech. Div., p.859-877.1969.

[73] Lysmer J. and Waas G. Shear waves in plane infinite structures. Journal of the Engineering Mechanics Division, Proceedings of the ASCE, 98(EM1):85-105, 1972.

[74] Mamlouk M. S. and Davies T.G. Elasto-dynamic analysis of pavement deflections. Journal of Transportation Engineering, Proceedings of the ASCE, 110(6):536-550, 1984.

[75] Marfurt K. J. Accuracy of finite-difference and finite-element modeling of the scalar wave equations. Geophysics 49, 533 -549. 1984.

[76] Merritt R.G. Effect of Foundation Compliance on the Earthquake Stresses in Typical Buildings, Ph.D. Thesis, Calif. Inst. of Tech., Pasadena, California. 1953.

[77] Miller G.F. and Pursey H. The field and radiation impedance of mechanical radiators on the free surface of a semi-infinite isotropic solid. Proceedings of the Royal Society, A223:521- 541, 1954.

[78] Mizuno H. Effects of Structure-Soil-Structure Interaction During Various Excitations, Proc. 7th World Conf. on Earthquake Eng., Vol. 5, 149-156. 1980.

[79] Mohammadi M. and Karabalis D.L. 3-D soil-structure interaction analysis by BEM: comparison studies and computational aspects. Soil Dynamics and Earthquake Engineering, 9(2):96-108, 1990.

[80] Moslem K. and Trifunac M.D. Effects of Soil Structure Interaction on the Response of Buildings During Strong Earthquake Ground Motions. Dept. of Civil Engrg, Report No. 86-04, Univ. of Southern California, Los Angeles, California. 1986.

[81] Ohtsuka Y., Fukuoka A., Yanagisawa E. and Fukudome H. Embedment Effect on Dynamic Soil-Structure Interaction, Proc. 10th world Conf. on Earthquake Eng., Vol. 3, 1707-1712. 1992.

[82] Oien M.A. Steady motion of a rigid strip bonded to an elastic half space. Journal of Applied Mechanics, Transactions of the ASME, 89:328-334, 1971.

[83] Oien M.A. Steady motion of a plate on an elastic half space. Journal of Applied Mechanics, Transactions of the ASME, pages 478 - 484, 1973.

[84] Patera A. T. A spectral element method for fluid dynamics : laminar flow in a channel expansion. J. Comput. Phys. 54, 468 - 488. 1984.

[85] Petrovski J. Influence of Soil-Structure Interaction Effects on Dynamic Response of Large Panel Prefabricated Buildings, Proc. Second International Conf. on Microzonation for Safer Construction-Research and Application, Vol. III, 1269-1277. 1978.

[86] Pluymers B., Desmet W., Vandepitte D. and Sas P. Application of an efficient wave-based prediction technique for the analysis of vibro-acoustic radiation problems. Journal of Computational and Applied Mathematics 168, 353–364, 2004.

[87] Ramirez-Centeno M. and Ruiz-Sandoval M. Experimental Study of the Soil-Structure Interaction Effects on Three Different Kinds of Accelerometric Bases, Proc. 11th World Conf. on Earthquake Eng., Disc 2, Paper No. 719, 1996.

[88] Rayleigh L. J. W. S. On waves propagated along the plane surface of an elastic solid. Proc. London Math. Soc. 17, 4-11. 1887.

[89] Règles Parasismiques Algériennes “RPA-99”, DTR 1999, Centre National de Recherche Appliquée en Génie Parasismique (CGS) Hussein Dey, 1999, Algiers, (in French).

[90] Rodrigues D. Simulation de la propagation d’ondes sismiques sur machine massivement parallèle. Thèse de Doctorat, École Centrale de Paris, Paris. 1993.

[91] Rosset J.M., Kausel E. Dynamic Soil-Structure Interaction. Proc. Second International Conference On Numerical Methods In Geomechanics, Blacksburg, Virginia, V 2, 3-19. 1976.

[92] Rubin S. Improved component-mode representation for structural dynamic analysis. AIAA Journal, 13(8):995-1006, August 1975.

[93] Şafak E. Propagation of seismic waves in tall buildings. Struct. Design Tall Build. 7, 295-306. 1998.

[94] Şafak E. Wave-propagation formulation of seismic response of multistory buildings. Journal of structural engineering. April 1999.

[95] Schneider S. Application of fast methods for acoustic scattering and radiation problems. Journal of Computational Acoustics 11, 387–401, 2003.

[96] Seriani G. and Priolo E. Spectral element method for acoustic wave simulation in heterogeneous media. Finite Elements in Analysis and Design 16, 337-348. 1994.

[97] Simo J. C. Algorithms for static and dynamic multiplicative plasticity that preserve the classical return mapping schemes of the infinitesimal theory. Comp. Meth. Appl. Mech. Eng. 99, 61-112. 1992.

[98] Sochaki J., Kubichek R., George J., Fletcher W. R. and Smithson S. Absorbing boundary conditions and surface waves, Geophysics 52 (1) 60–71, 1987.

[99] Song C. and Wolf J. P. The scaled boundary finite-element method " alias consistent infinitesimal finite-element cell method" for elastodynamics, Computer Methods in Applied Mechanics and Engineering 147 (3–4) 329–355, 1997.

[100] Stojek M. Finite T-elements for the Poisson and Helmholtz equations. Ph. D. thesis, ´Ecole Polytechnique Fédéral de Lausanne, Lausanne, 1996.

[101] Stokoe K.H.II, Mok Y.J., Lee N. and R. Lopez. In situ seismic methods: Recent advances in testing, understanding and applications. In Conferenze di geotecnica di Torino, XIV ciclo, Comportamento dei terreni e delle fondazioni in campo dinamico, 1989.

[102] Teixeira F. L. and Chew W. C. Unified analysis of perfectly matched layers using differential forms, Microwave and Optical Technology Letters 20 (2) 124–126, 1999.

[103] Teixeira de Freitas J. and Cisma siu C. Hybrid-Trefftz displacement element for spectral analysis of bounded and unbounded media. International Journal of Solids and Structures 40, 671–699, 2003.

[104] Thomson W.T. Transmission of elastic waves through a stratified solid medium. Journal of Applied Physcis, 21:89-93, 1950.

[105] Tordjman N. Éléments finis d’ordre élevé avec condensation de masse pour l’équation des ondes. Thèse de Doctorat, Université Paris IX Dauphine, Paris. 1995.

[106] Triantafyllidis T. and Prange B. Rigid circular foundation: dynamic effects of coupling to the half-space. Earthquake Engineering and Structural Dynamics, 14:391- 411, 1986.

[107] Trifunac M.D. Interaction of Shear Wall with the Soil for Incident Plane SH Waves, Bull. Seism. Soc. Amer., 62(1), 63-83. 1972a.

[108] Trifunac M.D., Ivanovic S.S., Todorovska M.I., Novikova E.I. and Gladkov A.P. Experimental Evidence for Flexibility of a Building Foundation Supported by Concrete Friction Piles, Soil Dynamics and Earthquake Eng., 18(3), 169-187. 1999

[109] Trifunac M.D. and Todorovska M.I. Recording and Interpreting Earthquake Response of Full Scale Structures, Proc. NATO Advanced Research Workshop on Strong Motion Instrumentation for Civil Eng. Structures, June 2-5, Istanbul, Kluwer. 1999a.

[110] Tsynkov S. V. Numerical solution of problems on unbounded domains. A review, Applied Numerical Mathematics 27 (4) 465–532, 1998.

[111] Ushnish Basu and Anil K. Chopra. Perfectly matched layers for transient elastodynamics of unbounded domains. International Journal for Numerical Methods in Engineering, 59(12), 2004.

[112] Van Hal B., Hepberger A., Priebsch H.-H., Desmet W. and Sas P. High performance implementation and conceptual development of the wave based method for steady-state dynamic analysis of acoustic problems. In Proceedings ISMA2002 - Noise and Vibration Engineering, Leuven, Belgium, pp. 817–826, 2002.

[113] Waas G. Linear two-dimensional analysis of soil dynamic problems in semi-infinite layer media. PhD thesis, Department of Civil Engineering, University of California, Berkeley, 1972.

[114] Wheeler L.T. and Sternberg E. Some theorems in classical elastodynamics. Archive for Rational Mechanics and Analysis, 31:51-90, 1968.

[115] Wolf J.P. Dynamic soil-structure interaction. Prentice-Hall, Englewood Cliffs, New Jersey, 1985.

[116] Wong H. and Luco J. Dynamic response of rigid foundations of arbitrary shape. Earthquake Engineering and Structural Dynamics, 4:579 - 587, 1976.

[117] Wong H. and Luco J. Dynamic response of rectangular foundations to obliquely incident seismic waves. Earthquake Engineering and Structural Dynamics, 6:3-16, 1978.

[118] Yun C. B., Kim D. K., Kim J. M. Analytical frequency-dependent infinite elements for soil-structure interaction analysis in two-dimensional medium, Engineering Structures 22 (3) 258–271, 2000.

[119] Zeng Y. Q., He J. Q. and Liu Q. H. The application of the perfectly matched layer in numerical modeling of wave propagation in poroelastic media, Geophysics 66 (4) 1258–1266, 2001.

[120] Zhang Y. G. and Ballmann J. Two techniques for the absorption of elastic waves using an artificial transition layer, Wave Motion 25 (1)15–33, 1997.

[121] Zielinski A. and Herrera I. Trefftz method: fitting boundary conditions. International Journal for Numerical Methods in Engineering 24, 871–891, 1987.